Imperial College London

Modelling the variability and reliability of high-performance composite materials

by

Marco Alexandre da Costa Alves

Department of Mechanical Engineering, Imperial College London,
South Kensington Campus, London SW7 2AZ, United Kingdom

This thesis is submitted for the degree of
Doctor of Philosophy of Imperial College London

2020

Abstract

Carbon-fibre reinforced polymers (CFRPs) are the material of choice for light-weight structural applications. The microstructure of CFRPs ranges from simple to more complex architectures, allowing them to be tailored for specific applications. However, composite material systems present intrinsic variability which leads to a stochastic mechanical response. The behaviour of composite materials under different loading conditions (ranging from static to complex cyclic loads) is still to be fully understood. This study aims to develop models to predict the variability and reliability of different composite architectures, leading to safer and more reliable composite structure designs.

Tow-Based Discontinuous Composites (TBDCs) are an up-and-coming class of high-performance discontinuous composites, which combine high manufacturability and good mechanical properties. Their architecture, composed by randomly oriented carbon fibre tows, results in a microstructure with the most extreme levels of variability. The spatial variability of TBDC strain fields was quantitatively characterised with a new proposed method, which enabled the identification of a relationship between the characteristic length-scales of the strain fields and the material's microstructural features. The intrinsic variability of these materials leads to a notch insensitive behaviour, that was experimentally characterised not only for circular notches of different diameters but also for non-circular notch geometries.

A stochastic Finite Element (FE) framework able to replicate the intrinsic variability of TBDC materials was proposed. The framework considers an implicit representation of the material's microstructure, by using a Stochastic Equivalent Laminate analogy, and predicts the elastic response, damage initiation and final failure of TBDCs under static loading. The FE framework was validated against experimental results for different TBDC material systems, with both random and preferential fibre orientations.

Numerical models were used to explore the design space of discontinuous composites, in order to identify optimal microstructure designs that maximise their stiffness and strength. Ultra-thin tapes (20 μm) of high modulus (425-760 GPa) carbon-fibres were used to manufacture and test TBDC under static loading. The experimental results showed increases of strength up to 100%, when compared with commercially available

TBDC systems, and resulted in a discontinuous composite with mechanical properties that match the strength and overcome the stiffness of aerospace-graded continuous-fibre quasi-isotropic laminates.

Composites are often subjected to cyclic loading, presenting further challenges in predicting their reliability. An analytical model to predict the fatigue response of unidirectional composites was also proposed. Due to its analytical formulation, the model was able to predict, for the first time in the literature, the evolution of the micromechanical fatigue damage in composites with any number of fibres. Strength reductions throughout fatigue life (up to 10 million cycles) are computed in less than sixty seconds. The model generates stochastic S-N curves and was successfully validated against experiments from the literature.

This work shows the potential of TBDCs to match the mechanical properties of continuous-fibre quasi-isotropic laminates while still having high manufacturability. The models developed throughout this work can be used to support material design, to identify optimal TBDC microstructures for enhanced mechanical performance.

Declaration of originality

The work hereby presented is based on research carried out by the author at the Department of Mechanical Engineering of Imperial College London, and it is all the author's own work except where otherwise acknowledged. No part of the present work has been submitted elsewhere for another degree or qualification.

Copyright declaration

The copyright of this thesis rests with the author and is made available under a Creative Commons Attribution Non-Commercial No Derivatives licence. Researchers are free to copy, distribute or transmit the thesis on the condition that they attribute it, that they do not use it for commercial purposes and that they do not alter, transform or build upon it. For any reuse or redistribution, researchers must make clear to others the licence terms of this work.

Contents

List of Figures **xiii**

List of Tables **xix**

Acknowledgements **xxi**

List of Publications **xxiii**

Acronyms and Abbreviations **xxvii**

Notation **xxix**

1 Introduction **1**

1.1 Background 1

1.2 Objectives 4

1.3 Thesis Outline 4

2 The influence of 3D microstructural features on the elastic behaviour of Tow-Based Discontinuous Composites **7**

2.1 Introduction 7

2.2 Model development 10

2.2.1 Microstructure generator 10

2.2.2 Stiffness model 12

2.3 Results 16

2.3.1 Computational efficiency and numerical convergence of the microstructure generator 16

2.3.2 Microstructure generator results and validation 18

2.3.3 Stiffness model validation and results 21

2.3.4 Guidelines for the modulus measurement of TBDCs 25

2.4 Discussion 27

2.4.1 Potential for optimising commercial TBDC systems 27

2.4.2 Relative influence of tow discontinuities and waviness on the properties of TBDCs . . . 27
2.4.3 Contribution of the microstructure generator and stiffness model to the state of the art . . . 27
2.5 Conclusion . . . 28

3 Ultra-strong and stiff randomly-oriented discontinuous composites: closing the gap to quasi-isotropic continuous-fibre laminates 31

3.1 Introduction . . . 31
3.2 Material Design . . . 33
3.2.1 Failure criteria for discontinuous composites . . . 33
3.2.2 Improving the strength of TBDCs via microstructure design . . . 36
3.3 Materials and experimental methods . . . 40
3.3.1 Materials and manufacturing procedure . . . 40
3.3.2 Testing and analysis . . . 42
3.4 Results . . . 42
3.4.1 Tensile test results . . . 42
3.4.2 Fracture surfaces . . . 45
3.4.3 Comparison with other material systems . . . 45
3.5 Discussion . . . 49
3.5.1 Effect of microstructure on mechanical properties . . . 49
3.5.2 Improvement over existing materials . . . 50
3.6 Conclusions . . . 53

4 Characterising and modelling the variability of TBDC material systems 55

4.1 Introduction . . . 55
4.2 Experimental characterisation of the spatial variability of strains in TBDCs 57
4.2.1 Materials and testing . . . 57
4.2.2 Direct results from DIC strain fields . . . 58
4.2.3 Spatial variability of the DIC strain fields . . . 58
4.3 Modelling the spatial variability of mechanical properties in TBDCs . . . 61
4.3.1 Explicit mesoscale representation of variability . . . 62
4.3.2 Modelling approach . . . 62
4.3.3 Implicit mesoscale representation of variability . . . 67
4.3.4 Results . . . 70
4.4 Discussion . . . 74
4.4.1 Novelty . . . 75

4.4.2 Potential impact 76
4.5 Conclusions 76

5 A 3D stochastic finite element framework for modelling the stochastic mechanical behaviour of TBDCs 79

5.1 Introduction 79
5.2 Materials and methods 81
5.3 Model development 82
5.3.1 3D assignment of stochastic mechanical properties 82
5.3.2 Failure criterion for an equivalent UD discontinuous ply 86
5.4 Results 91
5.4.1 Analysis and characterisation of the strain variability 92
5.4.2 Sensitivity to the mesh size and to numerical input parameters . 94
5.4.3 Model results and validation against experiments 95
5.5 Discussion 97
5.5.1 Reproducing the stochastic nature of TBDCs and the problem with the deterministic process simulation software 97
5.5.2 Novelty and potential impact 99
5.6 Conclusions 100

6 Prediction and experimental validation of the notch (in)sensitivity of Tow Based Discontinuous Composites 101

6.1 Introduction 101
6.2 Materials and experimental procedure 103
6.3 Failure analysis 104
6.3.1 Nonlocal failure index averaging 105
6.4 Results 107
6.4.1 Un-notched strength 107
6.4.2 Notch sensitivity analysis 107
6.5 Discussion 113
6.6 Conclusions 114

7 A computationally-efficient micromechanical model for the fatigue life of unidirectional composites under tension-tension loading 117

7.1 Introduction 117
7.2 Fatigue Model 120
7.2.1 Model idealisation 120
7.2.2 Static stress fields near a fibre-break considering a cohesive interface 121

7.2.3 Fatigue damage model for the interface . . . 124
7.2.4 Fatigue strength model . . . 125
7.2.5 Model implementation . . . 132
7.3 Results . . . 132
7.3.1 Static results . . . 132
7.3.2 Convergence study . . . 133
7.3.3 Parametric study . . . 134
7.3.4 Validation against experimental results . . . 137
7.4 Discussion . . . 139
7.4.1 Physical phenomena predicted by the model . . . 139
7.4.2 Uncertainty in model inputs and their influence in the predicted fatigue behaviour . . . 141
7.5 Conclusions . . . 142

8 Conclusions **145**

8.1 On modelling the variability of TBDCs . . . 145
8.2 On predicting failure of TBDCs . . . 146
8.3 On improving the mechanical performance of TBDCs . . . 147
8.4 On predicting the reliability of composites . . . 148
8.5 Novelty . . . 148
8.6 Impact . . . 150

9 Further work **151**

9.1 Characterising and manufacturing of TBDCs for structural applications 151
9.2 Broadening the applicability of the current stochastic FE framework for TBDCs . . . 152
9.3 Improvements to the analytical fatigue model . . . 152

Bibliography **155**

A Microstructure generator appendices **A1**

A.1 Derivation of the condition for maximum fibre content during tow deposition . . . A1
A.2 Auxiliary matrices for the stiffness model . . . A2
A.3 Details of the acquisition of the micro-CT images and measurement of the out-of-plane angle distributions . . . A3
A.4 Volume fraction distributions measured from micro-CT volumes . . . A4
A.5 . . . A6

B Orientation averaging technique **B1**

C Process simulation of plates and fibre orientation mapping to the specimen mesh **C1**

D Uncertainty of the definition of the notch failure region **D1**

E Fatigue model appendices **E1**

E.1 Geometry of the cross-section of a fibre bundle E1

E.2 Linear approximation to non-uniform stress fields near fibre/sub-bundle breaks E2

List of Figures

1.1 Example of a heterogeneous microstructure of TBDCs [2]. 2

2.1 Features of the microstructure generator developed in Section 2.2.1. The examples described in this figure use the inputs shown in Table 2.4. 13
2.2 Convergence of the statistics of the microstructure generator and the predicted longitudinal stiffness with the selected grid spacing dimensions, s_{grid}; model run times were obtained with a Intel(R) Core(TM) i7-6700 CPU at 3.40GHz. 17
2.3 Effect of V_{th}^{f} on the maximum volume fraction achieved and in the predicted modulus E_{xx}; three specimens were generated for each configuration. For each configuration, the value of $V_{\text{max}}^{\text{f}}$ is taken as the maximum fibre volume fraction obtained for the three specimens, and the value of E_{xx} is the average value of the three specimens; the error bars represent one standard deviation. 18
2.4 Cross sections of a TBDC specimen (Hexcel's HexMC-M77 [2]) obtained by (a) micro-CT and (b) high resolution optical microscopy. 18
2.5 Experimental validation of the microstructure generator's statistics (using HexMC-M77 specimens [2]). 19
2.6 Influence of the local in-plane angle distribution on the distributions of out of plane angles predicted by the microstructure generator. The orientation tensors that define the in-plane orientation distributions considered are defined in Appendix A.5. 20
2.7 Validation of the modulus predictions of the model against experimental results, for TBDCs with different tow geometries. 22
2.8 Parametric study on the effect of the tow geometry in the in-plane modulus reduction. For subfigures a-e, the blue dots represent the obtained modulus reduction for each virtual specimen; 10 virtual specimens were analysed for each configuration. The mean values for each configuration are connected with a black line and the grey region encapsulates the ± one standard deviation boundary. 24
2.9 Modulus uncertainty ratio for different combinations of tow and gauge lengths. 26

3.1 Model material systems used to represent TBDCs. 34
3.2 Governing failure criteria for discontinuous composites. 37
3.3 Analysis of the influence of the different microstructural features/properties on the mechanical properties of TBDCs. The baseline material system is the HexMC-M77 [2], as defined in Tables 3.1 and 3.2. 38
3.4 Manufacturing procedure of the TBDC plates. 41
3.5 Experimental tensile test results of the different TBDC configurations tested (scaled to $V^{\mathrm{f}} = 57\%$), and comparison against the commercially available HexMC-M77 [2]; the error bars represent one standard deviation. 44
3.6 Comparison between the numerical predictions and experimental results for the strength of three different plate configurations. 45
3.7 Fracture surfaces (50 × 50 mm) of specimens from the different plate configurations. 46
3.8 Micrographs of cross-sections of different material systems. 47
3.9 Comparison of the mechanical properties between the HM-20-1600 material proposed in this study, and discontinuous material systems reported in the literature (specified in Table 3.5). The mechanical properties of all materials have been linearly normalised to $V^{\mathrm{f}} = 57\%$ for comparison purposes. 48
3.10 Comparison between the mechanical properties of the HM-20-1600 and UHM-100-800 configurations and a continuous fibre QI laminate (specified in Table 3.5). 49

4.1 Analysis of the strain fields obtained with DIC for all the tested specimens. 59
4.2 Proposed method for the analysis of the spatial variability of the experimental DIC strain fields, based on the triangulation of strain peaks and troughs. 60
4.3 Cross-correlation analysis of the DIC strain fields. 61
4.4 Modelling approach with explicit representation of the microstructure: each partition of the virtual specimen is represented by a local stochastic equivalent laminate (SEL). 62
4.5 Analysis and characterisation of strain fields generated by FE models with explicit representation of the microstructure of TBDCs. 63
4.6 Longitudinal strain fields of plates with different tow geometries. 65
4.7 Cross correlation analysis of the influence of the in-plane tow geometry on the spatial length-scales of the associated strain fields; results are shown for a value of $l^{\mathrm{t}} = 50$ mm. 66
4.8 Characteristic length-scales of virtual specimens from the cross-correlation analysis (represented by the circular markers), and comparison with 2 analytical solutions (represented by the solid lines). 66

4.9 Variability analysis of the strain fields resulting from the different plate configurations of Table 4.3.. 68
4.10 Seed points at the nodes of an unstructured mesh. 69
4.11 Flow-chart of the proposed Finite Element Methodology. 71
4.12 Mesh size dependency analysis. 72
4.13 Analysis of the influence of s_{seed} on the characteristic length-scales of the predicted strain fields. 73
4.14 Spatial distribution analysis of the strain fields obtained with the implicit FE models. 74

5.1 The mapping of orientation tensors a_{ij} resulting from the process simulation to the seed points used in the stochastic FE framework. The direct mapping of the a_{ij} to each element of the structural mesh is also shown, and used in a deterministic FE approach (described in Section 5.4). 83
5.2 The modular implementation of the stochastic framework. 83
5.3 The three different coordinate systems CSYS defined in the model. 84
5.4 Transformation of the FOD function in from the global to the SEL reference system; representation of $\mathcal{F}^{\text{SEL}}(\theta, \frac{\pi}{2})$, highlighted by the dashed-line in Figure 5.4b. 86
5.5 Implementation flowchart of the stochastic framework. 87
5.6 Discretisation of the $\mathcal{F}^{\text{SEL}}(\theta, \frac{\pi}{2})$ and probabilistic stacking sequence reconstruction. 88
5.7 Approximated ITS failure surface. 89
5.8 Implementation flowchart of the UMAT used in the stochastic FE framework. 91
5.9 Analysis of the variability of the FE (deterministic and stochastic) and DIC strain fields for the HexMC-M77 material. 93
5.10 Fields of outputs obtained with the stochastic FE framework for a HexMC-M77 specimen. 94
5.11 Influence of N_{t} on the predictions of the stochastic FE framework for the HexMC-M77 material system. 95
5.12 Effects of numerical parameters on the predictions and efficiency of the framework for a given HexMC-M77 virtual specimen. 96
5.13 Validation of the stochastic FE framework against the experimental results of the CF-SMC. 97
5.14 Validation of the stochastic FE framework against the experimental results of the HexMC-M77. 98

6.1 Geometry specification of the water jet cut notched specimens; the red shaded area encloses the hole/notch failure region. 104
6.2 Nonlocal averaging scheme on the resulting F_{I} field obtained with the stochastic FE framework. 106

6.3 Un-notched stiffness and strength: comparison between experimental results and numerical predictions. 108
6.4 Comparison between the notch sensitivity experimentally measured with the open-hole specimens and the numerical predictions. Gross strength distributions are normalised by the average strength of the un-notched specimens. 109
6.5 Strength distribution of the specimens with modified notch geometries, and the correspondent Weibull distribution fit; comparison between the notch sensitivity experimentally measured with the one predicted by the FE framework (constant nonlocal averaging) - (b) % failure at the notch and (c) gross strength distributions. 110
6.6 Relation between: (a) the value of $|\nabla \bar{F}_{\mathrm{I}}|$ and the stress concentration factor k; (b) the internal length parameter l_{nl} and the $|\nabla \bar{F}_{\mathrm{I}}|$. 112
6.7 Comparison between the standard nonlocal averaging (with constant $l_{\mathrm{nl}} = 1.5$ mm) and the adaptive nonlocal averaging (where the value of l_{nl} is scaled based on the value of $|\nabla \bar{F}_{\mathrm{I}}|$). 113
6.8 Comparison between the notch sensitivity experimentally measured with the one predicted by the nonlocal FE framework (with the adaptive nonlocal averaging scheme) - (a) % failure at the notch and (b) gross strength distributions. 113

7.1 Hierarchical fibre bundles built in a square fibre arrangement [114]. 120
7.2 Static stress fields and length scales near a fibre-break within a level-[1] bundle. 122
7.3 Linear cohesive law of the interface under static shear stresses. 123
7.4 Stress fields and length scales in a level-[1] bundle during the crack propagation phase. 127
7.5 Stress fields and length scales in a fully debonded level-[1] bundle. 128
7.6 Evolution of the effective recovery length within a level-[4] bundle (i.e. interfacial crack propagating around a level-[3] sub-bundle) after the averaging process (using the inputs defined in Tables 7.2-7.4 associated to the material system `T/D`, with $\sigma^{\infty}_{\mathrm{peak}} = 2.5$ GPa and $R^{\infty} = 0.1$). 132
7.7 Flowchart of the numerical implementation of the model. 133
7.8 Static analysis assuming different behaviours of the interface: i) perfectly-plastic behaviour [114]; ii) cohesive behaviour and linear approximation of the stress fields in the sub-bundle; iii) cohesive behaviour and analytical stress fields in the sub-bundle (see Appendix E.2 for the difference between (ii) and (iii)). 134
7.9 Convergence analysis of the model with the adaptive cycle jump scheme. . . 135
7.10 Parametric study on the expected S-N curve predicted by the model. 136

7.11 Size-effects on the expected S-N curves predicted by the model, for the A/P material defined in Tables 7.2-7.4. 137
7.12 Validation of the expected S-N curves predicted by the model against a set of experimental results [91], and analysis of the effect of the Weibull parameters (measured at different gauge length l_0^f, see Table 7.3) on the predicted S-N curve. Model inputs are defined in Tables 7.2-7.4 (for the T/D fibre/matrix combination). 138
7.13 Validation of the model against experimental results. 138
7.14 Expected duration of the crack initiation and propagation phases (for several sub-bundle levels-[i]) in the overall fatigue life of the level-[18] bundle analysed in Figure 7.13b. 139

A.1 Measured out of plane angles distributions for two different window sizes. . A4
A.2 Measured volume fraction distributions for two different window sizes. . . . A6

C.1 Process simulation results. C2

D.1 Upper and lower bounds of the failure region for the different tested notched configurations. D2
D.2 Influence of the size of the failure region in the numerical prediction of the ratio of notch failures for both the open hole and modified notch specimens. D2

E.1 Shear lag perimeter of a level-[i] sub-bundle when considering a square fibre-packing and preferential interfacial failure [114]. E1
E.2 Comparison between the linear approximation and the analytical solution of stress concentration stress fields in the surviving fibre/sub-bundle $\mathcal{B}$. . . E2

List of Tables

2.1 Specification of the microstructural parameters for the HexMC-M77 material system, and for the validation of the microstructure generator. 16
2.2 Specification of the geometrical and numerical inputs for the virtually generated specimens used in Section 2.3. 16
2.3 Material properties used as input for the stiffness model (modulus values are in GPa). The UD material from which the tows are made is assumed to be transversely isotropic. 21
2.4 Specification of the microstructural inputs for the TBDC material system tested by Li et al. (2017) [15] and analysed in Figure 2.7a. 21

3.1 Tow properties used as model inputs for the TBDC baseline configuration (HexMC-M77). Modulus values are in GPa, strength values are in MPa, toughness values are in kJ/m^2 and volume fraction in %. The values of Y_{T} and S are correspond to the raw strength values, which are corrected for in-situ effects in $Y_{\mathrm{is,T}}$ and S_{is}. 39
3.2 Properties used in the analysis of the influence of the tow mechanical properties on the strength of TBDCs. 39
3.3 Mechanical properties of the different fibre types used in the experiments. . 41
3.4 Configurations of the different TBDC plates manufactured. 41
3.5 Configurations of the different CFRP systems compared in Figure 3.9. . . . 46

4.1 Specification of the microstructural elements of the material analysed. . . . 57
4.2 Specification of the geometry of the tested specimens. 57
4.3 Plate configurations for the study of the effect of the specimen and tow thicknesses. 67

5.1 Specification of the microstructural elements (tow length l^{t}, tow width w^{t}, tow thickness t^{t} and fibre volume fraction V^{f}) of the material systems analysed; dimensions are in mm and volume fractions in %. 81
5.2 Specification of the geometry and number of the tested specimens and of the numerical inputs. 92

5.3 Tow material properties used as model inputs. Modulus values are in GPa, strength values are in MPa, toughness values are in kJ/m^2. 92

6.1 Experimental plan - specification of the number of un-notched and notched specimens tested. 104
6.2 Table of values relating k with $|\nabla \bar{F}_{\mathrm{I}}|$ and l_{nl}. 112

7.1 Calculation of length scales for the different phases of the fatigue life; the effective recovery length $l_{\mathrm{e}}^{[i]}$ is calculated from the Paris law in Eq. 7.13. . . 130
7.2 Nominal model inputs for validation against experimental results. 138
7.3 Fibre properties for model validation; for fibre type T, Deng et al. [131] provide 4 sets of Weibull parameters for the single-fibre strength distribution, measured at 4 different fibre lengths l_0^{f}. 139
7.4 Interface properties for model validation. 139

C.1 The calibrated parameters of the iARD model, used for the process simulation. C1

Acknowledgements

To Soraia Pimenta, my supervisor, for sharing her time, her knowledge, brilliance, and her support throughout my PhD. I feel that I have learnt so much during these past 3 years, thank you for everything.

To the EU for funding this project through a Marie Skłodowska-Curie actions grant.

To Automobili Lamborghini and Oxeon AB for supplying the material systems tested in this work.

To Prof. Leif Asp for sharing his knowledge and experience, for all the insightful talks we shared and for his support and interest in the work developed.

To Prof. Ian Sinclair, Mark Mavrogordato, Richard Boardman, Orestis Katsamenis and Kathryn Rankin from the μ-VIS X-Ray Imaging Centre in the University of Southampton for the help and guidance provided during my secondment there.

To Prof. Stepan Lomov, Yentl Swolfs and the rest of the members of the CMG group in Leuven, for the support and guidance provided during my secondment in KU Leuven.

To Sherry, Luca, David, Martinus and Sebastian for all the collaborative work.

To my colleagues at Imperial College London, with whom I shared very good moments throughout this PhD journey: Lorenzo, Fabio, Rui, Muneeb, Joel, Finley, Rikka, Bo, Alison, Alex, Ian, James, Fabian, Catalin, Geena, Emily, Mike, George. The list goes on much longer, even if your name is missed, my appreciation is no less.

To my colleges and friends from the FiBreMoD project for all the good times and fruitful discussions during all the travels and trainings we had in this project.

To Ricardo Lopes, Andrei Bonya, Tomás Chuaqui, Luis Varandas and André Leite for their friendship, and for always being there for me in both good and bad moments.

To Martha Patouris, for her incredible support, motivation, and for being such a positive soul, you truly helped me getting through the finish line.

To my family, in particular my parents Jorge and Maria Alves for their unconditional love and support, you mean the world to me.

A special thanks to my brother Paulo Alves for his friendship and scientific guidance, and for being a true inspiration to me.

List of publications

Parts of the work presented in this thesis have been disseminated through a number of written publications and oral communications; these are listed below, as of January 2020.

Peer–reviewed journal publications

[p1] M. Alves, S. Pimenta, "A computationally-efficient micromechanical model for the fatigue life of unidirectional composites under tension-tension loading", *International Journal of Fatigue*, 116: 677 – 690, 2018.

[p2] M. Alves, S. Pimenta, "The influence of 3D microstructural features on the elastic behaviour of Tow-Based Discontinuous Composites", *Composite Structures*, submitted, 2019.

[p3] M. Alves, D. Carlstedt, F. Ohlsson, L. Asp, S. Pimenta, "Ultra-Thin and Stiff Randomly-Oriented Discontinuous Composites: closing the gap to quasi-isotropic continuous laminates" n *Composites Part A*, accepted for publication, 2020.

[p4] M. Alves, Y. Li, S. Pimenta, "Characterising and modelling the variability of TBDC material systems", *to be submitted*, 2020

[p5] M. Alves, L. Martulli, Y. Swolfs, S. Lomov, S. Pimenta "A Finite element framework for modelling the stochastic behaviour of tow-based discontinuous composites", *to be submitted*, 2020.

Refereed conference publications

[c1] M. Alves, S. Pimenta, "Analysing the effect of fibre waviness on the stiffness of tow-based discontinuous composites", in *ECCM 18, 18th European Conference on Composite Materials*, (Athens, Greece), 24–28 June 2018.

[c2] M. Alves, D. Carlstedt, F. Ohlsson, L. Asp, S. Pimenta, "Ultra-Thin and Stiff Randomly-Oriented Discontinuous Composites" in *ASC 34th Annual Technical Conference*, (Atlanta, USA), 23–25 September 2019.

[c3] S. Pimenta, A Mersch, M. Alves, "Predicting damage accumulation and fatigue life of UD composites under longitudinal tension", 2018 IOP Conf. Ser.: Mater. Sci. Eng. 388.

[c4] L. M. Martulli, M. Alves, S. Pimenta, M. Kerschbaum, S. V. Lomov, Y. Swolfs, "Prediction of carbon fibre sheet moulding compound (CF-SMC) mechanical properties based on local fibre orientation", in *ECCM 18, 18th European Conference on Composite Materials*, (Athens, Greece), 24–28 June 2018.

[c5] M. Widjaja, M. Alves, M. Mavrogordato, S. Joannes, A. Bunsell, G. Mair, A. Thionnet, "Effect of the time dependent loading of type IV cylinders using a multi-scale model", ICHS8, (Adelaide, Australia), September 2019.

Conference abstracts

[a1] M. Alves, S. Pimenta, "3D effects on the mechanical behaviour of tow based discontinuous composites", in *ECCM 18, 18th European Conference on Composite Materials*, (Athens, Greece), 24–28 June 2018 (oral presentation).

[a2] M. Alves, S. Pimenta, "Hierarchical fatigue model for unidirectional composites", in *The 7th International conference on the Fatigue of Composites*, (Vicenza, Italy), 4–6 July 2018 (oral presentation).

[a3] M. Alves, Y. Li, T. Naveed, F. Gaudron, S. Pimenta "Prediction and experimental validation of the notch (in)sensitivity of tow based discontinuous composites", in *9th International Conference on Composites Testing and Model Identification*, (Luleå, Sweden), 27–29 May 2019 (oral presentation).

[a4] M. Alves, D. Carlstedt, S. Pimenta, L. Asp, F. Ohlsson, "Ultra-Thin and Stiff Randomly-Oriented Discontinuous Composites", in *ASC 34th Annual Technical Conference*, (Atlanta, USA), 23–25 September 2019 (oral presentation).

[a5] L. M. Martulli, M. Alves, S. Pimenta, M. Kerschbaum, S. V. Lomov, Y. Swolfs, "Prediction of carbon fibre sheet moulding compound (CF-SMC) mechanical properties based on local fibre orientation", in *ECCM 18, 18th European Conference on Composite Materials*, (Athens, Greece), 24–28 June 2018 (oral presentation).

[a6] L. M. Martulli, L. Muyshondt, M. Alves, S. Pimenta, M. Kerschbaum, , S. V. Lomov, Y. Swolfs, "Experimental characterization on the orientation dependent

fatigue response of strand-based carbon SMC", in *The 7th International conference on the Fatigue of Composites*, (Vicenza, Italy), 4–6 July 2018 (oral presentation).

[a7] L. M. Martulli, M. Alves, M. Kerschbaum, S. Pimenta, S. V. Lomov, Y. Swolfs, "Multiscale modelling of a thick carbon fibre sheet moulding compound automotive component: from manufacturing to structural simulation", in *9th International Conference on Composites Testing and Model Identification*, (Luleå, Sweden), 27–29 May 2019 (oral presentation).

[a8] M. Widjaja, M. Alves, M. Mavrogordato, S. Joannes, A. Bunsell, G. Mair, A. Thionnet, "Effect of the time dependent loading of type IV cylinders using a multi-scale model", in *The 8th International Conference on Hydrogen Safety* (Adelaide, Australia), 24–26 September 2019 (oral presentation).

Acronyms and Abbreviations

BaM	Brick And Mortar
CDF	Cumulative Distribution Function
CFRP	Carbon Fibre Reinforced Polymer
CLT	Classical Laminate Theory
CT	Computed Tomography
DCFP	Direct Carbon Fibre Preforming
DIC	Digital Image Correlation
EL	Equivalent Laminate
FE	Finite Element
FFT	Fast Fourier Transform
FOD	Fibre Orientation Distribution
IDW	Inverse Distance Weighted
ITS	Interactive Tensile Shear
HM	High Modulus
HSL	Hierarchical Scaling Law
PDF	Probability Density Function Moulding Compound
QI	Quasi Isotropic
RVE	Representative Volume Element
RRVE	Random Representative Volume Element
SEL	Stochastic Equivalent Laminate
SMC	Sheet Moulding Compound
TBDC	Tow Based Discontinuous Composite
UHM	Ultra High Modulus
UD	UniDirectional
UMAT	User MATerial subroutine
WLT	Weakest Link Theory

Notation

Uppercase Roman variables

A	cross-sectional area
A_0	reference area for the nonlocal averaging
C_I	iARD model parameter
C_M	iARD model parameter
$\mathrm{CI}_{95\%}$	95% confidence interval
$C_\mathrm{int}^\mathrm{II}$	Paris law constant
C_K	stress concentration strength parameter
E	Young's modulus
$\bar{E}$	normalised Young's modulus
$\tilde{E}_\mathrm{N}$	average modulus of a batch of N specimens
$\mathcal{F}$	fibre orientation distribution function
F	failure probability
F_I	failure index of a UD discontinuous ply
F_ip	failure index associated to in-plane failure
F_op	failure index associated to out-of-plane failure
$\lvert\nabla F_\mathrm{I}\rvert$	magnitude of the gradient of the global failure index
$\bar{F}_\mathrm{I}$	nonlocal global failure index
F	failure probability
$\mathcal{G}_\mathrm{int}^\mathrm{IIc}$	interface mode-II critical energy release rate
$\mathcal{G}_\mathrm{int}^\mathrm{IIth}$	interface mode-II threshold energy release rate
G	shear modulus
N	fatigue cycle number
N_c	number of points along the tow's centreline
N^t	Total number of tows
$N_\mathrm{grid}^\mathrm{t}$	Number of tows along one grid point
P^t	Generic tow elastic property
P	perimeter
S	survival probability
S_is	in-situ shear strength
S_z	interlaminar shear strength
T	characteristic thickness
U	dissipated energy
V	volume
V^f	fibre volume fraction
$\bar{V}^\mathrm{f}$	normalised fibre volume fraction
$V_\mathrm{TBDC}^\mathrm{t}$	tow volume fraction in the TBDC
X	longitudinal strength
X_z^T	interlaminar tensile strength
X_D^∞	tensile strength of a BAM composite
Y	transverse strength
$\mathbf{A}$	fourth order fibre orientation tensor
$\mathbf{C}$	stiffness matrix
$\mathbf{R}$	Reuters matrix
$\mathbf{S}$	compliance matrix
$\mathbf{T}$	transformation matrix

Lowercase Roman variables

$\mathbf{a}$	second order fibre orientation tensor
$\bar{\mathbf{a}}$	stochastic second order fibre orientation tensor
a_{ij}	second order fibre orientation tensor component
a	crack length
$\mathbf{e}$	eigenvector
e_s	element size
$\mathbf{d}$	damage tensor
d_L	longitudinal damage parameter
d_T	transverse damage parameter
d_Z	out-of-plane damage parameter
g	grayscale value
k	stress concentration factor
l	length
m	Weibull shape parameter
$m_\mathrm{int}^\mathrm{II}$	Paris law exponent
p	IDW average exponent
r	radial averaging distance
s_grid	spacing between grid points
s_ls	spatial length scale
$\bar{s}_\mathrm{ls}$	characteristic spatial length scale
t	thickness
$\bar{t}$	normalised thickness
w	width
ws	window size
$\bar{z}$	tow level

Greek variables

α	iARD model parameter
ϵ	strain
$\boldsymbol{\epsilon}$	strain field
η	geometric coefficient
γ	shear strain
δ_N	threshold parameter
θ	in-plane angle
ϕ	out of plane angle
ϕ^f	fibre diameter
ν	Poisson's ratio
$\boldsymbol{\sigma}$	stress field
σ	standard deviation
ξ	geometric coefficient
λ	shear-lag numerical constant
λ_i	i eigenvalue
ω	spatial frequency
σ	stress
τ	shear stress
Ψ	nonlocal function
Ψ_0	basic nonlocal function

Superscripts

∞	remote
D	property relative to the UD discontinuous material
f	fibre
g	global coordinate system
i	bundle level
l	local coordinate system
m	matrix
s	specimen
SEL	SEL coordinate system
t	tow
TBDC	property relative to the TBDC
UD	property relative to the UD material
w	waviness

Subscripts

$\mathcal{A}$	fibre/sub-bundle $\mathcal{A}$
$\mathcal{B}$	fibre/sub-bundle $\mathcal{B}$
char	characteristic
c	control length
C	compression

crt	critical
debond	debond
D	property relative to the UD discontinuous material
e	effective recovery length
eff	effective tow length
est	estimated number of tows
fd	fully debonded
fail	failure strain
fpz	length of the fracture process zone
g	global coordinate
gauge	gauge length
init	initiation phase
int	pristine interface properties
is	in-situ
K	linear stress concentrations field
$\mathcal{K}$	one sub-bundle fails and the other survives
L	linear stress field
l	local coordinate
nl	characteristic length of the nonlocal continuum
peak	highest value of the cyclic load
prop	propagation phase
r	reference length
s	static
spec	specimen
t	tow
trough	lowest value of the cyclic load
T	tensile
U	uniform
$\mathcal{U}$	both sub-bundles survive
w	wavy tow

Chapter 1

Introduction

1.1 Background

Carbon-Fibre Reinforced Polymers (CFRPs) are widely used in the aerospace and the high-performance automotive industries, as they require materials that combine light weight with high mechanical properties, in order to ensure the desired load bearing capacity. CFRPs offer a large design flexibility, as different microstructures can be engineered and tailored for specific properties suitable for specific applications. A large range of complexity of microstructures exists, from simple unidirectional (UD) fibre arrangements (which are the "building block" of many composite architectures) to complex microstructures (eg. with discontinuities, and random fibre orientations). Increasing the complexity of the microstructure of CFRPs generally leads to more challenges in predicting their mechanical response.

Being able to predict the mechanical response of CFRPs is essential in designing efficient and reliable structures. In-service composite structures are subjected to different loading types, ranging from simple uni-axial tension/compression to multiaxial cyclic loads. Despite unidirectional composites being the most simple composite architecture, predicting their mechanical response still remains a challenge, even for simple loading cases [1]. In order to predict the mechanical response and reliability of composites with complex microstructures subject to complex loadings, one must first understand the effect of more complex loads on simple microstructures, and the effect of simple loads on more complex microstructures.

In the last decade, regulations limiting the carbon emissions in the automotive industry have become more demanding, and have challenged car manufacturers to produce more efficient vehicles. This led to a surge in the use of composite materials in the automotive industry. However, the long manufacturing time and high costs of

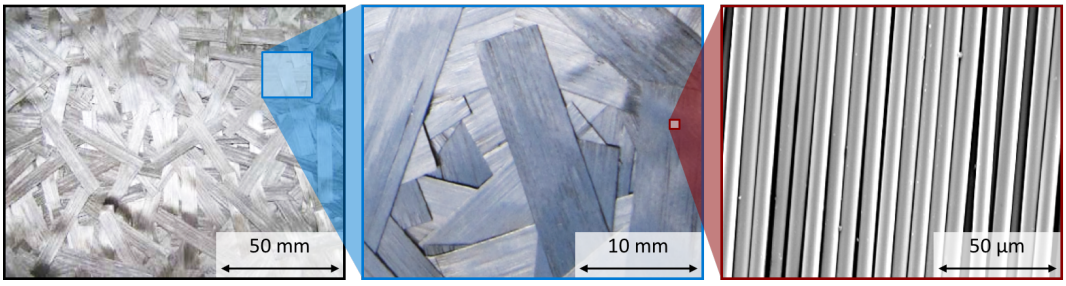

Figure 1.1: Example of a heterogeneous microstructure of TBDCs [2].

continuous fibre CFRPs has always been a limiting factor in the use of these materials for large scale industries. The use of Discontinuous-Fibre Composites (DFCs) has been presented as a potential solution to this problem, as they allow for improved manufacturability. However, typical DFCs present low fibre contents which limits their strength and stiffness, and therefore are not suitable to replace conventional materials (such as steel) widely used in the automotive industry.

Recent advancements in the manufacturing process of DFCs have led to the emergence of high-performance discontinuous composites, which are here referred to as Tow-Based Discontinuous Composites (TBDCs). TBDCs are composed by long chopped carbon fibre tows (typically between 20-50 mm in length) randomly distributed in a polymeric matrix. The resulting microstructure (see Figure 1.1) has a high fibre-content, and leads to high values of stiffness, strength and toughness [3–6]. The main routes to manufacture TBDCs are (i) chopped-prepreg tows [2], (ii) direct fibre preforming [7] and (iii) Sheet Moulding Compounds (SMCs) [8]. For parts manufactured with TBDCs, the carbon fibre tows are either processed into preforms or directly applied into moulds, before compression-moulding. This allows for the manufacture of complex shaped parts at high production rates.

The combination of manufacturability (compared to continuous CFRPs) and high mechanical properties (compared to typical DFCs) is what makes TBDCs such an attractive solution for both high volume (automotive) and high performance (aerospace) industries. Commercially available TBDCs have been shown to have stiffness values between 40 and 50 GPa, which are comparable to those of quasi isotropic (continuous) laminates [9, 10], hence making them a good alternative to continuous fibre composites for stiffness driven designs. Nonetheless, strength values ranging from 250 to 350 GPa [2, 11] preclude the application of these materials to primary load bearing structural components. Some examples of current commercial applications of TBDCs include window frames of the 787 Dreamliner [12], the inner monocoque and suspension control arm (of the "Sesto Elemento" concept car from Automobili Lamborghini) [13], and helicopter tailboom frames [14].

It is well known [6, 7, 9, 10, 15, 16] that the mechanical performance of TBDCs is highly dependent on the properties and geometry of the tows. Longer tows have been shown to improve both the modulus and tensile strength of the material [6, 7, 9, 10]. Slender tows, with a high length to thickness aspect-ratio have also been shown to lead to significant improvements on the material's modulus and strength [9, 15]. The effect of using longer and slender tows leads to modulus values that converge to that of quasi-isotropic continuous laminates [9, 10].

The heterogeneous nature of the microstructure of TBDCs leads to features like variable fibre volume fraction, local preferential orientations, tow waviness, resin rich regions and/or voids. These characteristic features of TBDCs lead to significant variability in their mechanical properties, complex stress transfer mechanisms and complex failure mechanisms. The combination of these features raises several challenges when it comes to modelling the mechanical behaviour of these materials.

The challenge in modelling the variability in the mechanical properties of TBDCs has been tackled in different ways in the literature. The two main approaches are generally based on (i) explicit representation (i.e. each tow of the microstructure is explicitly represented and modelled) [17–21] or (ii) on an implicit representation of the material's microstructure (i.e. the microstructure is idealised/represented by an equivalent laminate analogy) [22, 23]. Models based on explicit representations are coupled with microstructure generators, and despite being able to predict the statistical distribution of mechanical properties, they are limited to small and simple geometries. On the other hand, models based on implicit representations of the microstructure are often based on an equivalent laminate analogy [22, 23]. This approach is less computationally demanding and is scalable to model large and more complex geometries. However, capturing the spatial variability of the mechanical properties, and how the spatial variability relates to the microstructural features of the material (such as the tow geometry), remains a challenge with this approach.

The increasing use of CFRPs across several industries has led to a significant amount of waste material from both end-of-life of in-service components and material waste generated during the manufacturing process [24]. This has raised an environmental and economic awareness for the need to recycle the CFRPs [24]. The current recycling processes of CFRPs are only able to recover the fibres/bundles in short lengths; this necessarily implies that components made of recycled carbon fibres have a discontinuous microstructure [25,26]. The growth in the use of DFCs, followed by new developments in manufacturing processes and modelling/design tools, will certainly contribute to close the loop in the life-cycle of CFRPs, ensuring a better and more sustainable future.

1.2 Objectives

This study aims to expand the general understanding of discontinuous composites and to develop numerical models to predict their stochastic dominated response. Moreover, the development of numerical models to predict the reliability of simpler composite microstructures under fatigue loading is also a focus of this study. This requires addressing the following challenges:

- To investigate and develop numerical models/tools to reliably predict the mechanical response of TBDCs while accounting for the intrinsic variability of the material and of local features of the microstructure.
- To integrate the developed numerical models in an efficient Finite Element framework that is able to predict the stochastic mechanical performance of TBDCs.
- To use the numerical models to identify optimal microstructures that lead to significant improvements in the mechanical performance of TBDCs.
- To develop an analytical model capable of predicting the fatigue life of unidirectional composites under tension-tension loading.

1.3 Thesis Outline

The general overview of the background for this work has been laid-out in Section 1.1. In the beginning of each chapter, a literature review on the relevant topic to be explored will be presented in more detail.

Chapter 2 presents a microstructure generator that is able to recreate 3D features of the microstructure of TBDCs, such as tow waviness and volume fraction variations. The statistics of such features are successfully validated against experimental measurements from micro-CT scans. The generator is coupled with a stiffness model, and is used to assess the influence of the out of plane angle distribution of the tows on the material stiffness reduction, for a range of tow geometries. This study also gives some insight on the uncertainty associated with the modulus measurements of TBDCs according to current standards, and suggests potential improvements to current available standards for these materials.

Chapter 3 details the fundamental analytical modelling approach to predict the mechanical response of TBDCs, and how this was used to identify the use of ultra-thin and stiff tapes as a route to manufacture TBDCs with significantly improved ultimate strength and stiffness. The manufacturing and testing procedures of TBDC plates with ultra-thin and stiff tapes are detailed. The results obtained are compared to those of commercially available and other TBDC material system presented in the literature.

Chapter 4 presents a detailed analysis of the variability of mechanical properties in TBDCs, where two methods to quantify the spatial variability of strain fields measured with Digital Image Correlation (DIC) are presented and compared. The microstructure generator presented in Chapter 2 is used to generate FE models with an explicit representation of the material's microstructure, from which a relation between the in-plane tow geometries and the characteristic length-scale of the resulting field of mechanical properties is derived. Furthermore, an efficient stochastic FE framework based on an implicit representation of the material's microstructure is presented. The strain fields obtained with the proposed FE framework are successfully validated against experimental observations.

Chapter 5 extends the capabilities of the stochastic FE framework presented in Chapter 4. The framework is divided in three modules: (i) the coupling with fibre orientation results from process simulations; (ii) the assignment of 3D stochastic material properties; and (iii) a physically based failure criterion and stiffness reduction scheme used to predict final failure. The predictions of the stochastic FE framework are successfully validated against experimental results for two TBDC material systems.

Chapter 6 details the experimental characterisation of the notch-sensitivity of TBDC specimens with circular and modified notched geometries under longitudinal tension. A method based on the nonlocal averaging of damage initiation is proposed to predict the mechanical response of notched and un-notched specimens, from linear elastic simulations. The proposed method uses the FE framework detailed in Chapter 5 to predict fields of failure indices that reflect the extent of damage initiation of the material. The results obtained are validated against the experimental results.

Chapter 7 presents an analytical model to predict the fatigue response of UD composites under longitudinal tension-tension cyclic loading. The model allows for the determination of stochastic S-N curves and associated size effects from constituent properties, and is validated against experimental results.

Finally, the main conclusions of this work are summarised in Chapter 8. Some suggestions of new research avenues and further developments that can increase the impact of the work developed are detailed in Chapter 9.

Chapter 2

The influence of 3D microstructural features on the elastic behaviour of Tow-Based Discontinuous Composites

2.1 Introduction

The microstructure of TBDCs is complex, raising several challenges when modelling the mechanical behaviour of these materials. Examples of such challenges include the inherent tow waviness (which leads to out of plane orientations), tow thickness variations and local fibre volume fraction variations (and/or voids). However, most existing models [20, 22, 23, 27, 28] to predict the mechanical behaviour of TBDCs are based on a 2D representation of their actual microstructure, and ignore the waviness of the tows in the through-the-thickness direction, which may lead to erroneous predictions of the mechanical properties of TBDCs, as will be discussed below.

Selezneva et al. [9] manufactured and tested TBDCs with tow widths ranging from 3 to 12 mm and tow length from 6 to 50 mm; it was found that the Young's modulus of TBDCs manufactured with narrower and shorter tows were significantly lower than that of continuous-fibre quasi-isotropic equivalent laminates. Li et al. [15] manufactured and tested TBDCs with different tow thicknesses; it was reported that thicker tows lead to more irregular microstructures and, consequently, to lower values of stiffness due to the out-of-plane orientations (i.e. waviness) of the tows. Wan et al. [29] have done micro-CT scans on TBDCs made of ultra-thin carbon fibre tapes and analysed the distribution of the out of plane orientations of the chopped tows with different lengths.

The authors found that longer tows lead to more regular microstructures, with narrower out of plane angle distributions, hence having better mechanical performance.

Selezneva et al. [20] modelled the mechanical behaviour of TBDCs by considering a 2D random network of tows created by random sequential adsorption; the resulting network was represented by local tow layups, from which 2D Finite Element (FE) models were then created. This approach neglects fibre volume fraction variations within the specimen, and does not impose any constraints to the random sequential adsorption tow deposition algorithm to avoid unrealistically-high local concentrations of tows. Due to the 2D assumptions of this model, it neglects the effects of the out of plane orientations of the tows, which are likely influenced by the tow dimensions; therefore, these assumptions may have been the reason for the inaccurate stiffness predictions (when compared to experimental observations) of specimens with short and narrow tows, since these lead to microstructures with more pronounced out of plane orientations [9].

More complex models that try to capture the 3D features of the microstructure of TBDCs have also been presented in the literature. Harper et al. [18] generated 3D representative volume elements (RVEs) with a random sequential adsorption algorithm combined with an elevation method to avoid tow intersections, and a spline interpolation algorithm to produce more realistically distorted tows. A constant fibre volume fraction and thickness were assumed for all tows; moreover, the maximum overall fibre volume fraction of a generated specimen (reported to be around 50%) is limited by the maximum packing achievable with the combination of the random adsorption algorithm and the tow elevation method. The authors were able to recreate FE models of the generated RVEs, and reported tensile modulus calculations with errors around 5% only. However, due to the high computational cost, this approach is limited to small RVE sizes and is not efficiently scalable to larger geometries; consequently, this approach is not able to fully characterise the stochastic nature of the mechanical properties of TBDCs.

Kravchenko et al. [21] modelled virtual specimens (also created based on a random sequential adsorption algorithm) using FE voxel meshes, in which each element was mapped with a local tow orientation. This approach was able to capture the complex interactions between the tows, but it does not take into take into account local volume fraction variations nor the waviness of the tows due their through-the-thickness nesting. Furthermore, because the authors generated voxel-based meshes from the virtual specimens, this discretisation of the microstructure may generate non-realistic stress concentrations due the non-smooth representation of the tow boundaries, which can lead to erroneous results. Moreover, the large computational demand of this FE-based approach hinders the potential of a full stochastic characterisation of larger structures.

The models described above [20, 21] are based on depositing tows on a specimen using simple random sequential adsorption algorithms; therefore, they generally lead to unrealistically-high local concentrations of tows due to the random nature of the algorithm. Moreover, most models [18, 20, 21] neglect fibre volume fraction variations within tows and/or within the virtual TBDC specimens generated, although the fibre volume fraction varies significantly in real specimens [9, 15].

An attempt to solve these problems was proposed by Li et al. [15], who imposed a numerical limit to tow density variations in the random sequential adsorption algorithm, and who assumed a proportional relationship between the local density of tows and local fibre content; however, the numerical limit to tow density used has no physical meaning. Li et al. [23] then calculated the stiffness of TBDCs using an equivalent ply-by-ply laminate analogy (in which the in-plane tow orientation distribution of the TBDC is discretised into unidirectional plies); the longitudinal stiffness of each ply (composed by tows with the same geometry as in the original TBDC) was calculated using a shear-lag model [30]; however, their approach was still limited to a 2D analysis (i.e. neglecting tow waviness).

The work presented in this chapter aims to accurately predict the stiffness of TBDC materials in an efficient numerical framework, while taking into account the complex 3D nature of the material's microstructure. This aim can be divided in two main goals: the first goal is to develop a new virtual microstructure generator able to create representative TBDC microstructures, accounting for the intrinsic waviness of the tows due to their through-the-thickness nesting, as well as for fibre volume fraction and thickness variations in the material; the second goal is to couple the statistical distributions of the 3D features obtained with the microstructure generator with an analytical model to predict the stiffness of TBDCs.

Section 2.2 describes the development and implementation of the microstructure generator, as well as the coupling of the latter with an analytical stiffness model. Section 2.3.1 analyses the computational efficiency and numerical convergence of the microstructure generator. Section 2.3.2 presents the comparison between (i) the statistical distributions of out of plane angles and local fibre volume fractions predicted by the microstructure generator and (ii) corresponding experimental distributions measured from micro-CT scans. Furthermore, in Section 2.3.3 the results from the stiffness model are validated against experimental results from the literature, and the influence of the out of plane angle distribution of the tows on the material stiffness are be quantified for a range of tow geometries, for the first time in the literature. In Section 2.3.4, the microstructure generator and stiffness model are used to quantify the uncertainty associated with the experimental measurement of the modulus of TBDCs, and to establish guidelines on the experimental campaign needed to achieve the required confidence

levels. Finally, the proposed model and results are discussed in Section 2.4, and the main conclusions of this work are drawn in Section 2.5.

2.2 Model development

2.2.1 Microstructure generator

The microstructure generator to be developed in this section has the objective to recreate, in a computationally efficient way, a realistic representation of the microstructure of TBDC specimens, including (i) the waviness due to nesting of the tows, (ii) local fibre volume fraction variations, and (iii) random and/or preferential in-plane orientations of the tows. The generator works as follows:

1. The tows are assumed to be the basic reinforcing units of the TBDC material, with a tow length l^{t}, and a rectangular cross-section defined by the tow width w^{t} and nominal thickness t^{t}, with a nominal fibre volume fraction V^{f}. The geometry of the generated specimen is defined by the specimen's length l^{s}, width w^{s} and thickness t^{s}. The estimated total number of tows to be placed in the specimen ($N^{\mathrm{t}}_{\mathrm{est}}$) is obtained by considering a tow volume fraction within the TBDC equal to $V_{\mathrm{t}}^{\mathrm{TBDC}}$; therefore, $N^{\mathrm{t}}_{\mathrm{est}}$ is defined as the ratio between the volume of the specimen V^{s} times $V_{\mathrm{t}}^{\mathrm{TBDC}}$ and the volume of each tow (i.e. $N^{\mathrm{t}}_{\mathrm{est}} = \frac{V^{\mathrm{s}} \cdot V_{\mathrm{t}}^{\mathrm{TBDC}}}{V^{\mathrm{t}}}$, with $V^{\mathrm{s}} = l^{\mathrm{s}} \cdot w^{\mathrm{s}} \cdot t^{\mathrm{s}}$ and $V^{\mathrm{t}} = l^{\mathrm{t}} \cdot w^{\mathrm{t}} \cdot t^{\mathrm{t}}$). Note that this estimated number of tows will be corrected to account for specimen edge effects (see Point 4).

2. A grid of points, spaced by a distance s_{grid} and which extends from $x = 0$ to $x = w^{\mathrm{s}}$ and from $y = 0$ to $y = l^{\mathrm{s}}$, is defined (see Figure 2.1a); each grid point j, with coordinates (x^j_{grid},y^j_{grid}), has the goal of tracking the local tow count N^{t}_j in the through-the-thickness direction, and the position of each tow in the through-the-thickness direction (hereby designated as "tow-level" $\bar{z}_{j,i}$, where $\bar{z}_{j,i} = 1$ if tow i is at the bottom surface of the specimen at grid point j, and $\bar{z}_{j,i} = N^{\mathrm{t}}_j$ if tow i is at the top surface of the specimen at grid point j).

3. Tow deposition via a random sequential adsorption algorithm: each tow i (with $i \in \{1, ..., N^{\mathrm{t}}_{\mathrm{est}}\}$) is placed in the specimen by randomly sampling its centre point coordinates (x_i, y_i) from uniform distributions: $x_i \rightsquigarrow \mathcal{U}(0, w^{\mathrm{s}})$ and $y_i \rightsquigarrow \mathcal{U}(0, l^{\mathrm{s}})$; the in-plane angle θ_i of each tow is sampled from the in-plane Fibre Orientation Distribution (FOD) of the specimen, which is reconstructed based on a second order orientation tensor, a_{ij} [31] (provided as an input to the microstructure generator). In order to avoid unrealistic concentrations of tows in some grid points, after each tow is deposited, the generator checks whether the following

condition is verified:

$$\max\{N_j^{\mathrm{t}}\} \leq \mathrm{floor}\left[\frac{V_{\mathrm{th}}^{\mathrm{f}}}{V^{\mathrm{f}}} \cdot \bar{N}_i^{\mathrm{t}}\right] + 1, \tag{2.1}$$

where $V_{\mathrm{th}}^{\mathrm{f}}$ is the user-defined threshold for the maximum fibre volume fraction allowed in the specimen, $\bar{N}_i^{\mathrm{t}}$ is the mean tow count of all grid points after tow i is deposited and floor is an operation to round the argument to the lowest nearer integer. The derivation of this equation uses the tow thickness normalisation and fibre volume fraction variation procedures explained in Steps 5 and 6, as described in Appendix A.1. If Eq. 2.1 is not verified, the tow is removed, and the steps described in Point 3 are repeated. In this work, the theoretical maximum volume fraction for a tight hexagonal packing (0.91) was selected for the value of $V_{\mathrm{th}}^{\mathrm{f}}$.

4. Correction of the total number of tows: the tows that are placed across the edges of the specimen are cropped, and their effective length $l_{\mathrm{eff},i}$ corresponds to the length of tow i (along its centre-line) that falls within the edges of the specimen to be generated. Therefore, after depositing $N_{\mathrm{est}}^{\mathrm{t}}$ tows in the specimen, the total effective volume of tows deposited ($\sum_{i=1}^{N_{\mathrm{est}}^{\mathrm{t}}} l_{\mathrm{eff},i} \cdot w^{\mathrm{t}} \cdot t^{\mathrm{t}}$) is still lower than the target volume of tows in the specimen $V^{\mathrm{s}} \cdot V_{\mathrm{t}}^{\mathrm{TBDC}}$. In order to generate a specimen with the target volume, more tows are placed in the virtual specimen until the following criterion is met:

$$\sum_{i=1}^{N^{\mathrm{t}}} l_{\mathrm{eff},i} \cdot w^{\mathrm{t}} \cdot t^{\mathrm{t}} \geq V^{\mathrm{s}} \cdot V_{\mathrm{t}}^{\mathrm{TBDC}}, \tag{2.2}$$

where N^{t} is the final total number of tows is the specimen.

5. Tow thickness normalisation: after the deposition of all N^{t} tows, each grid point (x_j,y_j) will have a different tow count N_j^{t} (see Figure 2.1b). Since the generated specimen must have a constant thickness t^{s}, the tow thickness at each grid point is normalised as

$$\bar{t}_j^{\,\mathrm{t}} = t^{\mathrm{s}}/N_j^{\mathrm{t}}. \tag{2.3}$$

This normalisation results in a statistical distribution of tow thicknesses that can be seen in Figure 2.1c; the mean value of this distribution is mathematically equal to the input nominal tow thickness t^{t}.

6. Volume fraction variation: due to the thickness variation of the tows (introduced by Eq. 2.3), the grid points that contain a high tow count must consequently have thinner tows. Assuming a constant tow width and a constant number of fibres in the cross-section of each tow, an inverse relation between the local normalised tow thickness $\bar{t}_j^{\,\mathrm{t}}$ and the local normalised fibre volume fraction $\bar{V}_j^{\mathrm{f}}$ must exist,

where the latter is given by

$$\bar{V}_j^{\mathrm{f}} = V^{\mathrm{f}} \frac{t^{\mathrm{t}}}{\bar{t}_j^{\mathrm{t}}}. \tag{2.4}$$

This normalisation results in a spatial distribution of fibre volume fractions; the mean of this distribution is mathematically equal to the input nominal fibre volume fraction V^{f}.

7. Determination of the central tortuous path of each tow: a set of equally spaced centreline-points (each represented by the index $c = \{1, ..., N_c = l^{\mathrm{t}}/s_{\mathrm{grid}} + 1\}$ and with a spacing of s_{grid}) is defined along the centreline of each tow i (see Figure 2.1d), effectively discretising each tow into $N_c - 1$ segments of length s_{grid}. The centreline-point of tow i is characterised by its in-plane position ($x_{c,i}$, $y_{c,i}$) (which is determined directly from the tow's centreline-point coordinates x_i, y_i and orientation θ_i, see Step 3 above) and by its tow-level $\bar{z}_{c,i}$ (which is determined by linearly interpolating the tow-level $\bar{z}_{j,i}$ at the nearest grid points, see Step 2 above). Since the tow-level will generally vary along the centreline (i.e $\bar{z}_{c+1,i} \gtreqless \bar{z}_{c,i}$), this interpolation results in a through-the-thickness tortuous path, defining the tow's *raw* waviness, as shown in Figure 2.1e.

8. Determination of the out of plane orientation distribution: the selected grid spacing s_{grid} defines the resolution limit of the raw waviness calculated in Step 7 (see Figure 2.1e). By filtering all frequencies $\omega \geq 1/s_{\mathrm{grid}}$ in the raw waviness (using a *Fast Fourier Transform* algorithm), a smooth and more realistic wavy path of the tow is obtained (see Figure 2.1f). The angle $\phi_{c,i}$ of each segment that connects the centreline-points c and $c+1$ along the centreline is then calculated as $\phi_{c,i} = \tan^{-1}\left(\frac{[\bar{z}_{c,i} - \bar{z}_{c+1,i}] \cdot \bar{t}_i^{\mathrm{t}}}{s_{\mathrm{grid}}}\right)$, where $\bar{t}_i^{\mathrm{t}}$ is the normalised thickness of tow i, given by the average of the linearly interpolated values of $\bar{t}_j^{\mathrm{t}}$ to the centreline points of tow i; therefore, by combining the out-of-plane angles $\phi_{c,i}$ of all segments ($c = \{1,...,N_c - 1\}$) of all tows ($i = \{1, ..., N_{\mathrm{t}}\}$), the out of plane angle distribution, which results from the nesting of the tows in the generated specimen, is obtained.

The numerical implementation of the presented microstructure generator was done in MATLAB; the code is available in the following repository:
https://github.com/meComposites/MicGenerator.

2.2.2 Stiffness model

The stiffness model presented in this section predicts the stiffness of TBDCs in five steps: (*i*) generation of a virtual specimen (using the microstructure generator described above); (*ii*) prediction of the local (i.e. in the local coordinate system of the tow, see Figure 2.1d) equivalent stiffness tensor of each individual tow neglecting

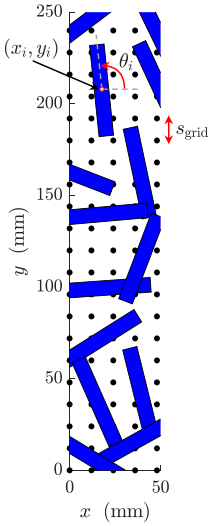

(a) Tow placement in a grid with a spacing $s_{\text{grid}} = 12.5$mm.

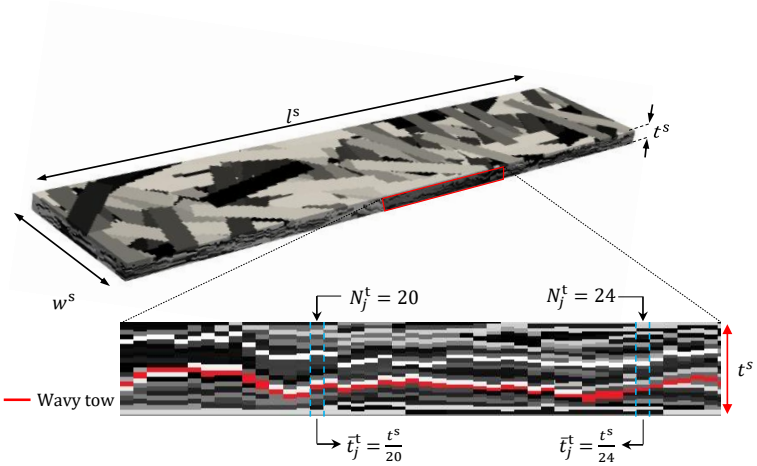

(b) Normalised tow thickness variation and tow waviness along the cross-section of a virtually generated specimen. The different shades of grey represent different tows. For clarity, the zoomed-in side view is stretched in the thickness direction.

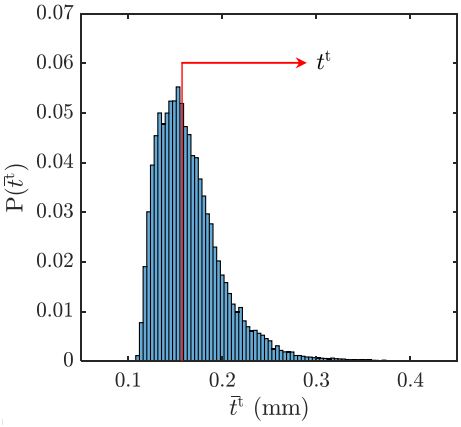

(c) Distribution of the tow's normalised thickness, with a mean value equal to t^t.

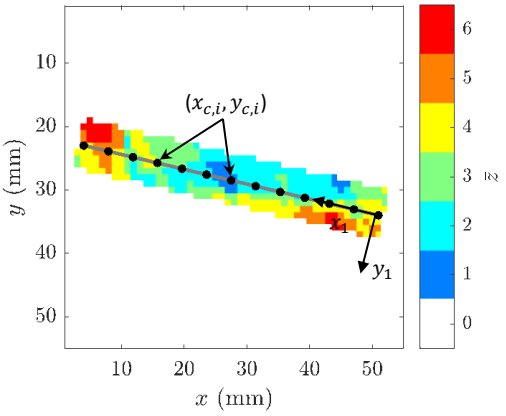

(d) A tow i with its local coordinates (x_1, y_1), centreline-points $(x_{c,i}, y_{c,i})$ and tow-levels $(\bar{z})$

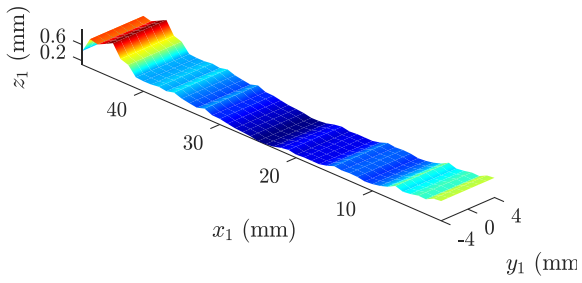

(e) Raw waviness of a tow.

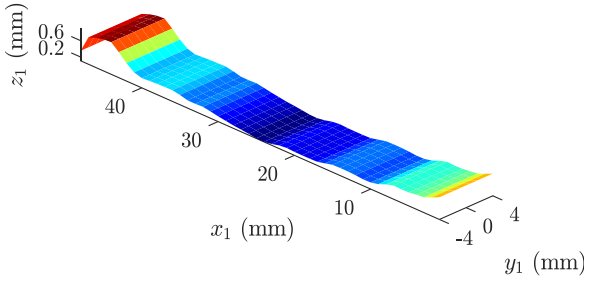

(f) Filtered waviness of a tow.

Figure 2.1: Features of the microstructure generator developed in Section 2.2.1. The examples described in this figure use the inputs shown in Table 2.4.

its waviness; (*iii*) and (*iv*) rotation of the tow stiffness tensor to the global coordinate

system according to the out of plane ϕ_i and in-plane θ_i orientations of each tow in the specimen; (v) calculating of the overall stiffness tensor by averaging the contribution of all tows in the specimen. Steps $ii - v$ are further detailed below:

(ii) In order account for the discontinuous nature of TDBCs, the equivalent longitudinal Young's modulus of a perfectly straight tow i in its natural coordinate system (in which direction 1 is aligned with the fibres, see Figure 2.1d), is determined from a shear-lag model [30, 32] as

$$E_{1,i}^{\mathrm{D}} = \frac{E_1^{\mathrm{t}}}{1 + \frac{1}{\lambda_i \cdot l_{\mathrm{char}} \cdot \tanh(\lambda_i l_{\mathrm{char}})}} \cdot V_{\mathrm{t}}^{\mathrm{TBDC}}, \text{ with } \lambda_i = \sqrt{2G_{12}^{\mathrm{t}}/(t_{\mathrm{char},i} \cdot \bar{t}_i^{\mathrm{m}} \cdot E_1^{\mathrm{t}})}, \tag{2.5}$$

where E_1^{t} is the longitudinal Young's modulus of the UD continuous tow material from which the tows are made, and G_{12}^{t} is the in-plane shear modulus. The shear-lag characteristic dimensions of the tows are $l_{\mathrm{char}} = l^{\mathrm{t}}/8$ and $t_{\mathrm{char},i} = w^{\mathrm{t}} \cdot \bar{t}_i^{\mathrm{t}}/[2(w^{\mathrm{t}} + \bar{t}_i^{\mathrm{t}})]$ [30,32], where $\bar{t}_i^{\mathrm{t}}$ is the average thickness of tow i (calculated by averaging the tow thickness t_j^{t}, derived in Eq. 2.3, of all grid points j which include tow i). Assuming a square packing of the fibres and neglecting resin-rich regions between the tows, the average matrix thickness surrounding tow i is given by the interfibre distance $\bar{t}_i^{\mathrm{m}} = (\sqrt{\pi/(4\bar{V}_i^{\mathrm{f}})} - 1) \cdot \phi_{\mathrm{f}}$, where ϕ_{f} is the fibre diameter, and $\bar{V}_i^{\mathrm{f}}$ is the average fibre volume fraction of tow i (calculated by averaging the fibre volume fraction V_j^{f}, derived in Eq. 2.4, of all grid points j which include tow i).

The equivalent transverse elastic properties of a tow are derived from the Halpin-Tsai general expression [33] for a property P in direction b (where the superscripts "D", "m", "t" correspond to the discontinuous tow, matrix and unidirectional (continuous) tow, respectively):

$$P_{b,i}^{\mathrm{D}} = P^{\mathrm{m}} \frac{1 + \eta_{b,i}\xi_{b,i}V_{\mathrm{t}}^{\mathrm{TBDC}}}{1 - \eta_{b,i}V_{\mathrm{t}}^{\mathrm{TBDC}}}, \text{ with } \eta_{b,i} = \frac{\frac{P_b^{\mathrm{t}}}{P^{\mathrm{m}}} - 1}{\frac{P_b^{\mathrm{t}}}{P^{\mathrm{m}}} + \xi_{b,i}}. \tag{2.6}$$

The Halpin-Tsai geometric coefficients are $\xi_{22,i} = 2(w^{\mathrm{t}}/\bar{t}_i^{\mathrm{t}})$, $\xi_{33,i} = 2(\bar{t}_i^{\mathrm{t}}/w^{\mathrm{t}})$ and $\xi_{12,i} = \xi_{13,i} = \xi_{23,i} = 1$, assuming tows with a rectangular cross-section [27] and a transverse isotropic behaviour. The equivalent stiffness tensor of a discontinuous non-wavy tow in local coordinates $\mathbf{C}_{\mathrm{t},i}^{\mathrm{l}}$ can therefore be defined (see Appendix A.2).

(iii) From the out of plane angles obtained with the microstructure generator for each segment of tow i, the equivalent stiffness tensor of a non-wavy tow $\mathbf{C}_{\mathrm{t},i}^{\mathrm{l}}$ can be rotated accordingly, leading to the local stiffness tensor of a wavy tow segment $\mathbf{C}_{\mathrm{wt},i,c}^{\mathrm{l}}$,

$$\mathbf{C}^{\mathrm{l}}_{\mathrm{wt},i,c} = \mathbf{R}\mathbf{T}_{\phi_{i,c}}{}^{-1}\mathbf{R}^{-1}\mathbf{C}^{\mathrm{l}}_{\mathrm{t},i}\mathbf{T}_{\phi_{i,c}}, \tag{2.7}$$

where $\mathbf{R}$ and $\mathbf{T}_{\phi_{i,c}}$ are the Reuters matrix and the out of plane transformation matrix [34] (both defined in Appendix A.2).

The stiffness tensor of a wavy tow is then calculated by averaging the stiffness tensor of each wavy segment (by considering an iso-strain assumption):

$$\mathbf{C}^{\mathrm{l}}_{\mathrm{wt},i} = \frac{1}{l_{\mathrm{eff},i}} \cdot \sum_{c=1}^{N_c-1} l_{\mathrm{eff},i,c} \cdot \mathbf{C}^{\mathrm{l}}_{\mathrm{wt},i,c}, \tag{2.8}$$

where $l_{\mathrm{eff},i,c}$ corresponds to the length of segment c of tow i within the edges of the specimen.

(*iv*) This is followed by the rotation of $\mathbf{C}^{\mathrm{l}}_{\mathrm{wt},i}$ to the global coordinate system (xyz) according to the in-plane angle θ_i of each tow, resulting in the stiffness tensor of a wavy tow in the global coordinates,

$$\mathbf{C}^{\mathrm{g}}_{\mathrm{wt},i} = \mathbf{R}\mathbf{T}_{\theta}{}^{-1}\mathbf{R}^{-1}\mathbf{C}^{\mathrm{l}}_{\mathrm{wt},i}\mathbf{T}_{\theta}, \tag{2.9}$$

where $\mathbf{T}_{\theta_i}$ is the in-plane transformation matrix, defined in Appendix A.2.

(*v*) Considering an iso-strain condition, the contributions of all tows to the overall stiffness of the specimen are combined through the following expression:

$$\mathbf{C}^{\mathrm{g}}_{\mathrm{s}} = \frac{\sum_{i=1}^{N^{\mathrm{t}}} \mathbf{C}^{\mathrm{g}}_{\mathrm{wt},i}}{N^{\mathrm{t}}}. \tag{2.10}$$

(*vi*) The Young's modulus E_{xx} of the generated specimen can be calculated by

$$\mathbf{S}^{\mathrm{g}}_{\mathrm{s}} = \mathbf{C}^{\mathrm{g}-1}_{\mathrm{s}}, \tag{2.11}$$

$$E_{xx} = \frac{1}{S^{\mathrm{g}}_{\mathrm{s}\,11}}. \tag{2.12}$$

The remaining engineering constants can be obtained from the compliance tensor $\mathbf{S}^{\mathrm{g}}_{\mathrm{s}}$ (see Appendix A.2).

The model described above accounts for the through-the-thickness waviness of the tows through step (*iii*); alternatively, one can use a similar strategy to calculate the stiffness properties of a TBDC material while neglecting the waviness of the tows, by not performing step (*iii*) (i.e. by not rotating the stiffness matrix of the tows accordingly to the out-of-plane angles $\phi_{c,i}$, and replacing $\mathbf{C}^{\mathrm{l}}_{\mathrm{wt},i}$ by $\mathbf{C}^{\mathrm{l}}_{\mathrm{t},i}$ in step (*iv*)). The importance of considering the waviness of the tows will be demonstrated in Section 2.3.3, where the full model (i.e. including step (*iii*)) will be referred to as "model with waviness"

and the modified model (i.e. excluding step (*iii*)) will be referred to as "model without waviness".

2.3 Results

The geometric inputs for the virtually generated specimens used in Sections 2.3.1, 2.3.2 and 2.3.3.2 are detailed in Tables 2.1 and 2.2.

2.3.1 Computational efficiency and numerical convergence of the microstructure generator

Table 2.1: Specification of the microstructural parameters for the HexMC-M77 material system, and for the validation of the microstructure generator.

Material	l^{t} (mm)	w^{t} (mm)	$t^{\mathrm{t}\dagger}$ (mm)	$V^{\mathrm{f}\ddagger}$ (%)	$V_{\mathrm{t}}^{\mathrm{TBDC}}$ (%)
HexMC-M77 [2]	50	8	0.125 ± 0.16	56 ± 6	100

† Mean and standard deviation of the tow thickness values measured from micro-CT images.
‡ Mean and standard deviation volume fraction values measured from high resolution micrographs (see Figure 2.4b).

Table 2.2: Specification of the geometrical and numerical inputs for the virtually generated specimens used in Section 2.3.

l^{s} (mm)	w^{s} (mm)	t^{s} (mm)	s_{grid} (mm)	$V_{\mathrm{th}}^{\mathrm{f}}$(%)
150	50	2.5	1	91

The microstructure generator's accuracy is dependent on the selected grid spacing s_{grid}: if a very coarse grid is used, tow waviness and tow thickness variations will not be accurately captured; however, if a very fine grid is used, the computational cost increases exponentially (as shown in Figure 2.2a). Therefore, to ensure the optimum balance between computational cost and result accuracy, a convergence study on the modulus prediction and on the predicted out of plane orientation distribution is presented in Figures 2.2b-2.2d. Figure 2.2b shows that the modulus value predicted by the generator converges for $s_{\mathrm{grid}} \leq 1$mm. The peak of the distribution of out of plane angles (Figure 2.2c) seems to have slower convergence than the modulus values; however, analysing the convergence of the standard deviation of the out of plane angles (Figure 2.2d), one can see it also converges for $s_{\mathrm{grid}} \leq 1$mm. Therefore, for all the subsequent analysis, a value of $s_{\mathrm{grid}} = 1$ mm was used.

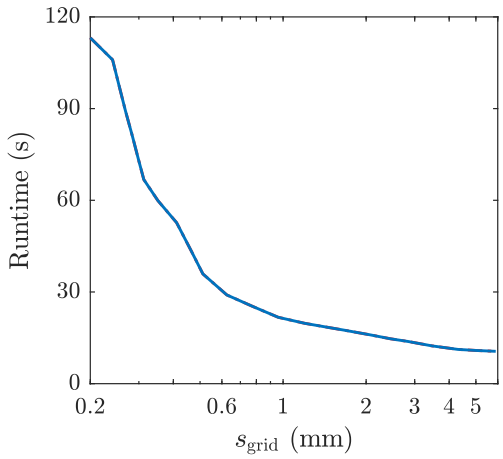

(a) Model run time for different values of s_{grid}.

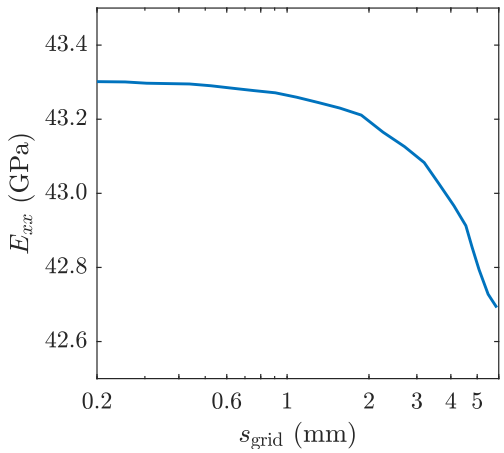

(b) Convergence of E_{xx} for different values of s_{grid}.

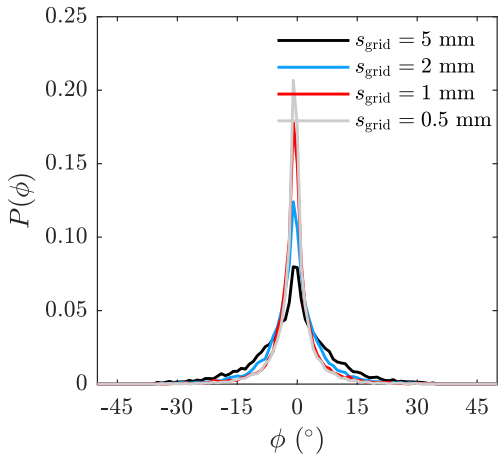

(c) Convergence of the out of plane angle distribution.

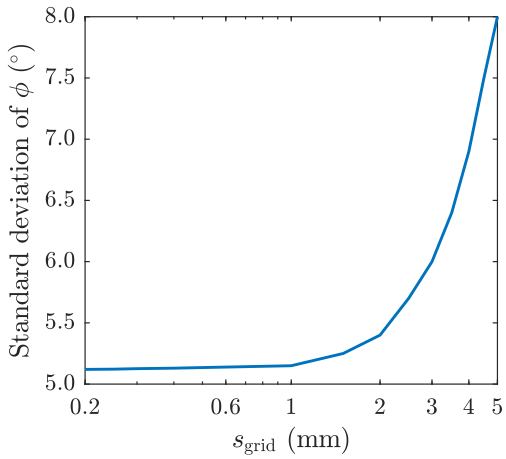

(d) Convergence of the standard deviation of the out of plane angle distribution.

Figure 2.2: Convergence of the statistics of the microstructure generator and the predicted longitudinal stiffness with the selected grid spacing dimensions, s_{grid}; model run times were obtained with a Intel(R) Core(TM) i7-6700 CPU at 3.40GHz.

Figure 2.3 shows the effect of the user-defined fibre volume fraction threshold V_{th}^{f} on (i) the maximum fibre content observed and (ii) the Young's modulus predicted for a virtually generated specimen. The value of V_{th}^{f} only restricts the maximum volume fraction for values lower than 0.8, after which it effectively dictates the maximum volume fraction in a generated specimen. Figure 2.3b shows that V_{th}^{f} has a negligible impact in the predicted specimen modulus E_{xx}.

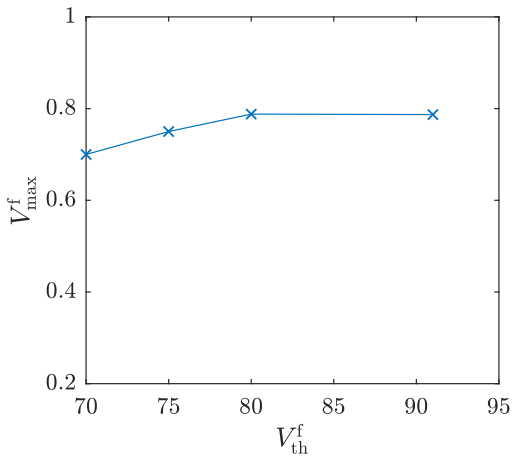

(a) Effect of $V^{\mathrm{f}}_{\mathrm{th}}$ on the maximum volume fraction ($V^{\mathrm{f}}_{\mathrm{max}}$) achieved in a specimen.

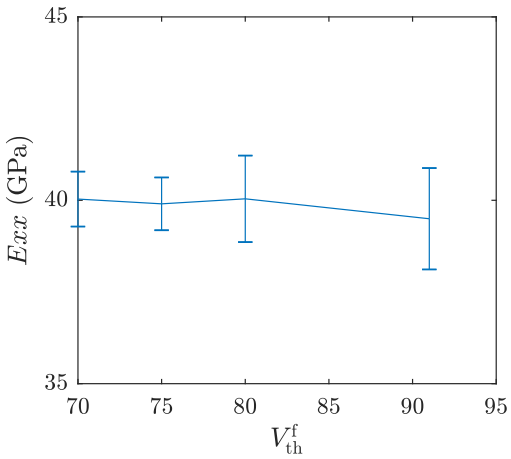

(b) Effect of $V^{\mathrm{f}}_{\mathrm{th}}$ on the predicted modulus E_{xx} of specimens.

Figure 2.3: Effect of $V^{\mathrm{f}}_{\mathrm{th}}$ on the maximum volume fraction achieved and in the predicted modulus E_{xx}; three specimens were generated for each configuration. For each configuration, the value of $V^{\mathrm{f}}_{\mathrm{max}}$ is taken as the maximum fibre volume fraction obtained for the three specimens, and the value of E_{xx} is the average value of the three specimens; the error bars represent one standard deviation.

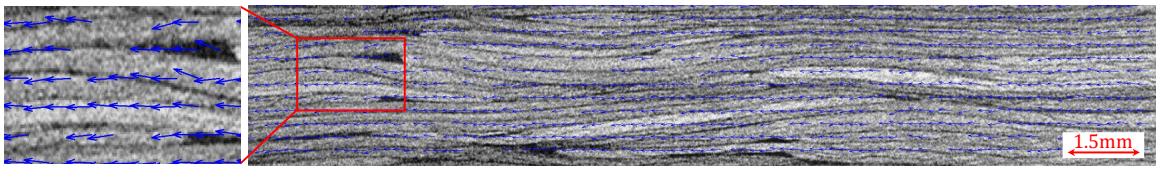

(a) Micro-CT image of the cross-section of a TBDC specimen, with the calculated local out of plane orientations shown by blue arrows.

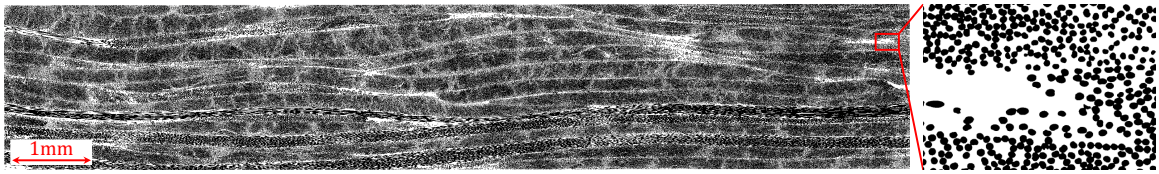

(b) High-resolution micrograph of the cross-section of a TBDC specimen, with a greyscale value threshold applied to show only the fibres.

Figure 2.4: Cross sections of a TBDC specimen (Hexcel's HexMC-M77 [2]) obtained by (a) micro-CT and (b) high resolution optical microscopy.

2.3.2 Microstructure generator results and validation

2.3.2.1 Out of plane angle distribution

In order to validate the out of plane angle distributions predicted by the microstructure generator, micro-CT images of two TBDC specimens [2] were acquired, and the

out of plane fibre orientations of the scanned volumes were obtained using a three dimensional structure tensor analysis. For this validation, a commercial material system was chosen (rather than a lab-based TBDC material) since it is more representative of the majority of TBDC materials used in real-life applications. The details of the acquisition and post-processing of the micro-CT images can be found in Appendix A.3.

Figure 2.4a shows one slice of one volume's cross section and the local out of plane orientations obtained with the structure tensor analysis. For the latter, a window size with the same in-plane dimensions as s_{grid} was used ($[1.0 \times 1.0 \times 0.4]$ mm); the selected window size has a negligible effect on the predicted out of plane angle distributions, as shown in Appendix A.3. Figure 2.5a shows the measured out of plane angle distribution of the scanned volumes, and the comparison with the distribution predicted by the microstructure generator, where a good agreement between both was found.

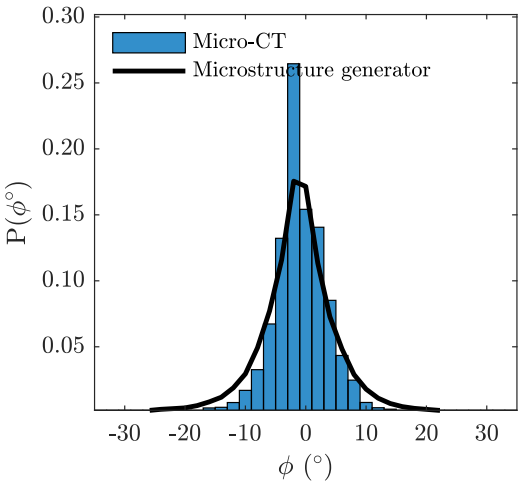

(a) Comparison of the out of plane angle distributions predicted by the microstructure generator with the one obtained from micro-CT measurements.

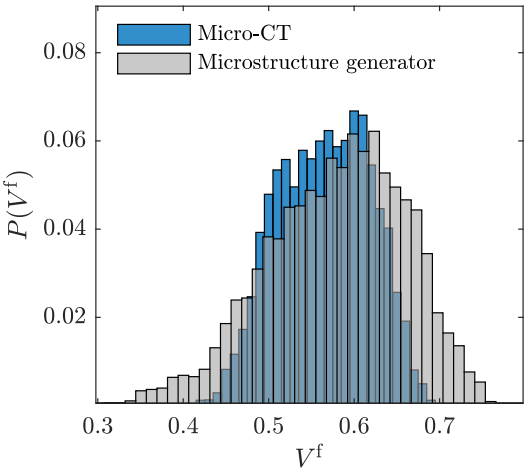

(b) Comparison of the volume fraction distributions predicted by the microstructure generator with the one obtained from micro-CT measurements.

Figure 2.5: Experimental validation of the microstructure generator's statistics (using HexMC-M77 specimens [2]).

2.3.2.2 Fibre volume fraction distribution

In order to validate the fibre volume fraction distributions predicted by the microstructure generator, the global fibre volume fraction was measured experimentally by thresholding high resolution micrographs of TBDC sections [2], shown in Figure 2.4b. The local variations of the material's volume fraction were inferred from the local distribution of the average greyscale values within $[1.0 \times 1.0 \times 0.4]$ mm windows in the

micro-CT volumes of the TBDC specimens. More details about this method can be found in Appendix A.4.

Figure 2.5b compares the fibre volume fraction distributions obtained with this method against the one predicted by the microstructure generator. It can be seen that the distribution predicted by the generator is slightly wider than the ones measured from the micro-CT scans, although both of them present a similar distribution shape. The difference between the two distributions may arise due to the threshold value for the fibre volume fraction selected, due to potential artefacts within the micro-CT volumes (that influence the average greyscale values), or due the fact that the generator does not consider any width distortions of the tows (while, in reality, a tow heavily squeezed in the thickness direction is likely to become wider, which will reduce the variability of the fibre content); furthermore, the generator does not explicitly consider resin-rich regions near the tow edges, which can be observed in real microstructures, and which can also affect local fibre volume fraction variations.

2.3.2.3 Effect of the in-plane orientation of the tows on the out of plane angle distributions

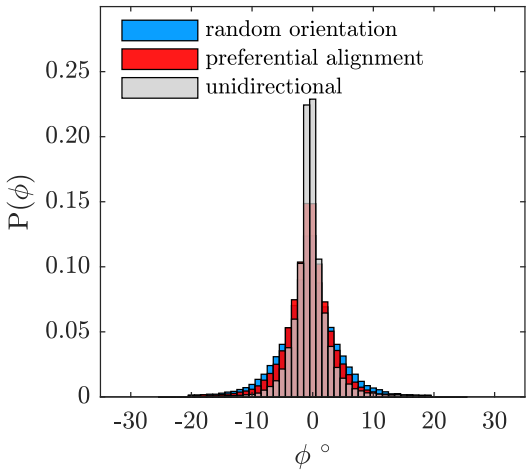

Figure 2.6: Influence of the local in-plane angle distribution on the distributions of out of plane angles predicted by the microstructure generator. The orientation tensors that define the in-plane orientation distributions considered are defined in Appendix A.5.

Figure 2.6 shows the influence of the in-plane tow orientation distribution on the out of plane angle distribution. An in-plane random configuration shows the widest range of out of plane orientations, and an unidirectional configuration the shows the narrowest range of orientations. This effect is related to the number of intersections each tow has with its surrounding counterparts, influencing the nesting of the tows: for the random orientation configuration, the number of tow intersections is the highest, thus leading to more significant waviness; the opposite occurs for a unidirectional configuration, where

the larger overlaps between tows lead to a lower average number of tow intersections, resulting in less distorted tows.

2.3.3 Stiffness model validation and results

2.3.3.1 Experimental validation

Table 2.3: Material properties used as input for the stiffness model (modulus values are in GPa). The UD material from which the tows are made is assumed to be transversely isotropic.

E_1^{t}	E_2^{t}	E^{m}	G_{12}^{t}	G_{23}^{t}	ν_{12}^{t}	ν_{23}^{t}	ν^{m}
129.00†	9.00*	4.00	5.60*	2.80*	0.34*	0.34*	0.40

† Values taken from uni-axial tensile tests on HexPly-M77 with $V^{\mathrm{f}}_{\mathrm{HexPly-M77}} = 51.3$ %, linearly scaled up to the nominal fibre content of the HexMC-M77 material ($V^{\mathrm{f}} = 57$ %)..
$*$ Estimated values based on literature results [35].

Table 2.4: Specification of the microstructural inputs for the TBDC material system tested by Li et al. (2017) [15] and analysed in Figure 2.7a.

l_{gauge} (mm)	w^{s} (mm)	t^{s} (mm)	l^{t} (mm)	w^{t} (mm)	t^{t} (mm)	V^{f} (%)
138	50	2.44	50	8	0.164	57.85
138	50	2.11	50	8	0.285	53.50

Figure 2.7a compares the model predictions for the longitudinal Young's modulus (E_{xx}) against a set of experimentally measured results [15]. Two different material systems are compared: one with thinner tows ($t^{\mathrm{t}} = 0.164$ mm) and the other with thicker tows ($t^{\mathrm{t}} = 0.285$ mm); the material properties and the microstructure features of the composites are described in Tables 2.3 and 2.4, respectively; a random in-plane orientation distribution of the tows was considered. As in the experiments, five virtual specimens were generated for each configuration (with thin and thick tows), with the same dimensions as the ones tested [15] (the length l^{s} of the virtual specimens was set to be the same as the gauge length used in the experiments, identified by l_{gauge} in Table 2.4). The results obtained with the microstructure generator in Figure 2.7a are in better agreement with the experimental results when the tow waviness effects are considered, in particular for the thicker tow configuration.

Figure 2.7b shows the comparison between modulus values predicted by the microstructure generator (with and without waviness effects) and the ones experimentally measured [9] using specimens with different tow geometries (tow lengths ranging from 6-50 mm and tow widths ranging from 3-12 mm; the specimen geometry for the model

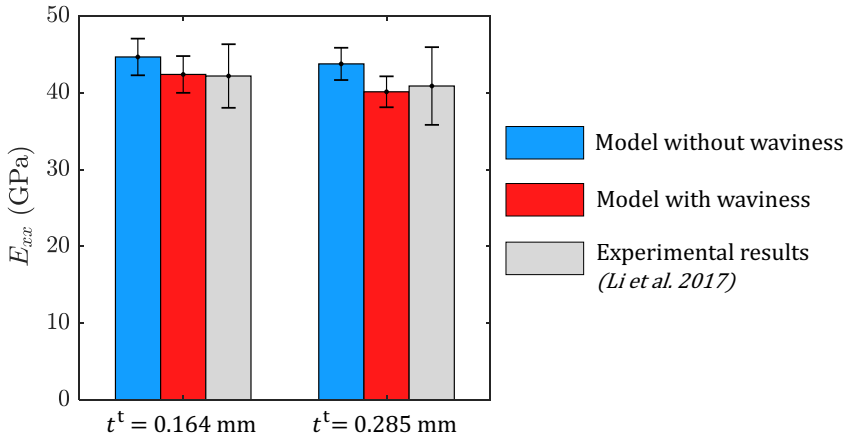

(a) Comparison between experimental results [15] and the model predictions for TBDCs with two different tow thicknesses. The error bars correspond to one standard deviation and the modulus values are normalised to a fibre volume fraction of 57%.

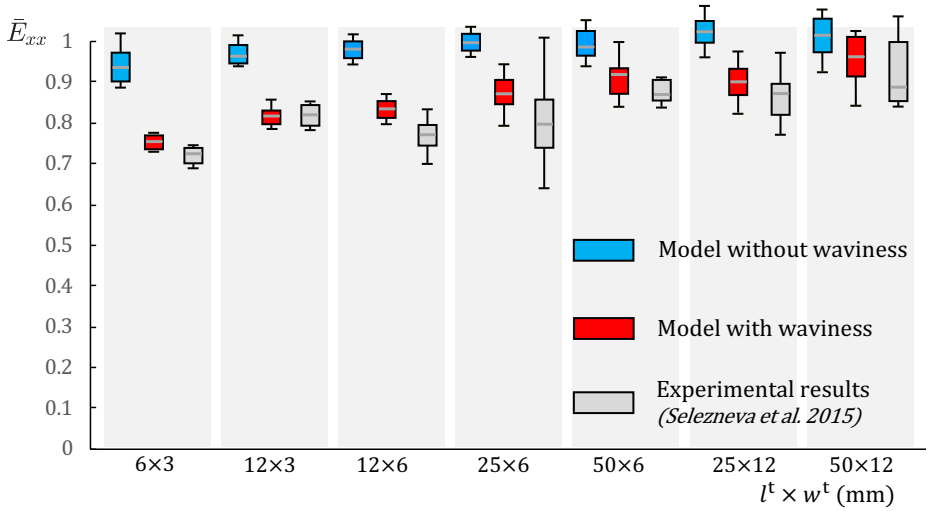

(b) Comparison between experimental results [9] and the model predictions, for TBDCs with seven different tow lengths and widths. The modulus of the TBDCs is normalised by the modulus of an equivalent quasi-isotropic continuous-fibre laminate.

Figure 2.7: Validation of the modulus predictions of the model against experimental results, for TBDCs with different tow geometries.

is defined in Table 2.4 for $t^t = 0.164$ mm). When the waviness effects were neglected, the model results failed to predict the reduction of modulus with decreasing tow dimensions shown in the experiments; however, the experimentally observed trends are accurately captured by the model once the waviness effects are taken into account. This comparison shows the importance of considering the tow waviness in the modulus calculation of TBDCs, as reductions that may go up to 25% can occur for short and narrow tows (6 × 3 mm).

2.3.3.2 Parametric study on the modulus reduction due to tow waviness

In order to assess the effect of the tow geometry in the in-plane modulus reduction due to tow waviness, a parametric study was carried out, as shown in Figure 2.8. The modulus reduction is here defined as the difference (in percentage) between the modulus predicted by the model with and without waviness (see Section 2.2.2). The baseline specimen and tow geometries used for the parametric study are presented in Tables 2.1 and 2.2, with a random in-plane angle distribution of the tows, unless stated otherwise. For each combination of tow and specimen geometrical properties considered in the parametric study, ten virtual specimens were generated; the main trends identified in the results are summarised below:

- Tow length l^{t} and tow width w^{t}: shorter and narrower tows are more prone to have out of plane orientations, which can lead to a significant reduction of the in-plane modulus (Figure 2.8a and2.8b); this effect is significantly dimmed as the tow length or width increase. The magnitude of the effect of the tow length and width predicted by the model is in good agreement with experimental results presented in the literature [9, 21], as shown in Figure 2.7b.
- Tow thickness t^{t}: a linear relation between the in-plane modulus reduction due to waviness and the tow thickness is predicted (Figure 2.8c), because thicker tows lead to more significant out-of plane orientations and consequently to higher in-plane modulus reductions. Figure 2.8e shows the effect of tow length for tows with a constant length-to-thickness ratio; no significant trend is found, which indicates that the effect of the increasing tow thickness is balanced by the increase in tow length, as these parameters have opposite effects on the in-plane modulus.
- Specimen thickness t^{s}: a small positive linear correlation between the specimen thickness and the in-plane modulus reduction is found (Figure 2.8d). However, this effect is less pronounced than that observed for the tows thickness (Figure 2.8c), which indicates that the tow thickness has a more significant influence on the distribution of the out of plane orientations when compared to the specimen thickness.
- The in-plane orientation of the tows also has an effect on the in-plane modulus reduction (see Figure 2.8f), with a random orientation distribution of the tows yielding the highest reduction, and the unidirectional configuration yielding the lowest reduction. This effect is directly related to Figure 2.6, where it was shown that the number of intersections each tow has with its surrounding counterparts influences the magnitude of its waviness and, consequently, the effect of waviness on the in-plane modulus.

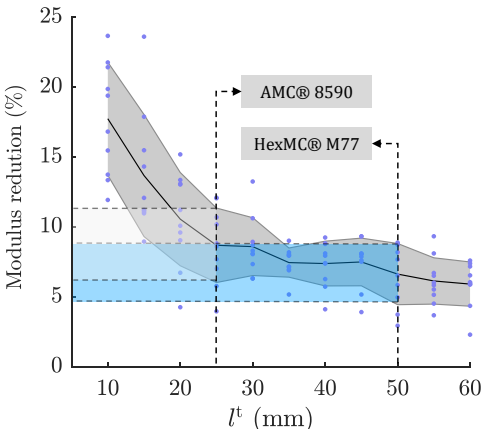

(a) Effect of tow length on the in-plane modulus reduction.

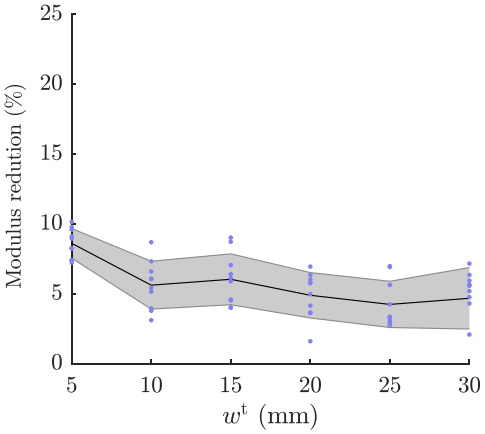

(b) Effect of tow width on the in-plane modulus reduction.

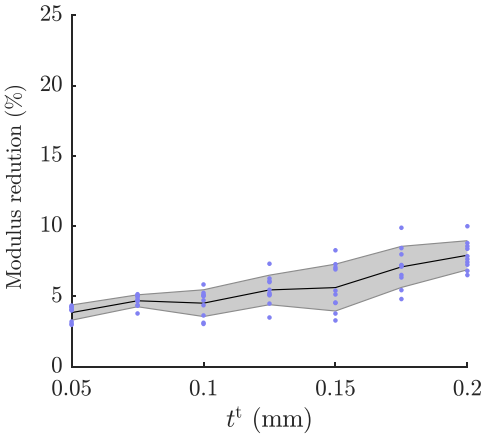

(c) Effect of tow thickness on the in-plane modulus reduction.

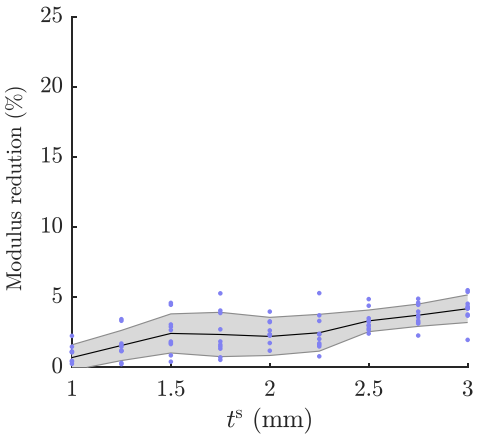

(d) Effect of specimen thickness on the in-plane modulus reduction.

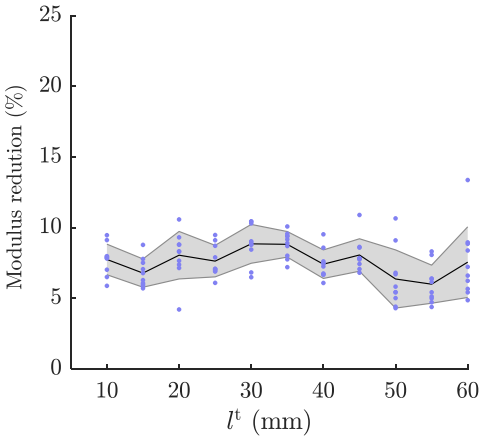

(e) Effect of tow size on the in-plane modulus reduction ($l^t/t^t = 300$).

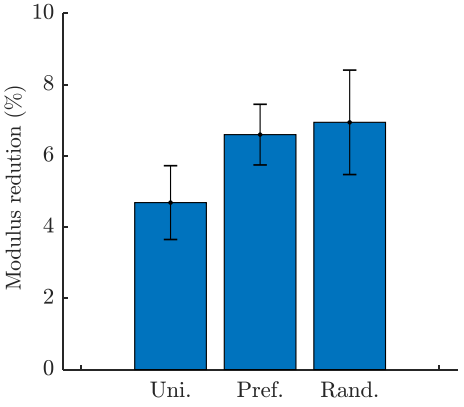

(f) Effect of the in-plane tow orientation (see Appendix A.5) on the in-plane modulus reduction.

Figure 2.8: Parametric study on the effect of the tow geometry in the in-plane modulus reduction. For subfigures a-e, the blue dots represent the obtained modulus reduction for each virtual specimen; 10 virtual specimens were analysed for each configuration. The mean values for each configuration are connected with a black line and the grey region encapsulates the ± one standard deviation boundary.

2.3.4 Guidelines for the modulus measurement of TBDCs

Due the random microstructure of TBDCs, the experimental determination of their elastic properties has an uncertainty associated to it, which depends on the number of specimens tested, the dimension of the specimens and, in particular, the ratio between the tow dimensions and the length of the gauge section. In order to suggest guidelines for the experimental testing of these materials, in this Section the microstructure generator and stiffness model are used to quantify the uncertainty of the predicted modulus values as a function of the tow and gauge lengths, as well as the number of tested specimens. The modulus uncertainty ratio, U_{E}, will be calculated for each batch size of N specimens as the ratio between the half width of the 95% confidence interval, $\mathrm{CI}_{95\%}$, and the average modulus value of the batch $\tilde{E}_N$:

$$U_{\mathrm{E}} = \frac{\mathrm{CI}_{95\%}}{2 \cdot \tilde{E}_N}. \tag{2.13}$$

Figure 2.9 shows the evolution of the modulus uncertainty with the number of virtual specimens tested for different combinations of the tow and gauge lengths. As expected, the uncertainty decreases as the number of tested specimens increases. However, the uncertainty is highly dependant on the relation between the tow and gauge lengths.

For the same gauge length, specimens with shorter tows lead to smaller uncertainties, since the tow count (i.e. number of tows) in the gauge section is higher than in specimens with the same gauge length but with longer tows. A low tow count results in a limited number of possible in-plane tow orientations within the gauge section, which leads to significantly different in-plane angle distributions of the tows across the different specimens within the same batch; this leads to significant variability in the measured modulus of each specimen, and consequently to high uncertainty values. Furthermore, a common trend that can be identified in Figure 2.9 is the high uncertainty in the modulus measurement that occurs for specimens with tow lengths equal or higher than the gauge length.

The standard ASTM D3039 [36] recommends testing 5 specimens in order to measure the modulus of randomly oriented discontinuous composites with a gauge length of 6 mm (using strain gauges) or 10-50 mm (using extensometers). These recommendations neglect the influence of the size of the tows/reinforcement of the discontinuous composite, which can potentially lead to high uncertainties (up to 20%) in the measured values, even when a gauge length of 50 mm is used, as shown in Figure 2.9c.

This analysis shows that the existing standards for measuring the modulus of composites are not suitable for TBDCs, due to the large tow dimensions in the latter. The

microstructure generator and stiffness model can therefore be used to define the experimental plan (i.e. number of specimens to be tested and strain gauge length) required to achieve a certain confidence level in the measured modulus of a TBDC material, as a function of its tow dimensions.

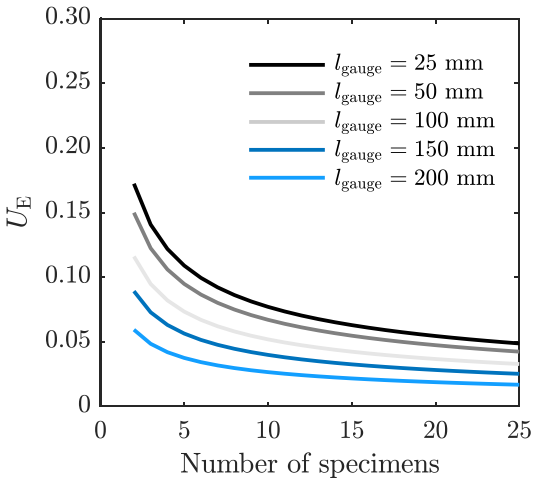

(a) Modulus uncertainty ratio for a constant tow length of 20 mm.

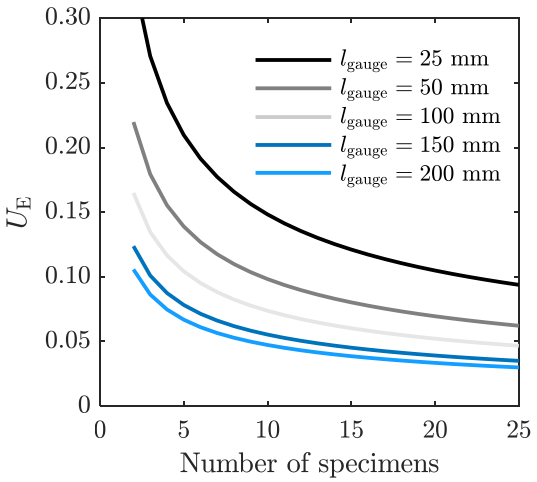

(b) Modulus uncertainty ratio for a constant tow length of 50 mm.

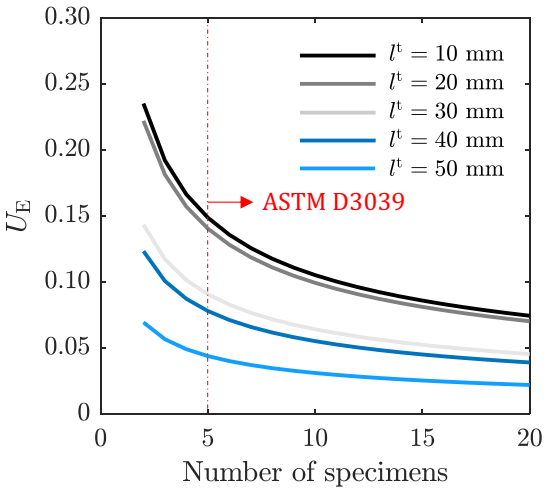

(c) Modulus uncertainty ratio for a constant gauge length of 50 mm.

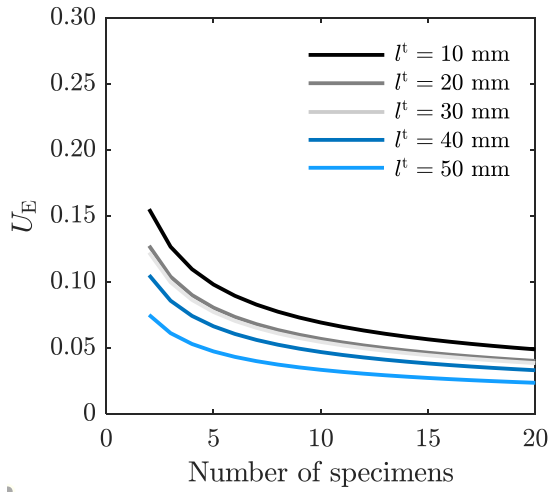

(d) Modulus uncertainty ratio for a constant gauge length of 150 mm.

Figure 2.9: Modulus uncertainty ratio for different combinations of tow and gauge lengths.

2.4 Discussion

2.4.1 Potential for optimising commercial TBDC systems

The parametric study shown in Figure 2.8 indicates that the tow length and thickness are the geometrical parameters that have the most significant influence in the modulus knock-down of TBDCs as a result of the tow waviness. Figure 2.8a highlights the predicted average modulus reduction due to tow waviness, for the tow length of two commercially available materials: HexMC-M77 ($l^{\mathrm{t}} = 50$ mm) and AMC-8590 ($l^{\mathrm{t}} = 25$ mm); the results suggest that the Young's modulus of these materials could be optimised by using longer and/or thinner tows, which would lead to a more regular microstructure (with narrower out of plane angle distributions) and also to more effective stress transfer mechanisms (governed by shear-lag [30]) between the tows; this would increase both the stiffness and strength of the material.

2.4.2 Relative influence of tow discontinuities and waviness on the properties of TBDCs

The Halpin-Tsai and the shear-lag parameters used in the stiffness model presented in Section 2.2.2 reflect the discontinuous nature of the material system; however, it is known that these widely used and computationally efficient models may induce a small degree of error in the predictions of stiffness properties of discontinuous composites [37]. However, Figure 2.7b shows (in particular for the short and narrow tow configurations) that the influence of the discontinuities alone (captured by the model results without waviness) only leads to a modulus reduction of about 6%, whereas the out-of-plane effects (captured by the model with waviness) lead to a modulus reduction of about 25%. This demonstrates that effect of the waviness is of greater significance than the effect of discontinuities.

The influence of the tow waviness will even be of more relevance when considering any through-the-thickness or compressive strengths. The proposed microstructure generator could be used to generate statistical information that could inform models for such predictions.

2.4.3 Contribution of the microstructure generator and stiffness model to the state of the art

The models developed in Section 2.2 and the results obtained in Section 2.3 make the following contributions to the state of the art:

- The proposed microstructure generator captures out-of-plane fibre orientations due to the nesting of the tows along the thickness direction; moreover, the proposed stiffness model accounts for the resulting tow waviness in the prediction of elastic constants. This is a significant improvement to previous work in the literature [20, 22, 23], as it is shown (in Figure 2.7b) that accurate predictions of the modulus of specimens manufactured with short and narrow tows can only be achieved when considering the effect of the tow waviness.
- The proposed microstructure generator imposes a threshold for the local fibre volume fraction (Eq. 1), thus avoiding creating microstructures with unrealistically high local fibre contents.
- The proposed microstructure generator assumes an inverse relation between the local tow thickness and the local fibre volume fraction, which implicitly accounts for the tow compactation process that occurs during manufacturing. It also includes the effect of variations in tow thickness and fibre volume fraction on the stiffness predictions, which had not been considered in previous work reported in the literature [18, 20, 22, 23].
- The microstructure generator and stiffness model proposed in this chapter are the first approach in the literature to capture the effect of tow waviness and fibre volume fraction variations in TBDCs *analytically*; this allows for faster but still accurate predictions of stiffness than FE-based simulations reported in the literature [18, 20, 22].

2.5 Conclusion

A microstructure generator able to recreate the 3D features of the microstructure of tow based discontinuous composites has been developed and implemented in a Matlab code; the generator is able to generate realistic distributions of both out of plane angle orientations (due to tow waviness) and fibre-volume fraction. The statistics of the generator have been coupled with an analytical stiffness model allowing for the assessment of the effect of the tow waviness on the in-plane modulus of TBDCs. The main conclusions of this work are here summarised:

- The statistics obtained with the microstructure generator (out of plane orientation and fibre volume fraction distributions) have been validated with 3D measurements done on micro-CT scans of TBDC specimens. The predicted out of plane angle distributions are in good agreement with the ones obtained with a structure tensor analysis of the reconstructed volumes, and the measured volume fractions distributions have similar shapes to the ones obtained by the generator.

- The microstructure generator is implemented in a efficient numerical scheme (as it can generate a virtual specimen and predict its elastic properties in less than 100 seconds), enabling it to be used for parametric studies on the effect of microstructure and micromechanical properties on the elastic properties of TBDCs.
- The effect of tow waviness on the modulus of TBDCs has been quantified for the first time in the literature: for certain tow geometries (short, narrow and/or thick tows) the waviness effect can lead to in-plane modulus reductions of up to 25%, which hinders the application of pure 2D models for these cases.
- The model predictions for modulus have been compared against experimental results, and a good agreement has been found; the experimental trends for the effect of the tow geometry in the modulus of TBDCs have been successfully replicated by the model when waviness effects were included in the model.
- The microstructure generator has been used to quantify the uncertainty in the modulus measurements following the ASTM D3039 recommendations; it has been found that, for some TBDCs commercially available, those recommendations can lead to uncertainties up to 20% in the measured modulus values. The microstructure generator can therefore be used to plan experimental campaigns by defining a specific number of specimens and gauge length required to achieve a targeted confidence level, for any chosen tow geometry.

Chapter 3

Ultra-strong and stiff randomly-oriented discontinuous composites: closing the gap to quasi-isotropic continuous-fibre laminates

3.1 Introduction

Commercially available TBDCs are based either on chopped prepreg [2] or Sheet Moulding Compounds (SMC) [11]; in these commercially available systems, the in-plane randomness of the tows is achieved through proprietary processes. Lab-based TBDCs are usually manufactured by chopping prepreg [6, 10, 15]; in these lab-based systems, the in-plane randomness of the tows was achieved through a variety of processes, eg. by manually placing each individual tow in a location and orientation previously defined by a numerical random number generator [15], by a wet-type paper making process where the tows are randomly dispersed in water [6], or by scattering all tows at once until achieving a visually satisfactory degree of randomisation [10].

Compression moulded TBDC specimens have shown stiffness values comparable to those of quasi-isotropic continuous-fibre laminates [9, 10], hence making them a good alternative to continuous fibre composites for stiffness-driven designs. Moreover, due to the material architecture, with stiff inclusions embedded in a soft matrix, high damage tolerance has been achieved [5, 30].

However, the discontinuous architecture of TBDCs leads to stress concentrations near the tow-ends, which generate damage at the interface between tows, potentially leading to failure due to tow debonding and pull-out. For this reason, the strength values of commercially available TBDCs are significantly (between 30-60%) lower than those of quasi-isotropic continuous-fibre laminates [9].

It has been experimentally shown that the thickness of the tows has a significant effect on the mechanical properties of TBDCs [15, 38, 39]. Wan et al. [38] found that manufacturing TBDCs with thin tows (of approximately 50 μm) resulted in higher ultimate strength values (500 MPa), closer to those of continuous fibre composites. Li et al. [15] manufactured TBDC specimens using two different tow thicknesses (but similar specimen thickness), and found that the specimens with thicker tows led to lower mechanical properties, both in terms of modulus and strength. The latter was attributed to the earlier onset of tow pull-out that occurs with thick tow configurations, and to the higher variability of the microstructure (as a result of the lower average number of thick tows across the thickness of the specimens), increasing the probability of the occurrence of weak spots in the material.

The use of thin-plies has been shown to significantly increase the mechanical properties of continuous-fibre composite laminates as well. In earlier work by Dvorak and Laws [40], and later by Camanho et al. [41] and Arteiro et al. [42], experimental observations and numerical predictions have shown that the in-situ transverse tensile and shear strength increase with the reduction in ply thickness. Moreover, experimental studies by Sihn et al. [43] and Amacher et al. [44] have demonstrated that the stress for the onset of damage and the ultimate tensile strength of quasi-isotropic laminates increase with reduced ply thickness.

Li and Pimenta [23] have predicted the effect of tow thickness on the strength of TBDCs using analytical models specifically developed for these materials. These models were based on (i) equivalent laminates (in which each lamina is an unidirectional discontinuous ply with the same tow geometry as in the actual TBDC [15]) and (ii) shear-lag considering the the non-linear shear response of the matrix up to failure [30]. It was shown that it is fundamental to account for the finite fracture toughness of the matrix (or fibre-matrix interface) in the shear-lag formulation [30] in order to correctly predict the effect of tow thickness on the strength of TBDCs.

Other models to predict tensile response of TBDCs have also been presented in the literature [16, 18, 20, 22, 28, 39, 45, 46]; these models focus either on unidirectional [39, 46] or randomly-oriented [16, 18, 20, 22, 28, 45] composites using either analytical (and therefore efficient) or FE based (and therefore less efficient) formulations. However, some of these models [18, 20, 22] neglect the effect of delamination between the tows and are therefore unable to capture the effect of the absolute value of the tow thickness

on the mechanical response of the material; others [39, 46], have focused only on the effect of the tow aspect-ratio rather than on the effect of the absolute value of thickness.

The effect of the specimen thickness on the strength of TBDCs has also been reported in the literature [10, 16] It was shown that the strength decreases with the reduction of the specimen thickness; a strength knock-down of 50% was reported due to a specimen thickness reduction from 3.73 mm down to 0.82 mm. This effect was justified [10, 16] by the smaller average number of tows through-the-thickness of the thinner specimen, which increases the variability of properties from one point of the specimen to another, and therefore increases the probability of very weak spots (e.g. with preferentially transverse tows) that can trigger premature failure.

So far, only TBDC material systems with tow thicknesses ranging from 50-200 μm, standard- or intermediate-modulus fibres (below 300 GPa), and plate thickness above 1.5 mm have been tested and reported in the literature [2–4, 10, 11, 38]. The reported tensile-strength values of these TBDC systems range from 250-500 MPa [2–4, 10, 11, 38] which are still below the tensile strength of typical continuous-fibre QI laminates (600-900 MPa); moreover, typical tensile moduli of these materials are in the range of 30-50 GPa [2–4, 10, 11, 38], which barely competes with Aluminium in terms of specific stiffness. This leaves room in the design space of the material's microstructure to investigate whether it is possible to achieve higher mechanical properties with this type of architectures. In this work, TBDCs manufactured with ultra-thin (20 μm) and high modulus carbon fibres tows (425-750 GPa) are explored, with the objective to maximise the material's mechanical properties (especially its ultimate tensile strength) and assess its suitability for thinner structures.

In Section 3.2, physically based numerical models, developed for TBDCs, are used to explore the material's design space and guide the microstructural design. Section 3.3 details the manufacturing and testing procedures of TBDC plates with different microstructural configurations selected; experimental studies are performed to independently assess how the materials' mechanical properties are affected by the thickness and stiffness of the carbon-fibre tows. The experimental results are analysed and discussed in Sections 3.4 and 3.5, and the main conclusions are drawn in Section 3.6.

3.2 Material Design

3.2.1 Failure criteria for discontinuous composites

The longitudinal tensile strength and failure mechanisms of discontinuous composites depend on (i) the mechanical properties of the constituents (i.e. fibres and

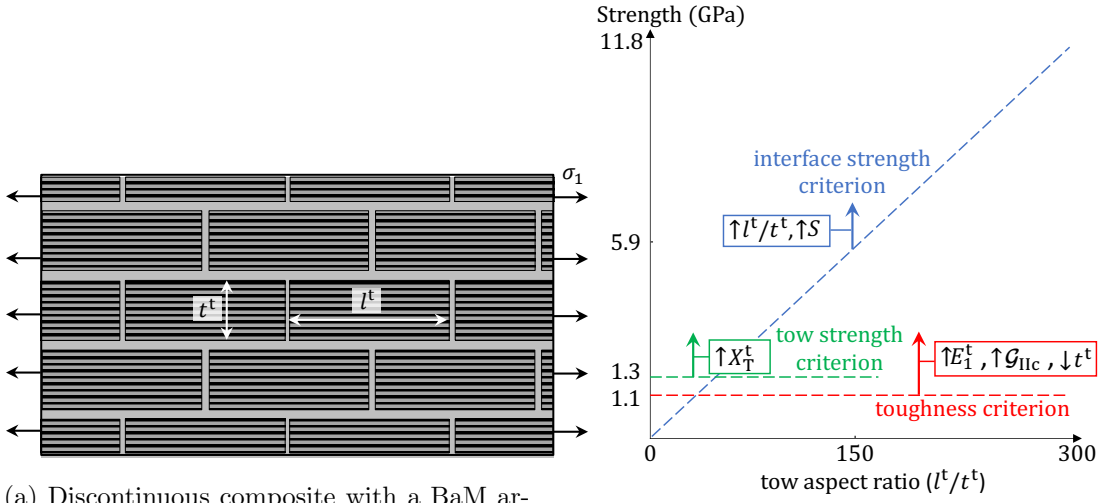

(a) Discontinuous composite with a BaM architecture [30].

(b) Longitudinal tensile strength of a BaM composite (see Eqs 3.1- 3.3); values are for a BaM with constituent properties of the HexMC-M77, and for a value of $k = 1$.

Figure 3.1: Model material systems used to represent TBDCs.

matrix), (ii) the geometry of the reinforcing units (rectangular tows, in the case of TBDCs), and (iii) the architecture of the reinforcing units within the composite; the latter is extremely complex in a TBDC material (as the tows are randomly oriented and randomly located), and extremely simple in a "Brick-and-Mortar" (BaM) composite (represented in Figure 3.1a). Therefore, in order to explore the design space of TBDCs and identify potential routes to improve their tensile strength, the failure mechanisms of an equivalent BaM composite under longitudinal tension will first be analysed.

Considering a BaM composite as shown in Figure 3.1a, where the bricks are tows (with thickness t^t and length l^t) and the mortar is the tow-to-tow interface (with negligible thickness), its ultimate longitudinal tensile strength is bounded by the following criteria [30]:

- Tow strength criterion: for high aspect-ratio (length divided by thickness) tows, the longitudinal stresses at the centre of the tow transferred via shear of the interface may exceed the longitudinal tensile strength of the tow X_T^t. In this case, failure of the composite is governed by tensile fracture of the tows (i.e. fibre failure), at the overall composite stress

$$X_D^\infty = \frac{X_T^t}{k}. \tag{3.1}$$

where k is the stress concentration factor due to the presence of tow end. For a a perfectly staggered BaM composite, as shown in Figure 3.1a, $k = 2$ and for a real TBDC with randomly located tow ends k is between 1 and 2 [23].

- Interface strength criterion: for low aspect-ratio tows, yielding of the interface limits the stress transfer to the tows [47], in a process that eventually leads to pull-out. Therefore, the overall composite strength, is limited by the interface shear strength (S), where the former is given by

$$X_{\mathrm{D}}^{\infty} = \frac{l^{\mathrm{t}} \cdot S}{2 \cdot t^{\mathrm{t}}}. \tag{3.2}$$

- Interface toughness criterion: for tows with high thickness, the strength of the discontinuous composite is bounded by a process governed by fracture mechanics, in which a mode-II crack propagates along the interface between tows [30], eventually also leading to pull-out of the tows. The strength of the composite, from a toughness-based formulation, is related to the interface mode-II fracture toughness $\mathcal{G}_{\mathrm{IIc}}^{\mathrm{m}}$, to the tow longitudinal Young's modulus E_1^{t}, and to the absolute value of tow thickness t^{t} by

$$X_{\mathrm{D}}^{\infty} = \sqrt{\frac{2E_1^{\mathrm{t}}\mathcal{G}_{\mathrm{IIc}}^{\mathrm{m}}}{t^{\mathrm{t}}}}. \tag{3.3}$$

  It is important to notice that, while in Eq. 3.2 the strength is governed by the aspect-ratio ($l^{\mathrm{t}}/t^{\mathrm{t}}$) of the tows, this is not the case for Eq. 3.3, which is governed by the absolute value of the tow thickness t^{t}.

These three failure criteria act as boundaries of the ultimate strength of BaM composites, and define the design space shown in Figure 3.1b. The failure mechanisms mentioned above also dominate the tensile strength of TBDCs [15], and models based on BaM composites have been successfully used to model the response of TBDCs [23]. Therefore, the design space shown in Figure 3.1b can be used to identify the qualitative effect of microstructural parameters on the tensile strength of TBDCs.

Considering the typical constituents (carbon-fibres and epoxy matrix) and tow dimensions (above 20 mm long and 0.1 mm thick) of TBDCs [2, 9–11], the boundary governed by the interface toughness criteria (Eq. 3.3) is typically the most limiting one to the strength of TBDCs (Figure 3.1b). This interface toughness boundary can be shifted to higher values of strength (closer to the boundary of the tow strength criterion) by using thinner tows with stiffer fibres, which will improve the tensile strength of a TBDC material. The remainder of this chapter will focus on exploring and demonstrating the effectiveness of this concept.

3.2.2 Improving the strength of TBDCs via microstructure design

A physically-based model previously developed in the literature [23] to predict the strength of TBDCs will be here used to quantify the benefits of using thin tows of high-stiffness carbon fibres as the basic reinforcement of a TBDC material system. The key aspects of the model are here summarised:

i) The random discontinuous material is locally idealised as an isotropic *equivalent laminate* (see Figure 3.2a), with each lamina being a unidirectional discontinuous ply (with stiffness and strength properties given by those of a discontinuous material system, with the same tow geometry as in the randomly-oriented TBDC [23]); a constant number of discontinuous plies is assumed, oriented at equally-spaced angles, forming an isotropic layup.

ii) A multiscale model is used to predict the mechanical properties of the equivalent laminate. The longitudinal modulus of a UD discontinuous ply is calculated based on a shear-lag model [48]; the remaining elastic constants are obtained using the Halpin-Tsai equations [33] (assuming a transverse isotropic behaviour for the tows). Classical laminate theory (CLT) is then used to homogenise the elastic properties of the equivalent laminate.

iii) An Interactive Tension-Shear (ITS) criterion is used to predict the failure of a UD discontinuous ply under an in-plane stress state $\boldsymbol{\sigma} = [\sigma_1, \sigma_2, \tau_{12}]$. It considers that failure of a UD discontinuous ply can occur due to a combination of three failure mechanisms: (i) tow fracture, due to longitudinal tensile stresses σ_1; (ii) shear failure of the interface between neighbouring tows, which may occur due to progressive yielding (as in the interface strength criterion in Figure 3.1b) or sudden debonding (as in the interface toughness criterion in Figure 3.1b), resulting from the interaction between σ_1, σ_2, and τ_{12}; and (iii) transverse tow/interfacial failure, due to σ_2 and τ_{12}. For the later, the matrix dominated failure criteria from the LaRC05 [49] is used, which includes the in-situ effect on the transverse tensile and shear strengths of the UD plies. The combination of these failure modes leads to the definition of the failure surface shown in Figure 3.2b, from which a failure index F_{I} can be calculated for a discontinuous ply; the failure of a UD discontinuous ply occurs when the correspondent failure index $F_{\mathrm{I}}(\sigma_1, \sigma_2, \tau_{12}) = 1$.

iv) The failure of the equivalent laminate is assumed to be governed by a first-ply-failure criterion [23], where the equivalent laminate fails as soon as the first ply fails.

It should be noted that this modelling approach neglects the intrinsic variability of TBDCs and therefore the predicted strength values are closer to those of a discontinuous

equivalent laminate than to a randomly oriented TBDC [23]. Nevertheless, the results of this model can still be used to identify the trends of the influence of micromechanical properties on the overall strength of randomly-oriented TBDCs.

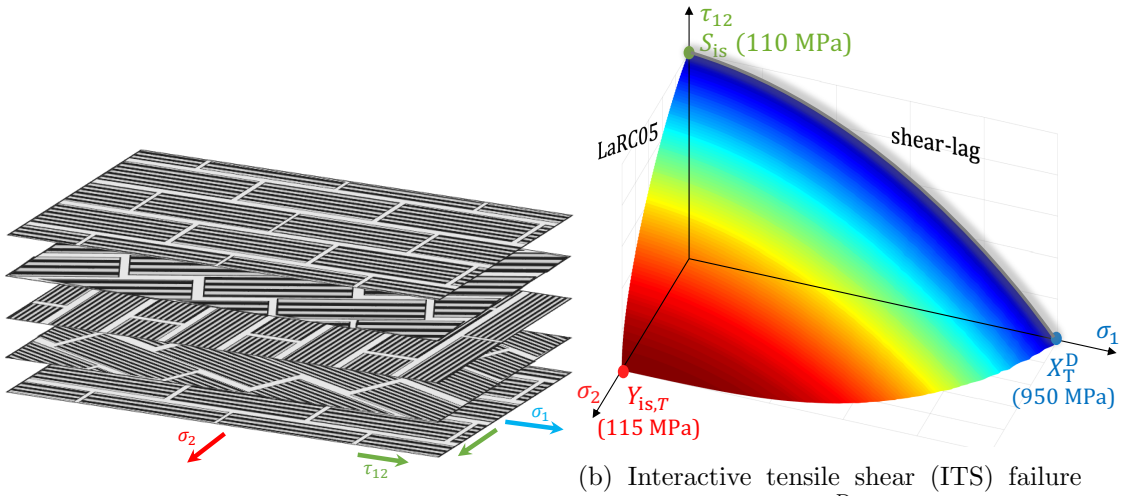

(a) Discontinuous equivalent laminate, where each lamina is a uni-directional discontinuous ply.

(b) Interactive tensile shear (ITS) failure surface [23], where X_T^D is the longitudinal tensile strength of a discontinuous UD equivalent ply, and $Y_{is,T}$ and S_{is} are the in-situ strengths of the UD composite under transverse tension and shear, respectively. The strength values presented refer to the HexMC-M77 (baseline) configuration.

Figure 3.2: Governing failure criteria for discontinuous composites.

The envelope of the ITS for a UD discontinuous equivalent ply defined by the interaction between the in-plane longitudinal tension and shear stresses (σ_1 vs. τ_{12}, with $\sigma_2 = 0$, see Figure 3.2b) is governed by the shear-lag stress transfer mechanism. Figures 3.3a and 3.3b show how this failure envelope is influenced by t^t and E_1^t respectively, using as baseline the microstructure properties of a commercial TBDC system, the HexMC-M77 [2] (specified in Tables 3.1 and 3.2). For stiffer and thinner tows, a significant shift of the failure envelope to higher values of σ_1 is predicted. This effect reflects the more efficient stress transfer that occurs through shear-lag, delaying the onset of a mode-II crack propagating along the tow's interface and ultimately leading to failure. This allows for a further exploitation of the mechanical properties of the fibres, maximising the mechanical properties of the TBDC.

The physically-based model is here used to explore the trends of the effect of the tow properties (tow strength X_T^t, stiffness E_1^t and thickness t^t) on the tensile strength of TBDCs. Table 3.1 summarises all the material inputs required for the model, and Table 3.2 presents several configurations with different tow properties analysed. The predicted TBDC strength for each configuration is presented in Figure 3.3c, where the following trends are can be identified:

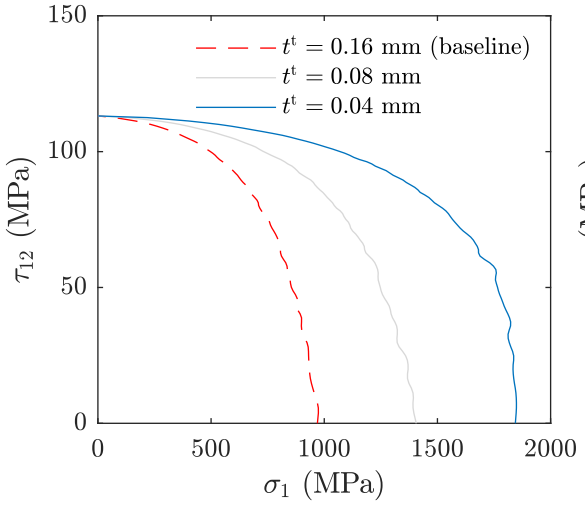

(a) Influence of t^t on the (σ_1 vs. τ_{12}) failure envelope of the ITS criterion for a UD discontinuous equivalent ply.

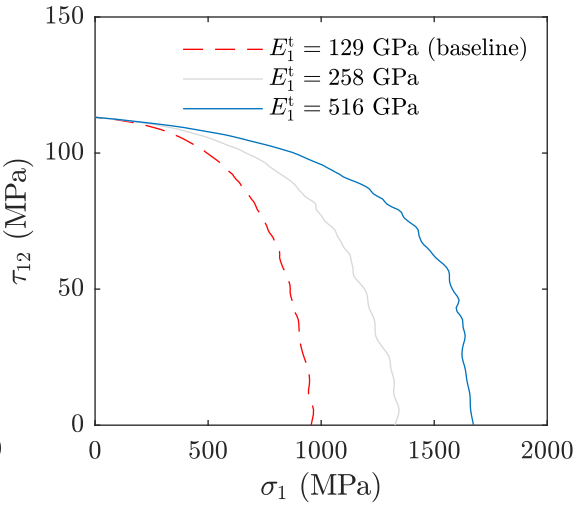

(b) Influence of E^t on the (σ_1 vs. τ_{12}) failure envelope of the ITS criterion for a UD discontinuous equivalent ply.

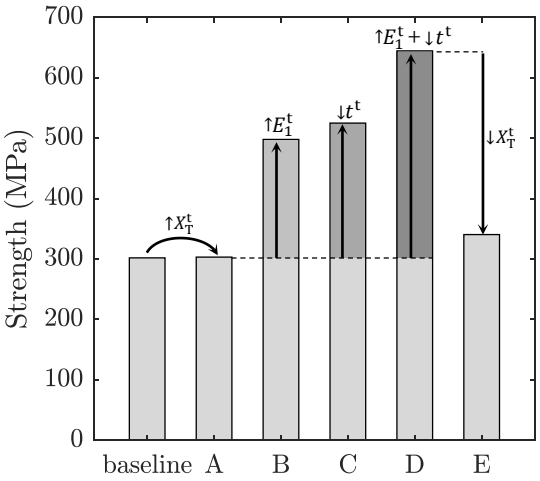

(c) Predicted tensile strength of TBDCs as a function of the tow geometric and mechanical properties (see Table 3.2 for the tow properties specified to materials A-E).

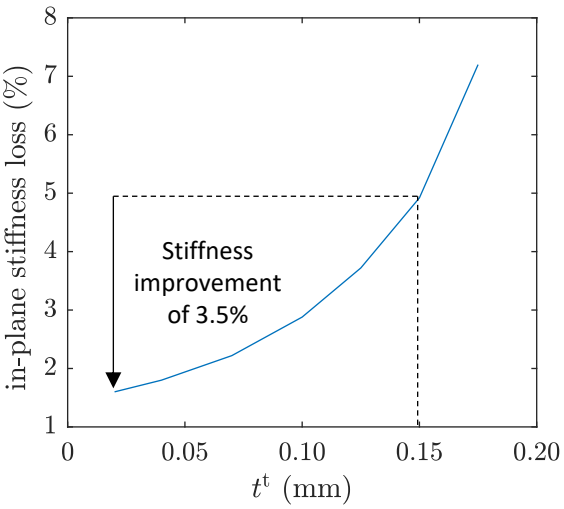

(d) Effect of the tow thickness on the predicted TBDC in-plane stiffness loss due to tow waviness.

Figure 3.3: Analysis of the influence of the different microstructural features/properties on the mechanical properties of TBDCs. The baseline material system is the HexMC-M77 [2], as defined in Tables 3.1 and 3.2.

- For configuration A, the increase in X_T^t over the baseline material does not lead to an increase in the TBDC strength, indicating that, for the baseline configuration, failure is governed by tow pull-out.
- For configurations B and C, the increase in the tow stiffness and the reduction of tow thickness (respectively) over configuration A lead to very significant increases in the TBDC strength. This is due to the shift to higher stress values of

Table 3.1: Tow properties used as model inputs for the TBDC baseline configuration (HexMC-M77). Modulus values are in GPa, strength values are in MPa, toughness values are in kJ/m^2 and volume fraction in %. The values of Y_T and S are correspond to the raw strength values, which are corrected for in-situ effects in $Y_{is,T}$ and S_{is}.

Material	E_1^t	E_2	G_{12}	ν_{12}	X_T^t	Y_T	Y_C	S	$\mathcal{G}_{int}^{IIc}$	V^f
HexPly-M77 [50]	129†	9.0*	5.6*	0.34*	1258†	73*	200*	78*	0.8*	57

† Values taken from uni-axial tensile tests on HexPly-M77 with $V^f_{HexPly-M77} = 51.3$ %, linearly scaled up to the nominal fibre content of the HexMC-M77 material ($V^f = 57$ %).

* Estimated values based on the literature [35].

Table 3.2: Properties used in the analysis of the influence of the tow mechanical properties on the strength of TBDCs.

Configuration	X_T^t (MPa)	t^t (mm)	E_1^t (GPa)
HexMC M77 - baseline	1258	0.164	129
A	2650	0.164	129
B	2650	0.164	516
C	2650	0.041	129
D	2650	0.041	516
E	1258	0.041	516

the toughness criterion boundary (see Figure 3.1b), as result of a more efficient stress transfer mechanism (governed by shear-lag, see Eq. 3.3), enabling a better exploitation of the tow tensile properties.

- Configuration D is the one that presents the highest predicted TBDC strength, as it combines the benefits of both stiffer and thinner tows over configuration A. However, the increase of the TBDC strength for this configuration D is not given by a linear combination of those in configurations B and C.
- Configuration E combines the benefit of thin and stiff tows as in configuration D, but with a lower tensile strength X_T^t. The TBDC strength predicted for configuration E is significantly lower than that of configuration D (and only slightly higher that that of the baseline), which indicates that the predominant failure mechanism in configurations D and E, is no longer tow pull-out but tow fracture instead; the strength of the TBDC in configuration E is therefore bounded by the low value of X_T^t.

In Chapter 2, it was demonstrated that the use of thinner tows has a positive effect on the TBDC's in-plane modulus, by reducing the probability of tows with significant out-of-plane orientations. This is due to the more regular and "layered" microstructure that results from these configurations, which leads to a lower impact of the tow waviness on the in-plane modulus of the TBDC material, as shown in Figure 3.3d.

3.3 Materials and experimental methods

3.3.1 Materials and manufacturing procedure

In order to demonstrate the potential improvements in the mechanical properties of TBDCs identified with the numerical models in Section 3.2, TBDC plates were manufactured using tows of high-modulus carbon-fibres spread into ultra-thin tapes and epoxy films, as described next. The spread tapes were produced by TeXtreme® spread tow technology (a state-of-the-art procedure for spreading tows into thin flat tapes with desired thickness and width) at Oxeon AB, using HS40 (High Modulus, HM) PAN-based and K13916 (Ultra High Modulus, UHM) pitch-based carbon-fibres. The nominal mechanical properties of the fibres (modulus E^{f}, strength X^{f} and strain to failure $\epsilon^{\mathrm{f}}_{\mathrm{fail}}$) are presented in Table 3.3. The spread tapes had a width of 20 mm, and an areal weight of 21 gsm (corresponding to a thickness of approximately 20 μm) or 105 gsm (corresponding to a thickness of approximately 100μm) for the HM fibres, and of 105 gsm for the UHM fibres; the spread tapes were cut in 50 mm long pieces, hereby referred to solely as tapes. The epoxy resin used was supplied by Oxeon AB in the form of thin resin films, with an areal wight of 30gsm.

The tapes were manually placed at random locations and orientations on resin films, forming one equivalent lamina (EL), as schematically represented in Figure 3.4a. In each EL (consisting in one resin film and 100 tapes) overlaps between the tapes were allowed, and the randomness of the tape positions and orientations was not constrained consciously . After the tape placement, heated de-bulks were performed on each EL; this consists in placing each EL in a vacuum bag on a heated RIFT table (at 70°C) for 10 min, in order to ensure a better resin infusion. The final TBDC plate was obtained by stacking several ELs (in order to produce plates with the number of tapes specified in Table 3.4), as shown in Figure 3.4a. During this stacking process, the reference direction of each EL was incrementally rotated by 90° in the stack, in order to further improve the randomness of tape orientations and the in-plane isotropy of the material. This stacking process was followed by a final heated de-bulk of the plate (ensuring a more uniform distribution of the resin along the through-the-thickness direction) before final curing; the plates were cured in an autoclave (with frayed edges and a caul plate) at 6 bars and 120°C for 1 hour, after an initial 30 min stage of at 75°C. Despite the use of the caul plate, some thickness and volume fraction variations occurred along the specimens, as shown in Table 3.4, due to the uneven number of tows along the thickness. Moreover, squeeze flow during the curing process was not monitored.

Five different plate configurations (described in Table 3.4 under IDs coded as <fibre type> - <nominal tape thickness> - <number of tapes in plate> - <testing direction>) were manufactured and tested in order to independently assess different effects:

Table 3.3: Mechanical properties of the different fibre types used in the experiments.

Fibre type	E^{f} (GPa)	X^{f} (MPa)	$\epsilon^{\mathrm{f}}_{\mathrm{fail}}$ (%)	Ref.
HS40 (HM)	425	4640	1.01	[51]
K13916 (UHM)	760	3000	0.40	[51]

Table 3.4: Configurations of the different TBDC plates manufactured.

Plate ID	Fibre type	nominal t^{t} (µm)	nominal N_{tapes}	measured thickness (mm)	measured V^{f} (%)	testing direction* (°)
HM-20-800-0	HS40	20	800	0.187 ± 0.021	47 ± 3.7	0
HM-20-800-90	HS40	20	800	0.194 ± 0.029	46 ± 3.5	90
HM-20-1600	HS40	20	1600	0.480 ± 0.040	46 ± 1.7	0
HM-100-800	HS40	100	800	0.902 ± 0.064	54 ± 3.2	0
UHM-100-800	K13916	100	800	0.715 ± 0.075	55 ± 5.0	0

* Testing direction of the specimens relative to the reference plate direction.

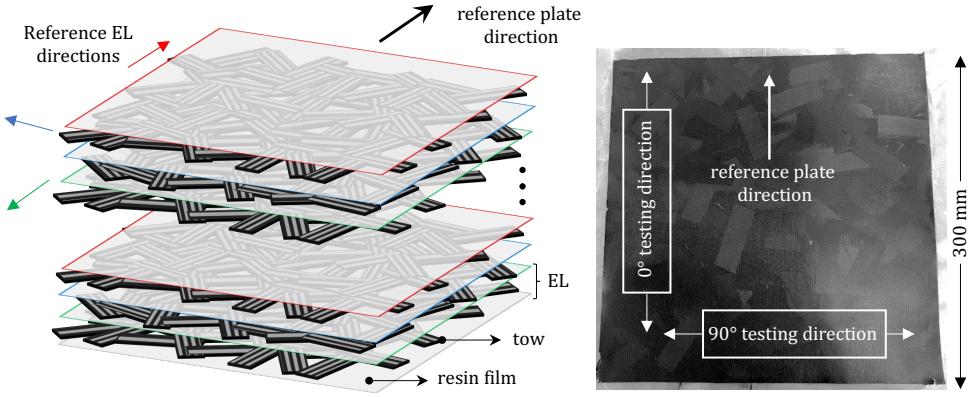

(a) Schematic representation of TBDC plate.

(b) Final manufactured TBDC plate.

Figure 3.4: Manufacturing procedure of the TBDC plates.

- In-plane isotropy (HM-20-800-0 and HM-20-800-90): both plates were manufactured with the same specifications, although the specimens of each plate were tested at different orientations (0° and 90°) to the reference plate direction.
- Effect of the areal tape coverage (HM-20-800 and HM-20-1600): both plates were manufactured with the same fibre type and tape thickness, but with different total number of tapes in the plate ($N_{\mathrm{tapes}} = 800$ and $N_{\mathrm{tapes}} = 1600$, respectively).

- Effect of the tape thickness (HM-20-800 and HM-100-800): both plates were manufactured with the same fibre type and number of tapes, but with different tape thicknesses (20 and 100 µm).

- Effect of the fibre stiffness (HM-100-800 and UHM-100-800): both plates were manufactured with the same tape thickness and number of tapes, but with different fibre types (HM and UHM).

3.3.2 Testing and analysis

Each plate was cut into 5 rectangular specimens, 250×50 mm in length and width respectively, which were then subjected to a standard uni-axial tensile test, with a gauge length of 150 mm (following the ASTM-D3039 standard [36], and with a head displacement of 1 mm/min). The strain in the specimens was measured with an optical strain gauge [52]; the total strain was taken as the average strain measured by three virtual extensometers, each with a strain gauge length of 75 mm, evenly spaced along the specimen's width. Furthermore, the modulus of each specimen was taken as the (best fit) slope of the measured stress-strain curve between 0.05% and 0.2% strain. Emery cloth was used between the specimens and the testing grips, and the majority of tested specimens failed within the gauge section.

Optical micrographs were used to analyse the resulting microstructure of each plate configuration at three distinct cross-sections; the volume fraction of each cross-section was obtained from processing these three micrographs ($[0.15 \times 0.40]$ mm) using simple threshold algorithms. Images of the fracture surface of each specimen were taken using a standard camera, in order to identify the predominant failure mechanism in each plate configuration.

3.4 Results

3.4.1 Tensile test results

The results of the tensile tests are shown in Figure 3.5; for all materials tested, the response was linear-elastic up to failure. All modulus and strength results presented in this section have been linearly scaled to a $V^{\mathrm{f}} = 57$ % (which is a typical value for commercial available TBDCs [2]), in order to allow for a direct comparison between different material systems. Figure 3.5a shows the measured stiffness of the specimens from each plate configuration. The modulus values of the plates made with the HM fibres is relatively constant across the different plate configurations; this suggests that the fibre volume fraction measurements shown in Table 3.4 are representative of the plates manufactured, and that the linear scaling to $V^{\mathrm{f}} = 57$ % is appropriate. The plate with the UHM fibres yielded the highest average stiffness value, as expected, although with a large standard deviation.

Figure 3.5b presents the both the average strength value measured for each plate configuration as well as the standard deviation:

- The highest tensile strength value of 600 MPa was achieved with the thin HS40 tapes, and in particular for the plate configuration with 1600 tapes.
- The strength difference between the HM-20-1600 plate and the HM-20-800 is quite significant, with a p-value = 0.06 (all p-values in this chapter refer to two-sample (unequal variance) two-tailed t-test); since these two plates only differ in the total number of tapes, this difference can be explained by a more even areal tape coverage along the thickness of the specimen in the HM-20-1600 plate configuration. This leads to a lower probability of finding regions with a small number of tapes along the thickness direction (which trigger premature failure). This reflects the difficulty of achieving a good fibre areal coverage in a randomly oriented TBDC with a low ratio between the plate and the tape thicknesses.
- The HM-100-800 plate, with the thicker tape configuration, presents a significantly lower average strength value when compared to the thinner tape configurations (HM-20-800), with a p-value = 0.05. This is due to a more efficient stress transfer in the latter, and to an increase in the TBDC strength-bound dominated by the interface toughness (Eq 3.3).
- The UHM-100-800 plate was the one that presented the lowest average strength; this is due to the combination of thick tapes, low fibre strength, and a lower total number of tapes. This was also the configuration with the most significant variability in the measured results, likely due to the fact that only 3 (out of 5) if the specimens produced valid failures (and only those 3 are included in Figures 3.5b-3.5d).

Figure 3.5c shows the failure strain of the TBDCs ($\epsilon_{\text{fail}}^{\text{TBDC}}$) tested; once again the HM-20-1600 configuration was the one that presented the highest $\epsilon_{\text{fail}}^{\text{TBDC}}$, and the UHM-100-800 configuration presented the lowest value. However, by analysing the ratio between the TBDC failure strain and the fibre failure strain ($\epsilon_{\text{fail}}^{\text{TBDC}}/\epsilon_{\text{fail}}^{\text{f}}$), as done in Figure 3.5d, one can better quantify the exploitation of the fibre strength within the TBDC, for each plate configuration: this suggests that the configuration with the UHM fibres (UHM-100-800) achieved a better exploitation of the fibre strength than the corresponding configuration with HM fibres (p-value = 0.17), due to a more efficient stress transfer mechanism promoted by the stiffer fibres in the former. However, the lower fibre strength of the UHM fibres (3000 MPa) compared to the HM fibres (4640 MPa) is limiting the TBDC strength value of the UHM material.

As previously mentioned in Section 3.3.1 and Table 3.4, HM-20-800 specimens were tested both at 0° and 90° testing directions, in order to verify whether in-plane isotropy was achieved. Figure 3.5 shows that the properties measured at the two testing

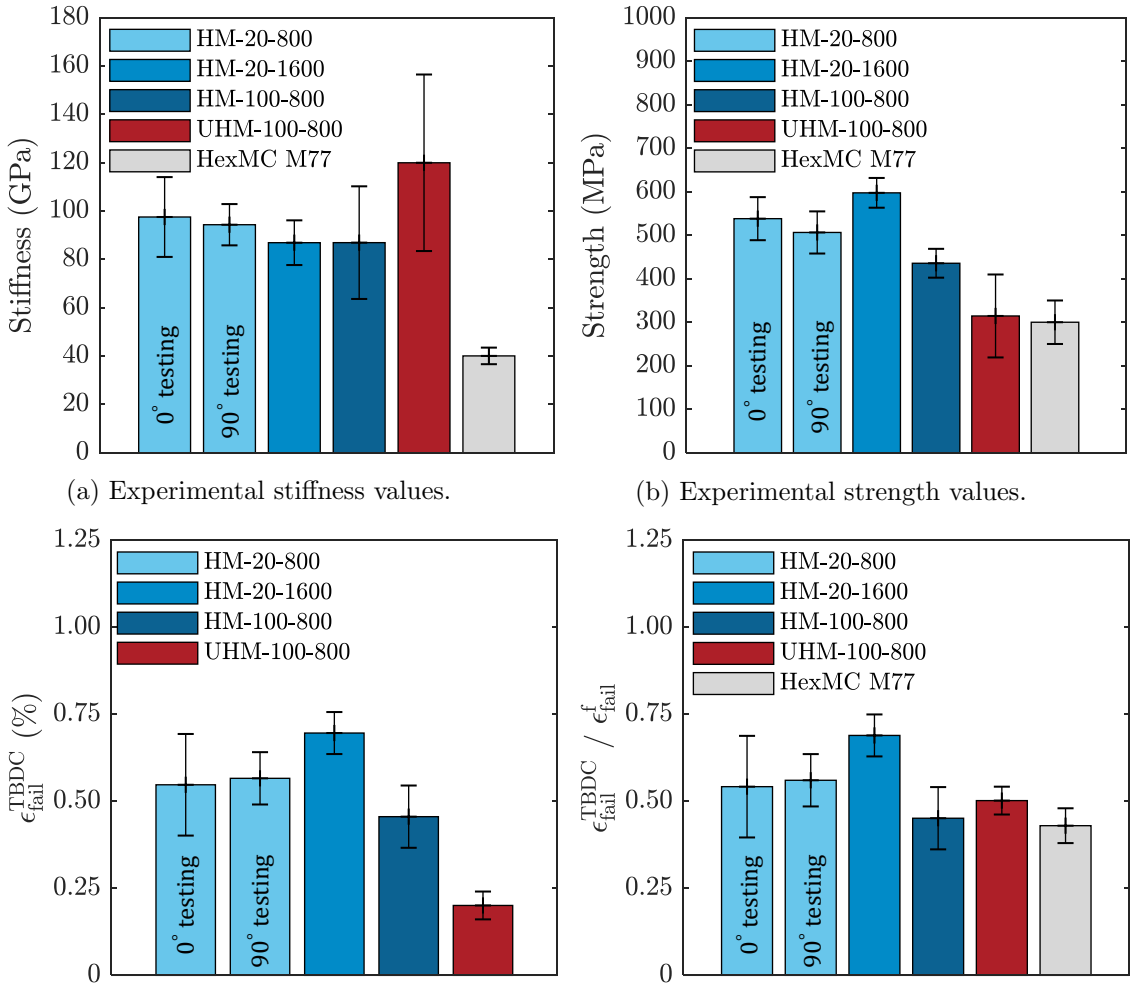

(a) Experimental stiffness values.

(b) Experimental strength values.

(c) Experimental failure strain of the different material configurations.

(d) Ratio between the experimental and respective fibre failure strain.

Figure 3.5: Experimental tensile test results of the different TBDC configurations tested (scaled to $V^{f} = 57\%$), and comparison against the commercially available HexMC-M77 [2]; the error bars represent one standard deviation.

directions are identical, which supports the conclusion that the manufacturing process described in Section 3.3.1 indeed resulted in in-plane isotropy.

Figure 3.6 compares the strength predicted by the model presented in Section 3.2 with the experimental results of three different plate configurations (HM-20-800, HM-100-800 and UHM-100-800). The numerical inputs for the model can be found in Table 3.3, except for the tape thickness t^{t} – which is shown in Table 3.4 for each plate configuration – and for the fibre-dominated tensile properties of the tows – which were taken as $E_1^{t} = E^{f} \cdot V^{f}$ and $X_T^{t} = X^{f} \cdot V^{f}$, with E^{f} and X^{f} as presented in Table 3.3. The analytical model captures the measured effect of the tape thickness and fibre stiffness on the strength of TBDCs, but predicts higher strength values when

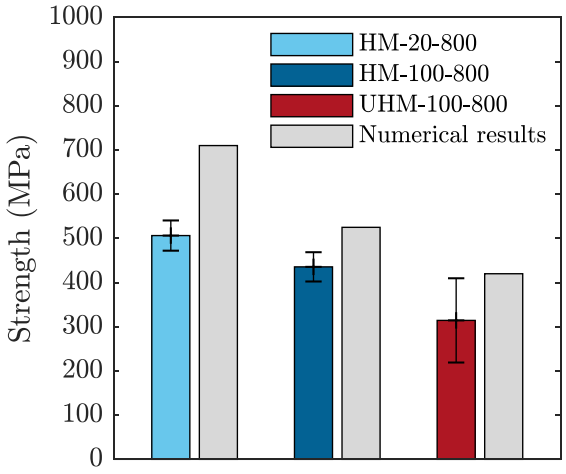

Figure 3.6: Comparison between the numerical predictions and experimental results for the strength of three different plate configurations.

compared to those measured experimentally, for all cases. This is due to the intrinsic variability of the TBDC material system (where local weak spots govern failure of the material), which is not directly incorporated in the analytical model (as it considers quasi-isotropic equivalent laminates, see Figure 3.2a). However, the relative magnitude of the influence of the different tape properties in the predicted TBDC strength are in good agreement with the experimental results.

3.4.2 Fracture surfaces

The fracture surfaces of a representative specimen taken from each plate configuration are shown Figure 3.7. The fracture surfaces for the thin tape configurations (Figures 3.7a and 3.7b) show no evidence of tape pull-out, and a clear evidence of tape fracture. For the thicker tape configurations (Figures 3.7c and 3.7d), a mixture of tape pull-out and tape fracture was observed, reflecting the less efficient stress transfer that occurs for thicker tape configurations. The fracture surfaces of the thin tape configurations are remarkably different from those of the thick tapes, and reflect the predictions from the design stage drawn in Section 3.2.

3.4.3 Comparison with other material systems

Figure 3.8 compares micrographs of four different materials systems: Figures 3.8a and 3.8b are cross-sections of two commercially available TBDC materials systems [2, 53]; the microstructures of these materials are very irregular, with the carbon fibre tows presenting significant through-the-thickness waviness and large resin rich regions. Figure 3.8c corresponds to a cross-section of a conventional continuous-fibre

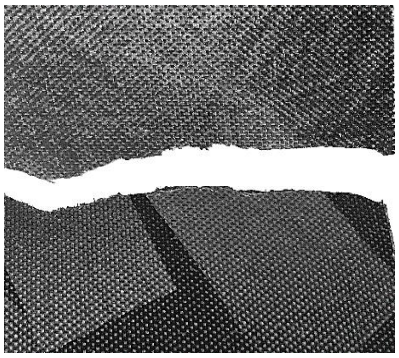

(a) Fracture surface of a HM-20-800 specimen.

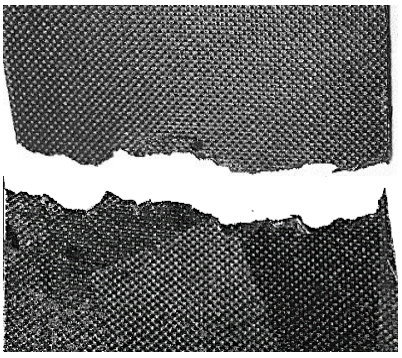

(b) Fracture surface of a HM-20-1600 specimen.

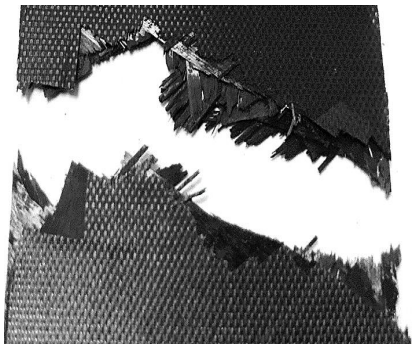

(c) Fracture surface of a HM-100-800 specimen.

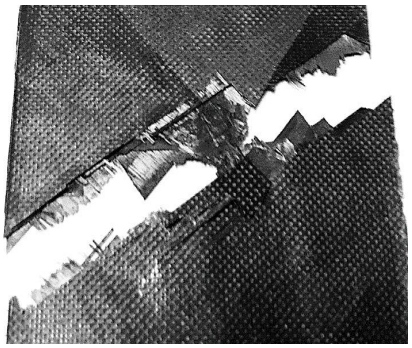

(d) Fracture surface of a UHM-100-800 specimen.

Figure 3.7: Fracture surfaces (50 × 50 mm) of specimens from the different plate configurations.

composite [54], with its conventional regular and well structured microstructure. Finally, Figures 3.8d and 3.8e show two different cross-sections of a HM-20-1600 specimen developed in this work (these two were taken from two different cross sections a specimen); the microstructure of this material system presents a very little amount of tape waviness, and is visually more similar to the microstructure of the quasi-isotropic material system in Figure 3.8c, than to the commercially available TBDCs in Figures 3.8a and 3.8b.

Table 3.5: Configurations of the different CFRP systems compared in Figure 3.9.

Material ID	Material system description	V^{f} (%)	Ref.
DCFP	T700 carbon fibre/epoxy, manufactured with modified DCFP	45	[3]
HexMC-M77	Carbon epoxy material system for compression moulding	57	[2]
AMC8593	PAN-based carbon epoxy material system (moulding compound)	47	[11]
APC-2/AS4	Carbon/PEEK CYTEC APC-2/AS4 material system	61	[4]
UT-CTT	Ultra-thin (50 µm) carbon fibre/thermoplastic system	55	[38]
AS4 8552	Continuous fibre quasi-isotropic laminate	60	[10]
UHM-100-800	Thin (100 µm) and UHM carbon fibre/epoxy system	54	
HM-20-1600	Ultra-thin (20 µm) and HM carbon fibre/epoxy system	46	

(a) HexMC-M77 [2] specimen.

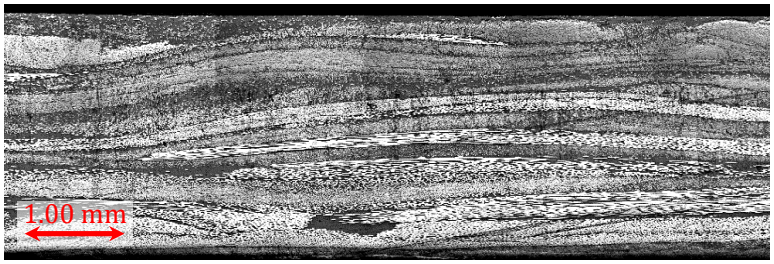

(b) SMC [53] specimen.

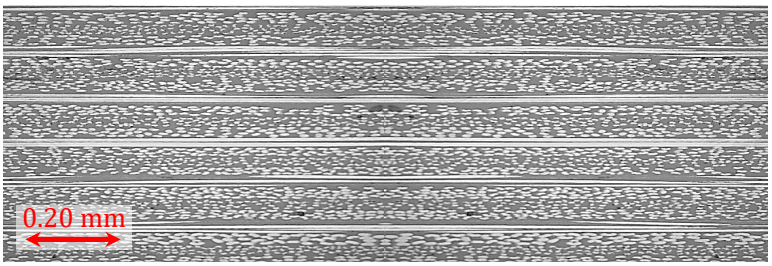

(c) Quasi-isotropic continuous-fibre specimen [54].

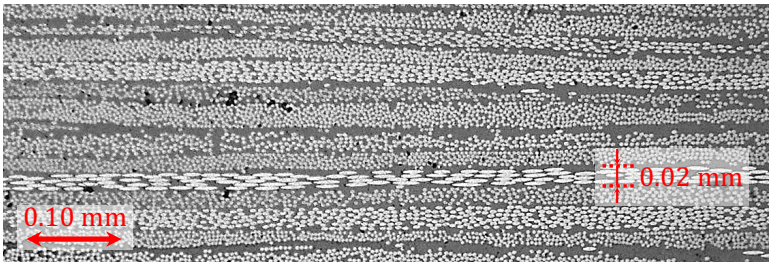

(d) First micrograph of a HM-20-1600 specimen.

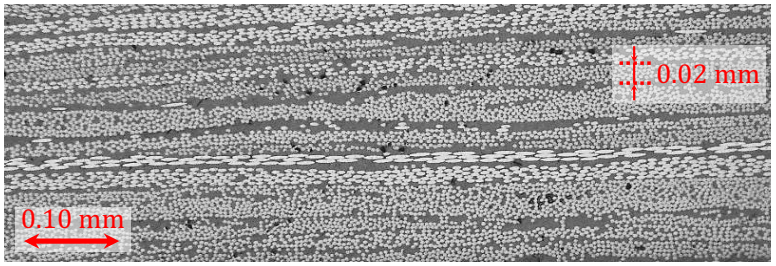

(e) Second micrograph of a HM-20-1600 specimen.

Figure 3.8: Micrographs of cross-sections of different material systems.

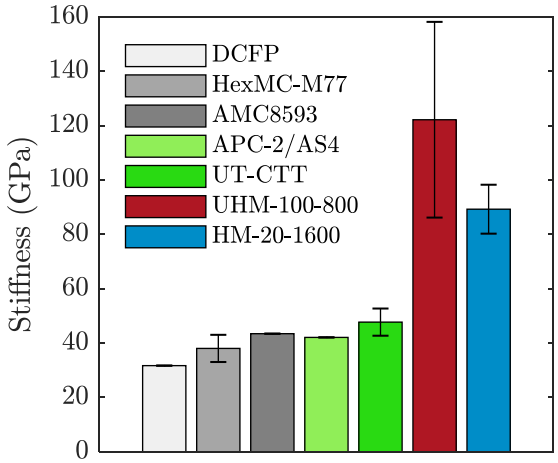

(a) Comparison between the stiffness of different TBDCs.

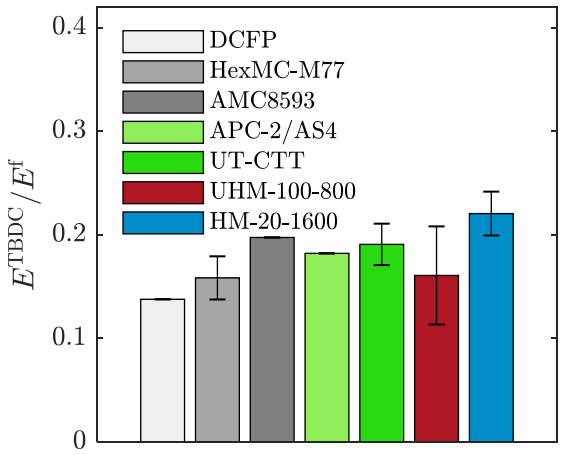

(b) Ratio between the measured stiffness of the TBDC and the respective fibre stiffness.

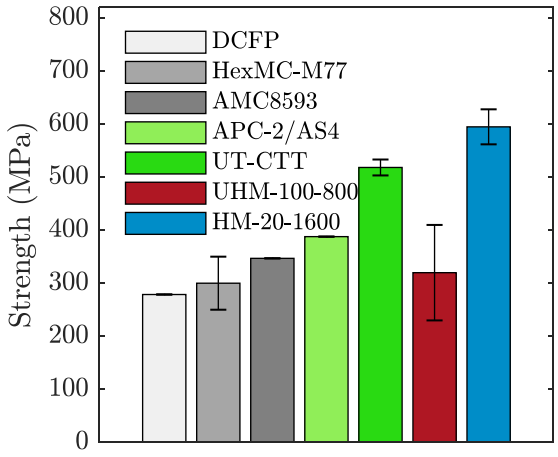

(c) Comparison between the strength of different TBDCs.

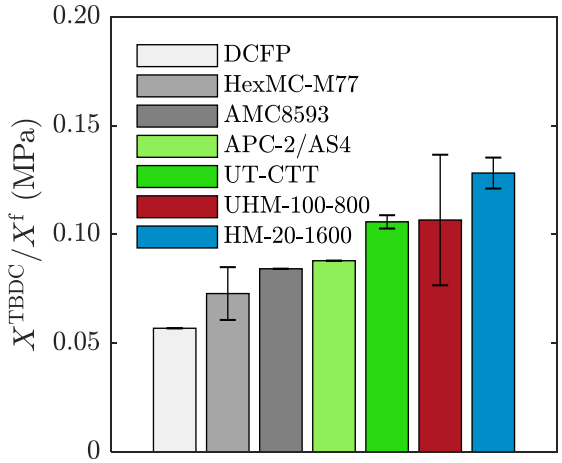

(d) Ratio between the measured strength of the TBDC and the respective fibre strength.

Figure 3.9: Comparison of the mechanical properties between the HM-20-1600 material proposed in this study, and discontinuous material systems reported in the literature (specified in Table 3.5). The mechanical properties of all materials have been linearly normalised to $V^{\mathrm{f}} = 57\%$ for comparison purposes.

The mechanical properties of the HM-20-1600 and UHM-100-800 configurations (which are the material systems that performed the best from the ones tested in this work) are compared to other carbon-fibre based material systems specified in Table 3.5; these include TBDC systems presented in the literature [3, 4, 38], the HexMC-M77 [2] and the AMC 8593 [11] commercially available TBDC material systems, and a widely-used aerospace-grade CF/epoxy continuous Quasi-Isotropic (QI) laminate. Figure 3.9a shows that the HM-20-1600 and UHM-100-800 materials system have significantly higher average stiffnesses when compared to all other TBDC material systems. In

Figure 3.9c the HM-20-1600 material system turned out to be the one that presents the highest average strength of all TBDC-type materials.

Figures 3.9b and 3.9d show how the ratio between the stiffness or strength of the TBDC and that of the fibre ($E^{\mathrm{TBDC}}/E^{\mathrm{f}}$ and $X^{\mathrm{TBDC}}/X^{\mathrm{f}}$) differs for all material system. These results clearly show that the proposed HM-20-1600 configuration is the one that best exploits the fibre properties, due to enhanced stress transfer mechanism enabled by the ultra-thin and stiff tapes.

The mechanical properties of the UHM-100-800 and HM-20-1600 configurations are compared to those of a widely-used aerospace-graded quasi-isotropic laminate of continuous fibres (AS4 8552 [10]) in Figure 3.10. Remarkably, the strength of HM-20-1600 (with a fibre tensile strength of 4640 MPa [51]) discontinuous material is practically the same as the one of the continuous fibre laminate (with a similar fibre tensile strength of 4619 MPa [55]). Moreover, due to the high modulus fibres used in both discontinuous configurations HM-20-1600 and UHM-100-800, the measured stiffness values are much higher than that of the AS4/8552 continuous fibre laminate.

3.5 Discussion

3.5.1 Effect of microstructure on mechanical properties

This work shows that, using ultra-thin tapes, TBDCs with a more regular microstructure are achieved (compared to conventional TBDCs with conventional thickness

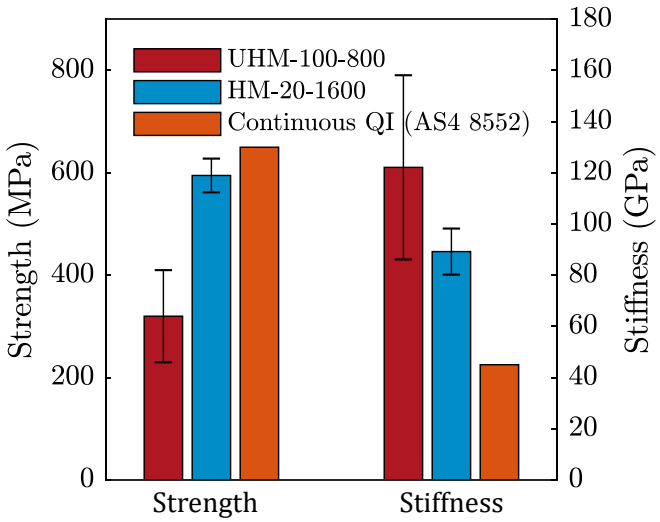

Figure 3.10: Comparison between the mechanical properties of the HM-20-1600 and UHM-100-800 configurations and a continuous fibre QI laminate (specified in Table 3.5).

tows), as shown in Figure 3.8d. This leads to improvements in stiffness (as previously suggested in the literature [10, 15, 38], and corroborated by the slightly higher Young's modulus of the HM-20-800 material compared to the HM-100-800 in Figure 3.5a), as the tapes present less out-of-plane orientations, and hence lower reductions of in-plane stiffness due to tow/tape waviness. For instance, Figure 3.3d suggests that using 20 μm tapes rather than 150 μm tows should lead to a 3.5 % improvement in the in-plane stiffness of a TBDC.

Furthermore, this more regular microstructure is also less prone to weak spots within the material (such as resin pockets) which generally trigger premature failure, and hence also contributes to the significant increase in the ultimate strength of the material (compare HM-20-800 with HM-100-800 in Figure 3.5b). In addition to the effect on the material's microstructure, the use of thin and stiff tapes also leads a more efficient stress transfer between the tapes, as it has been explained by the shear-lag models discussed in Section 3.2 (Eq. 3.3), and hence to a better exploitation of the mechanical properties of the fibres, as shown by the HM-20-1600 and UHM-100-800 configurations in Figure 3.5d.

3.5.2 Improvement over existing materials

3.5.2.1 Benchmark against other TBDCs

The stiffness improvements achieved with the ultra-thin and stiff tape based TBDCs shown in Figure 3.9a are essentially due to the higher stiffness of the HM and UHM fibres (see Table 3.3), compared to standard modulus fibres. However, there is a small difference between the stiffness of the HM-20-800 and HM-100-800 plate configurations, with the later presenting lower stiffness values (see Figure 3.5a). This may be due to the more wavy disposition of the thicker tapes in comparison to the thinner tapes, leading to higher stiffness knock-downs, which is in agreement with the numerical predictions shown in Figure 3.3d.

The average strength value of 600 MPa, obtained with the HM-20-1600 plate configuration (see Figure 3.5b), represents an increase of 100% when compared to the strength of the commercially available materials and of $\approx$ 20% when compared to the UT-CTT materials [38], which were the TBDC system with the highest strength previously reported in the literature. The enhancement of the stress-transfer mechanisms enabled by the use of ultra-thin and stiff tapes delays the on-set of tow pull-out (governed by toughness criterion, see Eq. 3.3) and promotes failure by tape fracture, as evidenced by the fracture surfaces of Figures 3.7a and 3.7b.

Although the tape-based composites proposed in this chapter have been only tested under tensile loading, the shear and compressive properties (stiffness and strength) are also expected to be higher than in conventional TBDCs, again due to the use of stiffer fibres and to the enhanced stress-transfer mechanism facilitated by the ultra-thin tapes. Moreover, compressive properties are expected to benefit even more from the more regular microstructure, with less pronounced out of plane orientations of the tapes, which will delay the onset of tow debonding and fibre kinking.

3.5.2.2 Benchmark against continuous-fibre composites

The comparison between the mechanical properties of the best proposed configurations (HM-20-1600 and UHM-100-800) against those of a continuous QI laminate in Figure 3.10, shows that it is possible to match the strength of a continuous fibre laminate and surpass its stiffness using a composite with a discontinuous microstructure.

While the two fibre-types used in the discontinuous HM-20-1600 composite and in the continuous AS4/8552 (respectively HS40 [51] and AS4 [55] are different, they have very similar single-fibre tensile strengths (around 4600 MPa). Therefore, the discontinuous HM-20-1600 is able to reach nearly the same strength as the AS4/8552 continuous composite not due to an improved fibre strength, but to an improved stress-transfer within the tapes. This improved stress-transfer has been facilitated by optimising the two microstructural parameters identified in Section 3.2.1: (i) the thickness of the tapes/plies ($\approx$ 20 μm in the discontinuous composite, and $\approx$ 125 μm in the continuous composite), and (ii) the stiffness of the fibres (425 GPa in the discontinuous composite, and 231 GPa [55] in the continuous composite).

The higher stiffnesses measured for the discontinuous composites (HM-20-1600 and UHM-100-800) compared to the continuous-fibre laminate (AS4/8552) are a direct result of using stiffer fibres in the former: the Young's moduli of the HM and UHM fibres are 425 and 760 GPa respectively (Table 3.3), and the Young's modulus of the AS4 fibres is 231 GPa. Nevertheless, one should note that the UHM fibres pose significant manufacturability challenges when used in a continuous-fibre composite, and that these challenges are alleviated in a discontinuous-fibre composite, as will be further discussed in the next section.

Altogether, the results in Figure 3.10 highlight the great potential that this new class of high-performance discontinuous composites offer, as they are able to bridge the gap in mechanical properties that typically exists between continuous and discontinuous fibre composites, while still retaining the advantages of design flexibility and manufacturability of discontinuous composites, as discussed in the next section.

3.5.2.3 Design flexibility and manufacturability

It has been suggested in the literature [10,15] that the strength of TBDCs increases with plate thickness (for a constant tow thickness); this is corroborated by the slightly higher strength and failure strain of the HM-20-1600 configuration when compared to the HM-20-800 configuration (see Figures 3.5b, 3.5c and 3.5d). This effect can be explained by two factors: firstly, thicker specimens have a smaller fraction of tapes at the surface of the specimen, and these surface tapes cannot transfer stresses as effectively as those well-embedded in the through-the-thickness direction; secondly, thicker specimens have a larger average number of tapes in the through-the-thickness direction, which increases the homogeneity of mechanical properties in comparison with thinner specimens. Consequently, there is a limitation for the minimum thickness that can be accepted in components manufactured with TBDC systems with conventional tow thicknesses. This limitation can be relaxed significantly through the use of ultra-thin tapes, as shown by the results in Figures 3.5 and 3.9:

- Firstly, the mechanical properties of the plates manufactured with ultra-thin tapes were considerably higher than those of conventional TBDCs (see Figures 3.5 and 3.9), even though the plate thickness of the former was below 0.5 mm.
- Secondly, the similar properties observed with the two HM-20-800 plates tested at different directions (see Figure 3.5) suggest that using ultra-thin tapes to make TBDCs enables the manufacture of shell-type structures with wall thicknesses lower than 0.2 mm, with in-plane isotropy.

Consequently, TBDCs manufactured with ultra-thin tapes offer much more design flexibility than conventional TBDCs, and allow for production of shell-type structures with very thin walls (which is useful e.g. for body-in-white parts of cars).

Figure 3.10 shows that TBDCs made of ultra-thin tapes of HM fibres combine (i) a similar strength and even higher stiffness than those of aerospace-graded composites with (ii) the improved manufacturability and design flexibility of a discontinuous and random microstructure. This concept has been proven in this work using a manual manufacturing method, but it could be realised at an industrial scale by creating SMC-type intermediate materials (similar to HexMC [2] and carbon-SMC [53]), but using ultra-thin (spread) tapes of (ultra-)high modulus fibres and fast-curing matrices; these intermediate materials could then be directly used in compression moulding, with several advantages over conventional continuous-fibre composites:

- Allowing for the production of parts within a matter of minutes and out-of-the-autoclave, and with minimal manual work;

- Allowing for the production of complex 3D geometries (rather than 2D shells) with local embedded reinforcements where they are needed most (rather than relying on ply-drops and bonded stiffeners, as often done with continuous-fibre composites).
- Possibility of using UHM fibres - which are extremely stiff but very brittle - to manufacture parts/components with complex geometries; this is enabled by the discontinuous architecture of TBDCs which allow the fibres to flow during the manufacturing process, and is not easily achievable with continuous-fibre architectures due to the combination of limited drapeability and fibre brittleness.
- Reducing significantly the amount of waste generated by material cut-offs.

3.6 Conclusions

This work has successfully proposed, designed and demonstrated a pathway to increase the stiffness and ultimate tensile strength of tow-based discontinuous composites. The main conclusions are summarised below:

- Quasi-isotropic TBDCs manufactured with ultra-thin (20 μm) and high-modulus (450 GPa) carbon-fibre tapes reached a tensile strength of 600 MPa and stiffness of 90 GPa. This represents a stiffness and strength increase of 100% when compared to commercially available TBDC materials, and of 20% when compared to the TBDC material system with the highest strength previously reported in the literature.
- This work demonstrates that TBDCs manufactured using ultra-thin and high-modulus carbon-fibre tapes can reach the tensile strength of conventional aerospace-grade QI laminated CFRP, and overcome their stiffness.
- The use of thin and stiff tapes in the manufacture of TBDCs leads to this significant improvement in mechanical properties by enhancing the stress transfer mechanisms within the material and suppressing matrix/interface dominated failure mechanisms. This allows for a better exploitation of the mechanical properties of the fibres, which has been demonstrated by the features of the fracture surfaces of these TBDCs, which were dominated by fibre-failure rather than by tape pull-out.
- Test results suggest that there is a reduction in tensile strength for specimens with a small ratio between the specimen thickness and tape thickness. This indicates that TBDCs with ultra-thin tapes can be used to manufacture components with very thin walls, removing several design barriers and offering more design flexibility over conventional TBDCs (based on tows with conventional thicknesses).

This work shows the potential of ultra-thin and stiff TBDCs as a high-performance and highly-manufacturable material, able to comply with the stiffness and strength requirements of primary structural applications and suitable for a wider range of part geometries and more automated manufacturing processes when compared to continuous-fibre composites. These materials can potentially change the way in which composite materials are used in several industries (automotive, aerospace, sport and others), and at the same time open the use of high-performance composite materials to new industries with different manufacturability constraints.

Chapter 4

Characterising and modelling the variability of TBDC material systems

4.1 Introduction

Due to the random orientation of the carbon-fibre tows used in TBDCs, their microstructure is highly inhomogeneous, resulting in mechanical properties with a large variability. The mechanical response of a TBDC is directly related to the variability of the local mechanical properties, as the failure of the material is triggered by local weak regions within the microstructure, and can lead to notch insensitive mechanical responses [56, 57].

This has been experimentally demonstrated by heterogeneous strain fields captured with DIC in specimens loaded under longitudinal tension [9, 16, 22, 57]. The variability of strain fields of TBDCs can be characterised in terms of (i) the quantitative variability of strain values and (ii) their spatial variability. The spatial variability of the strain fields is related to the spatial distribution of regions of strain peaks and troughs, which define a characteristic length-scale of the strain field. Feraboli et al. [22] attempted to characterise the spatial variability of TBDC strain fields, by analysing the alternating pattern of peaks and troughs along vertical lines of DIC fields. By isolating/filtering the peak and trough regions of the strain fields, the authors identified elliptical patterns with characteristic areas ranging from 136 mm^2 to 204 mm^2. Despite the qualitative characterisation presented in [22] no quantitative analysis of the spatial variability of TBDC strain fields has been presented in the literature, neither how the characteristic

length-scales are affected by the microstructural features of the material (such as the tow geometry).

Therefore, when modelling TBDC structures, it is essential to capture the correct quantitative and spatial variability of mechanical properties in order to be able to accurately predict their mechanical response. However, generating representative property fields with the correct spatial variability in large FE models can be challenging, since a fine balance between the computational cost and the details captured by the model has to be achieved. The most direct method to achieve this is by creating explicit representations of the material's microstructure, i.e. modelling each tow individually [18,20,21]. These models were able to predict the stiffness and ultimate strength of TBDCs; however, the explicit representation of the microstructure of TBDCs is generally coupled with microstructure generators, which are computationally expensive and limited to very simple geometries, hindering the scalability of this approach to larger and more complex models.

Feraboli et al. [22] proposed a modelling approach based on an implicit representation of the TBDC's microstructure. This approach is less computationally demanding than models based on explicit representations, and scalable to larger and complex geometries. Random Representative Volume Elements (RRVE) were used to define regions of uncorrelated material properties; each RRVE is characterised by a random layup, with local properties resulting from CLT. This approach was implemented in a Finite Element (FE) framework, where TBDC specimens were discretised in several RRVEs. The authors were able to capture the variability of the field of mechanical properties, and to obtain strain fields with good qualitative correlation to experimental strain fields measured with DIC. However, this approach is not able to recreate continuous strain fields across the RRVE partitions, and therefore suffers from mesh sensitivity.

In the literature, other methods can be found to assign random fields of material properties to FE simulations, with predefined length-scales. Some of these methods [58, 59] are based on generating continuous fields of material properties (eg. Gaussian random fields) based on series expansions, with a pre-defined spatial cross-correlation of those properties. Other methods [60] are based on generating a field of discrete points, with a predefined spacing between them, to which properties, sampled from a particular distribution, are independently assigned. For this type of stochastic approach, modelling at uncorrelated length-scales is required; this implies that the attribution of properties (either randomly sampled, or sampled from a specific distribution) should be done at uncorrelated length-scales [61].

This chapter aims to develop an efficient and flexible FE framework to model TBDC structures, with both simple and complex geometries, while taking into account the effect of the microstructural features (such as the tow geometry) on the spatial dis-

tribution of the mechanical properties. Section 4.2 proposes a numerical method to characterise quantitatively the spatial variability of strain fields of TBDC specimens measured with DIC. Section 4.3 analyses two FE modelling techniques to reproduce the spatial variability of mechanical properties of TBDCs: (i) - one based on explicit representation of the microstructure (Section 4.3.1), which is then used to establish a link between the effect of the in-plane tow dimensions and the spatial variability of the strain fields; and (ii) - another based on an implicit representation of the microstructure (Section 4.3.3), which is successfully validated against experimental results. The mains finding are discussed in Section 4.4 and the conclusions are drawn in Section 4.5.

4.2 Experimental characterisation of the spatial variability of strains in TBDCs

4.2.1 Materials and testing

The TBDC material system used in this study is the HexMC-M77 [2]; the specification of the microstructural elements of the material (nominal tow length l^{t}, tow width w^{t} and tow thickness t^{t} and fibre volume fraction V^{f}) can be found in Table 4.1. Ten specimens were tested under longitudinal tension, according to the ASTM-D3039 standard; the specimen geometry (length l^{s}, width w^{s}, thickness t^{s}, and gauge length $l^{\mathrm{s}}_{\mathrm{gauge}}$) are specified in Table 4.2.

Images of the front face of the specimens were acquired at an average remote stress of 120 MPa, and strain fields were obtained by DIC analyses using *GOM Correlate* software [62]; a subset size of 3 mm was used, over an gauge area of 138 × 50 mm. The average stress value selected is below half of the ultimate strength of the material system [2], and was selected in order to ensure that the strain fields remained within the linear elastic regime.

Table 4.1: Specification of the microstructural elements of the material analysed.

Material	l^{t} (mm)	w^{t} (mm)	t^{t} (mm)	V^{f} (%)
HexMC-M77 [2]	50	8	0.125	57

Table 4.2: Specification of the geometry of the tested specimens.

l^{s} (mm)	w^{s} (mm)	t^{s} (mm)	$l^{\mathrm{s}}_{\mathrm{gauge}}$ (mm)
250	50	3	138

4.2.2 Direct results from DIC strain fields

The longitudinal strain maps obtained through DIC for each tested specimen are presented in Figure 4.1a; in order to compare the variability in the measured strain values of all the specimens, the longitudinal strain fields of each specimen are normalised by the respective average strain value, thus obtaining a normalised strain field ($\bar{\epsilon}_{xx}$). Figure 4.1b shows the combined normalised strain distributions of all specimens, where a significant strain variability is observed; the normalised strain distribution is not symmetric, as it presents a longer tail for higher strain values, which corresponds to the strain fields in local hot-spots (in each specimen) which will likely trigger failure. The statistics of the strain fields ϵ_{xx} (mean value and the standard deviation), measured from the DIC strain fields of each individual specimen, are presented in Figure 4.1c.

4.2.3 Spatial variability of the DIC strain fields

In Section 4.2.2 the variability of the strain *values* was quantified; however, in order to fully characterise the strain fields, their *spatial* variability – i.e. the length-scales associated with the variability of strains in space – also has to be quantified. In this Section, two techniques will be used to quantify the spatial variability of the DIC longitudinal strain fields of TBDC specimens.

4.2.3.1 Triangulation of local strain peaks and troughs

A new method to quantify the spatial variability of the DIC strain fields of heterogeneous materials is here proposed, and has the following main steps:

1. Identification of local peaks and troughs (minimums and maximums) in the strain field, as shown in Figure 4.2a: this was done using the *fastpeakfind* function of *Matlab*.

2. Delaunay triangulation of the local peaks: this connects each local peak/trough to its closest neighbours, creating a network of segments as the one shown in Figure 4.2a.

3. Edge effect correction: in order to avoid edge effects on the length-scale distribution, the segments that connects local peaks (at the same boundary) and which belong to the same triangular element (that results from step 2) are removed.

4. Identification of the characteristic 'length-scale": the distribution of lengths of the valid segments in the triangulation of local peaks and troughs – s_{ls}, hereafter referred to as 'length-scales" – characterises quantitatively the spatial variability

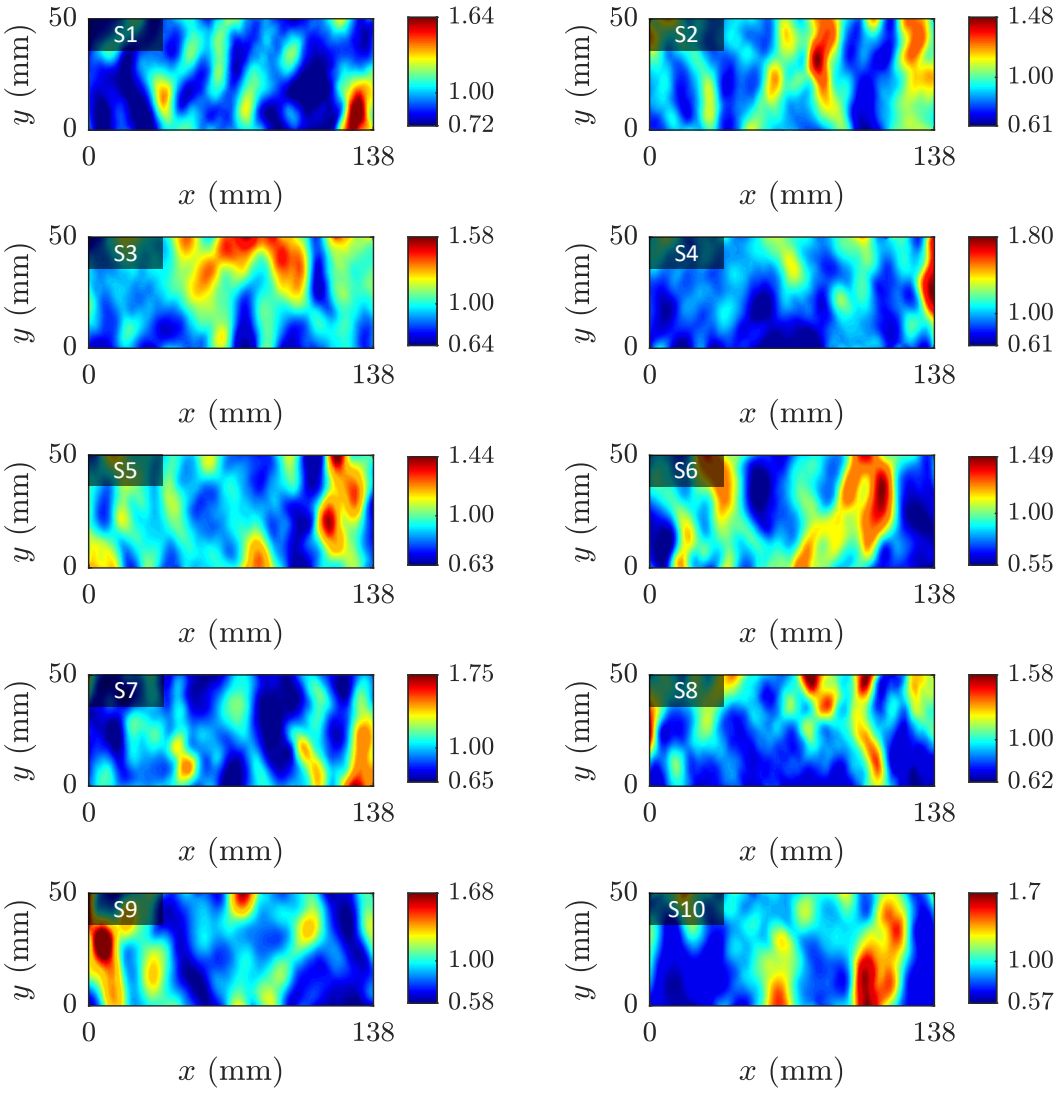

(a) Normalised strain fields ($\bar{\epsilon}_{xx}$) obtained with DIC from the 10 tested specimens.

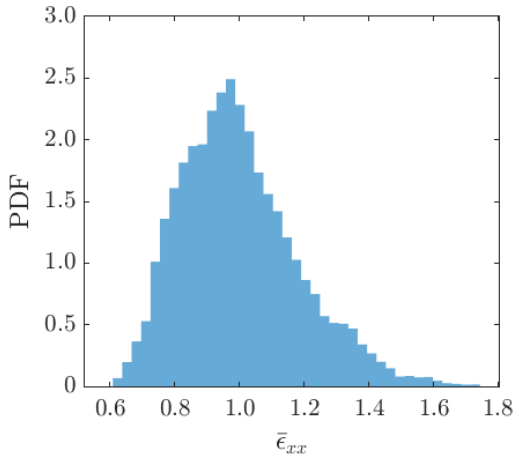

(b) Distribution of the $\bar{\epsilon}_{xx}$ of all tested specimens.

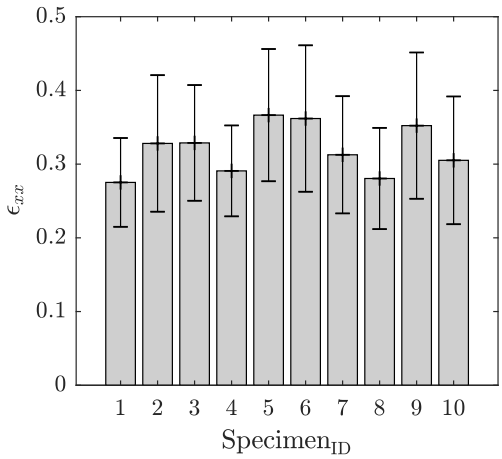

(c) Average and standard deviation of ϵ_{xx} (%) of each tested specimen.

Figure 4.1: Analysis of the strain fields obtained with DIC for all the tested specimens.

of the strain fields. The mean value of that distribution ($\bar{s}_{\mathrm{ls}}$) is assumed to be the characteristic length-scale of the strain field.

Figure 4.2b shows the distribution of the length-scales obtained for all the measured DIC strain fields; the mean value of the distribution ($\bar{s}_{\mathrm{ls}} = 14.2$ mm) indicates the characteristic length-scale of the tested TBDC material system.

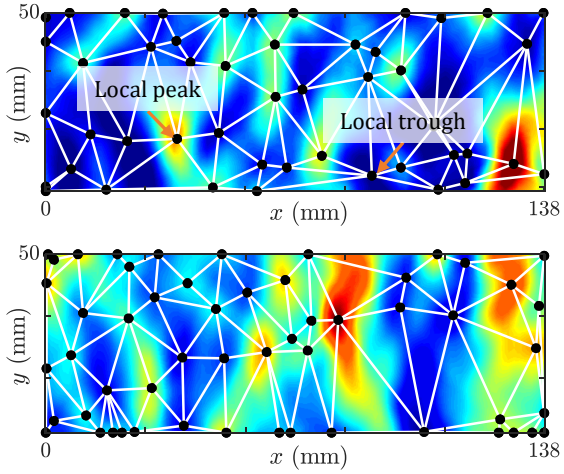

(a) Spatial variability analysis of the experimental DIC strain field of two specimens; the black dots mark the location of local peaks and troughs; the white segments represent the length-scales.

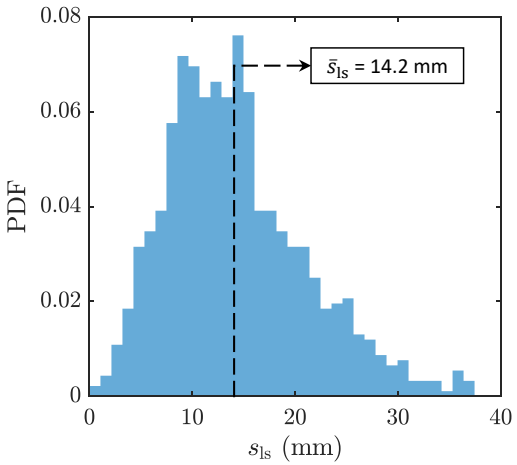

(b) Length-scale distribution obtained from all the experimental DIC strain fields of the tested specimens.

Figure 4.2: Proposed method for the analysis of the spatial variability of the experimental DIC strain fields, based on the triangulation of strain peaks and troughs.

4.2.3.2 Cross-correlation analysis of the DIC strain fields

A second method used to quantify the spatial variability of the DIC strain fields is based on a cross-correlation analysis. This method has been widely used to characterise the spatial variability in property fields of heterogeneous materials in the literature [61, 63] and is summarised as follows:

1. Random selection of a location in the strain field from which a template (with a pre-defined size w_{s}) is extracted, as shown in Figure 4.3a
2. Calculation of the cross-correlation between the template and the strain field, resulting in a correlation field as the one shown in Figure 4.3b. This was done using the *normxcorr2* function of *Matlab*.

3. Radial averaging of the correlation field, centred at the position from which the template was extracted. This allows for the determination of the average distance to the closest non-correlated region in the strain field.

4. Steps 1-3 are repeated for 1000 iterations, with each iteration using a different template (i.e extracted from a different location of the original strain field); the final radial average profile, shown in Figure 4.3c, is taken as the average of the radial profile resulting from all iterations for all specimens.

The influence of the selected size w_s of the template is shown in Figure 4.3c, where it is found that the radial averaged cross-correlation converges for small template sizes ($w_s = 8$ and 6 mm). For the particular case of the TBDC specimens analysed, the average radial cross-correlation that corresponds to the characteristic length-scale identified in Section 4.2.3.1 ($\bar{s}_{ls} = 14.2$ mm) is equal to 0.1 (for the template sizes $w_s = 8$ and 6 mm).

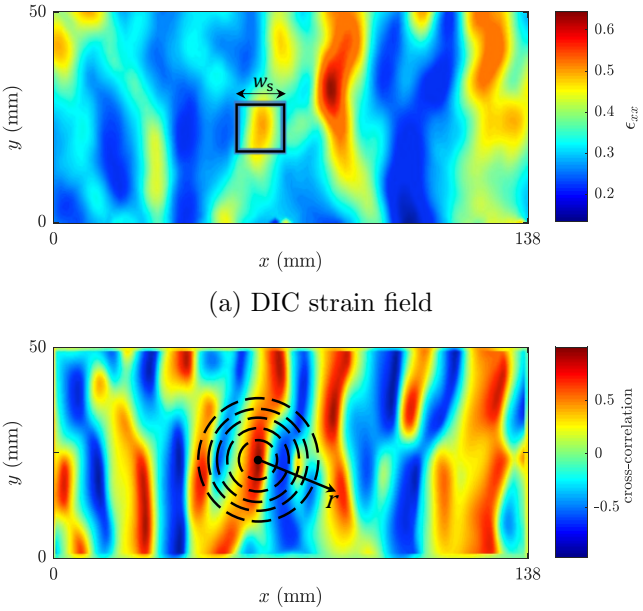

(a) DIC strain field

(b) Cross-correlation field.

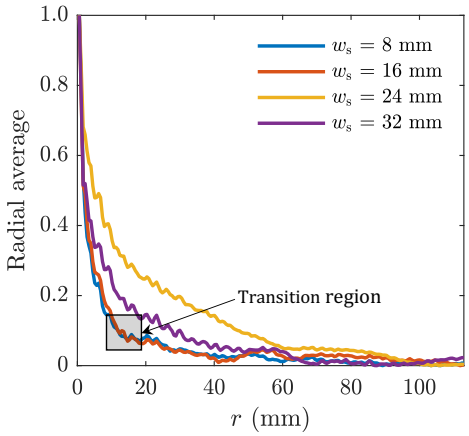

(c) Radial profile of the cross-correlation analysis, for different template sizes w_s.

Figure 4.3: Cross-correlation analysis of the DIC strain fields.

4.3 Modelling the spatial variability of mechanical properties in TBDCs

In this Section, two different Finite Element based approaches to model the mechanical behaviour of TBDC materials including their intrinsic variability of mechanical

properties will be analysed: (i) one based on an explicit representation of the material's mesostructure (4.3.1), and (ii) another based on an implicit representation of the material's mesostructure (4.3.3). The approaches presented in this Section are based on 2D (shell-type) linear elastic models (for which final failure of the material is not predicted) of specimens loaded under uniaxial tension. All the material properties used for the FE simulations of this chapter were defined in Table 3.1.

4.3.1 Explicit mesoscale representation of variability

4.3.2 Modelling approach

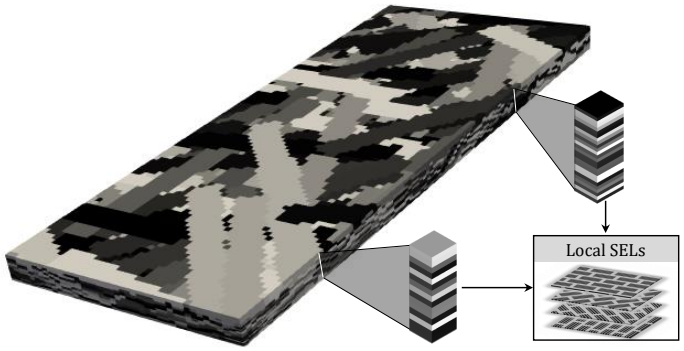

Figure 4.4: Modelling approach with explicit representation of the microstructure: each partition of the virtual specimen is represented by a local stochastic equivalent laminate (SEL).

The approach to model TBDCs through an explicit representation of the mesostructure is based on generating virtual specimens (an example of which is shown in Figure 4.4), using the microstructure generator developed in Chapter 2. The virtual specimen has dimensions of $[138 \times 50]$ mm and is discretised in square partitions of $[1 \times 1]$ mm [20]. In each partition, the material is idealised as an equivalent laminate with each ply consisting in a unidirectional discontinuous ply; the orientation of each ply is defined by the local tow orientation N_{θ_i} obtained from the microstructure generator. The stiffness tensor of each discontinuous ply (defined in Chapter 2) is rotated according to the associated tow orientation; using CLT, the stiffness tensor of the local partition is obtained. In order to obtain the strain fields that result from this approach, longitudinal uni-axial displacement along the length of each virtual specimens was applied, and linear elastic simulations were performed.

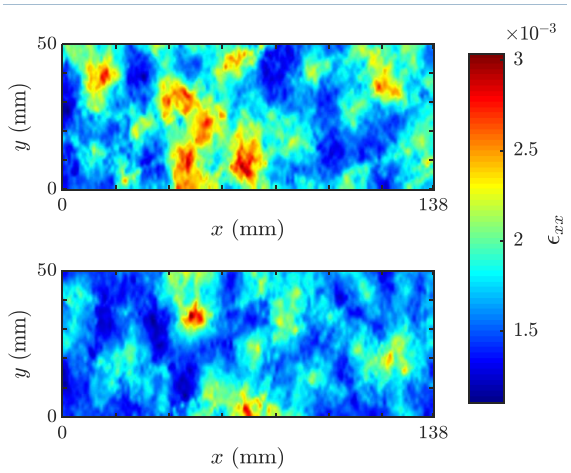

(a) Strain fields two specimens modelled.

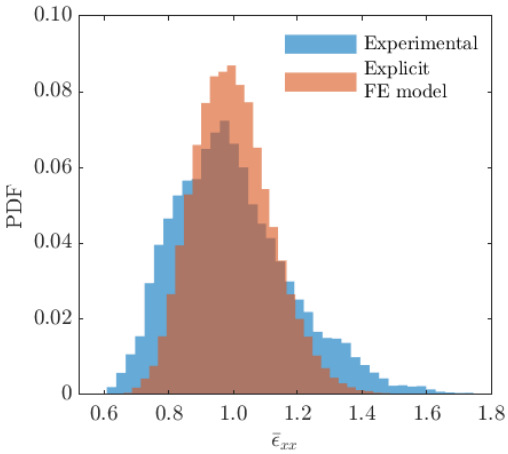

(b) Distribution of the normalised strain $\bar{\epsilon}_{xx}$.

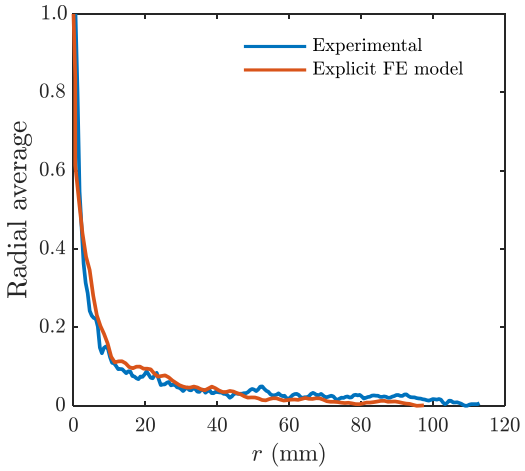

(c) Comparision of the cross-correlation analysis of the explicit FE strain fields and the DIC strain fields.

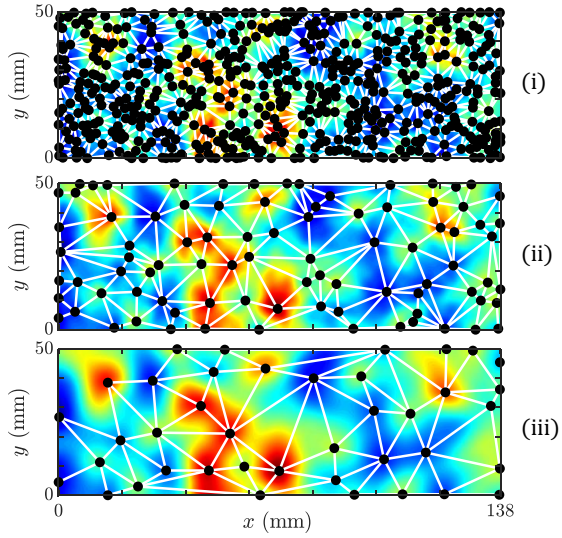

(d) Spatial variability analysis of FE strain fields with different filtering levels.

Figure 4.5: Analysis and characterisation of strain fields generated by FE models with explicit representation of the microstructure of TBDCs.

4.3.2.1 Validation against experiments

Figure 4.5a shows the longitudinal strain field of two virtual specimens (with the microstructure defined in Table 4.1) obtained with FE models based on a explicit representation of the microstructure. Figure 4.5b shows the combined normalised strain variability of 10 virtual specimens; this approach yields strain fields with similar variability to that presented by the DIC strain fields, although with small differences in

the tails of the distribution, which may be due to the different boundary conditions between the models and the experiments.

The two methods presented in Section 4.2.3 are here used to quantify the spatial variability of the strain fields obtained with the FE models. In Figure 4.5c, the radial average profiles that result from the cross correlation analysis of the FE and DIC strain fields are compared, and a good agreement between both is found. This shows that FE models based on explicit representations of the material's microstructure are able to reproduce accurate strain fields, both in terms of their spatial variability and the quantitative variability of strain values.

Figure 4.5d shows the triangulation of the local peaks and troughs in the strain field of the same specimen, but with different filtering levels: in Figure 4.5d-i, the original strain field is non-smooth, which leads to several local peaks in the strain field which are not associated to the material's spatial variability; Figure 4.5d-ii shows the strain field with a correct filtering (i.e. which preserves the characteristic length-scales), whereas Figures 4.5d-iii shows a over-filtered strain field (in which information about the characteristic length-scales is lost).

4.3.2.2 Effect of tow length and width

The spatial distribution of the mechanical properties of the HexMC-M77 TBDC material system, with a tow geometry of $[50 \times 8]$ mm, was characterised experimentally in Section 4.2. However, TBDC material systems can be manufactured with different tow geometries, and the characteristic length-scales of the resulting mechanical properties may vary as a consequence. In order to define a relation between the in-plane tow dimensions (l^{t} and w^{t}) and the associated characteristic length-scale, the modelling approach based on an explicit representation of the microstructure (Section 4.3.1) was used to generate virtual specimens (with dimensions [150 × 150] mm) with different tow geometries: l^{t} ranging from 15 to 50 mm, and w^{t} ranging from 5 to 10 mm.

Figure 4.6 shows some examples of the obtained strain fields for specimens with different tow dimensions. The influence of the in-plane tow geometry on the characteristic length-scales of the strain fields is noticeable, with shorter and narrower tows presenting smaller length-scales than those resulting from longer and wider tows. The cross-correlation technique was used to quantify the characteristic length-scales of each strain field; Figure 4.7a shows the radial averaging profiles for specimens with a constant tow length ($l^{\mathrm{t}} = 50$ mm) and different values of the tow width, and Figure 4.7b shows the radial averaging profiles for specimens with a constant tow width ($w^{\mathrm{t}} = 10$ mm) and different values of the tow length. For all tow configurations a template with $w_{\mathrm{s}} = 14$ mm was used.

The characteristic length-scale $\bar{s}_{\text{ls}}$ of the strain fields of all microstructures generated were estimated as the length-scale with a radial average cross-correlation of 0.1, as shown in Figure 4.7a. This value was selected based on the characteristic length-scale of the $[50 \times 8]$ mm configuration ($s_{\text{ls}} = 14.2$ mm), which was experimentally determined in Section 4.2. The resulting characteristic length-scales of all configurations modelled are shown in Figure 4.8; this reveals that the characteristic length-scale of strain fields increases with both tow width and tow length, albeit at a faster rate with the former than with the latter.

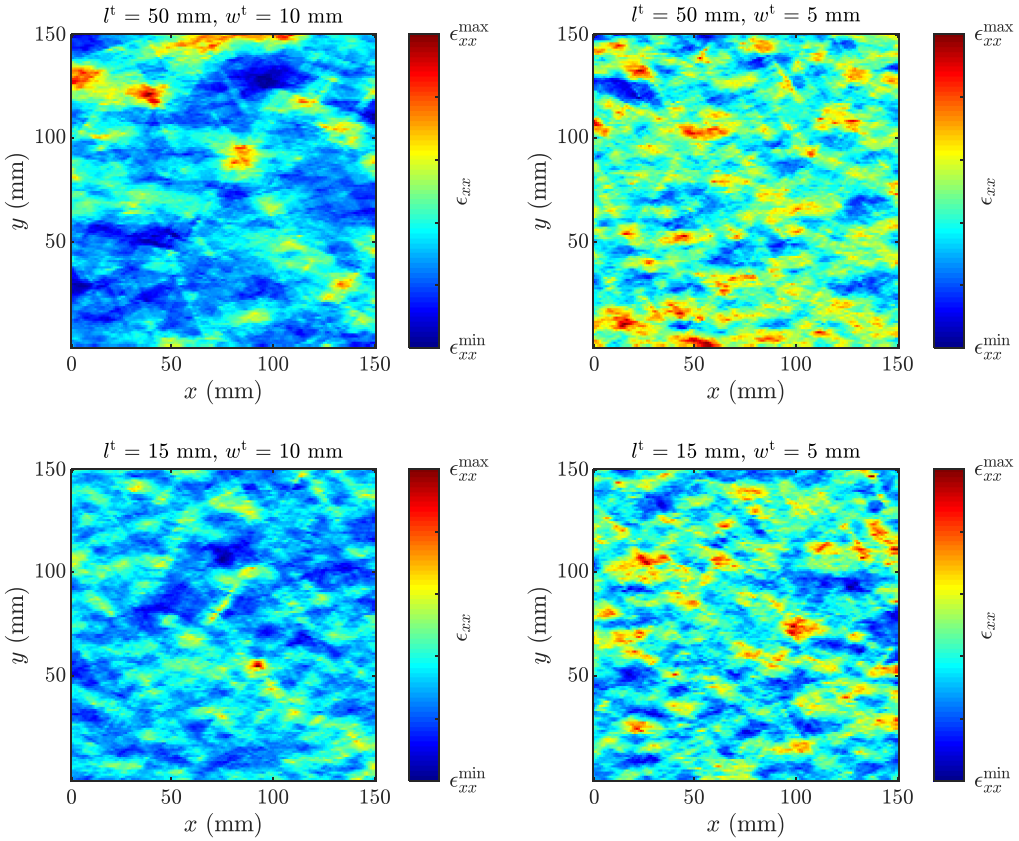

Figure 4.6: Longitudinal strain fields of plates with different tow geometries.

Based on the characteristic length-scales identified for the several configurations analysed explicitly through FE models, it would be interesting to identify a mathematical relationship between (i) the characteristic length-scale and (ii) the in-plane tow dimensions of the TBDC system. Two simple relationships are analysed in Figure 4.8: (a) estimating the characteristic length-scale as the arithmetic mean of the tow width and tow length, shown in Figure 4.8a, and (b) estimating the characteristic length-scale as the harmonic mean of the tow width and tow length, shown in Figure 4.8b.

The harmonic mean between l^{t} and w^{t} correlates remarkably well with the characteristic length-scales predicted, and therefore it is here proposed that the characteristic

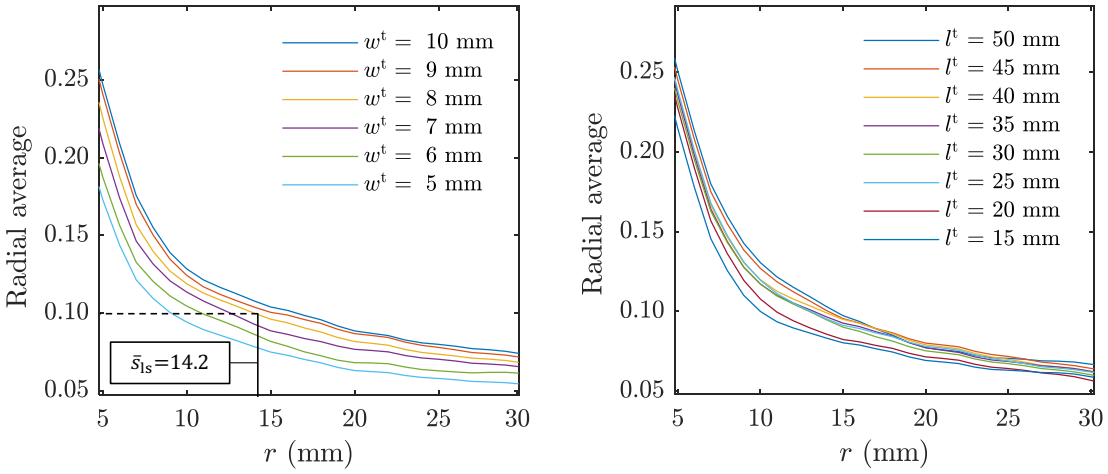

(a) Effect of the tow width for a constant tow length of 50 mm.

(b) Effect of the tow length for a constant tow width of 10 mm.

Figure 4.7: Cross correlation analysis of the influence of the in-plane tow geometry on the spatial length-scales of the associated strain fields; results are shown for a value of $l^{\mathrm{t}} = 50$ mm.

length-scale can be modelled by the harmonic mean of the in-plane tow dimensions, i.e.

$$\bar{s}_{\mathrm{ls}} = \frac{2}{\frac{1}{l^{\mathrm{t}}} + \frac{1}{w^{\mathrm{t}}}}. \tag{4.1}$$

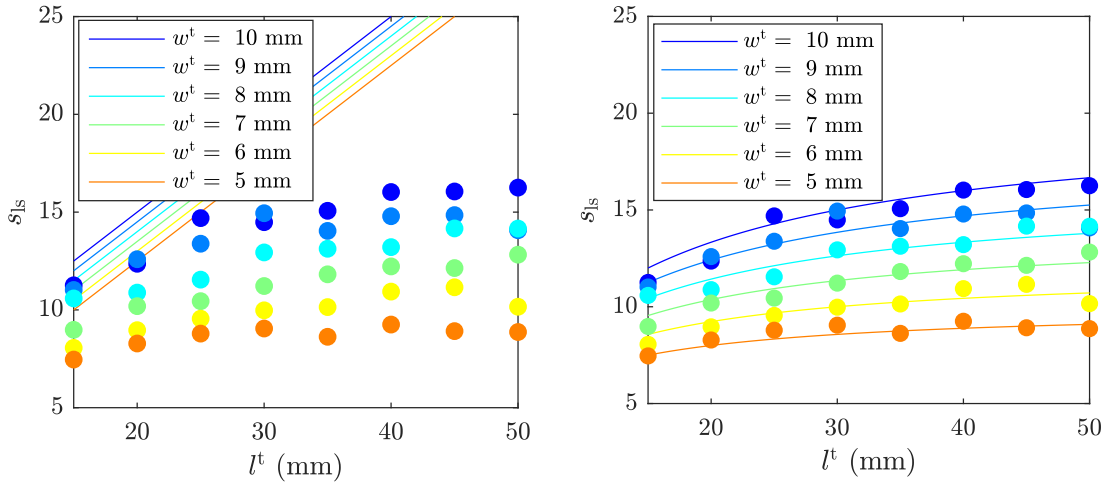

(a) Comparison against the arithmetic mean of tow width and tow length.

(b) Comparison against the harmonic mean of tow width and tow length.

Figure 4.8: Characteristic length-scales of virtual specimens from the cross-correlation analysis (represented by the circular markers), and comparison with 2 analytical solutions (represented by the solid lines).

4.3.2.3 Effect of the specimen and tow thicknesses

In order to relate the effect of the specimen and tow thicknesses (t^{s} and t^{t}) with the strain variability, four microstructural configurations (defined in Table 4.3) were analysed using the explicit modelling approach proposed in Section 4.3.1. The four

Table 4.3: Plate configurations for the study of the effect of the specimen and tow thicknesses.

	baseline	configuration 1	configuration 2	configuration 3
t^{t}	0.150	0.300	0.300	0.075
t^{s}	3.0	3.0	6.0	3.0
$\bar{N}_{\mathrm{t}}$	20	10	20	40

configurations differ either in the specimen or in the tow thicknesses, which leads to different values of the average tow count $\bar{N}_{\mathrm{t}} = t^{\mathrm{s}}/t^{\mathrm{t}}$ through the thickness of each specimen. For each configuration, 10 virtual specimens (with in-plane dimensions of $[138 \times 50]$ mm) were generated and analysed.

Figure 4.9a compares the variability of the strain values obtained for each configuration, with the error bars representing one standard deviation; a clear influence of average tow count in the strain variability is found, with the specimen with the lowest N_{t} (configuration 1) presenting the highest strain variability, and the one with the highest N_{t} (configuration 3) presenting the lowest strain variability. This indicates that the strain variability is related to the number of possible tow orientations that govern the local mechanical properties; a lower number of possible orientations increases the probability of having significantly different local mechanical properties in the material, whereas the opposite occurs for a higher number of possible orientations. This is further reinforced by the similar strain distribution of the baseline and configuration 2, which have different microstructural features (t^{t} and t^{s}) but the same value of N_{t}. Moreover, Figure 4.9b shows that the spatial variability of strains is not influence by the average tow count through the thickness, as the cross correlation analysis yielded similar radial average profiles for all configurations of Table 4.3.

4.3.3 Implicit mesoscale representation of variability

4.3.3.1 Proposed methodology

The explicit approach presented in Section 4.3.1 (in which the mesoscale features of the material are mapped from a virtual generated microstructure to a FE mesh) yielded accurate results in terms of the statistics of the predicted strain fields. However, models

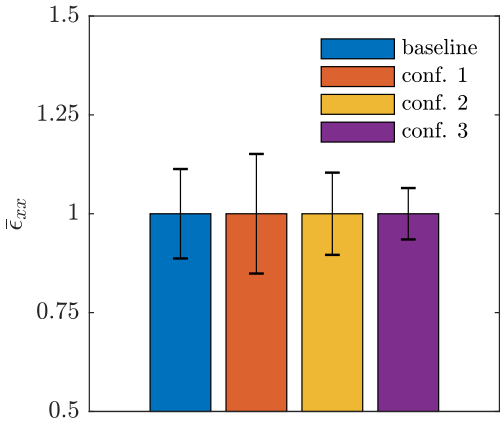

(a) Quantitative strain distributions of the strain fields resulting from the different plate configurations of Table 4.3.

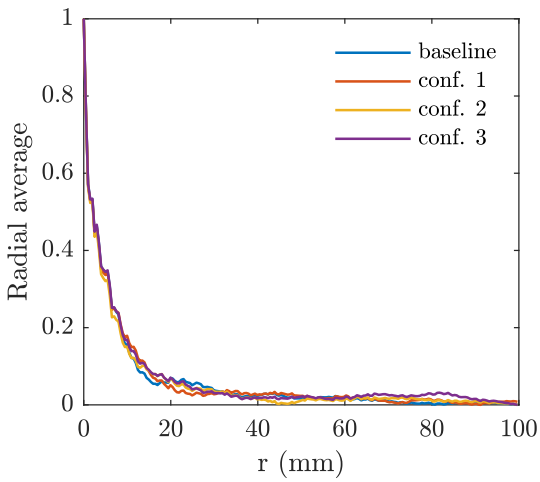

(b) Cross-correlation analysis of the strain fields resulting from the different plate configurations of Table 4.3.

Figure 4.9: Variability analysis of the strain fields resulting from the different plate configurations of Table 4.3..

based on this approach are not scalable to larger and more complex geometries. The objective to be addressed in this section is to propose an FE methodology for TBDCs, based on an implicit representations of their microstructure, that is able to recreate representative strain fields of the material while being flexible and efficient to be used for larger and more complex geometries.

4.3.3.2 Proposed material idealisation

The proposed FE methodology contrasts to the one presented in Section 4.3.1 as it is based on an implicit representation of the material's microstructure. The material is idealised as Stochastic Equivalent Laminates [22,23] (SELs) at discrete points, hereafter referred to as *seed points*. Each ply in the SEL is reinforced by tows with the same geometry and constituents as the tows in the original TBDC; each SEL consists of a lay-up of N_t discontinuous plies, each with a random in-plane orientation θ. The probability distribution function $\mathcal{F}(\theta)$ governing the orientation of the discontinuous plies can be assumed uniform $\mathcal{U}(-\pi/2, \pi/2)$ (e.g. for low-flow TBDCs), or reconstructed from orientation tensors (e.g. predicted from flow simulations).

The randomness of ply orientations in each SEL will lead to variability of mechanical properties from one seed point to another; because the ply orientations at each SEL are independent, the mechanical properties at one seed point will be uncorrelated from the properties at the neighbouring points. Therefore, the distance between seed points

must be equal to the distance between uncorrelated material points in the real TBDC to be modelled. Therefore, it is proposed that the average distance between seed points s_{seed} should be equal to the characteristic length-scale of the material; this can be characterised experimentally as reported in Section 4.2.3.1, or estimated using the harmonic mean of the tow width and length (given by Eq. 4.1).

The location of the seed points within the geometry to be modelled, is here taken to be the location of the nodes of a coarse unstructured mesh (see Figure 4.10), with an element size equal to the value of s_{seed}. This method takes advantage of the meshing capabilities of FE software, however, other approaches could be used to define the location of the seed points, such as using Random Sequential Adsorption algorithms to generate random points within the geometry domain, with a pre-defined average spacing between them.

After defining the microstructural features and the geometry of the model, the tow count N_t, given by the ratio between the specimen and the tow thicknesses, is defined. The in-plane orientations θ_i, of the N_t discontinuous plies of the SEL are randomly sampled from a generic fibre orientation distribution distribution function $\mathcal{F}(\theta)$. The local orientations of the SEL at a seed points, are represented by a stochastic second order orientation tensor $\bar{\mathbf{a}}$, given by

$$\bar{\mathbf{a}} = \frac{1}{N_{\text{t}}} \cdot \sum_{i=1}^{N_{\text{t}}} \begin{bmatrix} \cos(\theta_i) & \cos(\theta_i)\sin(\theta_i) \\ \cos(\theta_i)\sin(\theta_i) & \sin(\theta_i) \end{bmatrix}. \tag{4.2}$$

4.3.3.3 Continuous stochastic field of mechanical properties

The analysis of a TBDC structure will be carried out on a *structural mesh* (i.e. with an average element size significantly smaller than the average spacing between the SEL seeds), and requires defining a stiffness tensor at the integration point of each element of the refined mesh. This is done by interpolating each term of the stochastic orientation tensor from the seed points to the centroid of the refined mesh's elements. An adequate and flexible interpolation scheme must be used in order to allow for interpolations in complex geometries as well as to ensure a mesh independent approach.

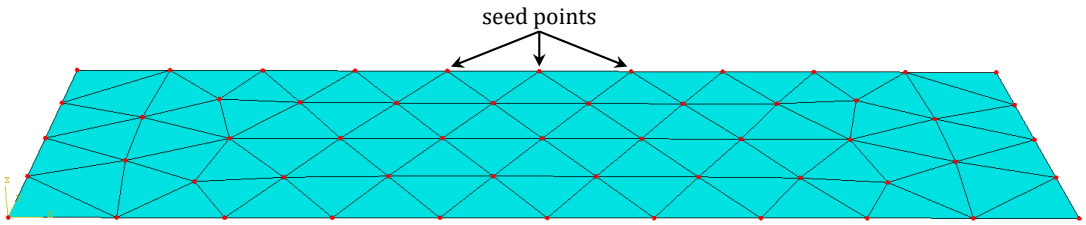

Figure 4.10: Seed points at the nodes of an unstructured mesh.

An inverse distance weighting (IDW) interpolation scheme is used to interpolate the terms of the stochastic orientation tensors from the seed points to each element of the refined mesh (target element of the interpolation). For each target element, only the seed points which are at a radial distance $\leq s_{\text{seed}}$ are used in the interpolation. This interpolation method assigns higher relative weights to the n seed points which are closer to the target element k, than those further away, i.e. the relative weights assigned to each seed point (used for the interpolation) are inversely proportional to the distance between the seed and the target element. Each term of the stochastic orientation tensor $\bar{a}_{ij}$ of the target element k is given by

$$\bar{a}_{ij}^{k} = \frac{\sum_{m=1}^{n} \frac{\bar{a}_{ij}^{m}}{d_{km}^{p}}}{\sum_{m=1}^{n} \frac{1}{d_{km}^{p}}}, \tag{4.3}$$

where p is a constant that controls the rate at which the relative weight of the interpolation ($\frac{1}{d_{ij}^{p}}$) decreases as the distance d_{km} (the distance between the target element m and the k^{th} seed point) increases. Typically a value of $p = 2$ is used [64], and was the value selected for all analyses of this work.

After defining a stochastic orientation tensor for each element of the structural mesh, the associated stiffness tensor $\mathbf{C}_{\text{TBDC}}$ can be obtained by the orientation averaging scheme presented by Advani and Tucker [31] (details on this method are presented in Appendix B). This requires defining the stiffness tensor of a UD discontinuous ply $\mathbf{C}_{\text{D}}$, which is obtained with the stiffness model presented in Chapter 2, and the second and forth order stochastic orientation tensors ($\bar{\mathbf{a}}$ and $\bar{\mathbf{A}}$, respectively). The later is obtained from $\bar{\mathbf{a}}$ using an orthotropic closure technique [65]. The proposed FE methodology is implemented in Abaqus via a Python script and a *UMAT* (User Material subroutine); the steps of the implementation are summarised in the flow-chart of Figure 4.11.

4.3.4 Results

4.3.4.1 Mesh size dependency

The IDW interpolation scheme enables the assignment of the local stochastic orientation tensors from the seeds of a coarse mesh, to a more refined structural mesh with any level of refinement, resulting in continuous fields of mechanical properties. In order to assess the robustness of this approach, two FE models of a plate (with in-plane dimensions of 150 × 150 mm) were created. Both models have the same seed mesh, with the same local orientation tensors at each corresponding seed point, but differ in the element size in the structural mesh. The most refined structural mesh has an element size of 1 mm and the coarser structural mesh has an element size of 2.5 mm.

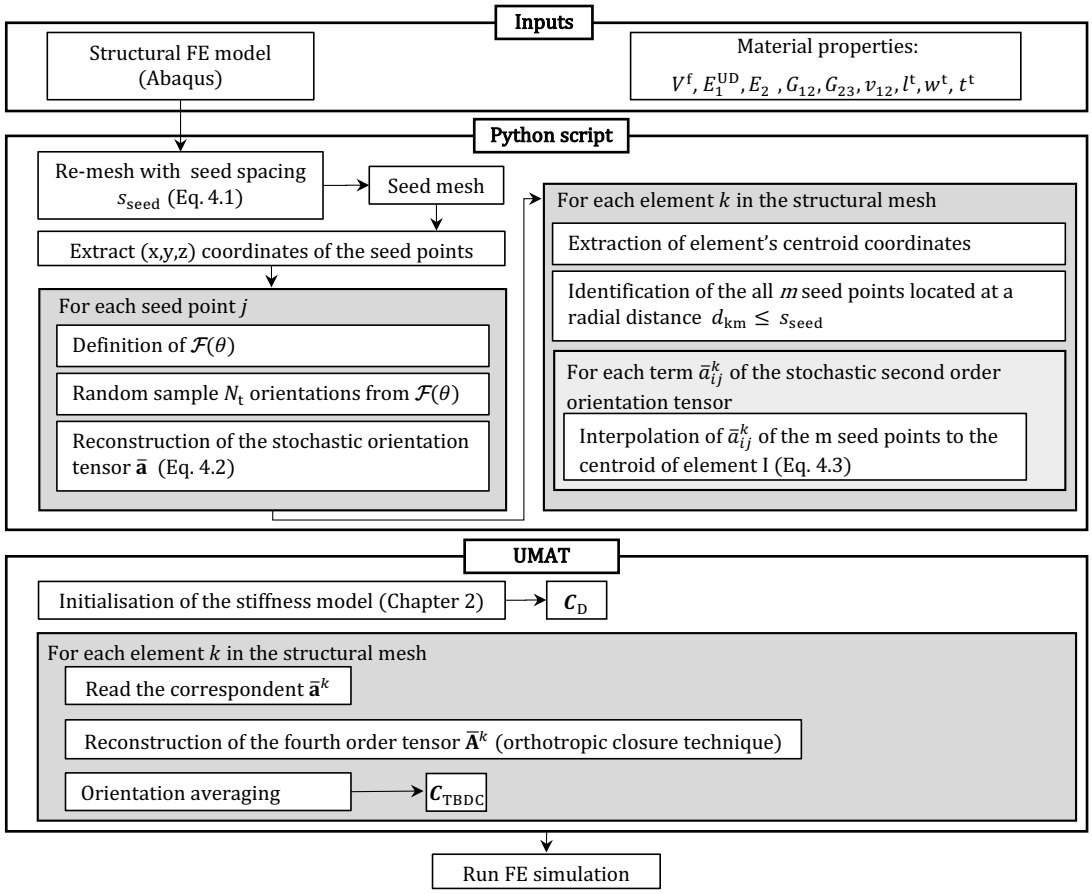

Figure 4.11: Flow-chart of the proposed Finite Element Methodology.

The resulting strain fields obtained with both FE models are shown in Figure 4.12; the features of the strain fields are identical, which demonstrates the robustness and mesh insensitivity of the proposed approach.

4.3.4.2 Spatial variability of the generated strain fields

In the proposed methodology, the length-scale of the material properties is controlled by the value of s_{seed}. In order to verify if the assignment of uncorrelated material properties to seed points spaced by s_{seed} translates to the desired spatial length-scales in the obtained strain field, the two methods described in Section 4.2 are used to assess the characteristic length-scales of strain fields obtained with FE models with different values of s_{seed}.

Figures 4.13a and 4.13b show the longitudinal strain field obtained with two FE models with different s_{seed} values, overlaid with the triangulation of the local strain peaks. The radial averaging profiles that result from the cross-correlation analysis of the generated strain fields are shown in Figure 4.13c and the distribution of s_{ls} obtained

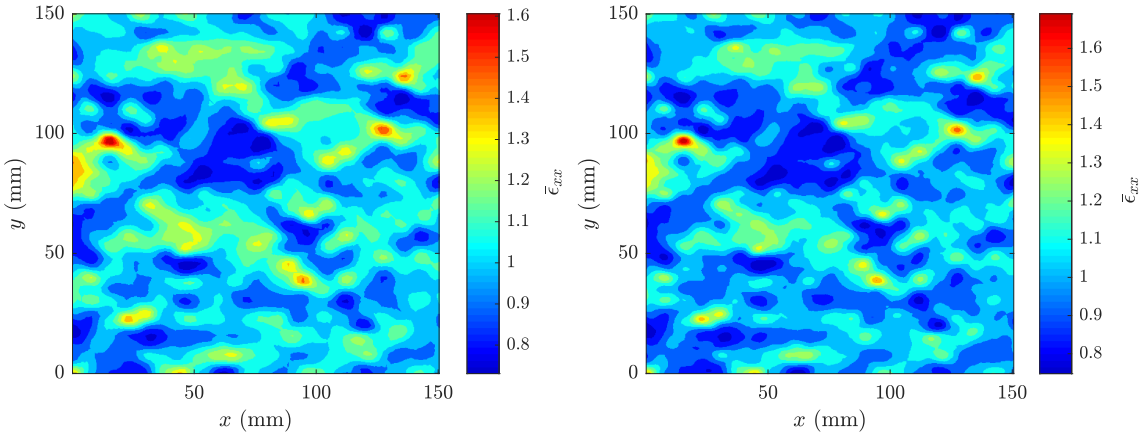

(a) Strain field obtained with a mesh element size of 2.5 mm.

(b) Strain field obtained with a mesh element size of 1.0 mm.

Figure 4.12: Mesh size dependency analysis.

with the peak triangulation method is shown in Figure 4.13d. Both methods show that value of s_{seed}, used in the FE models, translate to the characteristic length-scale of the resulting strain fields.

The spatial distribution of the seed points was obtained using the meshing capabilities of a FE software, by defining the seed points at the nodes of an uncorrelated mesh, which tends to create a repeated geometrical pattern of seed points, to which uncorrelated material properties are assigned. The strain fields that result from this approach do not show evidence of repeated patterns in the peaks and troughs, and instead are randomly dispersed in the structure, as shown in Figures 4.13a and 4.13b. This shows that the definition of the stochastic orientation tensors by random sampling in-plane orientations from uniform distributions, combined with the IDW interpolation to the refined mesh, govern the location of the strain peaks while the characteristic length-scales of the strains fields are governed by the average spacing between seeds points.

4.3.4.3 Validation against experiments

In order to validate the spatial and quantitative variability of the strain fields obtained with the proposed implicit FE methodology, 10 FE models of specimens with identical geometries to the one tested in Section 4.2 ($[138 \times 50]$ mm) and with a value of $s_{\text{seed}} = 13.8$ mm, which is a result of the harmonic mean (Eq. 4.1) between the in-plane tow dimensions of the HexMC-M77 material system (see Table 4.1), were analysed.

A longitudinal displacement along the length of each virtual specimen was applied, and the resulting longitudinal strain field of one of the virtual specimens is shown in

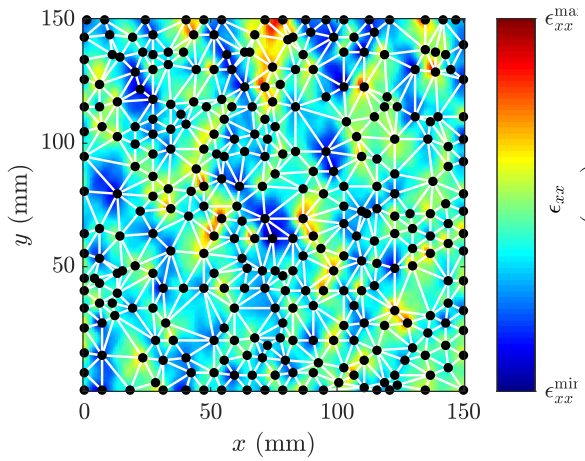

(a) Peak triangulation analysis of a strain field obtained with the proposed implicit FE methodology for a value of $s_{\text{seed}} = 8$mm.

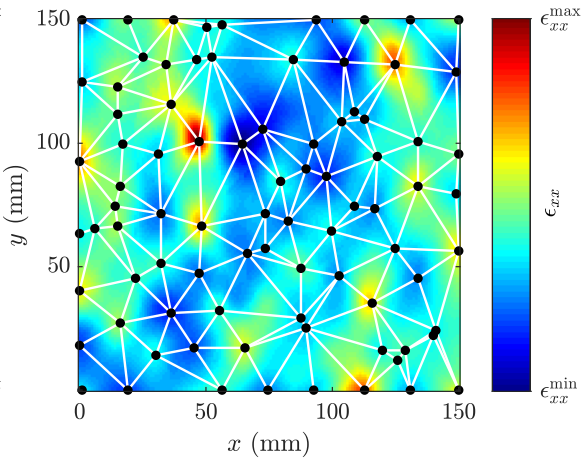

(b) Peak triangulation analysis of a strain field obtained with the proposed implicit FE methodology for a value of $s_{\text{seed}} = 20$mm.

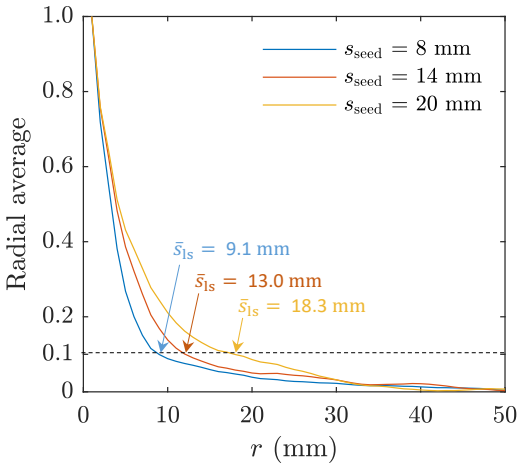

(c) Cross correlation analysis of the strain fields with the 3 different values for s_{seed}.

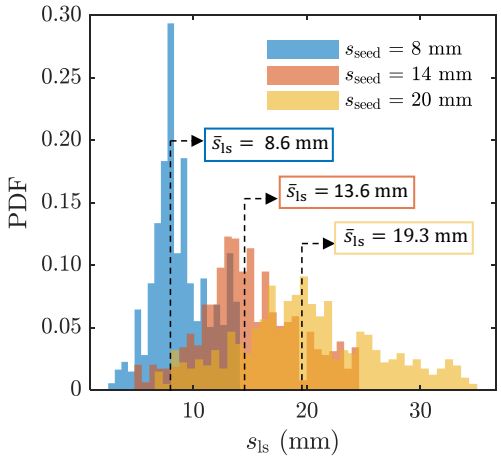

(d) Distribution of s_{ls} obtained with the triangulation method.

Figure 4.13: Analysis of the influence of s_{seed} on the characteristic length-scales of the predicted strain fields.

Figure 4.14a. Figures 4.14b and 4.14c show the spatial length-scale analysis of the DIC and implicit FE strain fields, obtained with the peak triangulation and the cross-correlation methods, respectively, where a good agreement in the obtained length-scale statistics was found. Figure 4.14d shows the variability of the strain values obtained with DIC and the implicit FE models, by comparing the distributions of the normalised longitudinal strain, where once again a very good agreement was found.

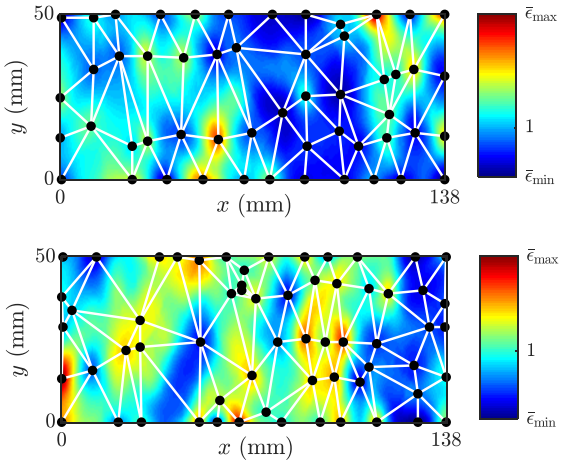

(a) Peak triangulation analysis of strain fields obtained with the proposed FE methodology.

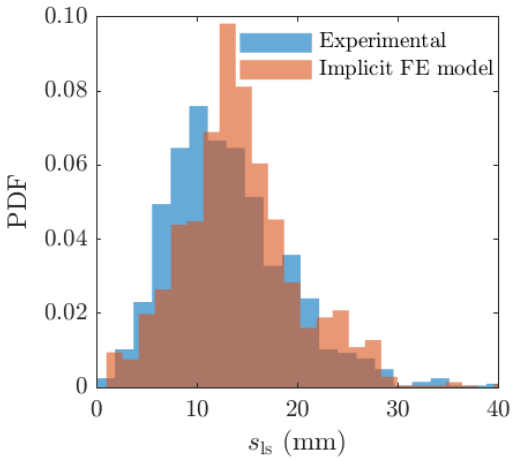

(b) Comparison between the spatial length distributions obtained from the DIC and implicit FE strain fields.

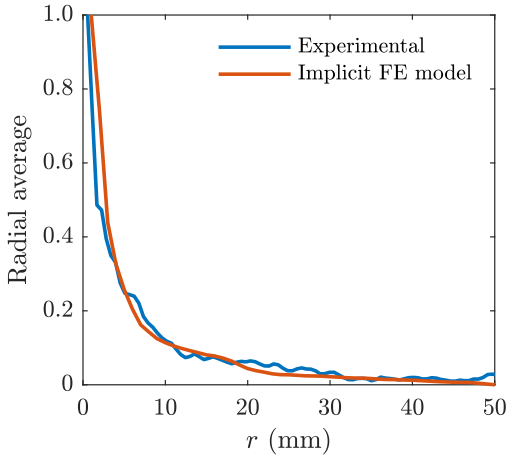

(c) Comparison between the cross correlation analysis of the DIC and implicit FE strain fields.

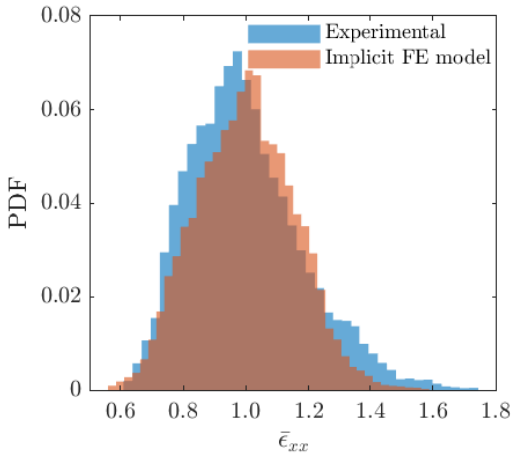

(d) Comparison between the normalised strain distributions obtained from the DIC and implicit FE strain fields.

Figure 4.14: Spatial distribution analysis of the strain fields obtained with the implicit FE models.

4.4 Discussion

The two methods to characterise the spatial variability described in Section 4.2.3 have some advantages and disadvantages over each other. The proposed method based on the triangulation of local peaks and troughs, requires smooth and/or non-noisy fields, since the location of the local peaks and/or troughs will be significantly affected by any discontinuity/noise. However, it can still be used for non-smooth fields if some noise filtering is done previously and if the characteristic length-scales are preserved,

as shown in Figure 4.5d. The advantage of this method is its ability to output a visual representation as well as a distribution of the length-scales of the analysed field. The cross-correlation approach has the advantage of being able to cope with both smooth and non-smooth fields. However, the downside of this method is that there is no clear definition of the transition region in order to output a value for the characteristic length-scale of the field. This is a method that is suitable for relative comparisons between the spatial distribution of different fields.

4.4.1 Novelty

This proposed implicit FE methodology is the first in the literature to combines the ability to recreate representative stochastic fields of mechanical properties of TBDC material systems, which are dependent on the microstructural features. The novel features of the framework are the following:

1. Material properties, based on a stochastic laminate analogy, are assigned to discrete seed points and governed by tailorable distribution functions $\mathcal{F}$. This allows for an implicit representation of the material's microstructure, and overcomes the limitations of other approaches in the literature [18, 20, 21] that require explicit generation of microstructures, which are computationally expensive and limited to simple planar geometries.
2. The characteristic length-scale of the field of mechanical properties to be assigned is dependent on the microstructural features (in-plane tow geometry) of the TBDC material system to be modelled. Compared to other models [22], this approach does not require any characterisation of experimentally measured strain fields.
3. The interpolation of the stochastic orientation tensors defined at the seed points to a refined structural mesh, leads to mesh a independent formulation and to smooth and realistic field of mechanical properties. This advances from current work in the literature [22] which also uses a stochastic laminate analogy in an FE framework, however yielding results that are mesh sensitive, and that require constant calibration with the characterisation of experimentally measured strain fields.
4. Despite the fact the only simple models and/or geometries were analysed in Section 4.3, the implementation of the proposed implicit FE methodology provides full flexibility to handle more complex 2D and 3D geometries.

4.4.2 Potential impact

The assignment of stochastic properties at the seed points is governed by distribution functions which can be linked to results from process simulations. This enables this FE methodology to be used for industrial relevant scenarios, where features like preferential fibre orientations can be modelled, while still capturing the intrinsic variability of the material.

The modular implementation of the proposed implicit FE methodology, where each module is independent of each other: (i) the calculation of the stochastic properties of the SELs, (ii) the assignment of spatially correlated properties (as a function of the microstructural features and independent of the mesh size) and (iii) the implementation of the material model in an FE framework. This allows for the proposed approach to be used to model other material systems, that also present a heterogeneous microstructure with a stochastic dominated response, by simply using a different and more suitable material model.

The ability to accurately model the stochastic mechanical response of TBDCs is dependent on the realistic representation of the variability and spatial distribution of the field of mechanical properties, that result from their heterogeneous microstructure. This inherent variability of material is responsible for certain characteristic mechanical behaviours, such as their notch insensitivity [56, 57]. The implicit representation of the material's microstructure used in the proposed FE methodology, enables its application to larger and complex models, while still capturing the effects of the materials' variability that occurs at the scale of the tows.

4.5 Conclusions

The variability of strain fields of a TBDC material systems was quantitatively characterised in terms of the variability of strain values and the characteristic length-scales. Moreover, a FE methodology, based on an implicit representation of the material's microstructure, and able to recreate realistic and representative distributions of mechanical properties was proposed. The main conclusions of this work are as follows:

- Two numerical methods to characterise the distribution of spatial length-scales in a continuum field were analysed: one proposed method based on a triangulation of local peaks and troughs, and one based on a cross-correlation analysis. The proposed method based on triangulation of local peaks is able to obtain a distribution of length-scales (with the mean value being the characteristic length-scale), and output a visual representation of the spatial length-scales of the continuum

field; however, it has the downside of not being able to directly handle non-smooth fields.

- The characteristic length-scales of TBDC strain fields are directly related to the tow geometry, and is governed by the harmonic mean between the tow width and the tow length. This analysis was done by generating strain fields of TBDCs with different in-plane tow geometries, using FE models with explicit representation of the microstructure of TBDCs.
- FE models based on explicit representations of the microstructure are coupled with microstructure generators, and despite being limited to simple geometries, these models are able to generate accurate and representative strain fields.
- A FE methodology based on implicit representations of the material's microstructure was proposed. In this approach, the material system is idealised as stochastic equivalent laminates at discrete seed points of uncorrelated material properties, which are represented by stochastic orientation tensors. The distance between the seeds govern the characteristic length-scales of the resulting field of mechanical properties.
- An adequate interpolation scheme is then used to interpolate the stochastic orientation tensors from the seed points to a refined structural mesh. This approach leads to smooth and continuous fields of mechanical properties with no mesh size dependency.

Chapter 5

A 3D stochastic finite element framework for modelling the stochastic mechanical behaviour of TBDCs

5.1 Introduction

A widespread use of TBDCs in structural application is currently hindered by the lack of FE models suitable for structural design. The complex nature of TBDC microstructures and their stochastic mechanical response, raises challenges to the development of computationally efficient models to predict failure of these materials.

Most models in the literature to predict the final failure of TBDCs are based in explicit representations of the material's microstructure [17, 18, 18–21]. Harper et al. [18] generated FE models of the 3D TBDC RVEs, and used maximum stress and von Mises Stress Criterion to evaluate different failure modes. The predicted stiffness and strength results obtained were within 5% compared to experimental values. A similar approach was adopted by Chen et al [17], where RVEs were created with a microstructure generator, for different global tow orientations, ranging from fully aligned to in-plane random. Both the predicted tensile stiffness and strength were in good agreement with experimental data. Kravchenko et al. [21] generated virtual specimens with a random sequential adsorption algorithm; FE models of the generated specimens were created using a voxel mesh, in which each element was mapped with a local tow orientation. This approach also yielded good predictions of the mechanical proprties; however, voxel based meshes tend to generate non-realistic stress concentrations due

the non-smooth representation of the tow boundaries, which in some cases can lead to over-predictions of the stress-concentrations near the tow boundaries and hence to erroneous results.

The aforementioned models were able to achieve good predictions of the mechanical response of TBDCs. However, the requirement of microstructure generators to obtain FE models with explicit representation of the microstructure, leads to high computation times and can only be used to model simple and small geometries. Therefore the use of these models for industrial design is limited, as faster computation times and the possibility to model larger and more complex geometries is generally required. Moreover, the possibility of linking these models with fibre orientation information that results from process simulations is a key feature for and efficient design of TBDC parts/structures, and is a topic still to be explored in the literature.

Overall, no models exist in the literature that account for effects of the manufacturing process (material flow during compression moulding) while having relatively low computational requirements, making them suitable for industrial design of TBDC parts. Therefore, in this chapter, the FE framework presented in Chapter 4 is extended to include final failure prediction and to account for fibre orientation information that results from compression moulding process simulations. The FE framework presented in this chapter will therefore consist in a simulation chain that includes process simulation results, a stochastic assignment of material properties and finally the structural simulation itself. Section 5.2 describes the two TBDC material systems tested under longitudinal tension used for validation of the framework. In Section 5.3 different modules of the framework are detailed: (i) the coupling with fibre orientation results from process simulations; (ii) the assignment of 3D stochastic material properties; and (iii) a failure criterion and stiffness reduction scheme used to predict final failure. Section 5.4 compared the experimental results of the two material systems with the predictions of the framework. The results are discussed in Section 5.5, and the main conclusions are summarised in Section 5.6.

The work presented in this chapter is the result of a joint collaboration between the author and Luca Martulli (Early Stage Researcher in Toyota Motor Europe/KU Leuven). The main contribution of each author are as follows:

- Process simulation and fibre orientation mapping: Luca Martulli
- Concept development of the stochastic orientation tensors based on the tensors obtained by process simulations: the author
- Assignment of variability and implementation of the 3D FE framework in a Python script: the author

- Development and implementation of the 3D failure initiation criterion for the plies of the SELs: the author
- Implementation of the stiffness reduction model: the author and Luca Martulli
- Implementation of the material model in a UMAT: Luca Martulli and the author

5.2 Materials and methods

In this work, two TBDCs material systems will be used for the experimental validation of the proposed model:

1) HexMC-M77 [2], a commercially available TBDC material system: the TBDC plates were manufactured with a charge coverage $\geq$ 80%, and are therefore a low-flow material system. This results in in-plane isotropic properties due to the uniform random orientation of the tows.

2) STR120N [53], a Carbon Fibre Sheet Moulding Compound (CF-SMC) provided by Mitsubishi Chemical Carbon Fiber and Composites GmbH: the CF-SMC plates were manufactured with a charge coverage of 20%, and are therefore a high-flow material. Manufacturing of oriented CF-SMC specimens is described in [66], and will be briefly described here for completeness. CF-SMC plates with dimensions 458 mm x 458 mm x 2.5 mm were compression moulded with a moulding temperature, pressure and time of 141.5°C, 215 bar and 180s, respectively. The high in-mould flow resulting from the low charge coverage reoriented the tows in the flow direction. Specimens were then waterjet cut from the plates at an angle with the main flow direction of 0°, 45° and 90°. In the rest of this chapter, they will be referred to as "0°", "45°" and "90°" CF-SMC specimens, respectively.

The microstructural features of each material system described above are defined in Table 5.1.

Table 5.1: Specification of the microstructural elements (tow length l^{t}, tow width w^{t}, tow thickness t^{t} and fibre volume fraction V^{f}) of the material systems analysed; dimensions are in mm and volume fractions in %.

Material	l^{t}	w^{t}	t^{t}	V^{f}
HexMC-M77 [2]	50.0	8.0	0.125	57
CF-SMC [53]	25.0	8.0	0.15	42

The HexMC-M77 and the CF-SMC specimens were both tested under longitudinal tension according to the ASTM D3039 standard [36]; the specimens geometry of each

material system is defined in Table 5.2. A displacement rate of 1 mm/min was used. Digital Image Correlation (DIC) was used to measure the strain fields on the surface of each specimen.

5.3 Model development

The proposed framework further extends the capabilities of the FE framework presented in Chapter 4, and has the modular implementation, represented in Figure 5.2. The different modules are described below:

1) Process simulation: a compression moulding simulation is performed to evaluate the process-induced fibre orientations. The fibre orientations are described by second order orientation tensors a_{ij} [31]. More details on this step are presented in Appendix C.

2) Spatial variability and local assignment of stochastic properties: the second order fibre orientation tensors a_{ij} resulting from the process simulation are mapped to seed points in a FE mesh (as shown in Figure 5.1), with a distance equal to the characteristic spacing given by Eq. 4.1. As described in Chapter 4, these seed points define points of uncorrelated material properties; the spacing between seeds governs the characteristic length-scale of the field of mechanical properties to be assigned. A stochastic process is used to convert each a_{ij} at the seed points to a stochastic orientation tensor $\bar{a}_{ij}$. These stochastic tensors are then interpolated from the seed points to the centroids of a refined *structural mesh* used in the structural simulation. Details of this module are described in Section 5.3.1.

3) Material model and structural simulation: the TBDC material is idealised as Stochastic Equivalent Laminates (SELs), generated from the stochastic orientation tensors. The failure initiation of the SELs is evaluated using a failure criterion, and the consequent stiffness reduction is modelled by a ply discount method. Details of this module are described in Section 5.3.2.

5.3.1 3D assignment of stochastic mechanical properties

5.3.1.1 Coordinate systems definition

Tows are assumed to remain planar entities after the compression moulding process [29, 66]. As a result, the local SELs are characterised by an average out-of-plane orientation and an in-plane distribution. Three different coordinate systems are used in the process of assigning stochastic mechanical properties (shown in figure 5.3):

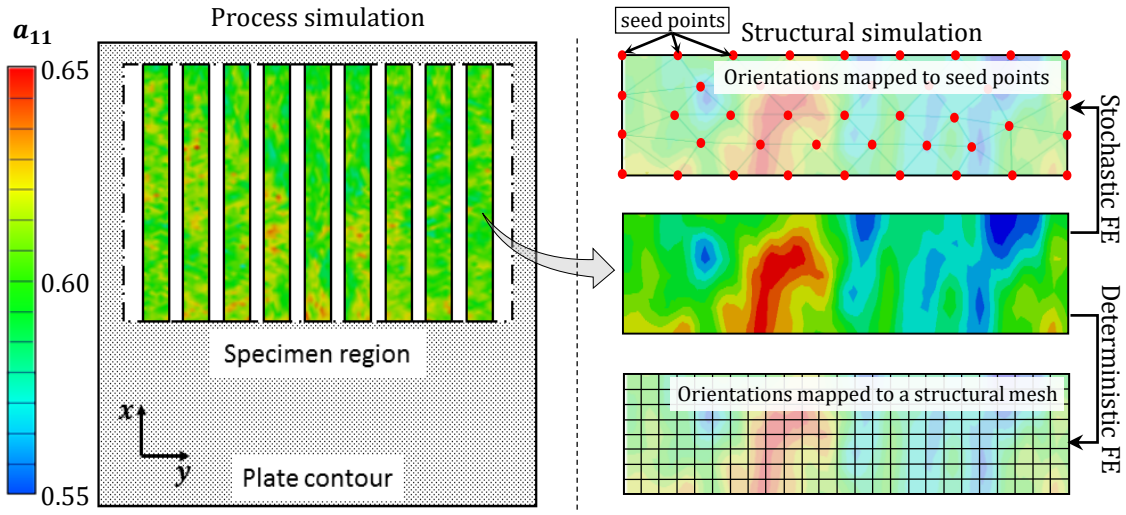

Figure 5.1: The mapping of orientation tensors a_{ij} resulting from the process simulation to the seed points used in the stochastic FE framework. The direct mapping of the a_{ij} to each element of the structural mesh is also shown, and used in a deterministic FE approach (described in Section 5.4).

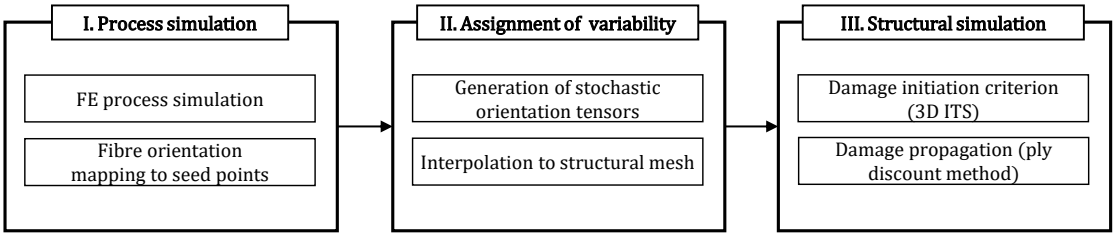

Figure 5.2: The modular implementation of the stochastic framework.

1) Global coordinate system CSYS^{g}, with axis (XYZ) - this is the global coordinate system of the FE simulation.

2) Stochastic equivalent laminate coordinate system CSYS^{SEL}, with axis (xyz) - this is the coordinate system in which the SELs are generated. It is obtained by aligning the Z axis of CSYS^{g} with the direction normal to the local plane of the tows z, as described in Section 5.3.1.2. The angle between Z and z is ϕ^{*}, as shown in Figure 5.3.

3) Local coordinate system CSYS^{l}, with axis (123) - this is the local coordinate system of each discontinuous ply of the SEL, in which direction 1 is aligned with the fibre direction, direction 2 defines the transverse direction and direction 3 coincides with z.

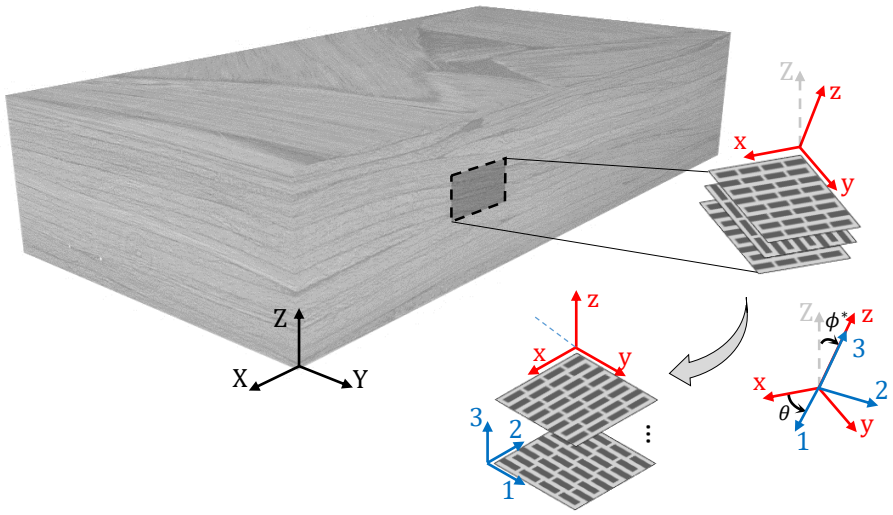

Figure 5.3: The three different coordinate systems CSYS defined in the model.

5.3.1.2 3D stochastic orientation tensors

The second order orientation tensors $\mathbf{a}^{\mathrm{g}}$ resulting from the process simulations and mapped to the seed points are defined in the global coordinate system $\mathrm{CSYS}^{\mathrm{g}}$. To generate an SEL, the planar Fibre Orientation Distribution (FOD) function in $\mathrm{CSYS}^{\mathrm{SEL}}$ defined by $\mathcal{F}^{\mathrm{SEL}}(\theta, \phi = \frac{\pi}{2})$ is required. In order to recover the associated $\mathcal{F}^{\mathrm{SEL}}(\theta, \frac{\pi}{2})$, the orientation tensors $\mathbf{a}^{\mathrm{g}}$ have to be expressed in $\mathrm{CSYS}^{\mathrm{SEL}}$ ($\mathbf{a}^{\mathrm{SEL}}$).

The unit-length eigenvectors ($\mathbf{e}_1$, $\mathbf{e}_2$ and $\mathbf{e}_3$) of $\mathbf{a}^{\mathrm{g}}$, define the principal directions of fibre orientation; the eigenvalues (λ_1, λ_2 and λ_3) indicate the statistical proportions of fibres oriented along those directions. The directional vector of axis z of $\mathrm{CSYS}^{\mathrm{SEL}}$ is defined by the eigenvector $\mathbf{e}_3$, which is associated with the smallest eigenvalue λ_3. The angle ϕ^* between the directional vectors $\mathbf{e}_3$ and $\mathbf{Z}$ (which is defined by (0,0,1) in the $\mathrm{CSYS}^{\mathrm{g}}$), as shown in Figure 5.3, is given by

$$\phi^* = \arccos(e_3^z), \tag{5.1}$$

where e_3^z is component of the third eigenvector along the Z axis. The coordinate transformation matrix $\mathbf{T}_{\mathrm{g/SEL}}$ from $\mathrm{CSYS}^{\mathrm{g}}$ to $\mathrm{CSYS}^{\mathrm{SEL}}$ is defined by a rotation around an axis $\mathbf{u}$ and by the angle ϕ^*. The axis of rotation $\mathbf{u}$ is given by $\mathbf{u} = \mathbf{e}_3 \times \mathbf{Z}$; and the transformation matrix $\mathbf{T}_{\mathrm{g/SEL}}$ is finally defined as

$$\mathbf{T}_{\mathrm{g/SEL}} = \begin{bmatrix} \cos\phi^* + u^{x2}\,(1-\cos\phi^*) & u^x u^y\,(1-\cos\phi^*) - u^z \sin\phi^* & u^x u^z\,(1-\cos\phi^*) + u^y \sin\phi^* \\ u^y u^x\,(1-\cos\phi^*) + u^z \sin\phi^* & \cos\phi^* + u^{y2}\,(1-\cos\phi^*) & u^y u^z\,(1-\cos\phi^*) - u^x \sin\phi^* \\ u^z u^x\,(1-\cos\phi^*) - u^y \sin\phi^* & u^z u^y\,(1-\cos\phi^*) + u^x \sin\phi^* & \cos\phi^* + u^{z2}\,(1-\cos\phi^*) \end{bmatrix}. \tag{5.2}$$

The orientation tensor $\mathbf{a}_{ij}^{\mathrm{g}}$ can therefore be represented in the CSYS$^{\mathrm{SEL}}$ by the following transformation:

$$\mathbf{a}^{\mathrm{SEL}} = \mathbf{T}_{\mathrm{g/SEL}} \mathbf{a}^{\mathrm{g}} \mathbf{T}_{\mathrm{g/SEL}}^{-1}. \tag{5.3}$$

The use of the cross-product $\mathbf{e}_3 \times \mathbf{Z}$ in the definition of $\mathbf{u}$, can lead to inaccuracies when $\mathbf{e}_3$ and $\mathbf{Z}$ are aligned. To avoid this problem, for values of $\phi^* \leq 0.1°$ it is assumed that the coordinate systems CSYS$^{\mathrm{SEL}}$ and CSYS$^{\mathrm{g}}$ are coincident.

The FOD function $\mathcal{F}^{\mathrm{SEL}}(\theta, \phi)$ can be reconstructed from $\mathbf{a}_{ij}^{\mathrm{SEL}}$ [31]. The recovery of the FOD from the $\mathbf{a}^{\mathrm{SEL}}$ requires the knowledge of the associated fourth-order orientation tensor $\mathbf{A}^{\mathrm{SEL}}$; the latter is obtained from the $\mathbf{a}^{\mathrm{SEL}}$ using an orthotropic closure approximation [65]. In Figure 5.4a, an example of a $\mathcal{F}(\theta, \phi)$ reconstructed from a generic $\mathbf{a}^{\mathrm{g}}$ is shown, and the same $\mathcal{F}(\theta, \phi)$ defined in CSYS$^{\mathrm{SEL}}$ is represented in Figure 5.4b.

To generate a stochastic orientation tensor in this reference system $\bar{\mathbf{a}}_{ij}^{\mathrm{SEL}}$, N^{t} in plane orientations θ_i^{SEL} are randomly sampled from the normalised planar orientation distribution function $\mathcal{F}^{\mathrm{SEL}}(\theta, \frac{\pi}{2})$, which is highlighted in Figure 5.4b. The value of N^{t} here is taken as a physical parameter which represents the tow count in the thickness direction – given by the ratio of the thickness of the geometry to be modelled and the nominal tow thickness (in case of a flat specimen $N^{\mathrm{t}} = t^{\mathrm{s}}/t^{\mathrm{t}}$). The characteristic out of plane orientation ϕ^{SEL} can be calculated from $\mathbf{a}^{\mathrm{SEL}}$ by,

$$\phi^{\mathrm{SEL}} = \arccos(\sqrt{a_{33}^{\mathrm{SEL}}}). \tag{5.4}$$

The stochastic orientation tensor $\bar{\mathbf{a}}^{\mathrm{SEL}}$ can therefore be reconstructed based on the N^{t} sampled in plane orientations θ_i and from the characteristic out of plane orientation ϕ^{SEL} from

$$\bar{\mathbf{a}}_{ij}^{\mathrm{SEL}} = \tfrac{1}{N^{\mathrm{t}}} \cdot \textstyle\sum_{i=1}^{N^{\mathrm{t}}} \begin{bmatrix} \sin^2(\phi^{\mathrm{SEL}})^2 \cos(\theta_i) & \sin^2(\phi^{\mathrm{SEL}}) \cos(\theta_i) \sin(\theta_i) & \sin(\phi^{\mathrm{SEL}}) \cos(\phi^{\mathrm{SEL}}) cos(\theta_i) \\ \sin^2(\phi^{\mathrm{SEL}}) \cos(\theta_i) \sin(\theta_i) & \sin^2(\phi^{\mathrm{SEL}}) \sin^2(\theta_i) & \sin(\phi^{\mathrm{SEL}}) \cos(\phi^{\mathrm{SEL}}) \sin(\theta_i) \\ \sin(\phi^{\mathrm{SEL}}) \cos(\phi^{\mathrm{SEL}}) cos(\theta_i) & \sin(\phi^{\mathrm{SEL}}) \cos(\phi^{\mathrm{SEL}}) \sin(\theta_i) & \cos^2(\phi^{\mathrm{SEL}}) \end{bmatrix}. \tag{5.5}$$

To transform the $\bar{\mathbf{a}}_{ij}^{\mathrm{SEL}}$ back to the global coordinate system, the following transformation is done

$$\bar{\mathbf{a}}^{\mathrm{g}} = \mathbf{T}_{\mathrm{g/SEL}}^{-1} \bar{\mathbf{a}}^{\mathrm{SEL}} \mathbf{T}_{\mathrm{g/SEL}}. \tag{5.6}$$

5.3.1.3 Interpolation of the stochastic orientation tensor from the seeds to the structural mesh

The structural simulation will be carried out in a more refined structural mesh (i.e. with an average element size significantly smaller than the average spacing between the

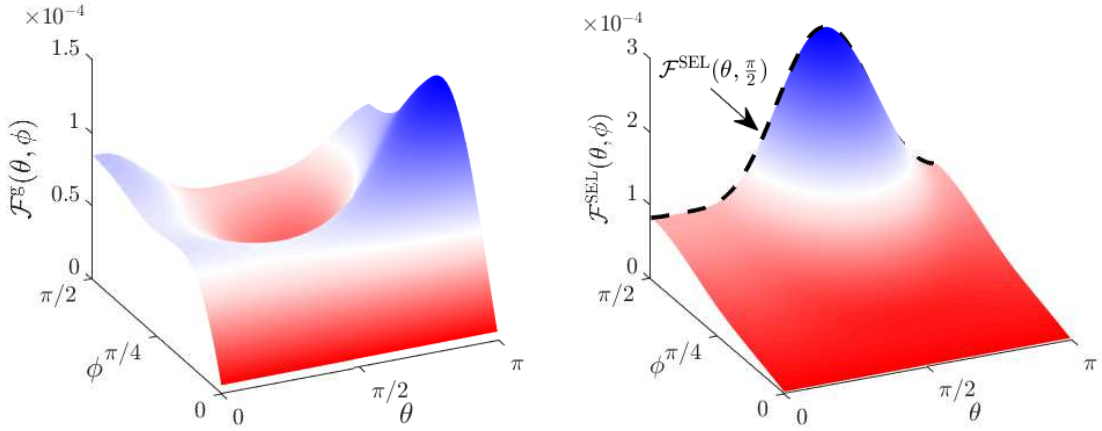

(a) Reconstruction of the 3D FOD in CSYS^{g}.

(b) Reconstruction of the 3D FOD in CSYS^{SEL}.

Figure 5.4: Transformation of the FOD function in from the global to the SEL reference system; representation of $\mathcal{F}^{SEL}(\theta, \frac{\pi}{2})$, highlighted by the dashed-line in Figure 5.4b.

SEL seeds); this requires the definition of the stiffness tensor at the integration points of the element of the structural mesh. Using the interpolation scheme presented in Chapter 4, each term of the stochastic orientation tensor $\bar{\mathbf{a}}^{g}$ is interpolated from the seed points to the centroid of the refined mesh's elements (Eq. 4.3).

The stiffness tensor for each element of the structural mesh $\mathbf{C}^{g}_{TBDC}$ is calculated using the orientation averaging scheme presented by Advani and Tucker [31] (details on this method are presented in Appendix B). This requires the definition of the stiffness tensor of a UD discontinuous ply $\mathbf{C}_{D}$, which is obtained with the stiffness model presented in Chapter 2, as well and the interpolated second order stochastic orientation tensor and the respective fourth order tensor.

The implementation of the stochastic FE framework is done in Abaqus via a Python script; the steps of the implementation are summarised in the flow-chart of Figure 5.5.

5.3.2 Failure criterion for an equivalent UD discontinuous ply

5.3.2.1 Stress transformation to the stochastic equivalent laminae

Following the SEL analogy, failure prediction requires the knowledge of the stress state at each ply. Since the terms of $\bar{\mathbf{a}}^{g}$ are interpolated from the seed points to each element of the structural mesh, a probabilistic stacking sequence associated to each element can be reconstructed based on the respective planar FOD $\mathcal{F}^{SEL}(\theta, \frac{\pi}{2})$. For this purpose, $\mathcal{F}^{SEL}(\theta, \frac{\pi}{2})$ (whose reconstruction from $\bar{a}_{ij}$ is detailed in Section 5.3.1.2) is

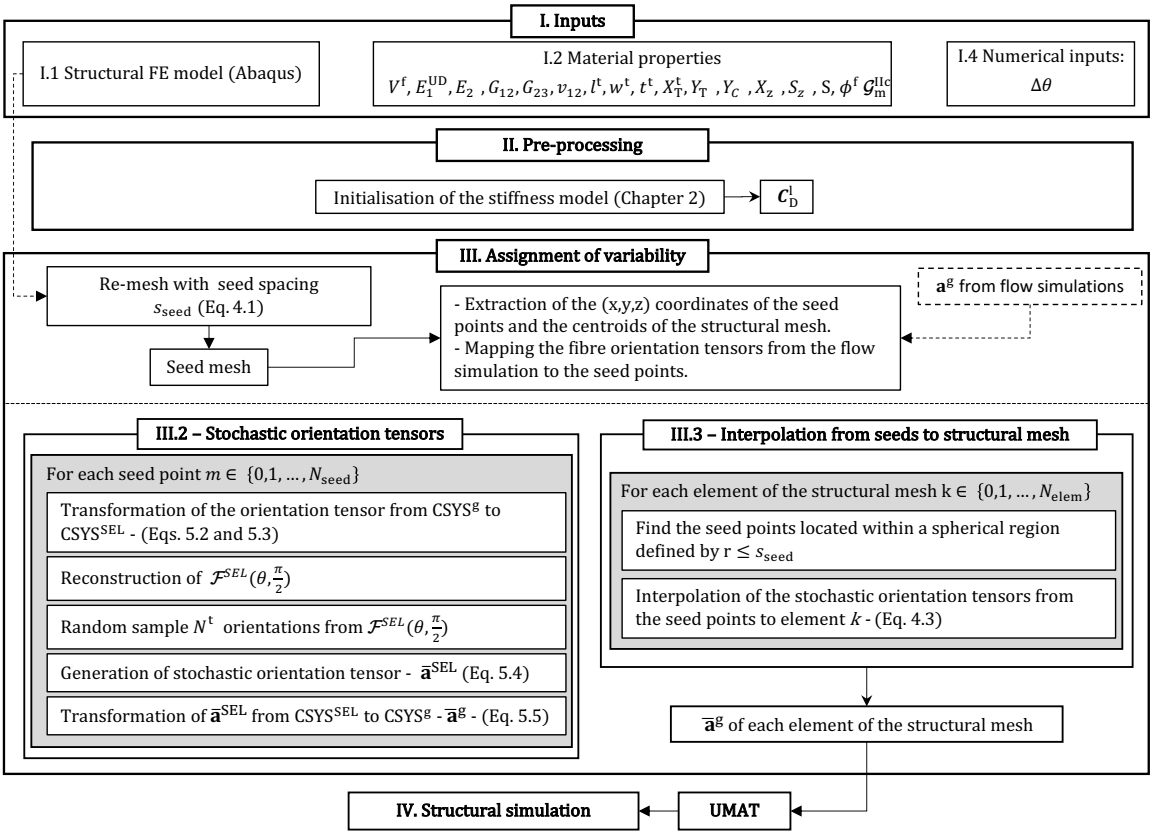

Figure 5.5: Implementation flowchart of the stochastic framework.

discretised in $N_\theta = \pi/\Delta\theta$ increments, each $\Delta\theta$ wide, as shown in Figure 5.6. Consider an interval centred at θ^* and bounded by the angles $\theta^* - \Delta\theta/2$ and $\theta^* + \Delta\theta/2$. The area r_{θ^*} below the $\mathcal{F}^{\mathrm{SEL}}(\theta, \frac{\pi}{2})$, bounded by those angles, represents the probability of a UD discontinuous ply having an in-plane orientation within the interval $\Delta\theta$ centred in θ^*. Since the total area below $\mathcal{F}^{\mathrm{SEL}}(\theta, \frac{\pi}{2})$ is 1, the probability r_{θ^*} can be used to assign a probability of having plies in the SEL with an in-plane orientation θ^*:

$$N_{ply}(\theta^*) = r_{\theta^*} = \mathcal{F}^{\mathrm{SEL}}(\theta^*, \frac{\pi}{2}) \cdot \Delta\theta. \tag{5.7}$$

The full probabilistic stacking sequence is obtained by repeating this procedure for all the angle intervals N_θ in which $\mathcal{F}^{\mathrm{SEL}}(\theta, \frac{\pi}{2})$ is discretised.

Once the probabilistic stacking sequence is obtained, using CLT, the global strain applied $\boldsymbol{\epsilon}^{\mathrm{g}}$ is expressed in the local coordinate system of each N_θ angle interval centered at θ_i:

$$\boldsymbol{\epsilon}^{\mathrm{l}}(\phi_i) = \mathbf{T}_{\theta_i}^{-1} \left(\mathbf{T}_{\mathrm{g/SEL}}^{-1} \, \boldsymbol{\epsilon}^{\mathrm{g}} \, \mathbf{T}_{\mathrm{g/SEL}} \right) \mathbf{T}_{\theta_i} = \mathbf{T}_{\theta_i}^{-1} \, \boldsymbol{\epsilon}^{\mathrm{SEL}} \, \mathbf{T}_{\theta_i} \tag{5.8}$$

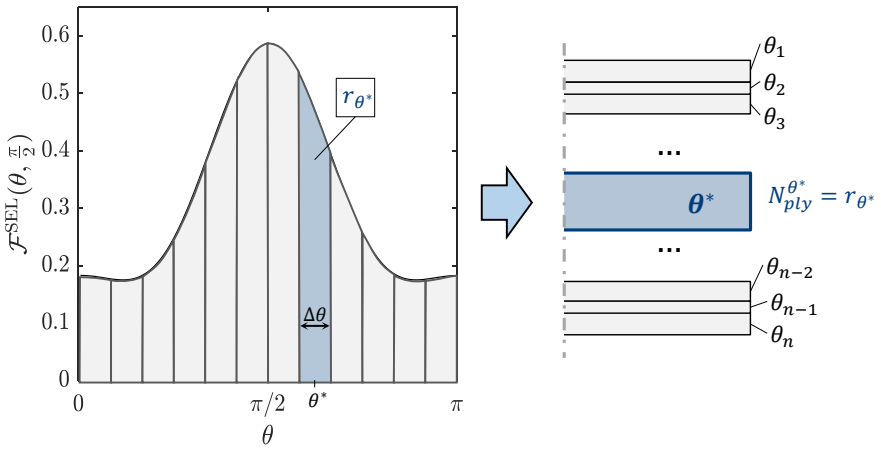

Figure 5.6: Discretisation of the $\mathcal{F}^{\mathrm{SEL}}(\theta, \frac{\pi}{2})$ and probabilistic stacking sequence reconstruction.

where $\mathbf{T}_{\theta_i}$ is the transformation matrix from CSYS$^{\mathrm{SEL}}$ to CSYS$^{\mathrm{l}}$ of each ply oriented at θ_i, given by,

$$\mathbf{T}_{\theta_i} = \begin{bmatrix} \cos\theta_i & -\sin\theta_i & 0 \\ \sin\theta_i & \cos\theta_i & 0 \\ 0 & 0 & 1 \end{bmatrix} \tag{5.9}$$

Using the stiffness tensor for a UD discontinuous ply ($\mathbf{C}_{\mathrm{D}}$) obtained in Section 5.3.1.3, the local stress field $\boldsymbol{\sigma}^l$ in the $N_{\mathrm{ply}}(\theta_i)$ plies with orientation θ_i is then given by:

$$\boldsymbol{\sigma}^l(\theta_i) = \mathbf{C}_{\mathrm{D}}^{\mathrm{l}} \boldsymbol{\epsilon}^{\mathrm{l}}(\theta_i). \tag{5.10}$$

5.3.2.2 3D Failure criterion for a discontinuous equivalent lamina

The interactive tensile-shear (ITS) failure criterion presented in [23] is here used to assess failure due to the interaction between the in-plane stresses: i.e longitudinal-tension (σ_1), transverse-tension (σ_2) and in-plane shear (τ_{12}). To increase the computational efficiency of the implementation of the model, the ITS failure surface (see Figure 3.2b) is approximated by the following analytical expression:

$$\frac{{\sigma_1}^2}{{X_{\mathrm{T}}^{\mathrm{D}}}^2} + \frac{{\sigma_2}^2}{{Y_{\mathrm{is,T}}}^2} + \frac{{\tau_{12}}^2}{{S_{\mathrm{is}}}^2} = 1 \tag{5.11}$$

where $X_{\mathrm{T}}^{\mathrm{D}}$ is the tensile strength of a UD discontinuous ply, $Y_{\mathrm{is,T}}$ and S_{is} are the respective in-situ tensile and shear strengths [49]. This failure surface defines an in-plane failure index F_{ip}. For a generic stress field $\boldsymbol{\sigma}$, an in-plane failure index F_{ip} can

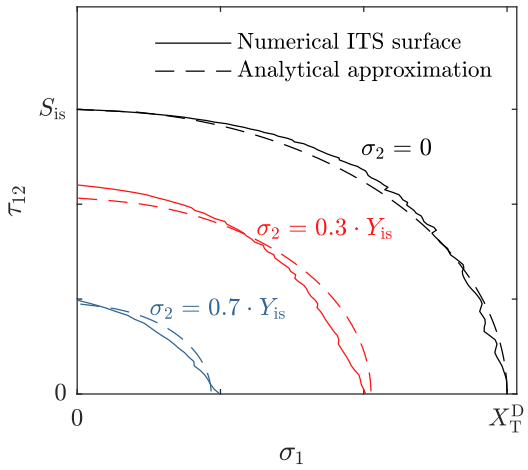

Figure 5.7: Approximated ITS failure surface.

be defined by

$$F_{ip} = \sqrt{\frac{{\sigma_1}^2}{{X_T^D}^2} + \frac{{\sigma_2}^2}{{Y_{is,T}}^2} + \frac{{\tau_{12}}^2}{{S_{is}}^2}}. \tag{5.12}$$

To capture failure due to out-of-plane loadings (eg. peel stresses), an out of plane failure index F_{op} is defined by the following maximum stress failure criterion,

$$F_{op} = \sqrt{\frac{\sigma_3^2}{X_z^2} + \frac{\tau_{13}^2}{S_z^2} + \frac{\tau_{23}^2}{S_z^2}}, \tag{5.13}$$

where X_z and S_z are the interlaminar tensile and shear strengths respectively.

The stress state in each UD discontinuous ply oriented at θ_i is known from equation 5.10. Therefore, combining quadratically the in-plane and out-of-plane failure indices, a global failure index $F_I(\theta_i)$ for the $N_{ply}(\theta_i)$ plies with orientation θ_i can be obtained

$$F_I(\theta_i) = \sqrt{F_{ip}^2(\theta_i) + F_{op}^2(\theta_i)}. \tag{5.14}$$

5.3.2.3 Stiffness reduction of the TBDC

Following a ply-discount method, it is assumed that a discontinuous ply with in-plane orientation θ_i fails and no longer carries any stress if the respective $F_I(\theta_i) \geq 1$. This reduces the stiffness of the SEL. This stiffness reduction can be represented by a damage tensor $\mathbf{d}^{SEL}$ which can be computed by the ratio of the components of the damaged $\mathbf{C}_{SEL,d}$ and pristine stiffness tensors $\mathbf{C}_{SEL,p}$ of the SEL [67]. Given the probabilistic stacking sequence of a SEL (as defined in Section 5.3.2.1), the corresponding

stiffness tensor $\mathbf{C}_{\mathrm{SEL}}$ can be obtained using CLT:

$$\mathbf{C}_{\mathrm{SEL}} = \sum_{i=1}^{N_\theta} \mathbf{C}^{i}_{\mathrm{D},\theta_i} \cdot r_{\theta_i} \tag{5.15}$$

where $\mathbf{C}_{\mathrm{D},\theta_i}$ is the stiffness tensor of the UD discontinuous ply rotated by the respective in-plane angle θ_i.

The pristine stiffness tensor $\mathbf{C}_{\mathrm{SEL,p}}$ is calculated with equation 5.15 using the original FOD $\mathcal{F}^{\mathrm{SEL}}(\theta, \frac{\pi}{2})$. The probability r_{θ_i} of the plies oriented at θ_i with $\mathcal{F}_{\mathrm{I}}(\theta_i) \geq 1$ is set to 0, and equation 5.15 is used to compute the damaged stiffness tensor $\mathbf{C}_{\mathrm{SEL,d}}$.

For the same applied strain, the surviving plies need to withstand the stress previously carried by the failed plies; therefore, following an iso-stress approach, $C_{\mathrm{SEL,d}}$ is used to compute a local strain increase resulting from the stiffness loss of the SEL (due to failure of the plies). This new strain is applied to the damaged SEL, and CLT is used to recalculate the stress redistribution to the surviving plies. If this stress redistribution triggers the failure of new plies, the stiffness tensor is updated again, until the damaged SEL is able to withstand the stress redistribution or it fails completely.

Following the approach presented in [67], the direct components of both $C^{\mathrm{SEL,p}}$ and $C^{\mathrm{SEL,d}}$ are used to calculate the damage tensor $\mathbf{d}^{\mathrm{SEL}}$ as:

$$\mathbf{d}^{\mathrm{SEL}} = \begin{bmatrix} D_{11} & 0 & 0 \\ 0 & D_{22} & 0 \\ 0 & 0 & D_{33} \end{bmatrix}, \qquad \text{with} \qquad D_{ii} = 1 - \frac{C_{\mathrm{SEL,d},ii}}{C_{\mathrm{SEL,p},ii}} \tag{5.16}$$

The stiffness tensor $\mathbf{C}^{\mathrm{g}}_{\mathrm{TBDC}}$, obtained with the orientation averaging scheme described in section 5.3.1.3, is assumed to undergo the same stiffness reduction (for the same loading conditions) as the stiffness tensor $\mathbf{C}^{\mathrm{p}}_{\mathrm{SEL}}$ of the SEL, obtained with CLT using the reconstructed probabilistic stacking sequence. The damage tensor $\mathbf{d}^{\mathrm{SEL}}$, calculated in Eq. 5.16, can thus be used to reduce the stiffness tensor $\mathbf{C}^{\mathrm{g}}_{\mathrm{TBDC}}$. However, this requires rotating $\mathbf{C}^{\mathrm{g}}_{\mathrm{TBDC}}$ from $\mathrm{CSYS}^{\mathrm{g}}$ to $\mathrm{CSYS}^{\mathrm{SEL}}$. By doing so, the damaged stiffness tensor $\mathbf{C}^{\mathrm{SEL,d}}_{\mathrm{TBDC}}$ is obtained as [67]:

$$\mathbf{C}^{\mathrm{SEL,d}}_{\mathrm{TBDC}} = \begin{bmatrix} d_{\mathrm{L}}^2 C^{\mathrm{SEL}}_{11,\mathrm{TBDC}} & d_{\mathrm{L}} d_{\mathrm{T}} C^{\mathrm{SEL}}_{12,\mathrm{TBDC}} & d_{\mathrm{L}} d_{\mathrm{Z}} C^{\mathrm{SEL}}_{13,\mathrm{TBDC}} & 0 & 0 & 0 \\ & d_{\mathrm{T}}^2 C^{\mathrm{SEL}}_{22,\mathrm{TBDC}} & d_{\mathrm{T}} d_{\mathrm{Z}} C^{\mathrm{SEL}}_{23,\mathrm{TBDC}} & 0 & 0 & 0 \\ & & d_{\mathrm{Z}}^2 C^{\mathrm{SEL}}_{33,\mathrm{TBDC}} & 0 & 0 & 0 \\ & & & d_{\mathrm{TZ}} C^{\mathrm{SEL}}_{44,\mathrm{TBDC}} & 0 & 0 \\ & sym. & & & d_{\mathrm{ZL}} C^{\mathrm{SEL}}_{55,\mathrm{TBDC}} & 0 \\ & & & & & d_{\mathrm{LT}} C^{\mathrm{SEL,p}}_{66,\mathrm{TBDC}} \end{bmatrix} \tag{5.17}$$

where:

$$d_L = 1 - D_{11}, \qquad d_T = 1 - D_{22}, \qquad d_Z = 1 - D_{33},$$
$$d_{\mathrm{TZ}} = \left(\frac{2d_{\mathrm{T}}d_{\mathrm{Z}}}{d_{\mathrm{T}} + d_{\mathrm{Z}}}\right)^2, \qquad d_{\mathrm{ZL}} = \left(\frac{2d_{\mathrm{Z}}d_{\mathrm{L}}}{d_{\mathrm{Z}} + d_{\mathrm{L}}}\right)^2, \qquad d_{\mathrm{LT}} = \left(\frac{2d_{\mathrm{L}}d_{\mathrm{T}}}{d_{\mathrm{L}} + d_{\mathrm{T}}}\right)^2 \tag{5.18}$$

The damaged stiffness tensor $\mathbf{C}_{\mathrm{TBDC}}^{\mathrm{SEL,d}}$ is then rotated back to CSYS$^{\mathrm{g}}$, where the new global stress state is calculated.

The implementation of the material model used in the proposed stochastic FE framework was done via a UMAT, and is summarised in Fig. 5.8.

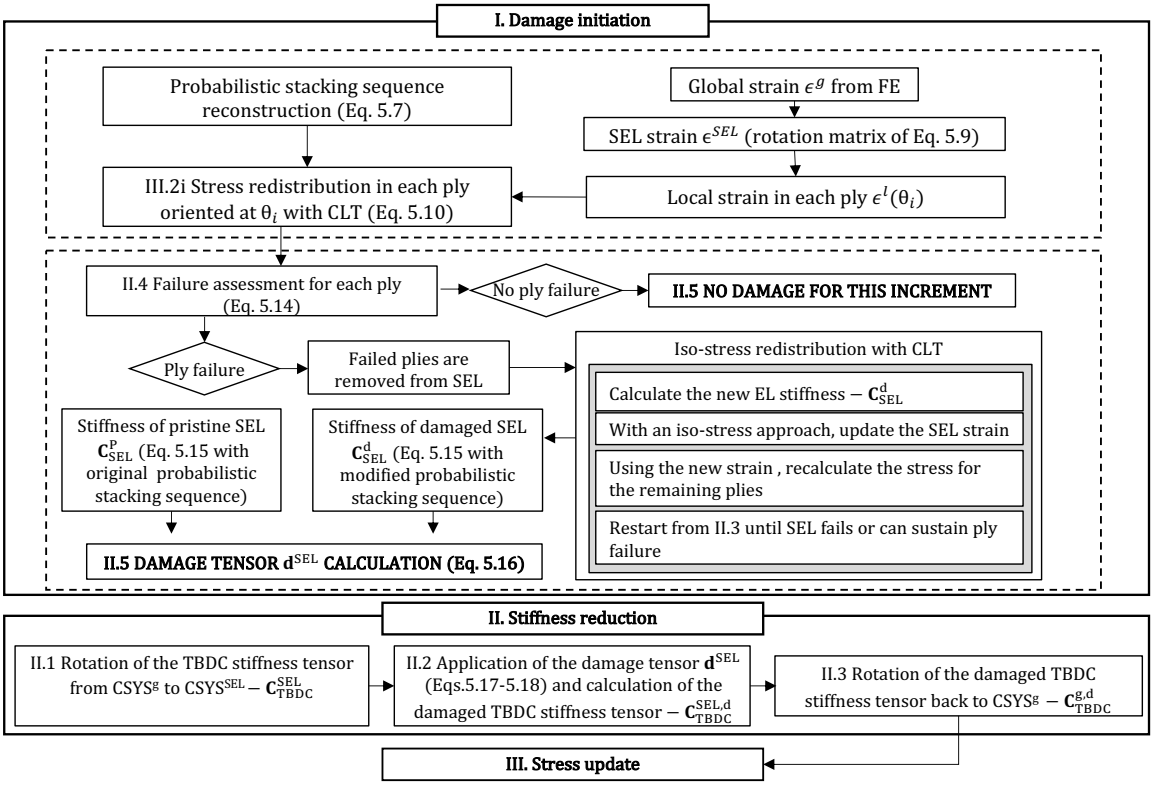

Figure 5.8: Implementation flowchart of the UMAT used in the stochastic FE framework.

5.4 Results

The proposed stochastic FE framework is validated against experimental tensile tests of the two materials presented in Section 5.2. The results of the stochastic FE framework are also compared to a deterministic FE approach, in which the fibre orientation tensors that result from a process simulation are directly mapped to the FE structural mesh (as shown in Figure 5.1), with no stochastic process involved. The

material properties used as inputs are summarised in Table 5.3, and the specimen geometries and numerical inputs are summarised in Table 5.2.

Table 5.2: Specification of the geometry and number of the tested specimens and of the numerical inputs.

Material	l^{s} (mm)	w^{s} (mm)	t^{s} (mm)	N^{t}	$\Delta\theta$ (°)
HexMc M77[†]	138	50	3.0	24	10
CF-SMC[‡]	150	25	2.5	15	10

[†] 10 specimens were tested for HexMC-M77.

[‡] 6 specimens were tested for the 0°, 45° and 90° CF-SMC configurations.

Table 5.3: Tow material properties used as model inputs. Modulus values are in GPa, strength values are in MPa, toughness values are in kJ/m^2.

Material	E_1^{t}	E_2	G_{12}	ν_{12}	$X_{\mathrm{T}}^{\mathrm{t}}$	Y_{T}	Y_{C}	S	X_z	S_z	$\mathcal{G}_{\mathrm{int}}^{\mathrm{IIc}}$
HexPly-M77 [50]	129[†]	9.0[*]	5.6[*]	0.34[*]	1258[†]	73[*]	200[*]	78[*]	73[*]	78[*]	0.8[†]
CF-SMC tows [68]	98	5.6	2.1	0.34	895	35	180	40	35	40	1.0[*]

[†] Values taken from uni-axial tensile tests of the UD material system, and linearly scaled to the fibre content of the respective TBDC material system.

[*] Estimated values based on the literature [35].

5.4.1 Analysis and characterisation of the strain variability

The variability of the strain fields obtained with the deterministic and stochastic FE models are here compared to the variability of strain fields measured with DIC from HexMC-M77 specimens, presented in Chapter 4. Figure 5.9a compares the predicted strain distribution to the one measured with DIC. It is found that the deterministic approach is not able to capture the correct strain distribution, whereas the stochastic approach recreates a similar strain distribution to those measured with DIC. The spatial length-scales of the strain fields are compared in Figure 5.9b, using the method based on the triangulation of peaks and troughs, proposed in Chapter 4. Once again, the deterministic FE approach fails to predict the spatial features of the strain fields, which is well reproduced by the stochastic FE approach. The characteristic length-scale ($\bar{s}_{\mathrm{ls}}$) of the strain fields obtained with the stochastic FE approach is in good agreement with that of the DIC strain fields. In contrast, the average length-scale of the strain fields predicted by the deterministic approach are significantly smaller than that of the DIC strain fields; this shows that this approach does not accurately reflect the influence of the microstructural features of the material.

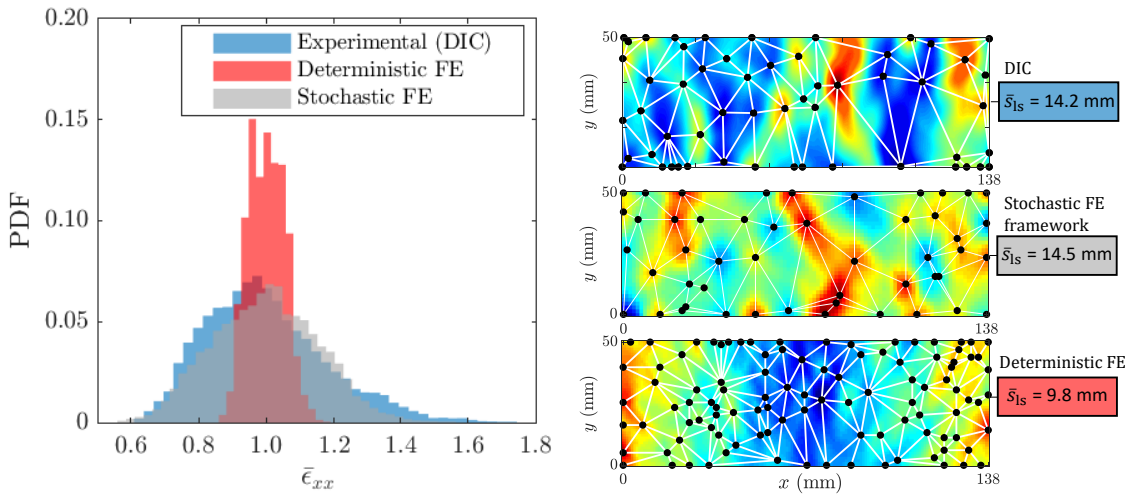

(a) Distribution of the normalised strain values.

(b) Representation of the characteristic length scales.

Figure 5.9: Analysis of the variability of the FE (deterministic and stochastic) and DIC strain fields for the HexMC-M77 material.

Figure 5.10 compares fields of different properties of a virtually generated specimen with the stochastic FE approach. It is shown that field of failure indices (F_{I}) , shown in Figure 5.10a, strongly depends on the longitudinal strain ϵ_x (Fig. 5.10b), which in turn is correlated with the field of $\bar{a}_{11}$ (Fig. 5.10c), where regions dominated by transverse fibre orientations present higher strains. The model thus captures correctly the TBDCs tendency to fail in high strain regions, as it was experimentally demonstrated by DIC investigations reported in the literature [9,66,69]. In contrast, the longitudinal stress field S_x (Fig. 5.10d) is not significantly correlated to the F_{I} field. Moreover, Figures 5.10e and 5.10f show the contribution of the in-plane and out of plane failure indices to the overall failure index F_{I}; as expected for the specimen geometry, the in-plane failure has the most dominant contribution to the failure prediction. This analysis demonstrates the importance of capturing the accurate variability of the field material properties to predict the mechanical response of TBDC material system.

Figure 5.11a shows the statistical distribution of the stochastic term $\bar{a}_{11}$(taken from the seed points of a virtual specimen) as a function of N^{t}. For values of $N_{\mathrm{t}} \leq 20$ there is a large scatter of $\bar{a}_{11}$ values, with the lower values defining the regions with dominant transverse fibre orientations (relative to the loading direction), and hence corresponding to weaker regions within the specimen. Figure 5.11b shows the resulting influence of N^{t} on the predicted average strength and standard deviation of 10 virtual specimens. It is shown that lower values of N^{t} lead to lower average predicted strength values with a higher standard deviation, and higher N^{t} values lead to higher strength values with a narrower standard deviation.

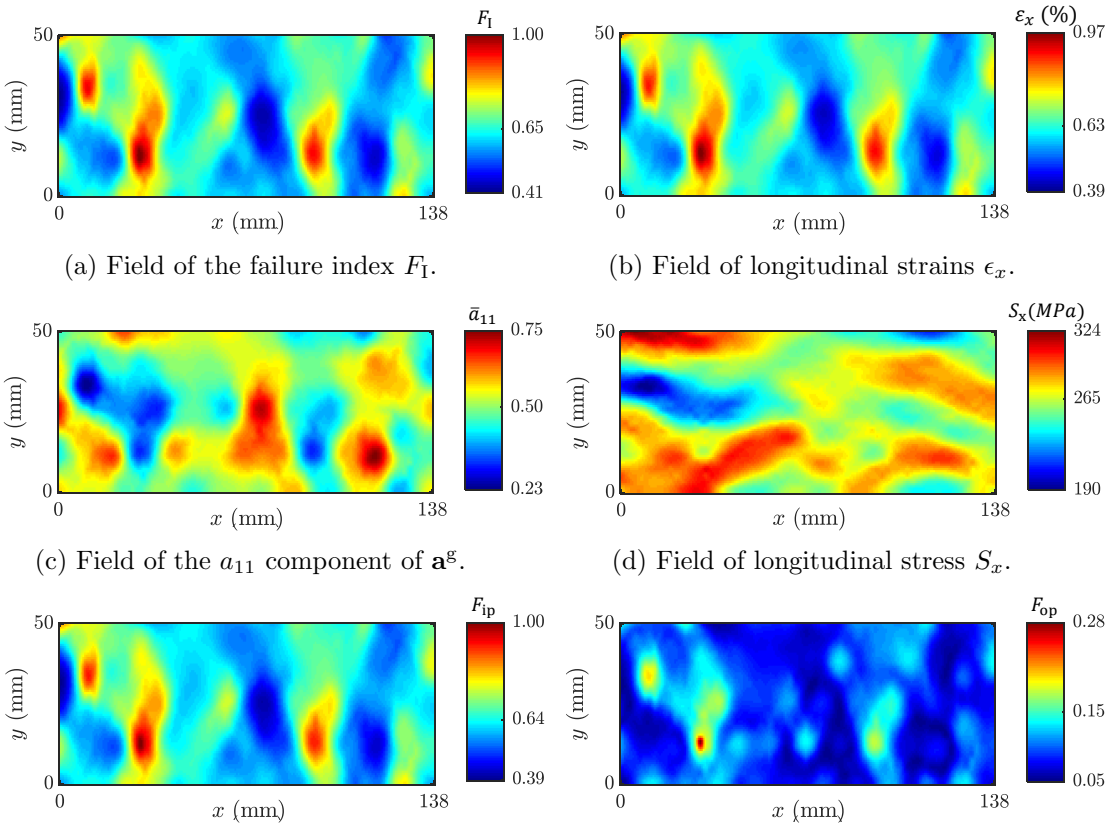

(a) Field of the failure index F_{I}.

(b) Field of longitudinal strains ϵ_x.

(c) Field of the a_{11} component of $\mathbf{a}^{\mathrm{g}}$.

(d) Field of longitudinal stress S_x.

(e) Field of the in-plane failure index F_{ip}.

(f) Field of the out of plane failure index F_{op}.

Figure 5.10: Fields of outputs obtained with the stochastic FE framework for a HexMC-M77 specimen.

5.4.2 Sensitivity to the mesh size and to numerical input parameters

Figures 5.12a and 5.12b show the influence of the mesh size used in the stochastic FE simulations, on the predicted stress-strain response and ultimate strength. For this analysis, the same specimen generated with the stochastic FE framework was discretised into different element sizes. For the smallest element size (0.5 mm), the load drop after failure of the virtual specimen was captured. This was no longer true for increasing element size, due to numerical convergence issues close to final failure. Therefore, for the remaining results of the FE simulations presented in this chapter, an element size of 0.5 mm was used.

The in-plane angle spacing $\Delta\theta$ was introduced as numerical parameter in the construction of the SEL (Section 5.3.2.1). Using the HexMC-M77 simulations, Figure 5.12c shows that the variation of the angle spacing $\Delta\theta$ has limited effect on the model accuracy; however, Figure 5.12d shows that computation time required increases expo-

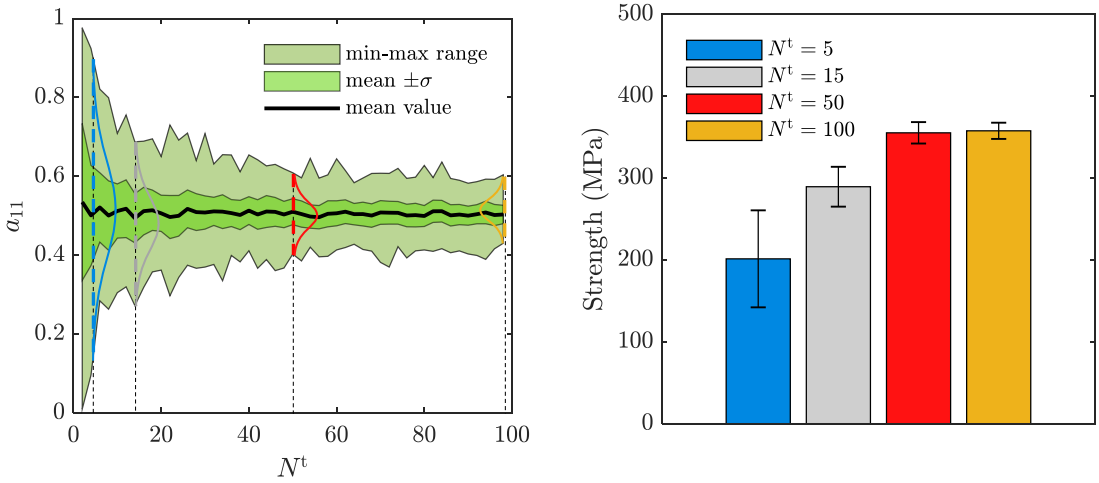

(a) Convergence of $\bar{a}_{11}$ with N^t.

(b) Effect of N^t on predicted ultimate strength.

Figure 5.11: Influence of N_t on the predictions of the stochastic FE framework for the HexMC-M77 material system.

nentially for finer angle discretisations. For all the FE simulations a value of $\Delta\theta = 10°$ was used.

5.4.3 Model results and validation against experiments

In this Section, the results of the stochastic framework are compared to the experimental tensile testes of the two materials described in Section 5.2 and to the results obtained with a deterministic FE approach. For each material system tested, a process simulation of a plate was performed (see Appendix C for more details). For the deterministic FE approach, the fibre orientation tensors were mapped to an FE mesh (with the respective specimen geometry, specified in Table 5.2); for the stochastic FE approach, the orientation tensors were mapped to the seed points of the FE mesh (with the same specimen geometry). Therefore, only one simulation is performed for the deterministic approach, and the number of simulations performed with the stochastic approach was the same as the number of specimens tested.

In Figure 5.13, the results predicted with both the deterministic and stochastic FE approaches are compared to the experimental results of the CF-SMC specimens with different preferential fibre orientations. The strength and stiffness predictions of the stochastic FE approach are in good agreement with the experimental results, whereas the deterministic FE approach, despite being able to predict accurate stiffness values, over-predicts the strength, in particular for the 45° and 90° specimens.

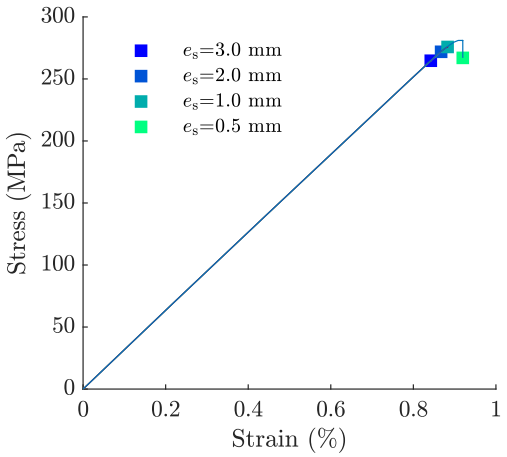

(a) Predicted stress-strain responses for different mesh sizes.

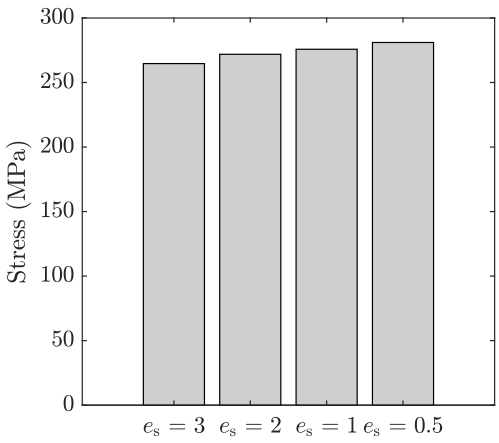

(b) Ultimate strength predicted for different mesh sizes.

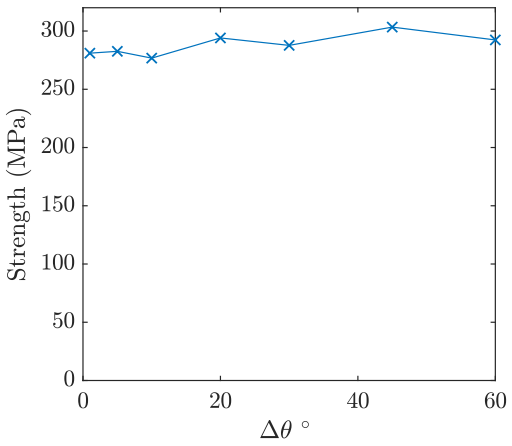

(c) Effect of $\Delta\theta$ on the predicted ultimate strength.

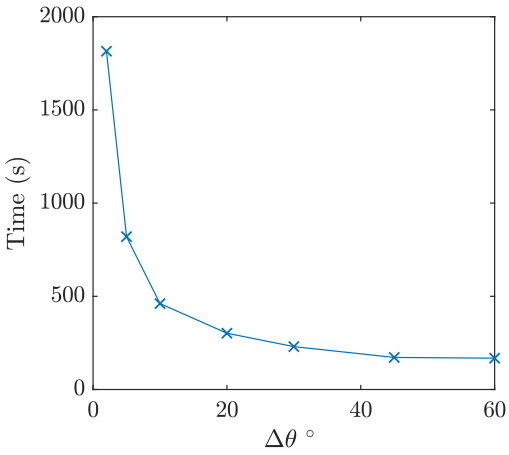

(d) Effect of $\Delta\theta$ on the simulation time.

Figure 5.12: Effects of numerical parameters on the predictions and efficiency of the framework for a given HexMC-M77 virtual specimen.

The predictions of both FE approaches are compared to the experimental results of the HexMC-M77 specimens (with $t^t = 0.125$ mm) in Figures 5.14a and 5.14b. Once again it is shown that the lack of variability in mechanical properties of the deterministic approach leads to over-predictions of the specimens' mechanical properties. On the other hand, the realistic variability included in the stochastic FE approach leads to more accurate predictions. The same HexMC-M77 material system but with a tow thickness of $t^t = 0.285$ mm has been tested and reported in the literature [15]. In Figure 5.14c, the strength and stiffness predictions with both FE approaches are compared to the experimental results reported in [15], where once again good predictions are obtained with the stochastic FE approach.

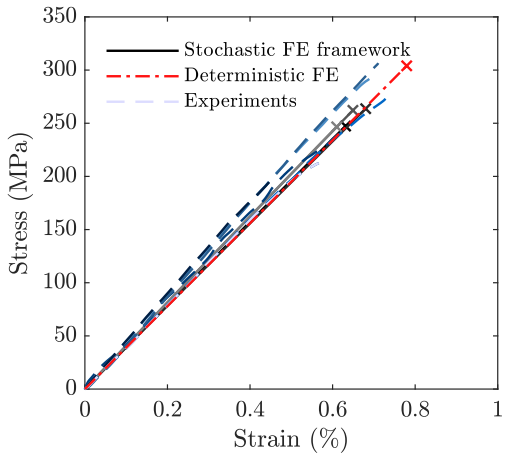

(a) Predicted and experimental stress strain curves for the 0° CF-SMC specimens.

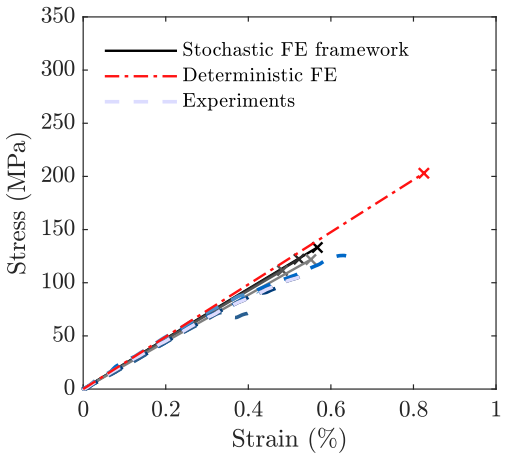

(b) Predicted and experimental stress strain curves for the 45° CF-SMC specimens.

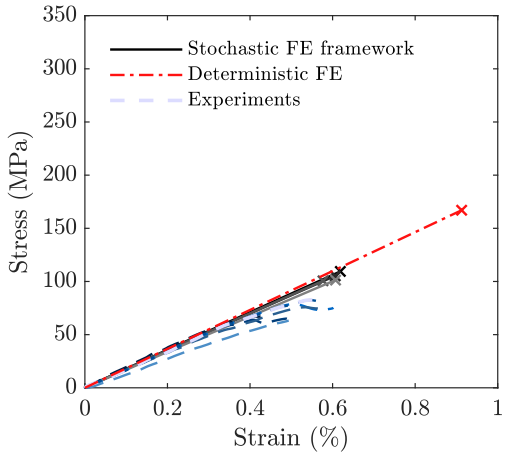

(c) Predicted and experimental stress strain curves for the 90° CF-SMC specimens.

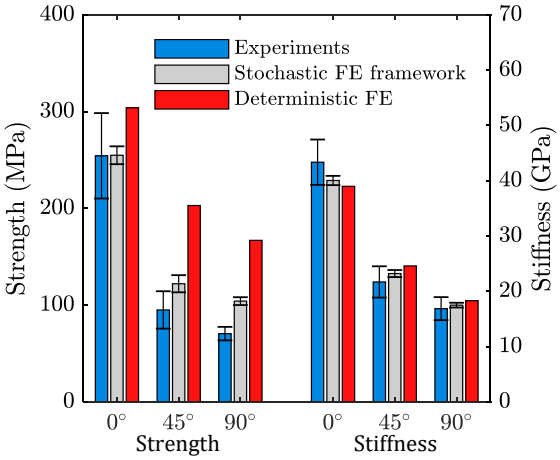

(d) Predicted and experimental strength and stiffness for all the CF-SMC specimens

Figure 5.13: Validation of the stochastic FE framework against the experimental results of the CF-SMC.

5.5 Discussion

5.5.1 Reproducing the stochastic nature of TBDCs and the problem with the deterministic process simulation software

The implicit description of the material's microstructure, in the deterministic FE approach, is directly linked to the local orientations tensors that result from process simulations. It was shown in Figure 5.9b that the spatial length-scales in the strain fields predicted by this approach do not reflect the characteristic length-scales of the material's microstructure (which is dependent on the tow geometry). Moreover, the

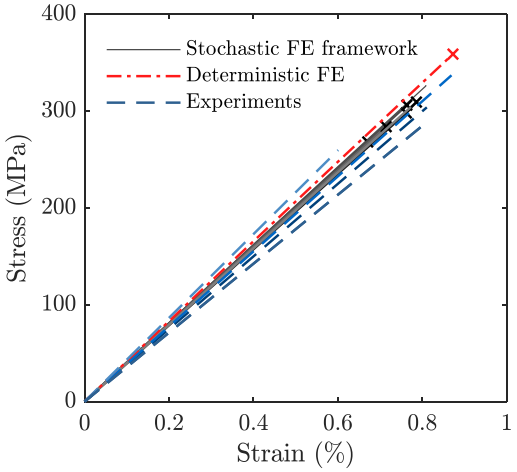

(a) Predicted and experimental stress strain curves for the HexMC-M77 (t^{t} = 0.164 mm).

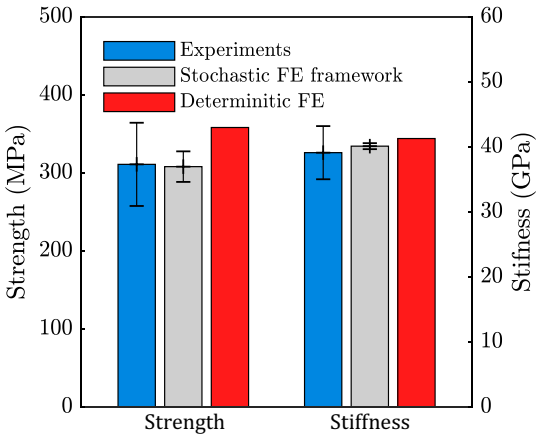

(b) Predicted and experimental strength and stiffness for the HexMC-M77 ($t^{\mathrm{t}} = 0.125$ mm).

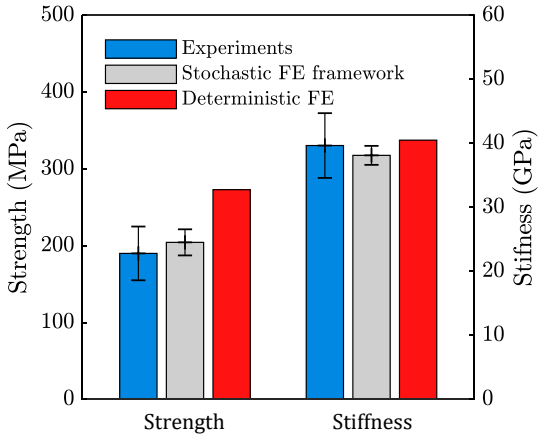

(c) Predicted and experimental strength and stiffness for the HexMC-M77 ($t^{\mathrm{t}} = 0.285$ mm) [15].

Figure 5.14: Validation of the stochastic FE framework against the experimental results of the HexMC-M77.

quantitative strain variability of the deterministic FE approach is significantly lower than that of the DIC strain fields. For this reason, and since failure of the material is associated to local strain peaks [66], as shown in Figure 5.10, the deterministic approach constantly over-predicts the strength of these materials.

The stochastic framework is able to capture more realistic strain peaks (which correspond to areas with tows more aligned in the transverse direction to the load); this is the consequence of the random sampling of orientations from the planar FODs, with the number of samples equal to the average tow count N^{t} along the thickness of the specimens. The influence of N^{t} on the predicted strength is shown in Figure 5.11b,

were it was shown that higher average strength values result from a higher tow count, which reduces the probability of local weak spots in the material that trigger premature failure, as shown in Figure 5.11a. This is in agreement with what has been reported in the literature [10, 16], on the effect of the specimen thickness on the material strength.

The stiffness predictions of both FE approaches are very similar and both are in good agreement with the experimental results. This is due to the fact that stiffness is mainly governed by the average fibre orientation state, rather then local features in the microstructure, and therefore the inherent local material variability does not play a significant role in the average stiffness. This shows that despite process simulations not being able to capture local material variability, they are able to predict the average fibre orientation state in a specimen. Moreover, in the stochastic FE approach, the orientation tensors that are mapped to the seed points (from the process simulation) and converted to stochastic orientation tensors, still preserve the original average orientation state; this was confirmed by the accurate stiffness predictions obtained.

5.5.2 Novelty and potential impact

The stochastic FE framework presented in this work is able to include fibre orientation tensors (that results from process simulations) in structural FE simulations, while still being able to reproduce the intrinsic variability of TBDC material systems. A failure criterion is used in combination with a ply discount method to predict final failure of the material. The implementation of the FE framework offers the efficiency and flexibility to model both simple and complex geometries, and perform Monte Carlo analysis to obtain the stochastic dominated response. Moreover, enabling the link between structural simulations and the manufacturing process can allow for the evaluation and optimisation of the charge patterns (used in the compression moulding process) that maximise the performance of a specific component; this can help engineers to manufacture more efficient and reliable TBDC structures and which comply with specific design allowables.

Capturing the variability in material systems with heterogeneous microstructures is essential to predict their mechanical properties. The applicability of this framework can also be extended to other material systems with such an heterogeneous microstructure; the modular implementation of the framework allows for the use of other material models (suitable for a particular material systems), enabling its use to model/predict the mechanical properties of a wider range of materials.

5.6 Conclusions

This work presents a FE framework to model the stochastic behaviour of TBDC material systems. Fibre orientation tensors resulting from flow simulations are integrated in the framework, and a failure criterion for an equivalent discontinuous ply is presented and combined with a ply-discount method to predict final failure. The main conclusions of this work are as follows:

- Using fibre orientations resulting from process simulations in a deterministic FE approach leads to inaccurate field of mechanical properties, both in terms of their quantitative variability and characteristic length-scales.
- Integrating the results from process simulations in the stochastic FE framework leads to accurate and representative field of mechanical properties, while still preserving the overall orientation state obtained with the process simulations.
- The framework was validated against experimental results of specimens of two different material systems loaded under tension: the HexMC-M77 (low flow) and a CF-SMC (with high flow, and three different preferential fibre orientations). The FE framework yielded accurate results, and was able to replicate the stochastic response of these materials.
- This is the first model in the literature with the flexibility to couple flow simulations and FE structural simulations in a stochastic process that assigns the realistic intrinsic material variability of the material system. The implicit representation of the microstructure of the material allows the framework to be used in an efficient way (compared to models with explicit representations of the microstructure), and to be scaled to larger and more complex models.

Chapter 6

Prediction and experimental validation of the notch (in)sensitivity of Tow Based Discontinuous Composites

6.1 Introduction

One unusual manifestation of intrinsic variability of TBDCs is the fact that notched specimens often fail in the un-notched region, and their strength is notch insensitive [56, 57]. This behaviour is caused by heterogeneities in the material microstructure, which can be seen as inherent material stress concentrations of a similar magnitude to the ones induced by geometrical notches, leading to specimen failure at material weak spots away from notches. TBDC components used in several industrial applications are often mechanically fastened to structures or to other components, and generally contain complex features which can act as notches/discontinuities in the material. For this reason, understanding the nature and being able to predict the material's notch sensitivity is of particular importance for industrial applications.

Feraboli et al. [56] carried out an experimental study to investigate the effect of the notch size on the mechanical response of TBDC open hole specimens, both under tension and compression. The authors reported a linear reduction of the gross strength with the increased notch diameter, thus demonstrating the notch insensitive behaviour of the material. The definition of an inherent material stress concentration was used to justify the tendency of the material to fail away from the notched regions, on the basis that these inherent material stress concentrations could be equal or larger to those

induced by geometrical notches. Qian et al. [57] also carried out open hole tensile tests in specimens manufactured with a Direct Carbon Fibre Preforming (DCFP) process, and studied the effect of notches with different diameters for both specimens with a constant width and with a constant hole-to-width ratio. The authors compared the experimental results of the DCFP specimens with those of Non Crimp Fabric (NCFs) and found that the DCFP material was notch insensitive, in contrast to the NCFs, which were found to be notch sensitive.

Some models, based on semi-empirical fracture criteria, have been presented in the literature [70–73] to predict the strength reduction of composites with geometrical notches. Whitney and Nuismer [70] have presented two stress based fracture criteria: (i) Point Stress Criterion (PSC), which assumes that the material fails when the stress at a characteristic distance ahead from the notch is equal or greater the the un-notched strength; and (ii) Average Stress Criterion (ASC), which assumes that failure occurs when the average stress over a characteristic distance ahead of the notch is equal or greater the un-notched strength. Pipes et al. [71] suggested a power law to represent the dependency of the characteristic distance on the notch geometry and the material's notch sensitivity, which is determined experimentally for each material system. These semi-empirical fracture criteria have been used [56,57] to predict the notched strength of TBDC material systems, and yielded predictions in good agreement with experimental results.

Nonlocal theories were originally developed for the description of linear elastic heterogeneous materials [74] and are often applied to linear elastic fracture mechanics problems in order to address the stress singularity that occurs at a crack tip [75]. This is achieved by evaluating the stress at each point based on weighted averages, governed by nonlocal functions, in the vicinity of that point. These nonlocal theories can also be included in a continuum damage mechanics approach, as this method allows for a well-established boundary value problem when modelling strain softening material behaviours. Pijaudier-Cabot et al. [76] proposed a nonlocal formulation to describe the evolution of damage in finite element analysis. In this formulation, the nonlocal damage at each point is obtained using a weighted average of stress concentrations in the vicinity of the point. Non-local methods have the advantage of being mesh insensitive [76] are more efficient than other continuum damage approaches and are relatively simple to implement in a FE framework. Nonetheless, similarly to semi-empirical fracture criteria, these methods also require parameters to be determined experimentally.

In this chapter the notch-sensitivity of the HexMC-M77 TBDC material system is experimentally characterised, for both circular and modified notch geometries. A large experimental campaign, detailed in Section 6.2, was carried out, where several specimens with different notch configurations were tested under longitudinal tension.

A proposed numerical method based on a nonlocal average of fields of failure indices, detailed in Section 6.3, is developed to predict the notched behaviour of the material. In Section 6.4, the results of the proposed method are compared to those predicted using the stochastic FE framework presented in Chapter 5. The main results are discussed in Section 6.5 and the conclusions are drawn in Section 6.6.

6.2 Materials and experimental procedure

The TBDC material system used in this study is the HexMC-M77 [2]; the specification of the microstructural elements of the material can be found in Table 5.1. In order to assess the notch sensitivity of this material system, several un-notched and notched specimens were tested under longitudinal tension. The overall dimensions of the tested specimens were 250 x 50 x 3 mm (length l^s, width w^s, thickness t^s) with a gauge section of 138 mm. Two different studies were conducted in order to separate the effect of the reduced net cross-sectional area (due to the presence of the notch) and the stress concentration factor induced by the notch:

i) open hole specimens, with circular notches with diameters varying from 4 to 12 mm; in this study, the notch sensitivity is mainly influenced by the gradual cross-sectional area reduction as the hole diameter increases with a constant specimen width.

ii) modified notched specimens, with different notch geometries; in this study, the notch sensitivity is assessed for different values of the stress concentration factor induced by different notch geometries, while keeping the net cross-sectional area the same for all specimens.

The un-notched and notched specimens were tested according to the ASTM-D3039 and ASTM-D5766 standards respectively, with a displacement rate of 1 mm/min. Table 6.1 summarises the experimental plan carried out, specifying the number of specimens tested for each configuration.

Figure 6.1 shows the geometry of the different notched specimens tested experimentally. The red regions in the specimens confine the the area in which any failure occurrence is assumed to be a failure due to the presence of the geometrical notch; this region was also used for the classification of the failure location used in the numerical analyses presented in Section 7.3.

Table 6.1: Experimental plan - specification of the number of un-notched and notched specimens tested.

Specimen ID	Specimen description	Number of tested specimens
UN	Un-notched	10
OH-4	open-hole diameter = 4 mm	10
OH-6	open-hole diameter = 6 mm	15
OH-7	open-hole diameter = 7 mm	15
OH-8	open-hole diameter = 8 mm	15
OH-10	open-hole diameter = 10 mm	15
OH-12	open-hole diameter = 12 mm	10
SN	slotted notch	10
RN	sharp notch	10

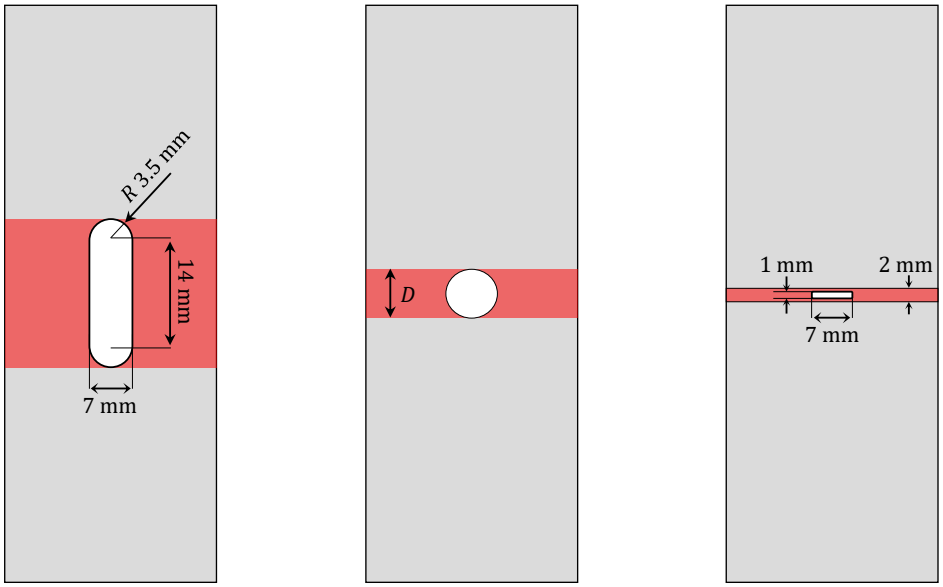

(a) Slotted notch. (b) Circular notch. (c) Sharp notch.

Figure 6.1: Geometry specification of the water jet cut notched specimens; the red shaded area encloses the hole/notch failure region.

6.3 Failure analysis

The stochastic FE framework presented in Chapter 5 is here used to predict the notch sensitivity of the HexMC-M77 material system. Final failure will be predicted using two different approaches: (i) using the stiffness reduction scheme based on the ply discount method (described in Chapter 5), and (ii) using an alternative approach based on the nonlocal average of damage initiation, as presented in Section 6.3.1.

6.3.1 Nonlocal failure index averaging

In this proposed method, failure is predicted based on the extent of damage initiation. Therefore, the stochastic FE framework of Chapter 5 is used to generate fields of the failure indices F_{I}, calculated using a first-ply failure criteria. For each element of the structural mesh, the associated stacking sequence (reconstructed from the associated stochastic orientation tensor) is obtained, and for a generic stress state $\boldsymbol{\sigma}$, the value of F_{I} is given by that of the critical ply. Since no stiffness reduction scheme is used, these F_{I} fields are obtained from linear elastic simulations.

Figure 6.2a shows an example of a local field of failure indexes $F_{\mathrm{I}}(x, y)$ from one iteration of the stochastic FE framework. The nonlocal average of the local $F_{\mathrm{I}}(x, y)$ field is obtained by a weighted average, governed by a nonlocal weight function Ψ (see Figure 6.2b) defined over an integration domain A, within a spatial vicinity of each point (x, y). In a similar approach to Eringen's nonlocal elasticity theory [74], considering $\xi = (x, y)$ as a generic point in the F_{I} field, and $\xi' = (x', y')$ a point in its vicinity at a distance of $\bar{\xi} = |\xi - \xi'|$, the nonlocal $\bar{F}_{\mathrm{I}}(x, y)$ field is given by

$$\bar{F}_{\mathrm{I}}(x, y) = \int_A \Psi(\bar{\xi}) F_{\mathrm{I}}(\xi') d\xi', \tag{6.1}$$

where $\Psi(\bar{\xi})$ is the nonlocal weight function. The nonlocal averaging scheme should not alter a uniform field. Therefore, following the same approach as in [77], the nonlocal weight function $\Psi(\bar{\xi})$ must satisfy the condition

$$\int_A \Psi(\bar{\xi}) d\xi' = 1 \quad \forall \xi \in A, \tag{6.2}$$

which requires the normalisation of the nonlocal function by its integral over domain A,

$$\Psi(\bar{\xi}) = \frac{\Psi_0(\bar{\xi})}{A_0} = \frac{\Psi_0(\bar{\xi})}{\int_A \Psi_0(\bar{\xi}) d\xi'}, \tag{6.3}$$

where A_0 is the reference area affected by the nonlocal averaging and $\Psi_0(\bar{\xi})$ is the basic nonlocal weight function, which is here assumed to be defined by a Gaussian distribution function,

$$\Psi_0(\bar{\xi}) = \exp\left[- \left(\frac{\bar{\xi}^2}{2 \cdot {l_{\mathrm{nl}}}^2} \right) \right], \tag{6.4}$$

with l_{nl} representing the characteristic length of the nonlocal continuum.

The reference area A_0 over which the nonlocal averaging is performed is here chosen to be related to the material's microstructure. Ko et al. [78] investigated size effects on the fracture behaviour of TBDCs and used Bazant's size effect law [79] to relate the nominal strength of the specimens with a characteristic size, taken as the width of the

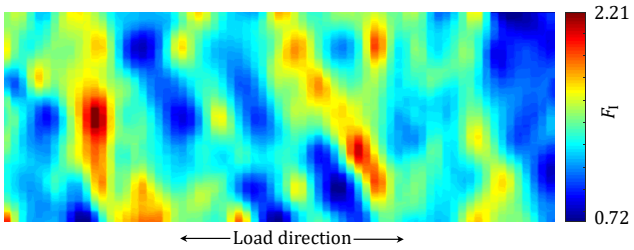

(a) Local F_I field resulting from a linear elastic FE analysis.

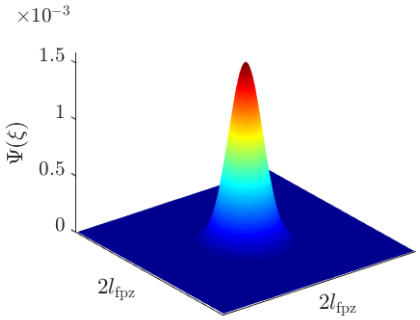

(b) Nonlocal function, $l_{nl} = 2$ mm.

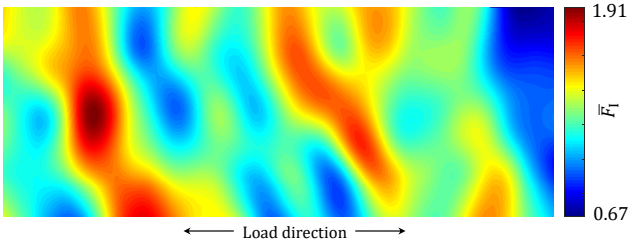

(c) Nonlocal $\bar{F}_I$ field.

Figure 6.2: Nonlocal averaging scheme on the resulting F_I field obtained with the stochastic FE framework.

specimen. The authors derived the size effect curves for TBDCs with different tow geometries, and derived the fracture energy and the effective length of the fracture process zone (l_{fpz}) (based on linear elastic fracture mechanics) for each tow configuration. For a tow geometry of 50×8 mm, the authors reported an $l_{fpz} \approx 7.5$ mm. Therefore, the reference area A_0 is defined by a square with a side length of $2l_{fpz}$.

Some attention is required when performing the nonlocal averaging of the F_I field close to a physical boundary; if the nonlocal function $\Psi(\bar{\xi})$ is kept unchanged near the boundaries, the condition imposed in Eq 6.2 is violated. To overcome this limitation, a local compliment method is applied [80, 81], in which the weight of the points of the nonlocal function $\Psi(\bar{\xi})$ situated inside the boundary are adjusted to compensate for the missing contribution of points situated outside the boundary. This is mathematically represented by

$$\Psi(\bar{\xi}) = (1 - \frac{A_r(\xi)}{A_0})\delta(\bar{\xi}) + \frac{\Psi_0(\bar{\xi})}{A_0}, \tag{6.5}$$

where $\delta(\bar{\xi})$ is the Dirac function and the term $1 - \frac{A_r(\xi)}{A_0}$ defines the area of the points located inside the boundary.

The final failure of the material is triggered when a point within the nonlocal field $\bar{F}_{\mathrm{I}}$ has a value of $\bar{F}_{\mathrm{I}} = 1$.

6.4 Results

All the results shown in this section were obtained with the input properties of the HexMC-M77 material identified in Tables 5.1 and 5.3, unless stated otherwise. All the subsequent results obtained with the nonlocal averaging scheme result from 100 realisations of linear elastic simulations with the FE framework, and the ones obtained with the full stochastic FE framework (presented in Chapter 5) derive from 10 realisations of the framework.

6.4.1 Un-notched strength

Figure 6.3a shows the CDF of the strength of the un-notched specimens tested, as well as the predicted strength distribution with the FE framework for different values of l_{nl}. A more local averaging (i.e an averaging with lower value of l_{nl}) leads to an under-prediction of the strength distribution, and a more nonlocal approach (with larger value of l_{nl}) has the opposite effect leading to an over-prediction of the strength distribution. The nonlocal averaging parameter $l_{\mathrm{nl}} = 10$ mm is the one that shows the best agreement between the predicted and experimental strength distributions.

Figure 6.3b compares the un-notched average strength prediction of the stochastic FE framework and the nonlocal averaging method ($l_{\mathrm{nl}} = 10.0$ mm) with the experimental results of the un-notched HexMC-M77 specimen (with $t^{\mathrm{t}} = 0.125$ mm); moreover, the predictions are also compared to the experimental results presented in [15] where un-notched specimens manufactured with the same material system but with a tow thickness $t^{\mathrm{t}} = 0.285$ mm were tested under longitudinal tension. Both numerical methods yield good predictions when compared to the experiments. In addition, the predictions of the nonlocal averaging method for both material configurations (i.e. with different tow thicknesses) were obtained using the same value of l_{nl}.

6.4.2 Notch sensitivity analysis

6.4.2.1 Circular notches

Figure 6.4a shows the percentage of the tested open-hole specimens in which failure occurred near the hole, and the respective numerical prediction. The number of specimens tested for each hole diameter are presented in Table 6.1. In the subsequent

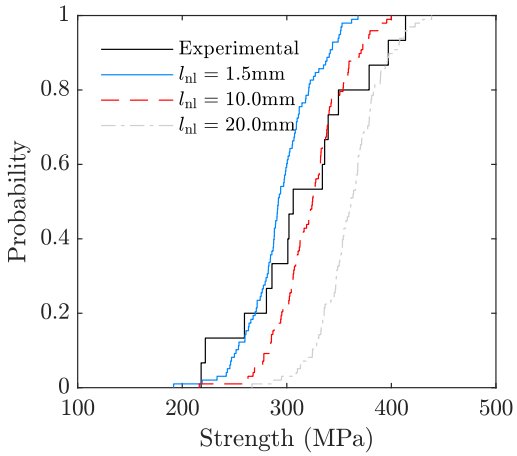

(a) Effect of the nonlocal parameter on the nonlocal FE predicted strength distributions; comparison against the experimental un-notched strength distribution.

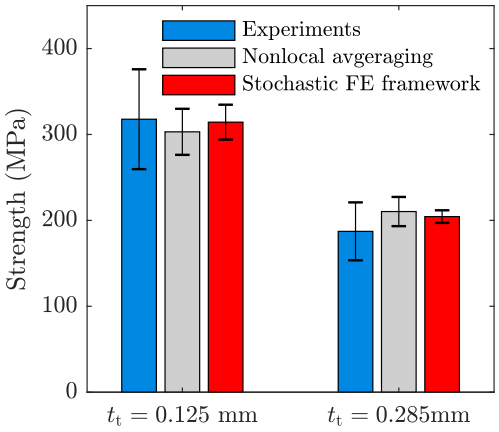

(b) Experimental results of the strength of TBDCs with different tow thickness, and comparison with the predictions of the nonlocal FE (l_{nl} = 10.0 mm) and stochastic FE framework.

Figure 6.3: Un-notched stiffness and strength: comparison between experimental results and numerical predictions.

results, a virtual failure is considered to be affected by the presence of a notch if the failure location, defined by the location of maximum value of $\bar{F}_I$, lies inside the red shaded region defined in Figure 6.1b. The uncertainty of the size of the failure location identified in the experiments and its effect on the numerical predictions is shown in Appendix D. Model predictions for different values of l_{nl} are presented in Figure 6.4a, where it is shown that a more local average (smaller values of l_{nl}) leads to a higher notch sensitivity in opposition to a more nonlocal average (larger values of l_{nl}). A value of l_{nl} = 1.5 mm yields very good agreement with the experimental results. Figure 6.4b shows both the measured and the predicted normalised gross strength for all the tested open hole configurations. The results are normalised by the respective measured and predicted un-notched strengths. The notch insensitivity of the TBDC material is clearly shown in both the experimental results as well as in the model predictions, as a linear decrease is the material's gross strength is verified for an increase in the hole diameter. This behaviour is significantly different to that of a continuous carbon fibre reinforced polymers, for which a sharp reduction in the gross strength is verified.

In Figure 6.4c the strength predictions of the stochastic FE framework (using a ply discount method to model stiffness degradation) are compared to the experimental results. It is found that this approach is not able to replicate the material behaviour, when notched geometries are considered, as the numerical predictions are significant different to the experimental observations.

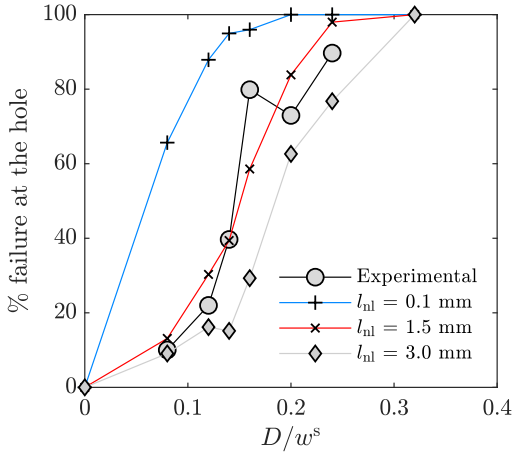

(a) Percentage of failures that occurred at the hole; nonlocal FE predictions for different values of l_{nl}.

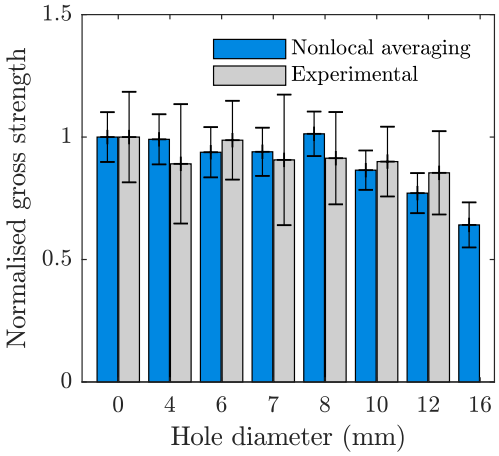

(b) Gross strength distributions (l_{nl} = 1.5 mm) - nonlocal FE and experimental results; error bars correspond to one standard deviation.

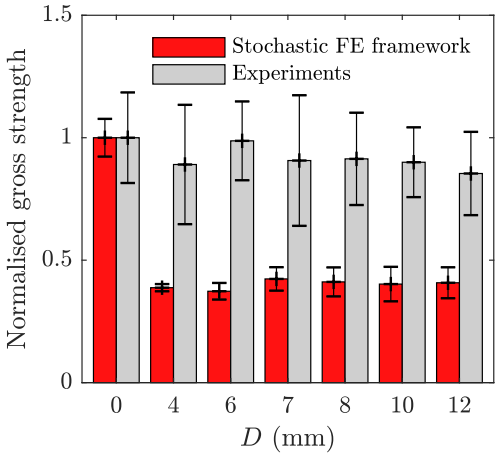

(c) Gross strength distributions (l_{nl} = 1.5 mm) - stochastic FE and experimental results; error bars correspond to one standard deviation.

Figure 6.4: Comparison between the notch sensitivity experimentally measured with the open-hole specimens and the numerical predictions. Gross strength distributions are normalised by the average strength of the un-notched specimens.

6.4.2.2 Modified notch geometries

Figure 6.5a shows the experimental strength distribution (fitted with a Weibull distribution) of specimens with different notch geometries: slotted, circular and sharp notches, with nominal stress concentrations k = 1.4, 2.7 and 5.7 respectively (calculated via FE models of specimens with homogeneous material properties). Since the net cross-sectional area was kept constant for the three notched configurations tested, the effect of the stress concentration factor (due to the notch geometry alone) can be assessed.

The experimental results show that considerable changes in the stress concentration factor do not lead to significant changes in the measured strength distributions of the material, which further highlights the notch insensitivity of TBDCs.

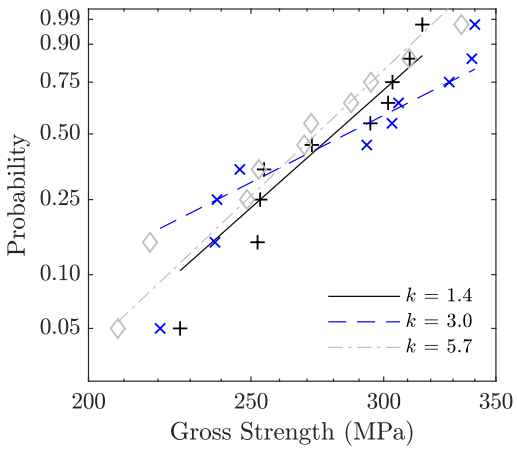

(a) Fitted Weibull distribution for the strength of the modified notched specimens.

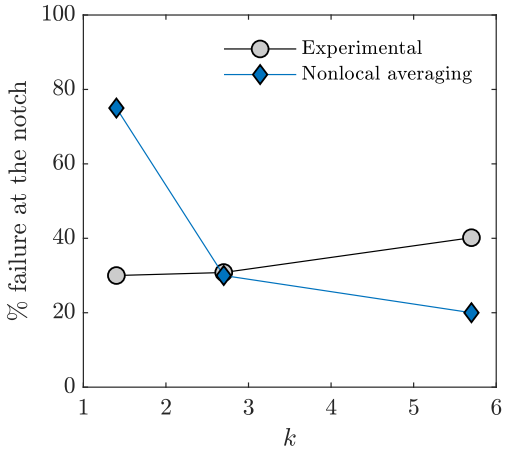

(b) Percentage of failures at the notch: experimental vs. nonlocal FE ($l_{\mathrm{nl}} = 1.5$ mm) results.

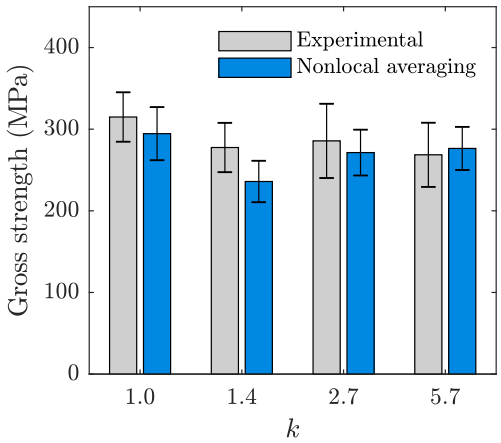

(c) Notched gross strength: experimental vs. nonlocal FE ($l_{\mathrm{nl}} = 1.5$ mm) results.

Figure 6.5: Strength distribution of the specimens with modified notch geometries, and the correspondent Weibull distribution fit; comparison between the notch sensitivity experimentally measured with the one predicted by the FE framework (constant nonlocal averaging) - (b) % failure at the notch and (c) gross strength distributions.

The percentage of specimens that failed near the notch obtained both experimentally and with the nonlocal averaging method ($l_{\mathrm{nl}} = 1.5$ mm) are shown in Figure 6.5b, with the correspondent gross strength shown in Figure 6.5c. The trends captured by the FE framework are significantly different from the ones observed in the experiments, as the model predicts a strength increase for higher values of k. The discrepancy between

the nonlocal averaging method and the experimental results is due to boundary effects near the notches during the nonlocal averaging of the F_{I} field. The extension of the region affected by stress concentrations, induced by the notch, is different for each notch geometry considered. For sharp notch configurations, high stress concentration values are localised in a small region near the notch tips; on the other hand, the lower stress concentrations induced by the slotted and circular notch configuration extend along larger regions around the notch. This suggests that the nonlocality (controlled by the value of l_{nl}) during the nonlocal averaging should be adjusted based on the local stress concentration, which in turn is related to the notch geometry. Regions with high-stress concentrations, due to the presence of sharp notches, require a more local averaging (with smaller values of l_{nl}) and vice-versa.

The magnitude of the gradients of the local failure index field $|\nabla F_{\mathrm{I}}(x,y)|$, calculated as

$$|\nabla F_{\mathrm{I}}(x,y)| = \sqrt{\Big(\frac{\partial F_{\mathrm{I}}(x,y)}{\partial x}\Big)^2 + \Big(\frac{\partial F_{\mathrm{I}}(x,y)}{\partial y}\Big)^2}, \tag{6.6}$$

is here used derive a relation between the value of l_{nl} and k. The average magnitude of $|\nabla F_{\mathrm{I}}|$ within a window of area A_0, here referred to as $|\nabla \bar{F}_{\mathrm{I}}|$, is used to reflect the influence of the stress concentration k induced by the geometric notch. Figure 6.6a shows how the average magnitude of $|\nabla \bar{F}_{\mathrm{I}}|$ near the boundary of the notches (i.e with a window A_0 centred at the respective notch) is influenced by the local stress concentrations. This analysis was done for 100 virtual specimens of each notch and un-notched configuration; the horizontal dashed lines in Figure 6.6a correspond to the average value of $|\nabla \bar{F}_{\mathrm{I}}|$ for each configuration. It is shown that a clear correlation between k and $|\nabla \bar{F}_{\mathrm{I}}|$ exists, with higher values of k leading to higher averages of $|\nabla \bar{F}_{\mathrm{I}}|$. This allows one to adjust the nonlocality of Ψ_0 based on the local values of $|\nabla \bar{F}_{\mathrm{I}}|$ within the field of failure indices $F_{\mathrm{I}}(x,y)$.

The optimal value of l_{nl}, for each notched configuration, is calibrated by comparing the FE predictions (using the conventional nonlocal averaging, i.e. with a constant l_{nl}) that yield better agreement with the experimental results (shown in Figures 6.5b and 6.5c), both in terms of gross strength, and percentage of failure at the notch. The optimal values of l_{nl} for each notch type (k) are summarised in Table 6.2. Finally, the relation between l_{nl} and $|\nabla \bar{F}_{\mathrm{I}}|$ is shown in Figure 6.6b, where a power law was used generalise the relation between the two parameters. The new nonlocal function $\Psi_0(\bar{\xi})$ can now be written as

$$\Psi_0(\bar{\xi}) = \exp\left[-\left(\frac{\bar{\xi}^2}{2 \cdot l_{\mathrm{nl}}(|\nabla \bar{F}_{\mathrm{I}}|)^2}\right)\right], \tag{6.7}$$

were l_{nl} is now dependent on the value of $|\nabla \bar{F}_{\text{I}}|$, which in turn is calculated for the entire domain of $F_{\text{I}}(x, y)$. Using the nonlocal function of Eq. 6.7 combined with Eq. 6.1, an adaptive nonlocal averaging scheme is derived.

Table 6.2: Table of values relating k with $|\nabla \bar{F}_{\text{I}}|$ and l_{nl}.

k	$\lvert\nabla \bar{F}_{\text{I}}\rvert$	l_{nl} (mm)
1.0	0.087	10.0
1.4	0.215	4.5
2.7	0.350	1.5
5.7	0.620	0.9

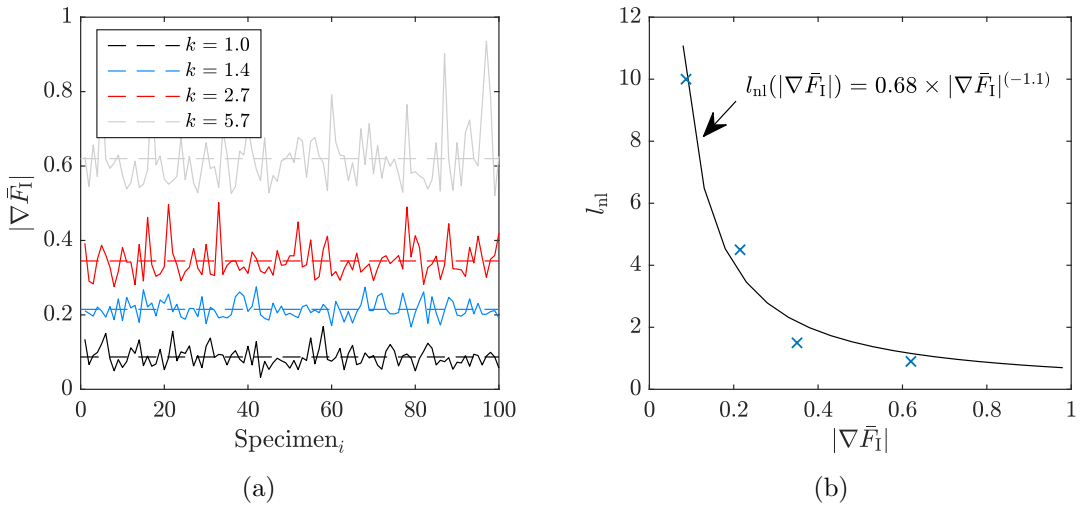

(a) (b)

Figure 6.6: Relation between: (a) the value of $|\nabla \bar{F}_{\text{I}}|$ and the stress concentration factor k; (b) the internal length parameter l_{nl} and the $|\nabla \bar{F}_{\text{I}}|$.

In Figure 6.7, the nonlocal field $\bar{F}_{\text{I}}$ near the boundaries of a sharp notch obtained with both the standard (i.e with a constant l_{nl}) and the adaptive nonlocal averaging scheme are compared; one can see that the with the adaptive approach, the local regions of high F_{I} values near the notch tips are preserved, whereas with the standard approach this is not the case. The numerical results obtained with the adaptive nonlocal averaging scheme are presented in Figures 6.8a and 6.8b; coupling the FE framework with the adaptive nonlocal averaging scheme yields results with much better agreement with the experimental ones, both in terms of percentage of notch failure and gross strength.

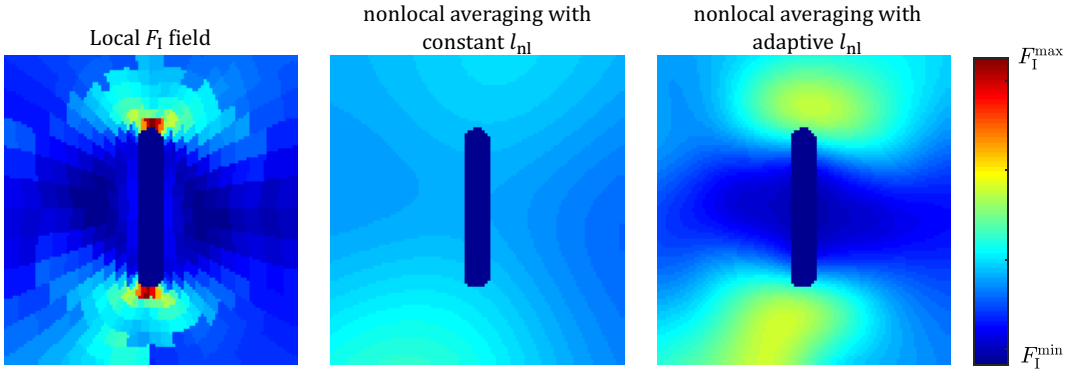

Figure 6.7: Comparison between the standard nonlocal averaging (with constant $l_{\mathrm{nl}} = 1.5$ mm) and the adaptive nonlocal averaging (where the value of l_{nl} is scaled based on the value of $|\nabla \bar{F}_{\mathrm{I}}|$).

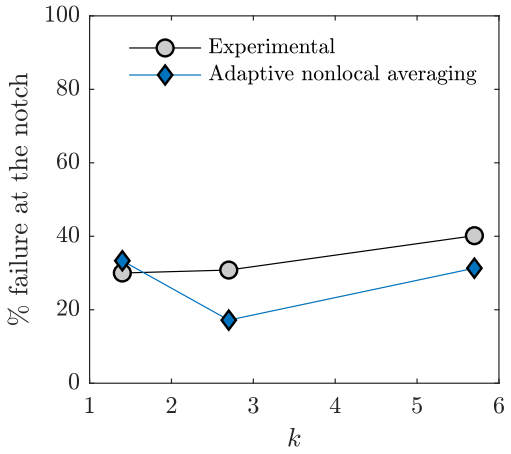

(a) Failure location of the different notched specimens: experimental vs. adaptive nonlocal FE results.

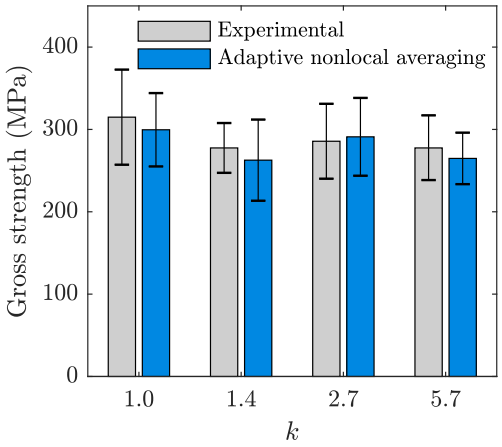

(b) Gross strength of the different notched specimens: experimental vs. adaptive nonlocal FE results.

Figure 6.8: Comparison between the notch sensitivity experimentally measured with the one predicted by the nonlocal FE framework (with the adaptive nonlocal averaging scheme) - (a) % failure at the notch and (b) gross strength distributions.

6.5 Discussion

The nonlocal averaging of a failure index field presented in this chapter allows for failure predictions of notched and un-notched specimens from linear elastic simulations. For this reason, the computational efficiency of this method is much higher than that of methods based on continuum damage mechanics. Moreover, the nonlocal averaging method was compared to results from the stochastic FE framework (presented in Chapter 5) which uses a ply discount method to model damage propagation in the material. It was shown that, for notched specimens, the stochastic FE framework pre-

dicts significantly lower strength values than those measured experimentally. Despite predicting accurate strength distributions for un-notched specimens, the ply discount method lacks the integration of the material's toughness to regularise the energy dissipation during the fracture process, which is essential to predict the response of notched configurations [82].

The adaptive nonlocal averaging approach relies on adjusting the value of l_{nl} based on the local average gradient $|\nabla F_{\mathrm{I}}|$ of the FI field. Since the gradients reflect the stress concentration induced by the geometrical notches, this method is flexible to handle notches of different geometries. However, the value of $|\nabla F_{\mathrm{I}}|$ is dependent on the remote load/displacement applied. In order to remove this dependency, a normalisation of $|\nabla F_{\mathrm{I}}|$ could be explored, and would enable failure prediction from pure linear elastic analysis. Nonetheless, the analysis presented in this work is still valid, as the same maximum displacement was applied in all the linear elastic simulations of the virtual specimens analysed.

The relation between l_{nl} and $|\nabla F_{\mathrm{I}}|$ was done by calibration of the numerical results with the experimental ones, and turned out to be governed by a power law, defined in Figure 6.6b. Pipes et al. [71], in the scope of their work on critical distance based methods to predict the notched strength of composite laminates, have also suggested a power law to relate the critical distance with the notch diameter. The identification of the power law relation between l_{nl} and $|\nabla F_{\mathrm{I}}|$ allows for a more practical and useful calibration of the adaptive nonlocal method. This can be done by using experimental results of only two different notched configurations rather than with four notched configurations, as was done in this work.

The nonlocal parameters used in this analysis were obtained by experimental calibration of the HexMC-M77 material system. It was shown in Figure 6.3b that the same value of l_{nl} used in the nonlocal averaging method yielded accurate strength predictions for TBDC systems with different tow thicknesses. However, Ko et al. [78] showed that TBDCs manufactured with different tow geometries (width and length) have different effective lengths of the associated fracture process zone, which suggests that the values of l_{nl} will also be dependent on these geometrical features.

6.6 Conclusions

The notch sensitivity of the HexMC-M77 TBDC material system was characterised experimentally by testing specimens with both circular and modified notch geometries. The stochastic FE framework was used to generate fields of failure indices, calculated based on a first ply failure criteria. A proposed nonlocal averaging scheme was used

to predict final failure from the resulting fields of failure indices, and compared the numerical predictions of the stochastic FE framework (detailed in Chapter 5). The main conclusions are summarised as follows:

- Tensile tests on circular notched TBDC specimens demonstrated the notch insensitivity of these materials; a gradual reduction of the gross strength with the increase in the notch diameter was found. The largest circular notch tested had a diameter/width ratio of 0.24, which lead to an average gross strength reduction of 20 %.
- The influence of the stress concentration of different notched geometries was assessed, for the first time in the literature. This was done by testing specimens with the same net cross-sectional area , but with modified notched geometries (inducing nominal stress concentrations ranging from $k = 1.4$ to $k = 5.7$), and it was found that the strength distributions of the different notched specimens were very similar. This experimental observation demonstrates the flexible and wide design space for parts/components manufacture with such TBDCs materials, as they combine a notch insensitive behaviour with the ability to be conformed into complex shapes.
- For the circular notch geometry, the nonlocal method with a constant value of l_{nl} was able to predict the notch sensitivity of the material, both in terms of gross strength as well as in the percentage of specimens failing at the notch.
- Using a stiffness reduction method which neglects the influence of the material's toughness during damage propagation, which is the case of the stochastic FE framework (presented in Chapter 5), leads to good predictions of un-notched specimens. However, it is not able to predict the strength distributions of notched geometries, and leads to significant under predictions of strength.
- For modified notched geometries, an adaptive nonlocal method was proposed, in which the nonlocality of the nonlocal functions are governed by the local average values of the magnitude of the gradients of failure indices. This leads to more accurate predictions of the experimental results when compared to using a constant value of l_{nl} for the nonlocal averaging scheme.

Chapter 7

A computationally-efficient micromechanical model for the fatigue life of unidirectional composites under tension-tension loading

7.1 Introduction

Many studies have shown that composite materials are sensitive to cyclic degradation, as experimental results show a significant reduction in the stiffness and strength of composites with the increasing number of fatigue cycles applied, both under simple and more complex loading cases [83–93]. Due to limited capabilities to predict the behaviour of composites across their entire life-time, large safety factors are often employed, leading to inefficient and over-designed components. It is therefore critical to be able to predict the life span of composites under cyclic loading, since fatigue is one of the main failure mechanisms in engineering structures (such as pressure vessels and aircraft components) [94].

Fibre-reinforced composites are inhomogeneous by nature and have a more complex behaviour than that of homogeneous materials, since different types of damage can occur in the different constituents; this fact makes the life-time prediction of composite materials a challenging task. Carbon fibres have an elastic behaviour and are generally considered to be insensitive to fatigue effects [95]; however, even a UniDirectional (UD) Carbon-Fibre Reinforced Polymer (CFRP) is vulnerable to degradation under tension-

tension cyclic loading, due to the formation of damage in the matrix and in the fibre-matrix interface [96, 97].

When a UD composite is loaded under uniform tension, due to the stochastic nature of the strength of single-fibres, dispersed breaks of the weaker fibres occur; these fibre-breaks generate stress concentrations in the neighbouring fibres, increasing their failure probability, which leads to progressive accumulation and clustering of fibre-breaks. The presence of these fibre- and cluster-breaks causes local shear damage of the matrix and/or fibre-matrix interface [83, 97]; consequently, under cyclic loading (and if the composite survived the first load cycle), the matrix and/or fibre-matrix interface surrounding the broken fibres will start to degrade further [83, 98]. This will increase the stress concentrations in the surrounding fibres along a longer distance, which eventually may lead to failure of the composite.

Talreja [97] introduced the concept of a "fatigue-life diagram" for the interpretation of the S-N curves of UD composites, which clearly distinguishes three regions: region-I, defined by a horizontal scatter band centred at the composite static failure strain or stress, dominated by fibre failure; region-II, characterised by a scatter band with a double-logarithmic relationship between the peak stress applied and the number of fatigue cycles to failure, dominated by progressive damage in the matrix and/or in the fibre-matrix interface; and region-III, that defines a region of no fatigue failure, governed by the fatigue limit of the matrix and fibre-matrix interface.

Predicting the failure of UD composites subjected to longitudinal tensile-tensile fatigue is a challenging task, since no measurable modulus degradation occurs, and no other type of macroscale damage can be experimentally measured. This urges the need for accurate and efficient models that are able to predict the accumulated fatigue damage that occurs in these materials at the microscale, and which leads to significant strength reductions.

The micromechanical damage that occurs in UD composites under tension-tension fatigue is related to matrix cracks and interfacial debonds that mainly initiate near fibre-breaks. On the one hand, brittle matrices tend to present cracks that grow under a mode-I component parallel to the plane of the fibre break, as well as interfacial debonds that can eventually kink out into the matrix and become bridged by other fibres [99]; tougher matrices, on the other hand, tend to present debonds that grow mostly in mode-II along the interface, leading to continuous stress redistributions on the neighbouring fibres [83, 97]. However, it has been shown that it is not necessary to explicitly include these different mechanisms to accurately predict longitudinal tensile failure of composites with a good level of accuracy (at least under static loading) [100].

The growth rate of matrix cracks and interfacial debonds can be modelled by a Paris power law [101–104].

Determining the Paris law constants for matrix cracks and debonds along the fibre-matrix interface is a challenging task: in the literature, a wide scatter of data can be found for the values of Paris law constants for mode-II debonding/delamination in composite materials [98,105–109]; moreover, there are also only a few experimental studies for the Paris law constants for interfacial debonding around individual fibres [110], and no experimental data for debonding around small bundles of fibres.

Fibre Bundle Models (FBMs) are a classical approach to predict the quasi-static tensile failure process of UD composites and the associated size effects. Most of the existing FBMs use simple constitutive laws for the matrix/interface behaviour (e.g. linear-elastic [111, 112], perfectly-plastic [113, 114], elastic-plastic [115, 116] and pre-debonded [117, 118]). More realistic behaviours of the matrix/interface (with a finite value of both the strength and toughness) have been implemented through Finite Element Analysis (FEA), where cohesive elements have been used to study delamination and debonding in composite materials both under static and fatigue loading [104, 106, 119–123]; however, such FE simulations have a high computational cost, and are therefore not suitable to simulate the micromechanics of longitudinal tensile failure of UD composites under cyclic load.

Only a few micromechanical approaches to predict fatigue of UD composite under cyclic longitudinal tension can be found in the literature. Ogin [124] used an analytical approach to predict the lifetime and residual strength of both UD and cross-ply composite laminates, by taking into account the fatigue growth of fibre/matrix interface debonds, as well as the statistical distribution of flaws along the fibres; however, the model neglected the formation of clusters of fibre-breaks, which has been recently shown to affect the failure process under fatigue [125]. Qian et al. [119] developed a FE fatigue model for UD composites, where the fatigue damage of unit-cells with 7 and 45 fibres was analysed and, with a multi-scale approach, the fatigue life of coupon-sized specimens were predicted; the model, besides being computationally expensive, also over-estimated the fatigue life of the coupons.

Overall, there is a lack of models in the literature able to accurately and efficiently predict the fatigue response of UD composites under longitudinal tension. Therefore, an analytical model to predict the fatigue life and the associated size effects of UD CFRPs under longitudinal tension-tension cyclic loading is proposed in this chapter. The model considers interfacial debonds propagating from fibre-breaks as the main fatigue mechanism, where the debond/crack growth rate is governed by the Paris law (Section 7.2.3). This gradual fatigue degradation of the matrix/interface under fatigue is coupled with an analytical micromechanical hierarchical fibre bundle model, in or-

der to capture cyclic effects on the longitudinal tensile strength of UD carbon-fibre composites (Section 7.2.4). The model allows for the determination of probabilistic S-N curves and associated size effects, and is validated against experimental results in Section 7.3. The findings and results of the model are discussed in Section 7.4, and the main conclusions are drawn in Section 7.5.

7.2 Fatigue Model

7.2.1 Model idealisation

The overall strategy of the model developed in this chapter is an extension of the Hierarchical Scaling Law (HSL) for the static strength of composite fibre bundles [114], and its general assumptions are the following:

(i) Hierarchical fibre bundles are generated by paring two level-[0] bundles (single fibres) into a level-[1] bundle and, through a recursive process, pairing two level-[i] bundles into one level-[$i+1$] bundle (Figure 7.1) [114, 117]. The number of fibres $n^{[i]}$ in a level-[i] bundle is given by

$$n^{[i]} = 2^i \quad \Leftrightarrow \quad i = \log_2 n^{[i]}. \tag{7.1}$$

(ii) Bundle failure propagates hierarchically in a self-similar way, assuming that the failure process of bundles of different scales are governed by the same mechanisms [126,127]. This way, the mathematical description of the failure of a level-[1] bundle (with 2 individual fibres), hereby designated as scaling law, can be used to describe the failure process of any level-[i] bundle. The scaling law to be developed for fatigue loading is detailed in Section 7.2.4.

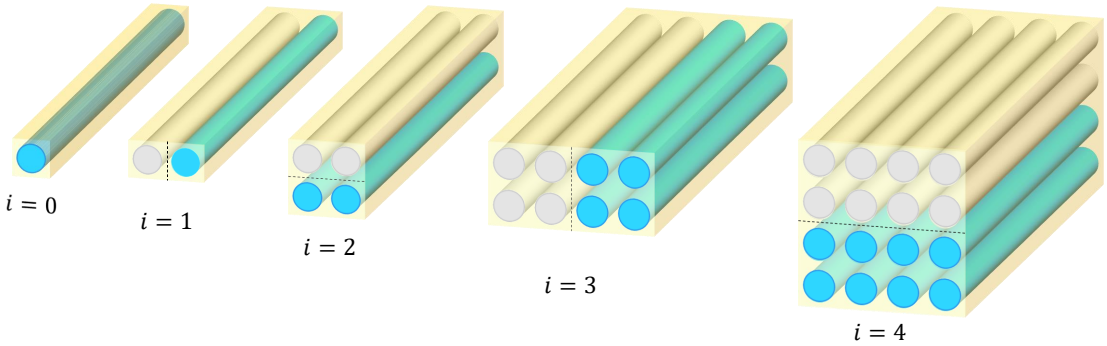

Figure 7.1: Hierarchical fibre bundles built in a square fibre arrangement [114].

(iii) The fibres are assumed to resist longitudinal stresses [111, 114, 117] and to be fatigue insensitive [95]. The strength of a single fibre under a uniform stress field σ^{∞} is given by a Weibull distribution, defined by the shape parameter m and scale parameter σ_0^{f}, measured at a reference length l_0^{f} [128]. This way, the survival probability of a single fibre ($S_{\mathrm{U}}^{[0]}$) under a uniform stress σ^{∞} can be defined and scaled to any length l by the Weakest Link Theory (WLT):

$$S_{\mathrm{U},l}^{[0]}(\sigma^{\infty}) = \exp\Big[-\frac{l}{l_0^{\mathrm{f}}}\cdot\Big(\frac{\sigma^{\infty}}{\sigma_0^{\mathrm{f}}}\Big)^{m}\Big]. \tag{7.2}$$

(iv) The matrix and/or fibre-matrix interface is responsible for the stress redistribution in the proximity of a fibre or sub-bundle-break, governed by shear-lag [129]. This shear-lag behaviour is represented by one single cohesive law (Figure 7.3) [121], which defines the combined shear response of the matrix and fibre-matrix interface; accordingly, the matrix and fibre-matrix interface will hereafter be simply referred to as the "interface". The interface will be subjected to both static and fatigue damage initiated from fibre-breaks, leading to debonding (or crack growth within the matrix); interface damage is assumed to grow in pure shear or mode-II (parallel to the broken fibre or sub-bundle), and any other micromechanical damage mechanism (e.g. mode-I matrix cracks growing parallel to the plane of the fibre breaks) are neglected. The static damage (initiated in the first loading cycle) will be analysed in Section 7.2.2, and the fatigue damage will be governed by a Paris power law [101–104], as detailed in Section 7.2.3.

(v) The length required for a broken level-[i] sub-bundle in the composite to recover the applied remote stress defines the *effective recovery length* $l_{\mathrm{e}}^{[i]}$, as well as the *control region* (with length $l_{\mathrm{c}}^{[i+1]}$) within which breaks in neighbouring level-[i] sub-bundles interact with each other (Figure 7.2). The increase of the effective recovery and control lengths with the increasing number of loading cycles (N) will be the main fatigue damage mechanism considered in this model [97].

7.2.2 Static stress fields near a fibre-break considering a cohesive interface

During the first loading cycle, the remote stress σ^{∞} will cause the break of the weaker fibres, according to the Weibull distribution characterising the stochastic single-fibre strength (defined in Eq. 7.2). This will generate local stress concentrations in the surviving fibres and shear stresses in the interface, as illustrated in Figure 7.2 for a 2-fibres (i.e. level-[1]) bundle. This section will analyse the stress fields generated in the neighbourhood of a fibre or sub-bundle break during the first loading cycle (i.e. at

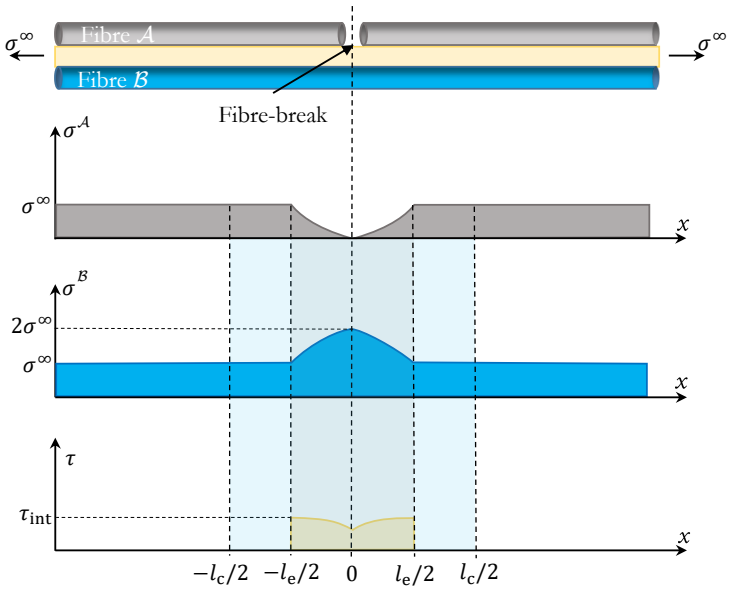

Figure 7.2: Static stress fields and length scales near a fibre-break within a level-[1] bundle.

$N = 0$, before the onset of fatigue effects), considering that the shear behaviour of the interface can be described by the linear cohesive law shown in Figure 7.3.

The choice of a linear cohesive law for the shear-lag stress transfer of the interface is motivated by two reasons: firstly, it accounts for the finite value of both the strength and the toughness of the interface between fibres, and is therefore more realistic than simpler constitutive laws [113–116] previously used in the literature. Secondly, the Paris law used to predict damage propagation under fatigue is usually formulated in energy-based terms [124,130], and therefore cannot be applied to the perfectly-plastic interface behaviour assumed in the original static formulation of the HSL [114]. The cohesive behaviour of the interface (see Figure 7.3) is defined by the mode-II fracture toughness $\mathcal{G}_{\text{int}}^{\text{IIc}}$, shear strength τ_{int}, and by the interface thickness t_{int} (which can be calculated from the average matrix thickness between the fibres in a square arrangement, see Appendix E.1 [114]).

The maximum shear strain γ_{int} and the shear tangent stiffness G_{int} of the cohesive law are defined as follows:

$$\gamma_{\text{int}} = \frac{2\mathcal{G}_{\text{int}}^{\text{IIc}}}{\tau_{\text{int}} \cdot t_{\text{int}}}, \tag{7.3a}$$

$$G_{\text{int}} = -\frac{\tau_{\text{int}}}{\gamma_{\text{int}}} = -\frac{\tau_{\text{int}}^2 \cdot t_{\text{int}}}{2\mathcal{G}_{\text{int}}^{\text{IIc}}}. \tag{7.3b}$$

In order to model interfacial debonding through an analytical implementation of this cohesive behaviour, the stress fields near a fibre or sub-bundle break are required. There-

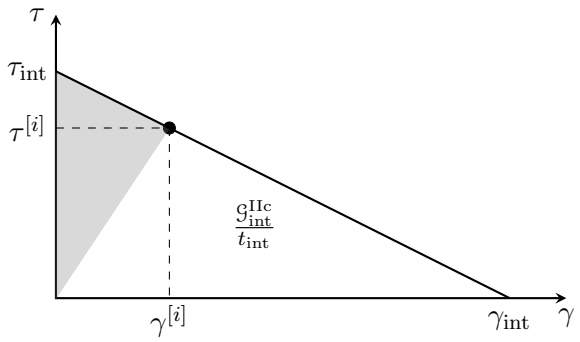

Figure 7.3: Linear cohesive law of the interface under static shear stresses.

fore, Pimenta and Robinson's [30] analytical shear-lag model is here applied within the effective recovery length of a level-$[i]$ broken sub-bundle (as shown in Figure 7.2 for $i = 0$), leading to the following differential equation [30]:

$$\frac{\mathrm{d}^2\Delta\sigma^{[i]}(x)}{\mathrm{d}x^2} = -{\lambda^{[i]}}^2 \cdot \Delta\sigma^{[i]}(x), \quad \text{with} \quad \lambda^{[i]} = \sqrt{\frac{2|G_{\text{int}}|}{T^{[i]} \cdot t_{\text{int}} \cdot E^{\text{f}}}} = \frac{\tau_{\text{int}}}{\sqrt{T^{[i]} \cdot E^{\text{f}} \cdot \mathcal{G}_{\text{int}}^{\text{IIc}}}}, \tag{7.4}$$

where $\Delta\sigma^{[i]}$ is the stress difference between the level-$[i]$ sub-bundles $\mathcal{B}$ (surviving) and $\mathcal{A}$ (broken), E^{f} is the Young's modulus of a single fibre, and $T^{[i]}$ is the equivalent shear-lag thickness of the level-$[i]$ sub-bundle, defined by the ratio between its cross-sectional area $A^{[i]}$ and the perimeter $P^{[i]}$ (see Appendix E.1). Following the stress fields shown in Figure 7.2, the boundary conditions for the differential equation can be defined as follows:

$$\Delta\sigma^{[i]}(x = l_{\text{e}}^{[i]}/2) = 0, \tag{7.5a}$$

$$\Delta\sigma^{[i]}(x = 0) = 2\sigma^{\infty}, \tag{7.5b}$$

$$\tau^{[i]}(x = l_{\text{e}}^{[i]}/2) = \tau_{\text{int}}. \tag{7.5c}$$

Considering the boundary conditions in Eq. 7.5, the solution of Eq. 7.4 allows one to define the following analytical stress field distributions:

$$\Delta\sigma^{[i]}(x) = \frac{2\tau_{\text{int}}}{\lambda^{[i]} \cdot T^{[i]}} \cdot \sin\Big(\lambda^{[i]}\Big[\frac{l_{\text{e}}^{[i]}}{2} - x\Big]\Big), \tag{7.6a}$$

$$\sigma^{\mathcal{A}}(x) = \sigma^{\infty} - \frac{\tau_{\text{int}}}{\lambda^{[i]} \cdot T^{[i]}} \sin\Big(\lambda^{[i]}\Big[\frac{l_{\text{e}}^{[i]}}{2} - x\Big]\Big), \tag{7.6b}$$

$$\sigma^{\mathcal{B}}(x) = \sigma^{\infty} + \frac{\tau_{\text{int}}}{\lambda^{[i]} \cdot T^{[i]}} \sin\Big(\lambda^{[i]}\Big[\frac{l_{\text{e}}^{[i]}}{2} - x\Big]\Big), \tag{7.6c}$$

$$\tau^{[i]}(x) = \tau_{\text{int}} \cdot \cos\Big(\lambda^{[i]}\Big[\frac{l_{\text{e}}^{[i]}}{2} - x\Big]\Big). \tag{7.6d}$$

The stress fields defined in Eq. 7.6 are valid only below a critical remote stress ($\sigma^{\infty}_{\text{crt}}$), above which the energy release rate associated with the propagation of a crack along the interface (initiating from a sub-bundle break) is higher than its fracture toughness $\mathcal{G}^{\text{IIc}}_{\text{int}}$. This critical remote stress depends on the level of the broken sub-bundle, and is given by [30]

$$\sigma^{\infty[i]}_{\text{crt}} = \sqrt{\frac{\mathcal{G}^{\text{IIc}}_{\text{int}} \cdot E^{\text{f}}}{T^{[i]}}}. \tag{7.7}$$

From the analytical stress fields near a fibre or sub-bundle-break defined in Eq. 7.6, the effective recovery length associated to the first loading cycle (i.e. under static loading with $N = 0$) can be obtained by imposing the boundary condition presented in Eq. 7.5b to the stress field defined in Eq. 7.6a:

$$\frac{l^{[i]}_{\text{e}}(\sigma^{\infty}, N = 0)}{2} = \frac{1}{\lambda^{[i]}} \cdot \text{asin}\left(\frac{\sigma^{\infty}}{\sigma^{\infty[i]}_{\text{crt}}}\right). \tag{7.8}$$

This effective recovery length allows one to determine the shear stress at the critical point ($x = 0$) of the level-[i] sub-bundle interface from Eq. 7.6d:

$$\tau^{[i]}_{\text{crt}}(\sigma^{\infty}, 0) = \tau_{\text{int}} \sqrt{1 - \left(\frac{\sigma^{\infty}}{\sigma^{[i]}_{\text{crt}}}\right)^2}. \tag{7.9}$$

7.2.3 Fatigue damage model for the interface

The stress fields defined in Section 7.2.2 are valid during the first loading cycle, as the remote load is applied to the fibre bundle up to $\sigma^{\infty} = \sigma^{\infty}_{\text{peak}}$; after this, cyclic loading takes place with a stress ratio $R^{\infty} = \sigma^{\infty}_{\text{trough}}/\sigma^{\infty}_{\text{peak}}$, where $\sigma^{\infty}_{\text{peak}}$ and $\sigma^{\infty}_{\text{trough}}$ are the peak and trough remote stresses applied during one fatigue cycle, respectively. During the cyclic loading, a mode-II interfacial crack may eventually be initiated from a sub-bundle break (at $x = 0$ in Figure 7.2), as will be described in Section 7.2.4; with further fatigue cycles, the crack growth rate, represented here by $\partial A^{[i]}/\partial N$ (where N is the number of fatigue cycles applied), is given by the Paris law as follows [98,121,130]:

$$\frac{\partial A^{[i]}(\sigma^{\infty}_{\text{peak}}, R^{\infty})}{\partial N} = \begin{cases} C^{\text{II}}_{\text{int}} \left(\frac{\Delta \mathcal{G}^{[i]}_{\text{II}}(\sigma^{\infty}_{\text{peak}}, R^{\infty})}{\mathcal{G}^{\text{IIc}}_{\text{int}}}\right)^{m^{\text{II}}_{\text{int}}} & \text{if } \mathcal{G}^{\text{IIth}}_{\text{int}} < \mathcal{G}^{[i]}_{\text{peak}}(\sigma^{\infty}_{\text{peak}}) < \mathcal{G}^{\text{IIc}}_{\text{int}}, \\ 0 & \text{otherwise.} \end{cases} \tag{7.10}$$

This formulation of the Paris law requires three parameters characterising the mode-II fatigue response of the interface: $C^{\text{II}}_{\text{int}}$ and $m^{\text{II}}_{\text{int}}$ are the Paris law constants, and $\mathcal{G}^{\text{IIth}}_{\text{int}}$ is the threshold mode-II energy release rate (below which no fatigue occurs). The term $\mathcal{G}^{[i]}_{\text{peak}}$ is the mode-II energy release rate applied to the crack-tip of the interface of a

broken level-$[i]$ sub-bundle, and $\Delta\mathcal{G}_{\mathrm{II}}^{[i]}$ is the variation of the energy release rate between the peak and trough of the loading cycle.

During the propagation of a mode-II interfacial crack around a broken level-$[i]$ sub-bundle, it can be shown that the energy release rate at the crack-tip is constant and independent of the crack length by assuming a shear-lag stress transfer (leading to a self-similar crack growth [104]) and, for this reason, $\mathcal{G}_{\mathrm{peak}}^{[i]}$ and $\Delta\mathcal{G}_{\mathrm{II}}^{[i]}$ can be obtained by rearranging the definition of $\sigma_{\mathrm{crt}}^{\infty[i]}$ in Eq. 7.7:

$$\mathcal{G}_{\mathrm{peak}}^{[i]}(\sigma_{\mathrm{peak}}^{\infty}) = \frac{T^{[i]} \cdot (\sigma_{\mathrm{peak}}^{\infty})^2}{E^{\mathrm{f}}} \quad \text{and} \quad \Delta\mathcal{G}_{\mathrm{II}}^{[i]}(\sigma_{\mathrm{peak}}^{\infty}, R^{\infty}) = \frac{T^{[i]}\left[(\sigma_{\mathrm{peak}}^{\infty})^2 \cdot (1 - R^{\infty 2})\right]}{E^{\mathrm{f}}}. \tag{7.11}$$

Associated with $\mathcal{G}_{\mathrm{int}}^{\mathrm{IIth}}$ is the threshold remote peak stress $\sigma_{\mathrm{th}}^{\infty[i]}$, below which the interface of a level-$[i]$ sub-bundle does not undergo any fatigue damage, given by

$$\sigma_{\mathrm{th}}^{\infty[i]} = \sqrt{\frac{\mathcal{G}_{\mathrm{int}}^{\mathrm{IIth}} \cdot E^{\mathrm{f}}}{T^{[i]}}}. \tag{7.12}$$

Although the Paris law is usually used to model propagation of fatigue damage once a crack-tip is formed (for the interface near a level-$[i]$ sub-bundle break, this condition corresponds to $\tau^{[i]}(\sigma_{\mathrm{peak}}^{\infty}, x = 0) = 0$), the fact that the crack propagation is self-similar suggests that the degradation of the interface before the initiation of a crack-tip can also be modelled by the Paris law. Neglecting the magnification of the energy release rate near the proximity of the fibre-break [104], the growth of the effective recovery length — within which the interface is either partially damaged or fully debonded — will therefore be described by the Paris law, defined in Eq. 7.10, both before (Figure 7.2) and after (Figure 7.4) the initiation of a crack-tip at $x = 0$. Combining this assumption with a cycle jump strategy [121] suitable for high-cycle fatigue modelling, the effective recovery length is calculated as follows:

$$\frac{l_{\mathrm{e}}^{[i]}(\sigma_{\mathrm{peak}}^{\infty}, R^{\infty}, N + \Delta N)}{2} = \frac{l_{\mathrm{e}}^{[i]}(\sigma_{\mathrm{peak}}^{\infty}, R^{\infty}, N)}{2} + \frac{1}{P^{[i]}} \cdot \frac{\mathrm{d}A^{[i]}}{\mathrm{d}N}(\sigma_{\mathrm{peak}}^{\infty}, R^{\infty}) \cdot \Delta N, \tag{7.13}$$

where ΔN is the cycle jump (a convergence study of the cycle jump size will be presented in Section 7.3.2). This growth of the effective recovery length leads to changes in the stress fields of the sub-bundles and the interface near fibre-breaks, as will be derived in Section 7.2.4 and shown in Figures 7.4 and 7.5.

7.2.4 Fatigue strength model

The static strength model for hierarchical fibre bundles [114] will be extended in this section to capture the strength degradation due to cyclic loading. The analysis of

the effective recovery length evolution — characterised by Eq. 7.13 — will be divided in three phases: crack initiation (Figure 7.2), crack propagation (Figure 7.4), and fully debonded state (Figure 7.5).

7.2.4.1 Crack initiation phase

During the crack initiation phase, the interface's ability to transfer shear stresses near fibre-breaks will gradually be reduced with progressive cyclic loading, leading to an increase in the recovery length governed by the Paris law 7.13. After a given number ($N_{\text{init}}^{[i]}$) of fatigue cycles, the amount of interface damage accumulated near the fibre-breaks (at $x = 0$) becomes sufficient to initiate an interfacial crack-tip, which defines the end of the crack initiation phase.

An interfacial crack-tip near a broken level-$[i]$ sub-bundle is characterised by an interface shear-stress $\tau^{[i]}(x = 0, N) = 0$. This condition would also be verified in the first loading cycle under the critical stress $\sigma_{\text{peak}}^{\infty} = \sigma_{\text{crt}}^{\infty[i]}$ (as defined in Eq. 7.7); the critical effective recover length $l_{\text{K}}^{[i]}$ which corresponds to this critical static case can be calculated analytically through Eq. 7.8 as

$$l_{\text{K}}^{[i]} = l_{\text{e}}^{[i]}(\sigma_{\text{crt}}^{\infty[i]}, N = 0) = \frac{\pi}{2\lambda^{[i]}}. \tag{7.14}$$

The number of cycles required for the crack initiation phase ($N_{\text{init}}^{[i]}$) around a level-$[i]$ sub-bundle can then be calculated by combining the definition of the critical value of the effective recovery length (Eq. 7.14) and the Paris law evolution (Eq. 7.13):

$$\begin{aligned} \frac{l_{\text{K}}^{[i]}}{2} &= \frac{l_{\text{e}}^{[i]}(\sigma_{\text{peak}}^{\infty}, 0)}{2} + \frac{1}{P^{[i]}} \cdot \frac{\text{d}A^{[i]}}{\text{d}N}(\sigma_{\text{peak}}^{\infty}, R^{\infty}) \cdot N_{\text{init}}^{[i]} \\ \Leftrightarrow \quad N_{\text{init}}^{[i]} &= \frac{\left(\frac{1}{\lambda} \cdot \left[\text{asin}\left(\frac{\sigma_{\text{peak}}^{\infty}}{\sigma_{\text{crt}}^{\infty[i]}}\right) - \frac{\pi}{2}\right]\right) \cdot P^{[i]}}{\frac{\text{d}A^{[i]}}{\text{d}N}(\sigma_{\text{peak}}^{\infty}, R^{\infty})}. \end{aligned} \tag{7.15}$$

Eq. 7.15 is valid if $\sigma_{\text{peak}}^{\infty} < \sigma_{\text{crt}}^{\infty[i]}$, in which case a crack-tip will not be formed during the static loading (i.e. $\tau^{[i]}(x = 0, N = 0) > 0$); in this case, at the end of $N_{\text{init}}^{[i]}$ loading cycles, a crack will start propagating from the critical point ($x = 0$) of the level-$[i]$ interface of a broken sub-bundle. If the peak remote stress applied to the bundle exceeds the value of $\sigma_{\text{crt}}^{\infty[i]}$, unstable crack propagation is sparked during the first loading cycle (with the stress fields defined in Section 7.2.2) and thus the model assumes a fully debonded state (see Section 7.2.4.3) for all loading cycles $N > 0$.

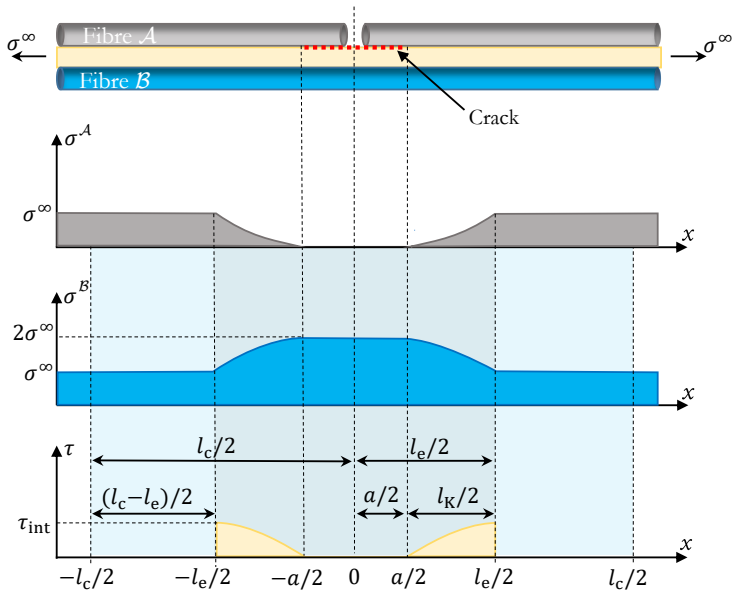

Figure 7.4: Stress fields and length scales in a level-[1] bundle during the crack propagation phase.

7.2.4.2 Crack propagation phase

During the crack propagation phase, the stress fields in a level-[1] bundle with one broken fibre are presented in Figure 7.4, where it is assumed that an interfacial crack propagates symmetrically to the mid-plane defined by the fibre-break (as observed experimentally [83]), in a self-similar way. Consequently, the effective recovery length is composed by two regions, separated by a crack-tip at $|x| = a^{[0]}/2$:

i) near the break in fibre $\mathcal{A}$ ($|x| < a^{[0]}/2$), the interface is debonded and no longer transfers shear stresses between the broken fibre (which is under no longitudinal stresses, $\sigma^{\mathcal{A}} = 0$) and the surviving fibre (which is under a uniform stress $\sigma^{\mathcal{B}} = 2\sigma^{\infty}$). The debonded area grows according the to the Paris law (previously defined in Eq. 7.10);

ii) between the crack-tip and the end of the recovery region ($a^{[0]}/2 < |x| \leq l_e^{[0]}/2$), the interface is damaged, but still transfer shear stresses between the two fibres $\mathcal{A}$ and $\mathcal{B}$. The length of the damaged region remains constant during the propagation phase, at the value $l_K^{[0]}$ previously calculated in Eq. 7.14.

This analysis can also be applied to calculate the effective recovery length during the crack propagation phase around a broken sub-bundle of any level-[i]:

$$\frac{l_e^{[i]}(\sigma^{\infty}_{peak}, R^{\infty}, N)}{2} = \frac{l_K^{[i]}(\sigma^{\infty\,[i]}_{crt})}{2} + \frac{1}{P^{[i]}} \cdot \frac{dA^{[i]}}{dN}(\sigma^{\infty}_{peak}, R^{\infty}) \cdot (N - N^{[i]}_{init}). \tag{7.16}$$

The end of the crack propagation phase occurs when the effective recovery length reaches the length of the specimen l_{spec}. Therefore, the number of cycles of the propagation phase ($\Delta N^{[i]}_{\text{prop}}$) is calculated by

$$\frac{l_{\text{spec}}}{2} = \frac{l^{[i]}_{\text{K}}(\sigma^{\infty\,[i]}_{\text{crt}})}{2} + \frac{1}{P^{[i]}} \cdot \frac{\mathrm{d}A^{[i]}}{\mathrm{d}N}(\sigma^{\infty}_{\text{peak}}, R^{\infty}) \cdot \Delta N^{[i]}_{\text{prop}} \quad \Leftrightarrow \quad \Delta N^{[i]}_{\text{prop}} = \frac{\left(l_{\text{spec}} - l^{[i]}_{\text{K}}(\sigma^{\infty\,[i]}_{\text{crt}})\right) \cdot P^{[i]}}{2 \cdot \frac{\mathrm{d}A^{[i]}}{\mathrm{d}N}(\sigma^{\infty}_{\text{peak}}, R^{\infty})}. \tag{7.17}$$

7.2.4.3 Fully debonded phase

When the interfacial crack reaches the length of the specimen, the bundle enters the fully debonded phase, where the surviving sub-bundle (fibre $\mathcal{B}$ in Figure 7.5) is the one carrying the total remote load applied to the bundle (see Figure 7.5). In this phase, the effective recovery length is limited by the physical length of the specimen, and therefore remains unchanged during further fatigue cycles (i.e. $l^{[i]}_{\text{e}}(\sigma^{\infty}_{\text{peak}}, R^{\infty}, N \geq N^{[i]}_{\text{debond}}) = l_{\text{spec}}$, with $N^{[i]}_{\text{debond}} = N^{[i]}_{\text{init}} + \Delta N^{[i]}_{\text{prop}}$).

7.2.4.4 Scaling law

Due to continuous changes in the phases of the bundles with increasing loading cycles (see Figures 7.2, 7.4 and 7.5), the static scaling law derived in the literature for the initial static case [114] is not valid for fatigue loading. Therefore, a general scaling law valid for all phases of the fatigue analysis will be derived in this section. For the

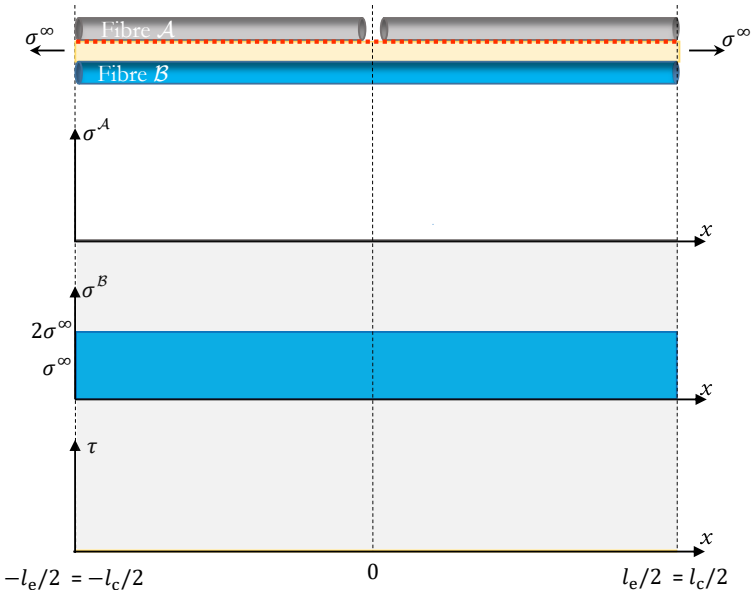

Figure 7.5: Stress fields and length scales in a fully debonded level-[1] bundle.

sake of a simplicity, the survival probabilities $S^{[i]}$ are represented only as functions of the applied remote peak stress (hereby represented only as σ^{∞}), although they are calculated for each cycle N of the fatigue analysis and also depend on the loading ratio R^{∞}; the dependency of the length scales ($l_{\mathrm{e}}^{[i]}$, $l_{\mathrm{K}}^{[i]}$, $a^{[i]}$ and $l_{\mathrm{c}}^{[i]}$ defined in Table 7.1) on these same variables will also be omitted.

The scaling law calculates the survival probability of a level-$[i+1]$ bundle within the bundle control length $l_{\mathrm{c}}^{[i+1]}$. The survival probabilities of the level-$[i]$ sub-bundles used as inputs are calculated at the associated recovery length $l_{\mathrm{e}}^{[i]}$ by

$$\ln S_{\mathrm{U,e}}^{[i]}(\sigma^{\infty}) = \frac{l_{\mathrm{e}}^{[i]}(\sigma^{\infty})}{l_0^{\mathrm{f}}} \cdot \ln S_{\mathrm{U},0}^{[i]}(\sigma^{\infty}), \tag{7.18}$$

where $S_{\mathrm{U},0}^{[i]}(\sigma^{\infty})$ is the survival probability of a level-$[i]$ sub-bundle under a uniform remote stress σ^{∞} with a length l_0^{f}. The scaling law considers two possible survival scenarios of the level-$[i+1]$ bundle:

• both level-$[i]$ sub-bundles are able to withstand the uniform remote stress σ^{∞} within the level-$[i+1]$ control length. The probability of this scenario is given by the WLT, considering that the level-$[i+1]$ bundle of length $l_{\mathrm{c}}^{[i+1]}$ contains 2 level-$[i]$ sub-bundles

$$S_{\mathcal{U}}^{[i+1]}(\sigma^{\infty}) = \left[S_{\mathrm{U,e}}^{[i]}(\sigma^{\infty})^{\frac{l_{\mathrm{c}}^{[i+1]}}{l_{\mathrm{e}}^{[i]}}} \right]^2; \tag{7.19a}$$

• one level-$[i]$ sub-bundle breaks under the remote stress, and the neighbouring level-$[i]$ sub-bundle is able to withstand the resulting stress concentrations. The probability of this scenario is given by

$$S_{\mathcal{K}}^{[i+1]}(\sigma^{\infty}) = 2 \cdot \underbrace{[1 - S_{\mathrm{U,e}}^{[i]}(\sigma^{\infty})^{\frac{l_{\mathrm{c}}^{[i+1]}}{l_{\mathrm{e}}^{[i]}}}]}_{\mathrm{I}} \cdot \underbrace{S_{\mathrm{U,e}}^{[i]}(2\sigma^{\infty})^{\frac{a^{[i]}}{l_{\mathrm{e}}^{[i]}}}}_{\mathrm{II}} \cdot \underbrace{S_{\mathrm{K,e}}^{[i]}(\sigma^{\infty})^{\frac{l_{\mathrm{K}}^{[i]}}{l_{\mathrm{e}}^{[i]}}}}_{\mathrm{III}} \cdot \underbrace{S_{\mathrm{U,e}}^{[i]}(\sigma^{\infty})^{\frac{l_{\mathrm{c}}^{[i+1]} - l_{\mathrm{e}}^{[i]}}{l_{\mathrm{e}}^{[i]}}}}_{\mathrm{IV}}, \tag{7.19b}$$

where the exponents in each term of Eq. 7.19a and 7.19b are defined in Table 7.1.

In Eq. 7.19b, term I corresponds to the failure probability of the weakest level-$[i]$ sub-bundle under the uniform stress σ^{∞} within the level-[i+1] control length; term II corresponds to the survival probability of the surviving level-$[i]$ sub-bundle under a uniform stress $2\sigma^{\infty}$ within the debonded length $a^{[i]}$; term III corresponds to the survival probability of the surviving level-$[i]$ sub-bundle under the stress concentrations field within the interface damaged region (with length $l_{\mathrm{K}}^{[i]}$, defiend in Table 7.1); term IV

Table 7.1: Calculation of length scales for the different phases of the fatigue life; the effective recovery length $l_{\mathrm{e}}^{[i]}$ is calculated from the Paris law in Eq. 7.13.

Length scales	$N=0$	$0<N\leq N_{\mathrm{init}}^{[i]}$	$N_{\mathrm{init}}^{[i]}<N\leq N_{\mathrm{debond}}^{[i]}$		$N\geq N_{\mathrm{debond}}^{[i]}$
$l_{\mathrm{K}}^{[i]}(\sigma_{\mathrm{peak}}^{\infty},R^{\infty},N)$	$l_{\mathrm{e}}^{[i]}(\sigma_{\mathrm{peak}}^{\infty},0)$	$l_{\mathrm{e}}^{[i]}(\sigma_{\mathrm{peak}}^{\infty},R^{\infty},N)$	$l_{\mathrm{K}}^{[i]}$ (Eq. 7.14)		0
$a^{[i]}(\sigma_{\mathrm{peak}}^{\infty},R^{\infty},N)$	0	0	$l_{\mathrm{e}}^{[i]}(\sigma_{\mathrm{peak}}^{\infty},R^{\infty},N)-l_{\mathrm{K}}^{[i]}$		l_{spec}
$l_{\mathrm{c}}^{[i+1]}(\sigma_{\mathrm{peak}}^{\infty},R^{\infty},N)$	$2\cdot l_{\mathrm{e}}^{[i]}(\sigma_{\mathrm{peak}}^{\infty},0)$	$2\cdot l_{\mathrm{e}}^{[i]}(\sigma_{\mathrm{peak}}^{\infty},R^{\infty},N)$	if $l_{\mathrm{e}}^{[i]}\leq l_{\mathrm{spec}}/2$	if $l_{\mathrm{e}}^{[i]}>l_{\mathrm{spec}}/2$	l_{spec}
			$2\cdot l_{\mathrm{e}}^{[i]}(\sigma_{\mathrm{peak}}^{\infty},R^{\infty},N)$	l_{spec}	

corresponds to the survival probability of the surviving level-$[i]$ sub-bundle under the uniform remote stress σ^{∞}, outside the recovery region of the broken level-$[i]$ sub-bundle (i.e. within the length in which a break in the surviving sub-bundle would interact with the break in the weakest sub-bundle).

The stress fields in a level-$[i]$ sub-bundle were determined by considering a cohesive interfacial law (Eq. 7.6); however, in order to calculate the survival probability in term III ($S_{\mathrm{K,e}}^{[i]}(\sigma^{\infty})$) analytically, a linear approximation of the stress field in the surviving sub-bundle (defined in Eq. 7.6c) was made, as detailed in Appendix E.2. Using this linear approximation, the term $S_{\mathrm{K,e}}^{[i]}(\sigma^{\infty})$ is given by [114]:

$$\begin{aligned}\ln[S_{\mathrm{K,e}}^{[i]}(\sigma^{\infty})] &= \frac{l_{\mathrm{e}}^{[i]}}{l_0^{\mathrm{f}}}\cdot\frac{k\cdot\ln[S_{\mathrm{L},0}^{[i]}(k\cdot\sigma^{\infty})-\ln[S_{\mathrm{L},0}^{[i]}(\sigma^{\infty})]}{k-1}\ \text{, with}\\ \ln[S_{\mathrm{L},0}^{[i]}(\sigma)] &= \frac{1}{\sigma}\int_{\sigma_{\mathrm{L}}=0}^{\sigma}\ln[S_{\mathrm{U},0}^{[i]}(\sigma_{\mathrm{L}})]\mathrm{d}\sigma_{\mathrm{L}}\ \text{ and }\ k=2.\end{aligned} \tag{7.20}$$

It should be noted that, while this simplification leads to linear stress concentrations in the surviving sub-bundle within the interface damaged region (as previously obtained with a perfectly-plastic interface law [114]) the length of the interface damaged region calculated with the cohesive law ($l_{\mathrm{K}}^{[i]}$ defined in Table 7.1) is still larger than the one predicted using a perfectly-plastic interface, hence justifying the new derivations in Section 7.2.2, even for the static case.

Both scenarios in Eq. 7.19a and 7.19b are mutually exclusive, and therefore their probabilities can be added to define the general scaling law, which is valid for every phase of the fatigue analysis:

$$S_{\mathrm{U,c}}^{[i+1]}(\sigma^{\infty})=S_{\mathrm{U,e}}^{[i]}(\sigma^{\infty})^{\frac{2l_{\mathrm{c}}^{[i+1]}}{l_{\mathrm{e}}^{[i]}}}+2\cdot[1-S_{\mathrm{U,e}}^{[i]}(\sigma^{\infty})^{\frac{l_{\mathrm{c}}^{[i+1]}}{l_{\mathrm{e}}^{[i]}}}]\cdot S_{\mathrm{U,e}}^{[i]}(2\sigma^{\infty})^{\frac{a^{[i]}}{l_{\mathrm{e}}^{[i]}}}\cdot S_{\mathrm{K,e}}^{[i]}(\sigma^{\infty})^{\frac{l_{\mathrm{K}}^{[i]}}{l_{\mathrm{e}}^{[i]}}}\cdot S_{\mathrm{U,e}}^{[i]}(\sigma^{\infty})^{\frac{l_{\mathrm{c}}^{[i+1]}-l_{\mathrm{e}}^{[i]}}{l_{\mathrm{e}}^{[i]}}}. \tag{7.21}$$

During the different phases of the fatigue life of a level-$[i+1]$ bundle, the scaling law can be simplified as follows:

- initiation phase: $a^{[i]} = 0 \quad \wedge \quad l_{\mathrm{c}}^{[i+1]} = 2 \cdot l_{\mathrm{e}}^{[i]}$:

$$S_{\mathrm{U,c}}^{[i+1]}(\sigma^{\infty}) = S_{\mathrm{U,e}}^{[i]}(\sigma^{\infty})^4 \cdot [1 - S_{\mathrm{U,e}}^{[i]}(\sigma^{\infty})^2] \cdot S_{\mathrm{K,e}}^{[i]}(\sigma^{\infty}) \cdot S_{\mathrm{U,e}}^{[i]}(\sigma^{\infty}); \tag{7.22a}$$

- propagation phase: $a^{[i]} > 0 \quad \wedge \quad l_{\mathrm{c}}^{[i+1]} = 2 \cdot l_{\mathrm{e}}^{[i]}$:

$$S_{\mathrm{U,c}}^{[i+1]}(\sigma^{\infty}) = S_{\mathrm{U,e}}^{[i]}(\sigma^{\infty})^4 + 2 \cdot [1 - S_{\mathrm{U,e}}^{[i]}(\sigma^{\infty})^2] \cdot S_{\mathrm{U,e}}^{[i]}(2\sigma^{\infty})^{\frac{a^{[i]}}{l_{\mathrm{e}}^{[i]}}} \cdot S_{\mathrm{K,e}}^{[i]}(\sigma^{\infty})^{\frac{l_{\mathrm{K}}^{[i]}}{l_{\mathrm{e}}^{[i]}}} \cdot S_{\mathrm{U,e}}^{[i]}(\sigma^{\infty}); \tag{7.22b}$$

- fully debonded phase: $l_{\mathrm{c}}^{[i+1]} = l_{\mathrm{e}}^{[i]} = a^{[i]}$:

$$S_{\mathrm{U,c}}^{[i+1]}(\sigma^{\infty}) = S_{\mathrm{U,e}}^{[i]}(\sigma^{\infty})^2 + 2 \cdot [1 - S_{\mathrm{U,e}}(\sigma^{\infty})] \cdot S_{\mathrm{U,e}}^{[i]}(2\sigma^{\infty}). \tag{7.22c}$$

7.2.4.5 Effective recovery length averaging

An interfacial crack in a level-$[i+1]$ bundle can only initiate after a level-$[i]$ sub-bundle break occurs. Therefore, if a level-$[i]$ sub-bundle breaks during (for instance) the 2^{nd} remote fatigue cycle ($j = 2$), with associated probability $\Delta F_{\mathrm{U,e}}^{[i]}(\sigma^{\infty}, j = 2) = F_{\mathrm{U,e}}^{[i]}(\sigma^{\infty}, j = 2) - F_{\mathrm{U,e}}^{[i]}(\sigma^{\infty}, j = 1)$, the level-$[i]$ interfacial crack has grown for only 1 fatigue cycle by the remote fatigue cycle $N = 3$. Considering the possibilities of the level-$[i]$ sub-bundle breaking at the remote cycles $j = \{0, 1, 2, 3\}$, then the *averaged* effective recovery length ($\bar{l}_{\mathrm{e}}^{[i]}$) at the end of the 3^{rd} fatigue cycle ($N = 3$) is given by

$$\begin{aligned}\bar{l}_{\mathrm{e}}^{[i]}(\sigma^{\infty}, 3) = \Big[& l_{\mathrm{e}}^{[i]}(\sigma^{\infty}, 3) \cdot \Delta F_{\mathrm{U,e}}^{[i]}(\sigma^{\infty}, 0) + l_{\mathrm{e}}^{[i]}(\sigma^{\infty}, 2) \cdot \Delta F_{\mathrm{U,e}}^{[i]}(\sigma^{\infty}, 1) + \\ & l_{\mathrm{e}}^{[i]}(\sigma^{\infty}, 1) \cdot \Delta F_{\mathrm{U,e}}^{[i]}(\sigma^{\infty}, 2) + l_{\mathrm{e}}^{[i]}(\sigma^{\infty}, 0) \cdot \Delta F_{\mathrm{U,e}}^{[i]}(\sigma^{\infty}, 3) \Big] / F_{\mathrm{U,e}}^{[i]}(\sigma^{\infty}, 3),\end{aligned} \tag{7.23}$$

with

$$\Delta F_{\mathrm{U,e}}^{[i]}(\sigma^{\infty}, j) = \begin{cases} F_{\mathrm{U,e}}^{[i]}(\sigma^{\infty}, 0) & \text{for } j = 0, \\ F_{\mathrm{U,e}}^{[i]}(\sigma^{\infty}, j) - F_{\mathrm{U,e}}^{[i]}(\sigma^{\infty}, j-1) & \text{for } j \geq 1. \end{cases} \tag{7.24}$$

The outcome of this process is represented in Figure 7.6, where one can see that the averaged effective recovery length of the a level-[3] sub-bundle remains constant and equal to its static value $l_{\mathrm{e}}^{[3]}(\sigma^{\infty}, 0)$ until the failure probability of level-[3] sub-bundles ($F_{\mathrm{U,e}}^{[3]}$) starts increasing. The averaging of the effective recovery length can be

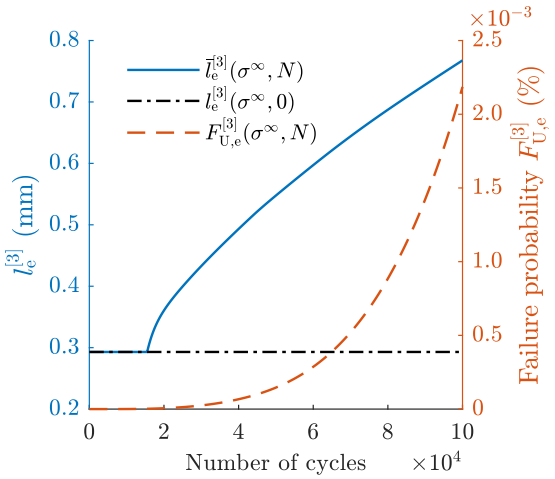

Figure 7.6: Evolution of the effective recovery length within a level-[4] bundle (i.e. interfacial crack propagating around a level-[3] sub-bundle) after the averaging process (using the inputs defined in Tables 7.2-7.4 associated to the material system `T/D`, with $\sigma^\infty_{\text{peak}} = 2.5$ GPa and $R^\infty = 0.1$).

generalised to any number N of fatigue cycles by

$$\bar{l}_e^{[i]}(\sigma^\infty, N) = \frac{\sum_{j=1}^{N} \left[l_e^{[i]}(\sigma^\infty, N-j+1) \cdot \Delta F_{U,e}^{[i]}(\sigma^\infty, j) \right]}{F_{U,e}^{[i]}(\sigma^\infty, N)}. \tag{7.25}$$

7.2.5 Model implementation

The model presented in the previous sections was implemented in Matlab, and an overview of the numerical implementation is presented in Figure 7.7.

7.3 Results

7.3.1 Static results

Figure 7.8a compares predictions for the static strength distribution $X_m^{[i]}(N = 0)$ obtained by the present model (considering a linear cohesive behaviour for the interface) against those obtained by the original version of the HSL available in the literature [114] (using a perfectly-plastic interface behaviour), considering the same input values as in Table 1 of the work presenting the static HSL [114], and a mode-II fracture toughness of the interface $\mathcal{G}_{\text{int}}^{\text{IIc}} = 1$ kJ/m^2. The results show that considering a cohesive behaviour and a finite fracture toughness for the interface leads to lower predictions of the static bundle strength compared to the results assuming a perfectly-plastic beha-

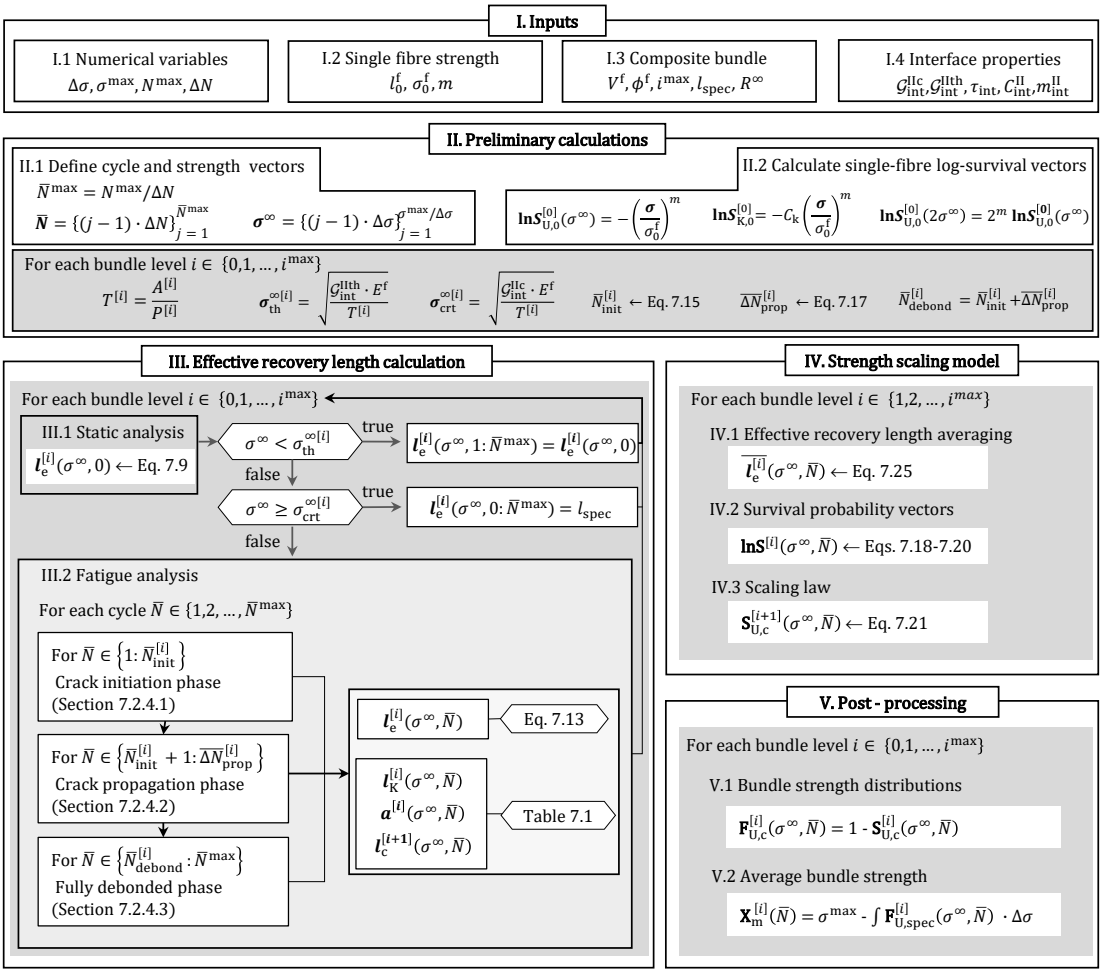

Figure 7.7: Flowchart of the numerical implementation of the model.

viour, albeit the difference is small. Furthermore, the influence of assuming linear stress concentration fields in the fibres rather than the full analytical solution (presented in Appendix E.2) is shown to be small, which ensures the accuracy of the approximation considered in Eq. 7.20.

Figure 7.8b shows that the relation between the effective recovery length and the applied remote stress is no longer linear when a cohesive behaviour for the interface is considered, in opposition to the linear relation found for a perfectly-plastic interface behaviour. Furthermore, the non-linear evolution of the effective recovery length is more pronounced as the remote stress approaches the critical value $\sigma_{\mathrm{crt}}^{\infty}$.

7.3.2 Convergence study

The model inputs for the convergence study presented in this section and for the parametric study detailed in Section 7.3.3 are the ones presented for the A/P

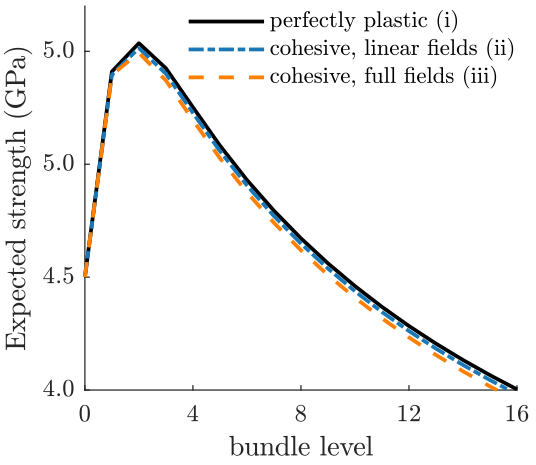

(a) Size effect on the expected static strength.

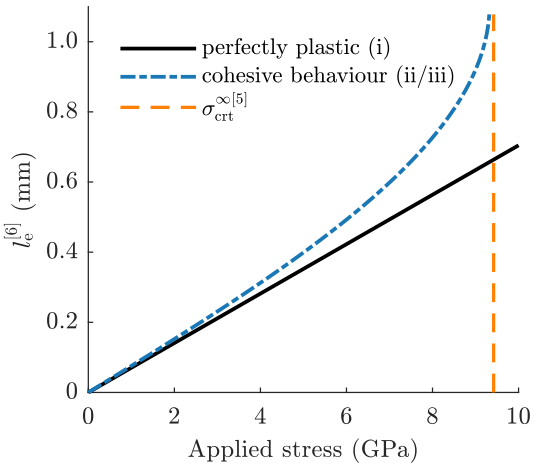

(b) Effective recovery length of a level-[6] sub-bundle.

Figure 7.8: Static analysis assuming different behaviours of the interface: i) perfectly-plastic behaviour [114]; ii) cohesive behaviour and linear approximation of the stress fields in the sub-bundle; iii) cohesive behaviour and analytical stress fields in the sub-bundle (see Appendix E.2 for the difference between (ii) and (iii)).

fibre/matrix combination in Tables 7.2-7.4 which were selected to represent the experimental results of Gamstedt and Talreja [83]. Figure 7.9a shows that the model requires small cycle jumps (ΔN) in order to accurately calculate the S-N curve in the region of low cycle fatigue, and progressively converges for larger cycle jumps as the number of applied cycles increases. In order to maximize the computational efficiency of the model, the numerical implementation of the model detailed in Figure 7.7 was combined with an adaptive cycle jump scheme, where the cycle jump is gradually increased throughout the analysis, as shown in Figure 7.9b. With this adaptive scheme, the whole S-N curve shown in Figure 7.9b can be obtained accurately within a model runtime of less than 60 seconds.

7.3.3 Parametric study

Figure 7.10a shows that $\mathcal{G}_{\mathrm{int}}^{\mathrm{IIth}}$ influences the fatigue life limit (or the region of no failure) in the S-N curves of UD composites: as $\mathcal{G}_{\mathrm{int}}^{\mathrm{IIth}}$ increases, the peak remote stress associated with the fatigue life limit also increases. This is in good agreement with the framework presented by Talreja [97], where the lower band of the fatigue life diagram of UD composites under longitudinal tension is associated with the fatigue limit of the interface.

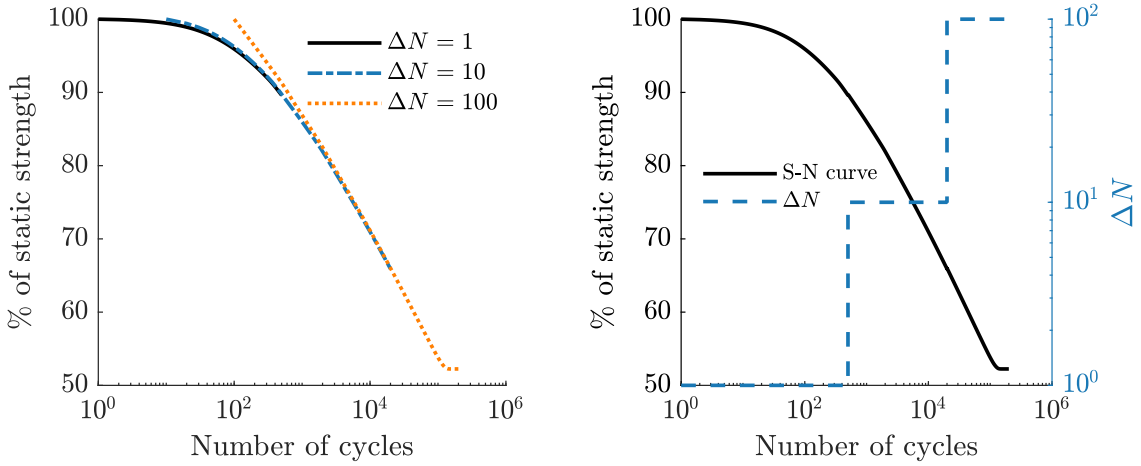

(a) Expected S-N curve obtained with different values of the cycle jump ΔN.

(b) Expected S-N curve obtained with the adaptive cycle jump scheme.

Figure 7.9: Convergence analysis of the model with the adaptive cycle jump scheme.

Figure 7.10b describes the influence of the interface's shear strength τ_{int} on the expected fatigue behaviour of UD composite bundles, where bundles with stronger interfaces show a more pronounced strength degradation due to fatigue. This creates a trade-off between the fatigue life and static strength of UD composites under longitudinal tension, as it has been demonstrated that stronger interfaces lead to higher values of the static strength [114]. The absolute value of the fatigue life limit of bundles remains unchanged for different values of τ_{int}, although this is not clear in Figure 7.10b due to the normalisation of the fatigue results relative to the expected static strength of the specimen (which is different for each value of τ_{int}).

Figures 7.10c and 7.10d demonstrate that the Paris law constants of the interface ($C_{\text{int}}^{\text{II}}$ and $m_{\text{int}}^{\text{II}}$) have a significant influence in the expected S-N curves of UD composites under longitudinal tension, as they directly affect the debond growth (see Eq. 7.10 and 7.13) and, consequently, the stress redistribution in the sub-bundles and in the interface.

The fatigue life of specimens with different number of fibres (represented by different levels-$[i]$) are shown as colour map in Figure 7.11a . Above the predicted specimen static strength $X_{\text{m}}^{[i]}$, the predicted number of cycles to failure is zero (i.e. the specimen will fail in the first loading cycle), as expected. Below a certain value of the peak applied stress, the model predicts an infinite fatigue life limit that can occur in one of the two following cases:

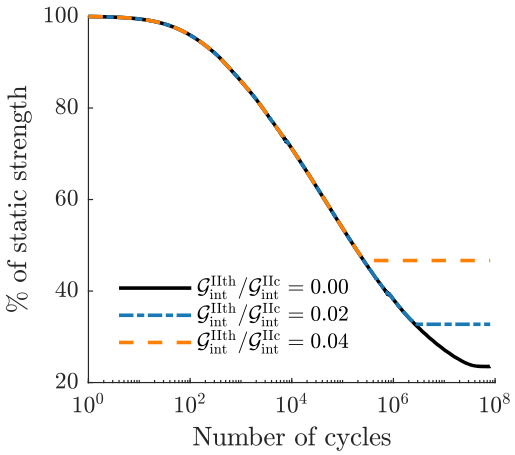

(a) Effect of the energy release rate threshold.

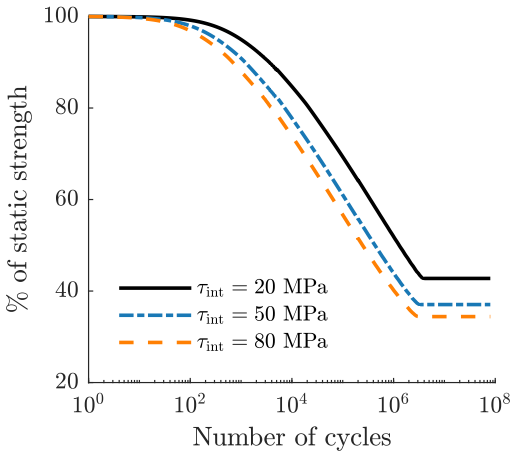

(b) Effect of the interface shear strength.

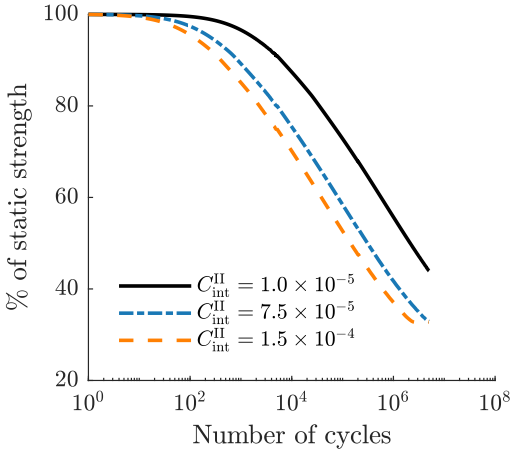

(c) Effect of the $C_{\text{int}}^{\text{II}}$ Paris law constant.

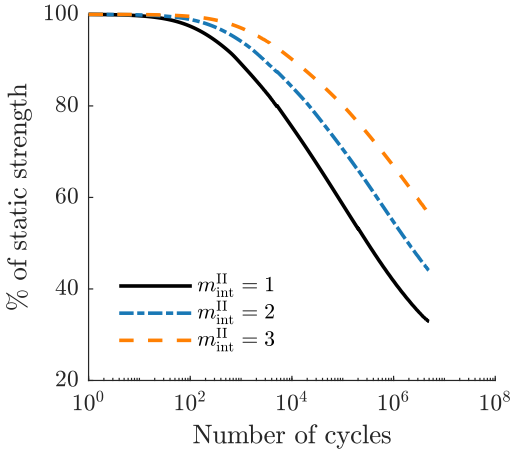

(d) Effect of the $m_{\text{int}}^{\text{II}}$ Paris law constant.

Figure 7.10: Parametric study on the expected S-N curve predicted by the model.

(i) no bundle of level $j < i$ is expected to fail, as be the peak remote stress applied is lower than the strength of a fully debonded specimen $X_{\text{fd}}^{[i]}$ (obtained by Eq. 7.22c); this case defines the fatigue life limit for small (i.e low level) specimens;

(ii) no interfacial crack growth occurs, as the peak remote stress applied is lower than the threshold stress value below which the matrix/interface near a fibre-break do not accumulate any damage ($\sigma_{\text{th}}^{\infty[0]}$, Eq. 7.12); this case defines the fatigue life limit for large (i.e high level) specimens.

Figure 7.11b shows the existence of size effects in the fatigue life of composite specimens, where smaller specimens present faster and higher degradation in their fatigue strength than the large ones. Furthermore, smaller specimens also present an infinite fatigue life limit at higher remote stress values, due to the higher average static

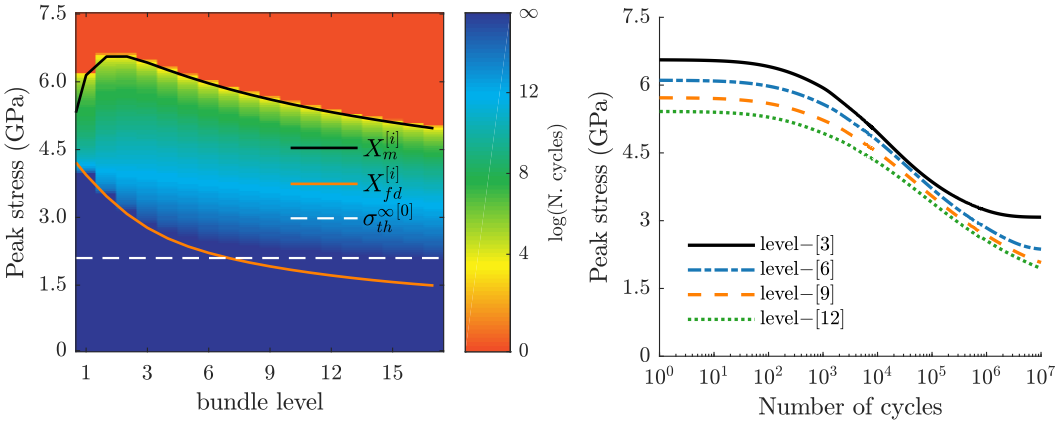

(a) S-N colour map of different bundle levels.

(b) Size effect on the S-N curve for different bundle levels.

Figure 7.11: Size-effects on the expected S-N curves predicted by the model, for the `A/P` material defined in Tables 7.2-7.4.

strength in the fully debonded case ($X_{\mathrm{fd}}^{[i]}$, which governs the fatigue life limit of small bundles, as explained in point (i) above.)

7.3.4 Validation against experimental results

Material and input parameters considered for all the subsequent model validation cases are shown in Tables 7.2 - 7.4. Figure 7.12 validates the model against the experimental results of Meziere et al. [91], where different values for the Weibull parameters of the fibres (each obtained from single-fibre tensile tests at different gauge lengths l_0^{f}) were considered [131]. For all sets of Weibull parameters originally measured in the literature, the S-N curves predicted by the model show a good correlation with the experimental results; interestingly the correlation is optimal with the combination of Weibull parameters that more accurately predicted the average static strength of the specimen measured experimentally.

Figure 7.13a shows a colour map with the stochastic S-N curves predicted by the model, as well as the experimental results obtained by Khatibi [88]. The experimental results for CF/PEEK obtained by Gamstedt and Talreja [83], presented in the form of a fatigue life diagram (where the cyclic peak strain is plotted against the number of cycles), are compared with the model predictions in Figure 7.13b.

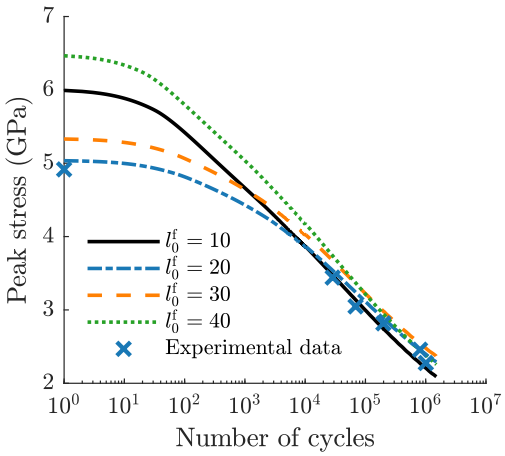

Figure 7.12: Validation of the expected S-N curves predicted by the model against a set of experimental results [91], and analysis of the effect of the Weibull parameters (measured at different gauge length l_0^f, see Table 7.3) on the predicted S-N curve. Model inputs are defined in Tables 7.2-7.4 (for the `T/D` fibre/matrix combination).

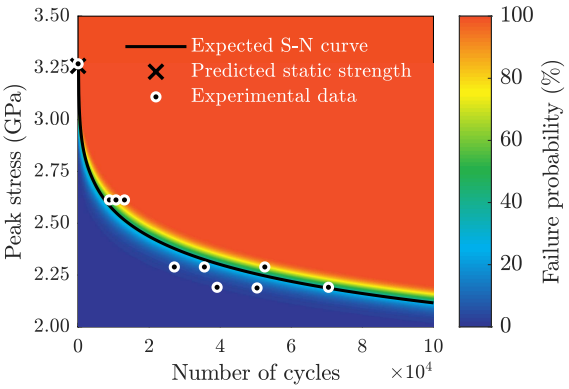

(a) Stochastic S-N curve and validation against experimental results [88]. Model inputs are defined in Tables 7.2-7.4 (for the `G/R` fibre/matrix combination).

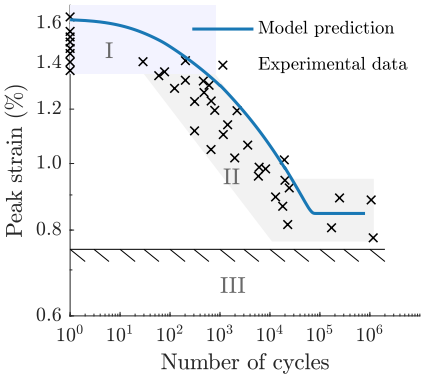

(b) Fatigue life diagram and validation against experimental results [83]. Model inputs are defined in Tables 7.2-7.4 (for the `A/P` fibre/matrix combination).

Figure 7.13: Validation of the model against experimental results.

Table 7.2: Nominal model inputs for validation against experimental results.

Exp. results	Fibre ref.	Interface ref.	$n^{[i]}$	V^f (%)	l_{spec}(mm)	R^∞
[91]	`T`†	`D`‡	10^5	60	180	0.1
[88]	`G`†	`R`‡	10^6	60	195	0.1
[83]	`A`†	`P`‡	10^5	60	127	0.1

† See Table 7.3 for detailed description.
‡ See Table 7.4 for detailed description.

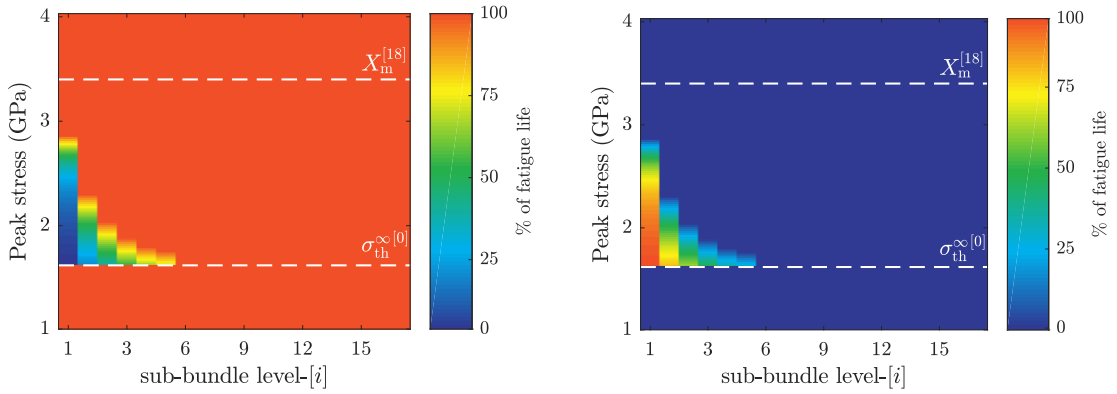

(a) Crack initiation.

(b) Crack propagation.

Figure 7.14: Expected duration of the crack initiation and propagation phases (for several sub-bundle levels-[i]) in the overall fatigue life of the level-[18] bundle analysed in Figure 7.13b.

Table 7.3: Fibre properties for model validation; for fibre type `T`, Deng et al. [131] provide 4 sets of Weibull parameters for the single-fibre strength distribution, measured at 4 different fibre lengths l_0^f.

Fibre ref.	Fibre type	E^f(GPa)	ϕ^f(µm)	l_0^f(mm)	m	σ_0^f(GPa)	Reference
`T`	T700	230	7.00	10	3.5	7.700	[131]
				20	5.0	6.200	[131]
				30	5.0	6.200	[131]
				40	3.7	6.000	[131]
`G`	G34-700	226	7.00	30	5.2	3.800	[131]
`A`	AS4	222	6.85	10	4.8	4.493	[132]

Table 7.4: Interface properties for model validation.

Interface ref.	τ_{int}(MPa)	$\mathcal{G}_{int}^{IIc}$(kJ/m^2)	$\mathcal{G}_{int}^{IIth}$(kJ/m^2)	C_{int}^{II}(mm^2/cycle)	m_{int}^{II}	Reference
`D`†	70	1	0.02*	1.0×10^{-3}*	2.0*	[91]
`R`†	70	1	0.025*	3.0×10^{-3}*	2.2*	[88]
`P`†	110	2	0.025*	2.0×10^{-3}*	2.0*	[83,133]

† `D` - Diglycidyl Ether of Bisphenol-A (DGEBA) epoxy fibre-break; `R` - RIGIDITE© 5228 toughened epoxy;
`P` - APC-2-PEEK toughened thermoplastic fibre-break.
* Estimated values.

7.4 Discussion

7.4.1 Physical phenomena predicted by the model

The model captures many characteristic features of the fatigue behaviour of UD composites under longitudinal tension:

a) The threshold value of the energy release rate $\mathcal{G}_{\text{int}}^{\text{IIth}}$ of the interface/matrix is an important parameter for the fatigue life of UD composite specimens, as it defines the infinite fatigue life region (Figure 7.10a). This parameter influences the peak remote stress required to propagate an interfacial crack around a single fibre-break ($\sigma_{\text{th}}^{\infty[0]}$ in Figure 7.11a), which triggers the fatigue damage mechanism. Removing the threshold value (i.e setting $\mathcal{G}_{\text{int}}^{\text{IIth}} = 0$) reduces the fatigue limit to the stress value that statistically causes no fibre-breaks ($X_{\text{fd}}^{[i]}$ in Figure 7.11a), in which case no fatigue occurs because there are no initiation points for interfacial cracks to develop.

b) The results of the developed model, when presented in the form of a fatigue life diagram (Figure 7.13b), clearly show the existence of three distinct regions, which have been reported and discussed in the literature [83, 97]. In region I, almost no fatigue damage is accumulated (leading to a horizontal orientation of the S-N curve), which demonstrates that the failure mechanism of a UD composite is dominated by fibre failure; region II is dominated by the fatigue degradation process, where the growth of interfacial debonds from fibre- or sub-bundle-breaks is the main fatigue damage mechanism. Finally, region III defines a fatigue limit below which failure does not occur, and where interfacial cracks either do not initiate, or have a rate of propagation too slow to lead to failure. The model is also able to recreate the main features captured by the experimental results (Figures 7.12 and 7.13).

c) The model results indicate that specimen failure at remote peak stresses close to the static strength is dominated by fibre-breaks, without the existence of any stable crack initiation or propagation at any sub-bundle level (Figure 7.14). Figure 7.14b also demonstrates that, as the applied peak stress decreases, crack propagation from individual fibre-breaks and small broken sub-bundles starts occurring for most of the fatigue life of a specimen; for even lower values of the applied peak stress, progressively larger sub-bundle-breaks form early in the fatigue life of the specimen, with interface cracks propagating for the majority of the fatigue life. Nevertheless, Figure 7.14b also shows that there is no stable initiation and propagation of interfacial cracks from broken sub-bundles above a certain number of fibres (level-[6] in Figure 7.14, which corresponds to a cluster of 64 fibres); this suggests the existence of a critical cluster size under fatigue loading, which could possibly be different from the one associated with static loading [134], although further analysis would be required in order to accurately define the critical cluster size under fatigue.

It is important to notice that the model neglects the effect of mode-I matrix cracks that propagate parallel to the fibre fracture plane (characteristic of brittle matrices), which alters the stress redistribution in the fibres and can increase their failure prob-

ability [99]; this assumption may lead to an overprediction of the fatigue life by the model, especially for composites with a more brittle matrix.

7.4.2 Uncertainty in model inputs and their influence in the predicted fatigue behaviour

There are certain model inputs whose availability in the literature is scarce. Therefore, the influence of these inputs and the importance of determining them experimentally are discussed below:

a) The values of $\mathcal{G}_{\text{int}}^{\text{IIth}}$ used for the validation of the model (Table 7.3) are slightly lower than values considered by other authors when studying delamination under fatigue loading, which are typically around 0.1 kJ/m^2 [121,135,136]. This difference in the values of $\mathcal{G}_{\text{int}}^{\text{IIth}}$ considered in Section 7.3 can be justified by the different fatigue mechanism in the present analysis (which govern interfacial crack propagation around single-fibre or sub-bundle breaks), compared to the one characterised in most experiments (corresponding to the propagation of cracks between plies which typically contain a resin-rich region, and which corresponds to fatigue delamination); this difference is also corroborated by Hojo et al. [110], who studied interfacial fatigue crack propagation using bi-fibre shear specimens and found that the threshold to fatigue crack growth of the fibre interface is lower than that to fatigue delamination in composite laminates. Moreover, the value of $\mathcal{G}_{\text{int}}^{\text{IIth}}$ used in the model should account not only for the threshold for propagation of debonds at the fibre-matrix interface, but also for propagation of matrix cracks, which is also difficult to determine experimentally.

b) The Weibull parameters of the strength distribution of single-fibres have a significant influence in the model results, particularly in the static strength predicted by the model (Figure 7.13b). Furthermore, the Weibull shape parameter m has a noticeable influence in the slope of the S-N curves, as shown in Figure 7.12. These results reveal the importance of accurately measuring the Weibull strength distribution of fibres experimentally.

c) The Paris law constants of the interface ($C_{\text{int}}^{\text{II}}$ and $m_{\text{int}}^{\text{II}}$) have an important effect on the composite S-N curves predicted by the model. Despite the lack of experimental results to determine these constants for interfacial debonding, an estimation of these parameters was made (see Table 7.4) based on values found in the literature [98, 105–109] for mode-II delamination propagation. This motivated the parametric study presented in Section 7.3.3 to demonstrate the sensitivity of the model to these parameters.

7.5 Conclusions

An analytical Hierarchical Scaling Law to predict the behaviour of composite fibre bundles under tension-tension fatigue was developed, implemented and validated against experimental results. The main conclusions of this chapter are as follows:

- The analytical formulation of the HSL, in combination with an adaptive jump cycle strategy, allows one to perform a stochastic analysis of the fatigue life of composite fibre bundles in a very efficient way; S-N curves can be obtained for a range of specimen sizes and different failure probabilities in a run-time of less than 60 seconds.
- The model shows good agreement when validated against different sets of experimental results [83, 88, 91], and is able to capture the characteristic trends of the fatigue behaviour of UD composites reported in the literature [97], as well as predicting the variability inherent to the experimental results.
- The debond growth was assumed to follow a Paris power law, whose constants have an important influence in the predicted S-N curves. Despite the lack of experimentally measured constants for the materials studied, the ones used for the model validation lie within the range of values found in the literature for mode-II fatigue delamination propagation. Nevertheless, determining the Paris law constants experimentally for mode-II debond growth in composites would be essential, as it would allow for a more accurate prediction and understanding of the fatigue behaviour of UD composites. Moreover, accounting for the interacting fatigue mechanisms at both the matrix and fibre-matrix interface could be explored in future developments of the model.

This chapter provides the first model in the literature to predict the full fatigue behaviour of UD composites under longitudinal tension and associated size effects; due to the computational efficiency and easy-to-use implementation of the model, it is expected to be applicable in the following scenarios:

- in an academic environment, the model can be used to provide quantitative information and detailed insight of the fatigue mechanisms in UD composites;
- for material development, the model can be used to evaluate the impact of improving constituent properties (e.g. improving the bonding between fibres and matrix, or decreasing the scatter in fibre-strength) on the evolution of the fatigue degradation of UD composites;
- for structural design and reliability, the model can be used to predict the scatter associated with fatigue life, and to scale fatigue tests from lab-scale specimens

to large structures, thus reducing the cost and time required for experimental characterisation of materials and qualification of structures.

Chapter 8

Conclusions

8.1 On modelling the variability of TBDCs

Following from experimental evidence in the literature of the intrinsic variability of the mechanical properties of TBDCs, Chapters 2, 4, 5 and 6 focus on characterising and successfully replicating the material's variability through numerical models, in order to predict their stochastic dominated mechanical response.

A microstructure generator was developed in Chapter 2, to capture effect of the 3D features of the microstructure of TBDCs, such as tow waviness and fibre volume fraction variations, on the elastic response of the material. The features of the generator were successfully validated against micro-CT measurements, and it was shown that for short and thick tows, the waviness can have a significant knock-down (up to 20%) on the stiffness of TBDCs.

Numerical tools to quantify the spatial variability of the field of mechanical properties of TBDCs were developed in Chapter 4. The influence of the tow geometry (length and width) on the characteristic length-scales of the resulting field of mechanical properties was established. This was achieved by using the microstructure generator presented in Chapter 2 to create FE models with explicit representation of TBDC microstructures, which are able to generate accurate and representative strain fields. Is was shown that the characteristic length-scales of the strain fields are governed by the harmonic mean between the tow length and width.

A stochastic FE framework based on an implicit representation of the material's microstructure was proposed in Chapters 4 and 5. This framework assigns mechanical properties at discrete and uncorrelated points. These mechanical properties are governed by fibre orientation distribution functions, which can be obtained from process simulations. Using an adequate interpolation scheme, the mechanical properties

at the seed points are interpolated to a refined structural mesh, leading to a mesh independent approach. A failure criterion was proposed to predict failure initiation in TBDC material systems, and was combined with a ply-discount method to predict ultimate failure. The stochastic FE framework was successfully validated against experimental results, both in terms of its ability to generate representative strain fields, and predicting ultimate failure of different TBDC material systems.

The results of Chapter 5 demonstrate that capturing the intrinsic variability of TBDC material systems is crucial to predict final failure. It was shown that using the FE framework in a deterministic approach, where the fibre orientations are mapped to FE models directly from process simulations, leads to erroneous predictions of the material's variability, and hence to over-predictions of the ultimate strength. However, integrating the mapped fibre orientations in the stochastic FE framework resulted in accurate predictions of the material's variability and mechanical response.

The intrinsic variability of the mechanical properties of TBDCs leads to local weak-spots in the material which act as internal stress concentrations. These internal stress concentrations can be in the same order of effect as those induced by geometrical notches in the material, which justifies their notch-insensitive behaviour, characterised in Chapter 6. It was shown that even for non-standard notch geometries, inducing stress concentrations up to $K = 5.7$ led to a small reduction only of the material's gross strength, when compared to its un-notched strength, was verified. This demonstrates the importance of capturing the intrinsic variability of the mechanical properties, in order to be able to replicate this notch insensitive behaviour with numerical models.

8.2 On predicting failure of TBDCs

In Chapter 3, a 2D failure criterion for a unidirectional discontinuous ply, presented in the literature, was combined with a model to predict the strength of TBDCs. This model accounts for different failure mechanisms such as fibre failure, tow interface failure which can be governed by a toughness dominated mechanism or by yielding of the matrix/interface. The model used in Chapter 3 does not take into account the intrinsic variability of TBDCs, and led to strength over predictions. Nonetheless, the relative influence of different microstructural features (such as tow thickness, strength and stiffness) on the ultimate strength of TBDCs was shown to be well correlated with experimental results.

In Chapter 5, the 2D failure criterion (used in Chapter 3) was extended to take into account 3D stress states. The failure criterion considers the quadratic combination of two independent failure indices: (i) in-plane failure index, which is governed by a

shear lag interaction (associated with the interaction between in-plane shear and tensile stresses, and which takes into account both failure due to tow fracture or interface failure) and by the matrix dominated failure mode taken from the LaRC05 criterion (associated with the interaction between shear and transverse stresses); and (ii) out-of-plane failure index, which takes into account the effect of out of plane stresses. Due to the idealisation of TBDCs as local SELs, the failure criterion is used by the stochastic FE framework to predict failure of each discontinuous ply, which is then combined with a ply discount method to predict final failure. The model was successfully validated against experimental results of the HexMC-M77 material system (with low flow during the manufacturing process) and a CF-SMC material system (with a large amount of flow during the manufacturing process creating flow induced preferential fibre orientations).

The stochastic FE framework was used in Chapter 6 to predict the notch sensitivity of the HexMC-M77 material system, and it was shown that predicting failure of notched specimens with ply discount method leads to under-predictions of the material's notched strength. This was justified by the lack of integration of the material's toughness to regularise the energy dissipation during the fracture process. To overcome this limitation, a nonlocal averaging scheme of fields of failure indices (that result from the stochastic FE framework) was proposed to predict failure from linear elastic simulations. The magnitude of gradients of the field of failure indices, which reflect the influence of the stress concentrations induced by the geometrical notches, were used to control the nonlocal parameter that governs the locality of the nonlocal functions, and were calibrated based on the experimental results of the notched and un-notched specimens.

8.3 On improving the mechanical performance of TBDCs

In Chapter 3, the model developed in the literature for failure prediction of TBDCs was used to explore the effect of the tow mechanical properties and geometries on the ultimate strength of these materials. It was shown that by combining the use of thin and stiff tows with matrix system with a high mode-II toughness, the stress transfer mechanism between the tows would be significantly enhanced, and would promote fibre failure by delaying the failure of the interface governed by a toughness dominated process. This allows for a further exploitation of the fibre properties within the TBDC material system, ultimately leading to significant improvements in the strength of the material. The influence of the tow thickness reduction and increased tow stiffness was demonstrated experimentally, by manufacturing specimens with different combinations of tow properties; the trends found experimentally were in good agreement with the numerical predictions.

TBDCs manufactured with ultra-thin (20 μm) and high-modulus (450 GPa) carbon-fibre tapes presented strength values of up to 600 MPa and a stiffness of 90 GPa. This represents an increase in mechanical properties of 100% when compared to those of commercially available material systems. Moreover, this experimental work demonstrated the possibility of achieving mechanical properties that match those of continuous-fibre quasi-isotropic laminates, using a discontinuous material system.

8.4 On predicting the reliability of composites

Predicting the reliability of composite materials is essential for designing safe composite structures. Accurate prediction of fatigue degradation of composites is challenging, not only due to the nature of the microstructure of the material, but also due to the computational resources required to model a composite subjected to millions of loading cycles. Chapter 7 presented an analytical model able predict the fatigue behaviour of UD composites under tension-tension loading. The model predicts the fatigue degradation of specimens with any number of fibres and predicts failure probabilities for different applied loads and fatigue cycles, yielding stochastic S-N curves. Moreover, the model is able to provide quantitative information and insight into the main fatigue mechanisms of UD composites, which can be included and/or used to inform fatigue models for more complex composite architectures such as composite laminates (where failure generally coincides with the failure of the 0° ply).

The model is an extension of an existing model in the literature to predict the tensile strength of composite fibre bundles under quasi-static tension, with a very high computational efficiency. The stochastic S-N curves shown were calculated in under 60 seconds, which despite representing a two order magnitude increase in computational time compared to the quasi-static model, is still extremely efficient, considering it can capture fatigue effects up to 10^8 cycles within this time-frame.

8.5 Novelty

The microstructure generator presented in Chapter 2 is the first one in the literature able to recreate the statistical 3D features of the microstructure of TBDCs, such as the tow waviness and volume fraction variations. The generator was coupled with an analytical stiffness model to quantify the effect of the tow waviness on the in-plane modulus reduction for different tow geometries. This model showed that considering the tow waviness is essential to accurately predict the modulus of TBDCs with short and narrow tows.

The FE framework detailed in Chapter 4 uses an implicit representation of the microstructure of TBDCs, and assigns mechanical properties at points with uncorrelated properties. For the first time in the literature, the influence of the tow geometry on the characteristic length-scale of the field of mechanical properties, and hence in the distance between the uncorrelated points, was quantified. An analytical expression was proposed to relate the in-plane tow geometry with the characteristic length-scale.

For the first time in the literature, a stochastic FE framework was linked with process simulation results in Chapter 5; it was shown how flow-induced fibre orientations can be coupled with a stochastic process that ensures the realistic/correct variability of assigned mechanical properties, while maintaining the overall fibre orientation state yielded by the process simulations. Moreover, a 3D failure criterion to predict damage initiation in TBDCs was proposed and coupled with a ply discount method to predict ultimate failure.

A nonlocal averaging scheme was proposed in Chapter 7, to predict final failure of notched and un-notched TBDC specimens from linear elastic simulations. The proposed method relies on adjusting the locality of nonlocal functions, used in the averaging process, based on the gradients of fields of failure indices, which reflect the stress concentrations induced by different notch geometries. Moreover, for the first time in the literature, the notch sensitivity of a TBDC material system was experimentally characterised for modified notch geometries, which induce stress concentrations ranging from $k = 1.4$ to $k = 5.7$, revealing a small reduction only of the material's gross strength. This further expands the knowledge of the notch insensitive behaviour of these materials, which has previously only been characterised for circular notches of different diameters.

In Chapter 3, the numerical models were used to guide the microstructure optimisation of TBDCs in order to improve their ultimate strength, by enhancing the stress transfer mechanisms between the tows. Ultra-thin and stiff carbon fibre tapes were used to manufacture TBDCs with mechanical properties that match those of continuous-fibre quasi-isotropic laminates, making them the TBDCs with the highest strength and stiffness reported in the literature.

For the first time in the literature, a model able to predict the full fatigue life of UD composites from constituent properties was proposed. Moreover, the efficient implementation of the model, allows for predictions of stochastic S-N curves of specimens with different sizes in less than 60 seconds.

8.6 Impact

The stochastic FE framework developed to predict the mechanical response of TBDC structures has been developed in a joint collaboration with Toyota Motor Europe. This framework is currently being implemented as a tool in Toyota's design ecosystem, enabling for a more streamlined design process of TBDC structures, and contributing to the reduction of certification through extensive and expensive experimental campaigns. Moreover, this framework is currently being used in undergraduate level projects at Imperial College London, focused on further improving its computational efficiency.

The development and manufacturing of the ultra-thin and stiff tape based discontinuous composites was a result of a collaboration with Chalmers University of Technology and with Oxeon AB (a Swedish composite manufacturer). Due to the high mechanical properties achieved, this work has demonstrated the possibility of using this class of TBDCs for primary structural applications, suitable for a wider range of part geometries when compared to continuous-fibre composites. Combining the advantage of a discontinuous CFRP material system with properties that match those of continuous CFRP laminates, can potentially open the use of high-performance composite materials to new industries with different manufacturability constraints. Moreover, the results of this collaborative work has attracted the interest of industrial leading car manufacturers; therefore, this has motivated other research projects at Imperial College London, Chalmers University of Technology and Oxeon AB, which focus on characterising the material properties under other loading conditions, and improving/streamlining the manufacturing process of these materials.

The fatigue model proposed in Chapter 7 can be used to support and provide essential insight for material design. The easy-to-use and efficient implementation of the model can assist manufacturers in optimising the fatigue resistance of UD composites (in the form of UD pre-pregs for instance), allowing for the design of more reliable and more durable composite structures. Moreover, the model was extended to predict damage accumulation under fatigue, (capturing the evolution of fibre-breaks and cluster development during fatigue loading), in a post-graduate project at Imperial College London

Chapter 9

Further work

9.1 Characterising and manufacturing of TBDCs for structural applications

The ultra-thin and stiff TBDC material systems manufactured in Chapter 3 were tested under longitudinal tension only. Characterising these material systems under compression and impact loadings is essential to allow for a reliable use of these materials in industrial applications. Moreover, assessing the improvement of the mechanical properties under compression and impact loadings of ultra-thin and stiff TBDCs over commercial available material systems, and comparing it to the improvements achieved under tension loadings would provide important insight for structural design and further material modelling.

The ultra-thin and stiff TBDCs were manufactured using dry carbon fibre tapes and ultra-thin resin films. The manufacturing process based on stacking equivalent laminates is time-consuming and not scalable. In order to improve the manufacturability of these materials, the ultra-thin tapes can be coated with a reactive binder, during their manufacturing process, containing the correct amount of resin to achieve a predefined fibre volume fraction; this would allow for the production of preforms which could be a possible route to scale up the manufacturing process.

The aforementioned activities are the scope of research projects that were initiated as a direct result of work described in this thesis. These research projects are a joint collaboration between Imperial College London, Chalmers University of Technology and Oxeon AB.

9.2 Broadening the applicability of the current stochastic FE framework for TBDCs

The failure criteria proposed in Chapter 5 only considers interactions between (longitudinal and transverse) tensile and shear loads, and can be extended to include the effect of compressive stresses. TBDCs fail under compression due to matrix cracking and buckling; including these failure mechanisms is important, as it would extend the applicability of the stochastic FE framework to model TBDC structures under more realistic and complex loadings.

The stochastic FE framework considers damage propagation in the material via a ply-discount method with no influence of the material's toughness. For this reason, it was shown in Chapter 6 that this assumption leads to under-prediction of the strength of TBDC structures with geometrical notches. Experimental results have been developed in the literature [5] to characterise the toughness of TBDC material systems. Therefore, developing a ply-discount method which ensures the correct energy dissipation (equal to the material's toughness) during the fracture process would further extend the applicability of the stochastic FE framework to models with geometrical notches.

The adaptive nonlocal averaging proposed in Chapter 6 adjusts the nonlocality of the nonlocal functions based on the local average gradient $|\nabla \bar{F}_{\mathrm{I}}|$ of the field of failure indices. However, the values of $|\nabla \bar{F}_{\mathrm{I}}|$ are dependent on the remote load/displacement applied, which inhibits the use of this method for independent linear elastic simulations. In order to achieve this, the dependency of $|\nabla \bar{F}_{\mathrm{I}}|$ on the remote load/displacement should be removed; this could potentially be achieved by an adequate normalisation of the field of $|\nabla \bar{F}_{\mathrm{I}}|$ using either the local values of F_{I} or an equivalent load/displacement. Moreover, the values of the nonlocal parameters used were calibrated for the HexMC material system, with a tow geometry of 50×8 mm (length × width). Understanding how the values of the nonlocal parameters are influenced by the material's microstructural features (such as the tow geometry) would further extend the applicability of this method.

9.3 Improvements to the analytical fatigue model

The fatigue model proposed in Chapter 7 considers fatigue crack propagation that initiate near fibre breaks and propagate (in mode-II) parallel to the fibre/matrix interface. This is a good assumption for composites with a more ductile matrix; however, for brittle matrices, mode-I cracks propagating parallel to the fibre fracture plane may interact with the cracks propagating along the fibre/matrix interface and alter the stress

redistribution in the fibres increasing their failure probability [83]. Including the influence of this transverse matrix cracks in the proposed model could increase the accuracy of the predicted stochastic S-N curves for a wider variety of material systems.

A Paris power law was used to model the debond propagation around fibre bundles; however, the influence of frictional shear stresses was neglected. Including the effect of friction during debond propagation under fatigue has been shown to have a significant effect on the debond growth [137], and could be included in the model to quantify its effect on the fatigue response of a UD composite.

Bibliography

[1] A. Bunsell, L. Gorbatikh, H. Morton, S. Pimenta, I. Sinclair, M. Spearing, Y. Swolfs, and A. Thionnet, "Benchmarking of strength models for unidirectional composites under longitudinal tension," *Composites Part A: Applied Science and Manufacturing*, vol. 111, pp. 138 – 150, 2018.

[2] "Hexcel corporation, HexMC User Guide, March 2014. Accessed: 2018-09-01,"

[3] L. Harper, D. Burn, M. Johnson, and N. Warrior, "Long discontinuous carbon fibre/polypropylene composites for high volume structural applications," *Journal of Composite Materials*, vol. 52, no. 9, pp. 1155–1170, 2018.

[4] M. Selezneva, K. Kouwonou, L. Lessard, and P. Hubert, "Mechanical properties of randomly oriented strands thermoplastic composites," in *ICCM19, Montreal, Canada*, July 2018.

[5] S. Pimenta, A. Ahuja, and A. Yong, "Damage tolerant tow-based discontinuous composites," in *ICCM20, Copenhagen, Denmark*, July 2015.

[6] Y. Wan and J. Takahashi, "Tensile and compressive properties of chopped carbon fiber tapes reinforced thermoplastics with different fiber lengths and molding pressures," *Composites Part A: Applied Science and Manufacturing*, vol. 87, pp. 271 – 281, 2016.

[7] L. Harper, T. Turner, N. Warrior, J. Dahl, and C. Rudd, "Characterisation of random carbon fibre composites from a directed fibre preforming process: Analysis of microstructural parameters," *Composites Part A: Applied Science and Manufacturing*, vol. 37, no. 11, pp. 2136 – 2147, 2006.

[8] L. de Otoa, "Carbon fibre innovation for high volumes: the forged composites," in *2nd International Composites Summit - Composites for Mass Production, Paris, March 2011*, March 2011.

[9] M. Selezneva and L. Lessard, "Characterization of mechanical properties of randomly oriented strand thermoplastic composites," *Journal of Composite Materials*, vol. 50, no. 20, pp. 2833–2851, 2016.

[10] P. Feraboli, E. Peitso, F. Deleo, T. Cleveland, and P. B. Stickler, "Characterization of prepreg-based discontinuous carbon fiber/epoxy systems," *Journal of Reinforced Plastics and Composites*, vol. 28, no. 10, pp. 1191–1214, 2009.

[11] Q. Composites, "AMC8590 Technical Data Sheet." `https://www.quantumcomposites.com/pdf/datasheets/amc/Quantum-AMC-8590%20126-76-8.pdf`, 2014. [Online; accessed 08-April-2019].

[12] ASDNews, "Nordam Pioneers Hexmc Composite Window Frames for Boeing 787 Dreamliner," 2007.

[13] P. Feraboli, F. Gasco, and B. Wade, ""Lamborghini "forged composite" technology for the suspension arms of the sesto elemento"," in *26th Annual Technical Conference of the American Society for Composites, Montreal, September 2011*, September 2011.

[14] S. Roy, A. Yousefpour, F. Bednar, and P. Beaulieu, "Compression Molding of Composite Tailboom Frames," in *70th American Helicopter Society International Annual Forum, Vol. 3, Montreal, May 2014*, May 2014.

[15] Y. Li, S. Pimenta, J. Singgih, S. Nothdurfter, and K. Schuffenhauer, "Experimental investigation of randomly-oriented tow-based discontinuous composites and their equivalent laminates," *Composites Part A: Applied Science and Manufacturing*, vol. 102, pp. 64–75, 2017.

[16] S. G. Kravchenko, D. E. Sommer, B. R. Denos, A. J. Favaloro, C. M. Tow, W. B. Avery, and R. B. Pipes, "Tensile properties of a stochastic prepreg platelet molded composite," *Composites Part A: Applied Science and Manufacturing*, vol. 124, p. 105507, 2019.

[17] Z. Chen, H. Tang, Y. Shao, Q. Sun, G. Zhou, Y. Li, H. Xu, D. Zeng, and X. Su, "Failure of chopped carbon fiber Sheet Molding Compound (SMC) composites under uniaxial tensile loading: Computational prediction and experimental analysis," *Composites Part A: Applied Science and Manufacturing*, vol. 118, no. December 2018, pp. 117–130, 2019.

[18] L. Harper, C. Qian, R. Luchoo, and N. Warrior, "3D geometric modelling of discontinuous fibre composites using a force-directed algorithm," *Journal of Composite Materials*, vol. 51, no. 17, pp. 2389–2406, 2017.

[19] Y. Li, Z. Chen, L. Su, W. Chen, X. Jin, and H. Xu, "Stochastic reconstruction and microstructure modeling of SMC chopped fiber composites," *Composite Structures*, vol. 200, no. May, pp. 153–164, 2018.

[20] M. Selezneva, S. Roy, S. Meldrum, L. Lessard, and A. Yousefpour, "Modelling of mechanical properties of randomly oriented strand thermoplastic composites," *Journal of Composite Materials*, vol. 51, no. 6, pp. 831–845, 2017.

[21] S. Kravchenko and B. Pipes, "Virtual tensile testing of prepreg platelet composite molded with stochastic morphology," *Sampe 2018*, no. May, 2018.

[22] P. Feraboli, T. Cleveland, P. Stickler, and J. Halpin, "Stochastic laminate analogy for simulating the variability in modulus of discontinuous composite materials," *Composites Part A: Applied Science and Manufacturing*, vol. 41, no. 4, pp. 557–570, 2010.

[23] Y. Li and S. Pimenta, "Development and assessment of modelling strategies to predict failure in tow-based discontinuous composites," *Composite Structures*, vol. 209, pp. 1005 – 1021, 2019.

[24] S. Pimenta and S. T. Pinho, "Recycling carbon fibre reinforced polymers for structural applications: Technology review and market outlook," *Waste Management*, vol. 31, no. 2, pp. 378 – 392, 2011. Environmental Implications of Alternative Materials in Construction and Treatment of Waste.

[25] R. Derosa, E. Telfeyan, and J. S. Mayes, "Current state of recycling sheet molding compounds and related materials," *Journal of Thermoplastic Composite Materials*, vol. 18, no. 3, pp. 219–240, 2005.

[26] S. Pickering, "Recycling technologies for thermoset composite materialscurrent status," *Composites Part A: Applied Science and Manufacturing*, vol. 37, no. 8, pp. 1206 – 1215, 2006. The 2nd International Conference: Advanced Polymer Composites for Structural Applications in Construction.

[27] Y. Li, S. Pimenta, M. Thierry, and W. Y. Tan, "Prediction of stiffness for tow-based discontinuous composites," in *ECCM17, Munich, Germany*, June 2016.

[28] M. Selezneva, S. Roy, L. Lessard, and A. Yousefpour, "Analytical model for prediction of strength and fracture paths characteristic to randomly oriented strand (ros) composites," *Composites Part B: Engineering*, vol. 96, pp. 103 – 111, 2016.

[29] Y. Wan, I. Straumit, J. Takahashi, and S. V. Lomov, "Micro-CT analysis of the orientation unevenness in randomly chopped strand composites in relation to the strand length," *Composite Structures*, 2018.

[30] S. Pimenta and P. Robinson, "An analytical shear-lag model for composites with 'brick-and-mortar' architecture considering non-linear matrix response and failure," *Composites Science and Technology*, vol. 104, pp. 111–124, 2014.

[31] S. G. Advani, "The use of tensors to describe and predict fiber orientation in short fiber composites," *Journal of Rheology*, vol. 31, no. 8, p. 751, 1987.

[32] J. Henry and S. Pimenta, "Modelling hybrid effects on the stiffness of aligned discontinuous composites with hybrid fibre-types," *Composites Science and Technology*, vol. 152, pp. 275 – 289, 2017.

[33] J. C. H. Affdl and J. L. Kardos, "The Halpin–Tsai equations: A review," *Polymer Engineering & Science*, vol. 16, no. 5, pp. 344–352.

[34] H. Hsiao and I. Daniel, "Elastic properties of composites with fiber waviness," *Composites Part A: Applied Science and Manufacturing*, vol. 27, no. 10, pp. 931 – 941, 1996.

[35] A. Kaddour and M. Hinton, "Maturity of 3d failure criteria for fibre-reinforced composites: Comparison between theories and experiments: Part b of wwfe-ii," *Journal of Composite Materials*, vol. 47, no. 6-7, pp. 925–966, 2013.

[36] ASTM International, "Standard test method for tensile properties of polymer matrix composite materials," West Conshohocken; PA, 2002.

[37] C. L. T. III and E. Liang, "Stiffness predictions for unidirectional short-fiber composites: Review and evaluation," *Composites Science and Technology*, vol. 59, no. 5, pp. 655 – 671, 1999.

[38] Y. Wan and J. Takahashi, "Tensile properties and aspect ratio simulation of transversely isotropic discontinuous carbon fiber reinforced thermoplastics," *Composites Science and Technology*, vol. 137, pp. 167 – 176, 2016.

[39] S. G. Kravchenko, D. E. Sommer, and R. B. Pipes, "Uniaxial strength of a composite array of overlaid and aligned prepreg platelets," *Composites Part A: Applied Science and Manufacturing*, vol. 109, pp. 31 – 47, 2018.

[40] G. J. Dvorak and N. Laws, "Analysis of Progressive Matrix Cracking In Composite Laminates II . First Ply Failure," *Journal of Composite Materials*, vol. 21, pp. 309–329, 1987.

[41] P. P. Camanho, C. G. Dávila, S. T. Pinho, L. Iannucci, and P. Robinson, "Prediction of in situ strengths and matrix cracking in composites under transverse tension and in-plane shear," *Composites Part A: Applied Science and Manufacturing*, vol. 37, pp. 165–176, 2006.

[42] A. Arteiro, G. Catalanotti, J. Reinoso, P. Linde, and P. P. Camanho, "Simulation of the mechanical response of thin-ply composites: From computational micro-mechanics to structural analysis," *Archives of Computational Methods in Engineering*, 2018.

[43] S. Sihn, R. Y. Kim, K. Kawabe, and S. W. Tsai, "Experimental studies of thin-ply laminated composites," *Composites Science and Technology*, vol. 67, pp. 996–1008, 2007.

[44] R. Amacher, J. Cugnoni, J. Botsis, L. Sorensen, W. Smith, and C. Dransfeld, "Thin ply composites: Experimental characterization and modeling of size-effects," *Composites Science and Technology*, vol. 101, pp. 121–132, 2014.

[45] Z. Chen, T. Huang, Y. Shao, Y. Li, H. Xu, K. Avery, D. Zeng, W. Chen, and X. Su, "Multiscale finite element modeling of sheet molding compound (smc) composite structure based on stochastic mesostructure reconstruction," *Composite Structures*, vol. 188, pp. 25 – 38, 2018.

[46] I. Taketa and H. Matsutani, "Effect of fiber length on the tensile strength of unidirectionally arrayed chopped strands," *Advanced Composite Materials*, vol. 0, no. 0, pp. 1–12, 2019.

[47] A. Kelly and W. Tyson, "Tensile properties of fibre-reinforced metals: Copper/tungsten and copper/molybdenum," *Journal of the Mechanics and Physics of Solids*, vol. 13, no. 6, pp. 329 – 350, 1965.

[48] J. Henry and S. Pimenta, "Semi-analytical simulation of aligned discontinuous composites," *Composites Science and Technology*, vol. 144, pp. 230 – 244, 2017.

[49] S. Pinho, R. Darvizeh, P. Robinson, C. Schuecker, and P. Camanho, "Material and structural response of polymer-matrix fibre-reinforced composites," *Journal of Composite Materials*, vol. 46, no. 19-20, pp. 2313–2341, 2012.

[50] Hexcel, "HexPly M77 Product Data." `https://www.hexcel.com/Resources/DataSheets/Prepreg`, 2017. [Online; accessed 04-April-2019].

[51] "Mitsubishi Chemical Carbon Fiber and Composites." `http://mccfc.com`, 2019. [Online; accessed 03-October-2019].

[52] "IMetrum, iMetrum LTD, Non Contact Precision Measurement. Simulia, 2018."

[53] Mitsubishi Chemical Corporation, "Pyrofil STR120 datasheet."

[54] L. Mencattelli and S. T. Pinho, "Ultra-thin-ply cfrp bouligand bio-inspired structures with enhanced load-bearing capacity, delayed catastrophic failure and high energy dissipation capability," *Composites Part A: Applied Science and Manufacturing*, p. 105655, 2019.

[55] Hexcel, "HexTow AS4 Product Data Sheet." `https://www.hexcel.com/user_area/content_media/raw/AS4_HexTow_DataSheet.pdf`, 2019. [Online; accessed 03-February-2020].

[56] P. Feraboli, E. Peitso, T. Cleveland, P. B. Stickler, and J. C. Halpin, "Notched behavior of prepreg-based discontinuous carbon fiber/epoxy systems," *Composites Part A: Applied Science and Manufacturing*, vol. 40, no. 3, pp. 289 – 299, 2009.

[57] C. Qian, L. Harper, T. Turner, and N. Warrior, "Notched behaviour of discontinuous carbon fibre composites: Comparison with quasi-isotropic non-crimp fabric," *Composites Part A: Applied Science and Manufacturing*, vol. 42, no. 3, pp. 293 – 302, 2011.

[58] S.-H. Jiang, D.-Q. Li, L.-M. Zhang, and C.-B. Zhou, "Slope reliability analysis considering spatially variable shear strength parameters using a non-intrusive stochastic finite element method," *Engineering Geology*, vol. 168, pp. 120 – 128, 2014.

[59] J. Zhang and B. Ellingwood, "Orthogonal series expansions of random fields in reliability analysis," *Journal of Engineering Mechanics*, vol. 120, no. 12, pp. 2660–2677, 1994.

[60] P. Spanos and A. Kontsos, "A multiscale monte carlo finite element method for determining mechanical properties of polymer nanocomposites," *Probabilistic Engineering Mechanics*, vol. 23, no. 4, pp. 456 – 470, 2008. Dedicated to Professor Ove Ditlevsen.

[61] S. H. R. Sanei and R. S. Fertig, "Uncorrelated volume element for stochastic modeling of microstructures based on local fiber volume fraction variation," *Composites Science and Technology*, vol. 117, pp. 191 – 198, 2015.

[62] GOM-GmbH, "Digital image correlation and strain computation basics," 2016.

[63] S. Sriramula and M. Chryssanthopoulos, "An experimental characterisation of spatial variability in gfrp composite panels," *Structural Safety*, vol. 42, pp. 1–11, 5 2013.

[64] U. Bronowicka-Mielniczuk, J. Mielniczuk, R. Obroślak, and W. Przystupa, "A comparison of some interpolation techniques for determining spatial distribution of nitrogen compounds in groundwater," *International Journal of Environmental Research*, vol. 13, pp. 679–687, Aug 2019.

[65] J. S. Cintra and C. L. Tucker, "Orthotropic closure approximations for flow-induced fiber orientation," *Journal of Rheology*, vol. 39, no. 6, pp. 1095–1122, 1995.

[66] L. M. Martulli, L. Muyshondt, M. Kerschbaum, S. Pimenta, S. V. Lomov, and Y. Swolfs, "Carbon fibre sheet moulding compounds with high in-mould flow:

Linking morphology to tensile and compressive properties," *Composites Part A: Applied Science and Manufacturing*, vol. 126, p. 105600, nov 2019.

[67] M. Zako, Y. Uetsuji, and T. Kurashiki, "Finite element analysis of damaged woven fabric composite materials," *Composites Science and Technology*, vol. 63, no. 3, pp. 507 – 516, 2003.

[68] Mitsubishi Chemical Corporation, "TR50s Datasheet."

[69] B. R. Denos, S. S. Kravchenko, and R. B. Pipes, "Progressive Failure Analysis in Platelet Based Composites Using CT-Measured Local Microstructure," in *International SAMPE Technical Conference*, (Seattle (WA)), 22-25 May, 2017.

[70] J. Whitney and R. Nuismer, "Stress fracture criteria for laminated composites containing stress concentrations," *Journal of Composite Materials*, vol. 8, no. 3, pp. 253–265, 1974.

[71] R. B. Pipes, R. C. Wetherhold, and J. John W. Gillespie, "Notched strength of composite materials," *Journal of Composite Materials*, vol. 13, no. 2, pp. 148–160, 1979.

[72] P. G. Potti, B. N. Rao, and V. Srivastava, "Notched tensile strength of randomly oriented e-glass composite laminates," *Materials Science and Engineering: A*, vol. 282, no. 1, pp. 59 – 66, 2000.

[73] P. Camanho, G. Erin, G. Catalanotti, S. Mahdi, and P. Linde, "A finite fracture mechanics model for the prediction of the open-hole strength of composite laminates," *Composites Part A: Applied Science and Manufacturing*, vol. 43, no. 8, pp. 1219 – 1225, 2012.

[74] A. C. Eringen, "On differential equations of nonlocal elasticity and solutions of screw dislocation and surface waves," *Journal of Applied Physics*, vol. 54, no. 9, pp. 4703–4710, 1983.

[75] G. Allegri and F. L. Scarpa, "On the asymptotic crack-tip stress fields in nonlocal orthotropic elasticity," *International Journal of Solids and Structures*, vol. 51, no. 2, pp. 504 – 515, 2014.

[76] G. PijaudierCabot and Z. P. Baant, "Nonlocal damage theory," *Journal of Engineering Mechanics*, vol. 113, no. 10, pp. 1512–1533, 1987.

[77] G. Pijaudier-Cabot and Z. P. Bazant, "Nonlocal damage theory," *Journal of Engineering Mechanics*, vol. 113, no. 10, pp. 1512–1533, 1987.

[78] S. Ko, K. Chan, R. Hawkins, R. Jayaram, C. Lynch, R. El Mamoune, M. Nguyen, N. Pekhotin, N. Stokes, D. N Wu, M. Tuttle, J. Yang, and M. Salviato, "Experimental and numerical characterization of the intra-laminar fracturing behavior in discontinuous fiber composite structures," University of Washington 2018.

[79] Z. P. Bazant, I. M. Daniel, and Z. Li, "Size effect and fracture characteristics of composite laminates," *Journal of Engineering Materials and Technology*, vol. 118, no. 3, pp. 317 – 324, 1996.

[80] G. Borino, B. Failla, and F. Parrinello, "A symmetric nonlocal damage theory," *International Journal of Solids and Structures*, vol. 40, no. 13, pp. 3621 – 3645, 2003.

[81] P. Grassl, D. Xenos, M. Jirsek, and M. Hork, "Evaluation of nonlocal approaches for modelling fracture near nonconvex boundaries," *International Journal of Solids and Structures*, vol. 51, no. 18, pp. 3239 – 3251, 2014.

[82] S. R. Hallett, B. G. Green, W.-G. Jiang, K. H. Cheung, and M. R. Wisnom, "The open hole tensile test: a challenge for virtual testing of composites," *International Journal of Fracture*, vol. 158, pp. 169–181, Aug 2009.

[83] E. K. Gamstedt and R. Talreja, "Fatigue damage mechanisms in unidirectional carbon-fibre-reinforced plastics," *Journal of Materials Science*, vol. 34, no. 11, pp. 2535–2546, 1999.

[84] E. K. Gamstedt, L. A. Berglund, and T. Peijs, "Fatigue mechanisms in unidirectional glass-fibre-reinforced polypropylene," *Composites Science and Technology*, vol. 59, no. 5, pp. 759–768, 1999.

[85] H. Kim, "Axial fatigue failure sequence and mechanisms in unidirectional fiberglass composites," *Journal of Composite Materials*, vol. 12, no. 2, pp. 139–152, 1978.

[86] Y. Al-Assaf and H. El Kadi, "Fatigue life prediction of unidirectional glass fiber/epoxy composite laminae using neural networks," *Composite Structures*, vol. 53, no. 1, pp. 65–71, 2001.

[87] Y. Shan and K. Liao, "Environmental fatigue behavior and life prediction of unidirectional glass-carbon/epoxy hybrid composites," *International Journal of Fatigue*, vol. 24, no. 8, pp. 847–859, 2002.

[88] A. Afaghi-Khatibi and Y.-W. Mai, "Characterisation of fibre/matrix interfacial degradation under cyclic fatigue loading using dynamic mechanical analysis," *Composites Part A: Applied Science and Manufacturing*, vol. 33, no. 11, pp. 1585 – 1592, 2002.

[89] Y. Shan, K. F. Lai, K. T. Wan, and K. Liao, "Static and dynamic fatigue of glass–carbon hybrid composites in fluid environment," *Journal of Composite Materials*, vol. 36, no. 2, pp. 159–172, 2002.

[90] Y. Zhou, "Fatigue strength characterization of E-glass fibers using fiber bundle test," *Journal of Composite Materials*, vol. 38, no. 22, pp. 2025–2035, 2004.

[91] Y. Meziere, A. R. Bunsell, Y. Favry, J. Teissedre, and A. T. Do, "Large strain cyclic fatigue testing of unidirectional carbon fibre reinforced epoxy resin," *Composites Part A: Applied Science and Manufacturing*, vol. 36, pp. 1627–1636, 2005.

[92] M. Quaresimin, L. Susmel, and R. Talreja, "Fatigue behaviour and life assessment of composite laminates under multiaxial loadings," *International Journal of Fatigue*, vol. 32, no. 1, pp. 2 – 16, 2010. Fourth International Conference on Fatigue of Composites (ICFC4).

[93] J. R. A. Tost, F. Heinrich, "Novel test method for characterization of unidirectional composite fatigue properties," in *European Conference on Composite Materials - ECCM17*, (Munich, Germany), June 2016.

[94] T. S. M. O. and C. P. M. S. T., "An overview of fatigue in aircraft structures," *Fatigue & Fracture of Engineering Materials & Structures*, vol. 40, no. 10, pp. 1510–1529.

[95] A. Somer and A. Bunsell, "The tensile and fatigue behaviour of carbon fibres," *Plastics Rubber Composites Processign and Applications*, vol. 18, p. 263, 1992.

[96] E. K. Gamstedt, "Effects of debonding and fiber strength distribution on fatigue-damage propagation in carbon fiber-reinforced epoxy," *Journal of Applied Polymer Science*, vol. 76, no. 4, pp. 457–474, 2000.

[97] R. Talreja and C. V. Singh, *Damage and Failure of Composite Materials*. Cambridge University Press, 2012.

[98] A. Pupurs, S. Goutianos, P. Brondsted, and J. Varna, "Interface debond crack growth in tension-tension cyclic loading of single fiber polymer composites," *Composites Part A: Applied Science and Manufacturing*, vol. 44, pp. 86 – 94, 2013.

[99] L. Zhuang, R. Talreja, and J. Varna, "Tensile failure of unidirectional composites from a local fracture plane," *Composites Science and Technology*, vol. 133, pp. 119 – 127, 2016.

[100] A. Bunsell, L. Gorbatikh, H. Morton, S. Pimenta, I. Sinclair, M. Spearing, Y. Swolfs, and A. Thionnet, "Benchmarking of strength models for unidirectional composites under longitudinal tension," *Composites Part A: Applied Science and Manufacturing*, 2018.

[101] P. A. Gradin and J. Backlund, "Fatigue debonding in fibrous composites," *International Journal of Adhesion and Adhesives*, pp. 154–158, 1981.

[102] A. DiBenedetto, "Measurement of the thermomechanical stability of interphases by the embedded single fiber test," *Composites Science and Technology*, vol. 42, no. 1, pp. 103 – 123, 1991. Special Issue Interfaces in Composites.

[103] R. A. Latour, J. Black, and B. Miller, "Fatigue behaviour characterization of the fibre-matrix interface," *Journal of Materials Science*, vol. 24, pp. 3616–3620, Oct 1989.

[104] A. Pupurs and J. Varna, "Unidirectional composite in mechanical fatigue: modelling debond growth from fibre breaks," *Plastics, Rubber and Composites*, vol. 39, no. 3-5, pp. 128–136, 2010.

[105] A. Amiri-Rad, M. Mashayekhi, and F. P. van der Meer, "Cohesive zone and level set method for simulation of high cycle fatigue delamination in composite materials," *Composite Structures*, vol. 160, pp. 61 – 69, 2017.

[106] L. F. Kawashita and S. R. Hallett, "A crack tip tracking algorithm for cohesive interface element analysis of fatigue delamination propagation in composite materials," *International Journal of Solids and Structures*, vol. 49, no. 21, pp. 2898–2913, 2012.

[107] R. Brighenti, A. Carpinteri, and D. Scorza, "Micromechanical crack growth-based fatigue damage in fibrous composites," *International Journal of Fatigue*, vol. 82, pp. 98 – 109, 2016. Fatigue at all Scales.

[108] L. Carreras, J. Renart, A. Turon, J. Costa, Y. Essa, and F. M. de la Escalera, "An efficient methodology for the experimental characterization of mode ii delamination growth under fatigue loading," *International Journal of Fatigue*, vol. 95, pp. 185 – 193, 2017.

[109] R. Panduranga and K. Shivakumar, "Mode-II total fatigue life model for unidirectional IM7/8552 carbon/epoxy composite laminate," *International Journal of Fatigue*, vol. 94, pp. 97 – 109, 2017.

[110] M. Hojo, Y. Matsushita, M. Tanaka, and T. Adachi, "Interfacial fatigue crack propagation in microscopic model composite using bifiber shear specimens," *Composites Part A: Applied Science and Manufacturing*, vol. 43, no. 2, pp. 239–246, 2012.

[111] B. W. Rosen, "Tensile failure of fibrous composites," *AIAA Journal*, vol. 2, pp. 169–177, 1964.

[112] Y. Swolfs, L. Gorbatikh, V. Romanov, S. Orlova, S. Lomov, and I. Verpoest, "Stress concentrations in an impregnated fibre bundle with random fibre packing," *Composites Science and Technology*, vol. 74, pp. 113 – 120, 2013.

[113] A. de Morais, "Prediction of the longitudinal tensile strength of polymer matrix composites," *Composites Science and Technology*, vol. 66, no. 15, pp. 2990 – 2996, 2006.

[114] S. Pimenta and S. T. Pinho, "Hierarchical scaling law for the strength of composite fibre bundles," *Journal of the Mechanics and Physics of Solids*, vol. 61, no. 6, pp. 1337–1356, 2013.

[115] S. Behzadi, P. T. Curtis, and F. R. Jones, "Improving the prediction of tensile failure in unidirectional fibre composites by introducing matrix shear yielding," *Composites Science and Technology*, vol. 69, no. 14, pp. 2421 – 2427, 2009. The Sixteenth International Conference on Composite Materials with Regular Papers.

[116] Y. Swolfs, R. M. McMeeking, I. Verpoest, and L. Gorbatikh, "Matrix cracks around fibre breaks and their effect on stress redistribution and failure development in unidirectional composites," *Composites Science and Technology*, vol. 108, pp. 16 – 22, 2015.

[117] W. I. Newman and A. M. Gabrielov, "Failure of hierarchical distributions of fibre bundles. 1," *International Journal of Fracture*, vol. 50, pp. 1–14, Jul 1991.

[118] H. E. Daniels, "The statistical theory of the strength of bundles of threads. i," *Proceedings of the Royal Society of London A: Mathematical, Physical and Engineering Sciences*, vol. 183, no. 995, pp. 405–435, 1945.

[119] C. Qian, T. Westphal, and R. P. Nijssen, "Micro-mechanical fatigue modelling of unidirectional glass fibre reinforced polymer composites," *Computational Materials Science*, vol. 69, pp. 62–72, 2013.

[120] P. Robinson, U. Galvanetto, D. Tumino, G. Bellucci, and D. Violeau, "Numerical simulation of fatigue-driven delamination using interface elements," *International Journal for Numerical Methods in Engineering*, vol. 63, no. 13, pp. 1824–1848, 2005.

[121] A. Turon, J. Costa, P. P. Camanho, and C. G. Dávila, "Simulation of delamination in composites under high-cycle fatigue," *Composites Part A: Applied Science and Manufacturing*, vol. 38, no. 11, pp. 2270–2282, 2007.

[122] P. W. Harper and S. R. Hallett, "A fatigue degradation law for cohesive interface elements – Development and application to composite materials," *International Journal of Fatigue*, vol. 32, no. 11, pp. 1774–1787, 2010.

[123] B. L. Bak, A. Turon, E. Lindgaard, and E. Lund, "A benchmark study of simulation methods for high-cycle fatigue-driven delamination based on cohesive zone models," *Composite Structures*, vol. 164, pp. 198–206, 2017.

[124] S. L. Ogin, "A model for the fatigue life and residual strength of unidirectional and cross-ply composite materials which fail by "wear-out" ," in *Fibre reinforced composites, 3rd International Conference*, (Liverpool, England), March, 1988.

[125] S. Garcea, I. Sinclair, and S. Spearing, "Fibre failure assessment in carbon fibre reinforced polymers under fatigue loading by synchrotron X-ray computed tomography," *Composites Science and Technology*, vol. 133, pp. 157 – 164, 2016.

[126] S. Pinho, P. Robinson, and L. Iannucci, "Fracture toughness of the tensile and compressive fibre failure modes in laminated composites," *Composites Science and Technology*, vol. 66, no. 13, pp. 2069 – 2079, 2006.

[127] S. Pimenta and S. T. Pinho, "An analytical model for the translaminar fracture toughness of fibre composites with stochastic quasi-fractal fracture surfaces," *Journal of the Mechanics and Physics of Solids*, vol. 66, no. 1, pp. 78–102, 2014.

[128] G.W.Weibull, "A statistical distribution function of wide applicability," *Journal of Applied Mechanics*, pp. 293 – 197, 1951.

[129] C. M. Landis and R. M. McMeeking, "A shear-lag model for a broken fiber embedded in a composite with a ductile matrix," *Composites Science and Technology*, vol. 59, no. 3, pp. 447–457, 1999.

[130] S. Spearing, P. Beaumont, and M. Ashby, "Fatigue damage mechanics of composite materials. II: A damage growth model," *Composites Science and Technology*, vol. 44, pp. 169–177, 1992.

[131] S. Deng, L. Ye, Y.-W. Mai, and H.-Y. Liu, "Evaluation of fibre tensile strength and fibre/matrix adhesion using single fibre fragmentation tests," *Composites Part A: Applied Science and Manufacturing*, vol. 29, no. 4, pp. 423–434, 1998.

[132] I. J. Beyerlein and S. L. Phoenix, "Statistics for the strength and size effects of microcomposites with four carbon fibers in epoxy resin," *Composites Science and Technology*, vol. 56, no. 1, pp. 75–92, 1996.

[133] "TenCate Advanced Composites. Datasheet: TenCate Cetex(R) TC1200 PEEK resin system," 2013, (accessed in December 2017).

[134] S. Pimenta, "A computationally efficient hierarchical scaling law to predict damage accumulation in composite fibre bundles," *Composites Science and Technology*, vol. 146, pp. 210–225, 2017.

[135] E. Armanios, R. Bucinell, D. Wilson, L. Asp, A. Sjogren, and E. Greenhalgh, "Delamination growth and thresholds in a carbon/epoxy composite under fatigue loading," *Journal of Composites Technology and Research*, vol. 23, no. 2, p. 55, 2001.

[136] H. Masaki, O. Shojiro, C. G. Gustafson, and T. Keisuke, "Effect of matrix resin on delamination fatigue crack growth in CFRP laminates," *Engineering Fracture Mechanics*, vol. 49, no. 1, pp. 35–47, 1994.

[137] B. F. Srensen and S. Goutianos, "Micromechanical model for prediction of the fatigue limit for unidirectional fibre composites," *Mechanics of Materials*, vol. 131, pp. 169 – 187, 2019.

[138] A. R. Khan, A. Cornea, L. A. Leigland, S. G. Kohama, S. N. Jespersen, and C. D. Kroenke, "3D structure tensor analysis of light microscopy data for validating diffusion MRI," *NeuroImage*, vol. 111, pp. 192–203, 2015.

[139] I. Straumit, S. V. Lomov, and M. Wevers, "Quantification of the internal structure and automatic generation of voxel models of textile composites from X-ray computed tomography data," *Composites Part A: Applied Science and Manufacturing*, vol. 69, pp. 150 – 158, 2015.

[140] B. R. Denos, D. E. Sommer, A. J. Favaloro, R. B. Pipes, and W. B. Avery, "Fiber orientation measurement from mesoscale ct scans of prepreg platelet molded composites," *Composites Part A: Applied Science and Manufacturing*, vol. 114, pp. 241 – 249, 2018.

[141] I. Straumit, *Prediction of the effective properties of textile composites based on X-ray computed tomography data.* PhD thesis, KU Leuven, Leuven, Belgium, 2017.

[142] H. C. Tseng, R. Y. Chang, and C. H. Hsu, "Improved fiber orientation predictions for injection molded fiber composites," *Composites Part A: Applied Science and Manufacturing*, vol. 99, pp. 65–75, 2017.

Appendix A

Microstructure generator appendices

A.1 Derivation of the condition for maximum fibre content during tow deposition

Replacing the expression for the local (i.e. at grid point j) normalised tow thickness ($\bar{t}_j^{\mathrm{t}}$ in Eq. 2.3.) into the expression for the normalised fibre volume fraction ($\bar{V}_j^{\mathrm{f}}$ in Eq. 2.4) yields

$$\bar{V}_j^{\mathrm{f}} = V^{\mathrm{f}} \frac{t_j^{\mathrm{t}}}{t^{\mathrm{s}}} \bar{N}_j^{\mathrm{t}}. \tag{A.1}$$

The ratio of specimen thickness t^{s} over nominal tow thickness t^{t} is, by definition, equal to the mean tow count of all grid points $\bar{N}^{\mathrm{t}}$:

$$\frac{t^{\mathrm{s}}}{t^{\mathrm{t}}} = \bar{N}^{\mathrm{t}}. \tag{A.2}$$

Replacing this equality into Eq. A.1 and rearranging with respect to the local tow count,

$$\bar{N}_j^{\mathrm{t}} = \frac{\bar{V}_j^{\mathrm{f}}}{V^{\mathrm{f}}} \bar{N}^{\mathrm{t}}. \tag{A.3}$$

Eq. A.3 defines a direct linear relationship between (i) the local tow count $\bar{N}_j^{\mathrm{t}}$ and (ii) the local fibre volume fraction $\bar{V}_j^{\mathrm{f}}$. Therefore, the maximum value of the two variables will occur at the same grid point j, and re-writing Equation A.3 at that point becomes

$$\max\{\bar{N}_j^{\mathrm{t}}\} = \frac{\max\{\bar{V}_j^{\mathrm{f}}\}}{V^{\mathrm{f}}} \bar{N}^{\mathrm{t}}. \tag{A.4}$$

Consequently, if one wants to impose that the maximum local fibre volume fraction does not exceed a certain threshold $V_{\mathrm{th}}^{\mathrm{f}}$, the following condition can be defined

$$\max\{\bar{N}_j^{\mathrm{t}}\} \leq \frac{V_{\mathrm{th}}^{\mathrm{f}}}{V^{\mathrm{f}}}\bar{N}^{\mathrm{t}}. \tag{A.5}$$

Eq. A.5 defines a condition to be verified at the end of the tow deposition process (i.e. after *all* tows are deposited); however, since this process follows a random *sequential* adsorption algorithm, it is more convenient to verify an equivalent condition after *each* tow is deposited, so that the deposition process can be corrected immediately if needed. Therefore, Eq. A.5 should be modified by replacing the *overall* mean tow count ($\bar{N}^{\mathrm{t}}$) with the mean tow count after *each* tow is deposited ($\bar{N}_i^{\mathrm{t}}$). This also requires a numerical adjustment to the right hand side of the condition, so that all grid points can receive at least one tow at the beginning of the tow deposition process (i.e. so that $\max\{\bar{N}_j^{\mathrm{t}}\} \geq 1$ is always verified). The condition for the maximum fibre content during tow deposition therefore becomes

$$\max\{\bar{N}_j^{\mathrm{t}}\} \leq \mathrm{floor}\left[\frac{V_{\mathrm{th}}^{\mathrm{f}}}{V^{\mathrm{f}}}\bar{N}^{\mathrm{t}}\right] + 1. \tag{A.6}$$

A.2 Auxiliary matrices for the stiffness model

The stiffness tensor of a non-wavy tow i in its local coordinates is given by

$$\mathbf{C}_{\mathrm{D}}^{\mathrm{l}} = {\mathbf{S}_{\mathrm{D}}^{\mathrm{l}}}^{-1} = \begin{bmatrix} \frac{1}{E_1^{\mathrm{D}}} & -\frac{\nu_{21}^{\mathrm{D}}}{E_2^{\mathrm{D}}} & -\frac{\nu_{31}^{\mathrm{D}}}{E_3^{\mathrm{D}}} & 0 & 0 & 0 \\ -\frac{\nu_{12}^{\mathrm{D}}}{E_1^{\mathrm{D}}} & \frac{1}{E_2^{\mathrm{D}}} & -\frac{\nu_{32}^{\mathrm{D}}}{E_3^{\mathrm{D}}} & 0 & 0 & 0 \\ -\frac{\nu_{13}^{\mathrm{D}}}{E_1^{\mathrm{D}}} & -\frac{\nu_{23}^{\mathrm{D}}}{E_2^{\mathrm{D}}} & \frac{1}{E_3^{\mathrm{D}}} & 0 & 0 & 0 \\ 0 & 0 & 0 & \frac{1}{G_{23}^{\mathrm{D}}} & 0 & 0 \\ 0 & 0 & 0 & 0 & \frac{1}{G_{13}^{\mathrm{D}}} & 0 \\ 0 & 0 & 0 & 0 & 0 & \frac{1}{G_{12}^{\mathrm{D}}} \end{bmatrix}^{-1}. \tag{A.7}$$

The Reuters matrix $\mathbf{R}$ and the out of plane transformation matrix $\mathbf{T}_\phi$ are given by [34]

$$\mathbf{R} = \begin{bmatrix} 1 & 0 & 0 & 0 & 0 & 0 \\ 0 & 1 & 0 & 0 & 0 & 0 \\ 0 & 0 & 1 & 0 & 0 & 0 \\ 0 & 0 & 0 & 2 & 0 & 0 \\ 0 & 0 & 0 & 0 & 2 & 0 \\ 0 & 0 & 0 & 0 & 0 & 2 \end{bmatrix}, \quad \mathbf{T}_\phi = \begin{bmatrix} m_\phi^2 & 0 & n_\phi^2 & 0 & 2m_\phi n_\phi & 0 \\ 0 & 1 & 0 & 0 & 0 & 0 \\ n_\phi^2 & 0 & m_\phi^2 & 0 & -2m_\phi n_\phi & 0 \\ 0 & 0 & 0 & m_\phi & 0 & -n_\phi \\ -m_\phi n_\phi & 0 & m_\phi n_\phi & 0 & m_\phi^2 - n_\phi^2 & 0 \\ 0 & 0 & 0 & n_\phi & 0 & m_\phi \end{bmatrix}, \tag{A.8}$$

with $m_\phi = \cos(\phi)$ and $n_\phi = \sin(\phi)$.

The in-plane transformation matrix $\mathbf{T}_\theta$ is given by

$$\mathbf{T}_\theta = \begin{bmatrix} m_\theta^2 & n_\theta^2 & 0 & 0 & 0 & 2m_\theta n_\theta \\ n_\theta^2 & m_\theta^2 & 0 & 0 & 0 & -2m_\theta n_\theta \\ 0 & 0 & 1 & 0 & 0 & 0 \\ 0 & 0 & 0 & m_\theta & -n_\theta & 0 \\ 0 & 0 & 0 & n_\theta & m_\theta & 0 \\ -m_\theta n_\theta & m_\theta n_\theta & 0 & 0 & 0 & m_\theta^2 - n_\theta^2 \end{bmatrix}, \tag{A.9}$$

with $m_\theta = \cos(\theta)$ and $n_\theta = \sin(\theta)$.

A.3 Details of the acquisition of the micro-CT images and measurement of the out-of-plane angle distributions

The micro-CT images presented in Section 2.3.2 were acquired using a XT H225 L micro-focus CT system, with a micro-focus 225 kV source fitted with a tungsten reflection target together with a Perkin Elmer XRD 1621 CN14 HS detector. The scan settings used were the following: 100 kVp, 156 µA, 177 ms exposure, 3142 projections acquired during a full 360° rotation using an average of 4 frames per projection. The source to object distance was set at 56 mm, with a source to detector distance of 750 mm, resulting in a 15 µm reconstructed voxel resolution. The reconstructions were performed using filtered back projection algorithms implemented within CTPro and CTAgent software packages (Nikon Metrology, UK). The sampled region of the specimens has a size of $[22 \times 7.2 \times 3]$ mm (length, width, thickness).

The structure tensor analysis infers local fibre orientations by analysing the gradients of the greyscale values (calculated through a finite difference scheme) of small windows within the reconstructed volume [138–140]. Figure A.1 shows the out of plane angle distributions calculated for two window sizes, $[0.5 \times 0.5 \times 0.2]$ mm and $[1 \times 1 \times 0.4]$

mm, where, for both cases, a Gaussian noise mitigation filter (with a normalised standard deviation $\sigma = 1.5$) was applied to each term of the structure tensor. Non-isotropic window sizes – smaller in the z direction than in the x and y directions – were used due to the fact that the thickness of the tows (in the z direction) is much smaller than the tow width and length (in the x and y directions); these non-isotropic window sizes were selected because they simultaneously (i) capture the high gradients of fibre orientations in the through-the-thickness direction (due to the smaller z dimension of the windows), and (ii) minimise the noise in the in-plane fibre orientations (due to the larger x and y dimensions of the windows).

Despite the volume difference of the two selected window sizes, the distributions obtained for both cases are very similar, supporting the choice of the range of window size values selected for the analysis in Section 2.3.2.

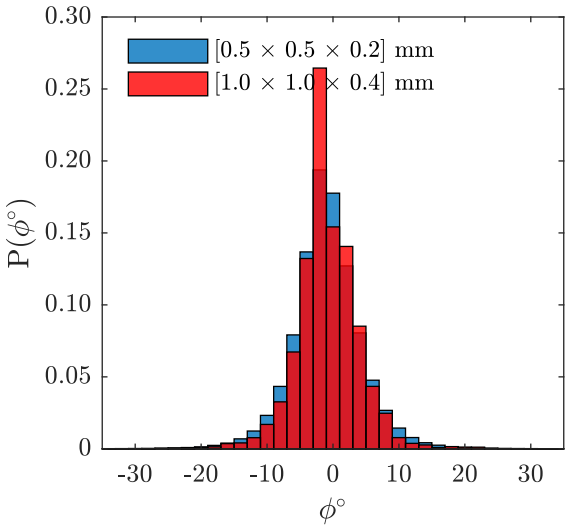

Figure A.1: Measured out of plane angles distributions for two different window sizes.

A.4 Volume fraction distributions measured from micro-CT volumes

The local variations of the fibre volume fraction V^{f} can be correlated to local variations in the greyscale values of volumes scanned by micro-CT [141]. The experimental fibre volume fraction distributions shown in Section 2.3.2.2 were obtained as follows:

1. definition of the average greyscale value of the matrix, g^{m}: this is done by analysing the greyscale values of several resin-rich regions of the micro-CT images. The value of g^{m} is taken as the average of the greyscale values of these regions.

2. definition of the average fibre volume fraction $\bar{V}^{\mathrm{f}}$ of the scanned specimen: the average fibre volume fraction of the material was obtained by analysing high-resolution micrographs of polished cross-sections (see Figure 2.4b), where each fibre's outline could be segmented. Two high-resolution cross-section micrographs (12×2 mm) were analysed, with measured average fibre volume fractions of 55.7 and 56.3%; given the consistency between these two values, the measurements were considered representative and the overall fibre volume fraction of the scanned specimen was taken as $\bar{V}^{\mathrm{f}} = 56\%$.

3. definition of the average greyscale value of the fibres, g^{f}: due to resolution limits, the characteristic greyscale value of the fibres can't be measured directly in the micro-CT scans, and is instead estimated based on the value of $\bar{V}^{\mathrm{f}}$. A large region of interest (where both fibres and matrix exist, and therefore a fibre volume fraction equal to $\bar{V}^{\mathrm{f}}$ is expected) is selected and its average greyscale value g^{R} is calculated; the value of g^{f} is then given by

$$g^{\mathrm{f}} = \frac{1}{\bar{V}^{\mathrm{f}}}[g^{R} - (1 - \bar{V}^{\mathrm{f}})g^{\mathrm{m}}]. \tag{A.10}$$

4. calculation of the local fibre volume fraction in small 3D windows: the reconstructed scanned volume is sub-divided into smaller windows of a predefined size; this is followed the calculation of the average greyscale value within each window g^{w}. Finally, the average fibre volume fraction of each window is calculated by,

$$V^{\mathrm{f}}(g^{\mathrm{w}}) = \frac{g^{\mathrm{w}} - g^{\mathrm{m}}}{g^{\mathrm{f}} - g^{\mathrm{m}}}. \tag{A.11}$$

   This method allows one to obtain a full spatial distribution of the fibre volume fraction across the entire scanned volume. The influence of the selected window size is shown in Figure A.2: two different window sizes were used and, for both, similar distributions of the local fibre volume fraction were obtained.

The accuracy of the fibre volume fraction calculated by this method is dependant on the calibration of average greyscale values of the fibres and matrix. Furthermore, due to the complexity of the microstructure, some artefacts may occur during the acquisition of the micro-CT images. For instance, the dependency of the fibres' attenuation values on their local orientation can affect the accuracy of calculating the volume fraction distributions based on local greyscale value variations.

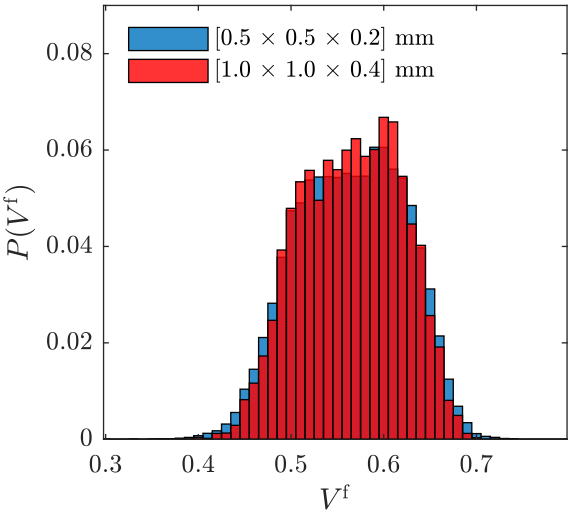

Figure A.2: Measured volume fraction distributions for two different window sizes.

A.5

The in-plane orientations (random, preferential orientation, and uni-directional) used in Figures 2.6 and 2.8f were defined by the following 2D orientation tensors:

$$a_{ij}^{\text{random}} = \begin{bmatrix} 0.5 & 0 \\ 0 & 0.5 \end{bmatrix}, \quad a_{ij}^{\text{preferential}} = \begin{bmatrix} 0.75 & 0 \\ 0 & 0.25 \end{bmatrix}, \quad a_{ij}^{\text{unidirectional}} = \begin{bmatrix} 1 & 0 \\ 0 & 0 \end{bmatrix}. \tag{A.12}$$

Appendix B

Orientation averaging technique

The orientation averaging technique proposed in [31] averages the (fourth order) stiffness tensor of a uni-directional element, which in the case of the work presented in this thesis is the stiffness of a UD discontinuous ply $\mathbf{C}_{\mathrm{D}}$, based on the fourth ($\mathbf{A}$) and second ($\mathbf{a}$) order fibre orientation tensors; this results in an stiffness tensor $\mathbf{C}_{\mathrm{TBDC}}$, and is given by

$$\begin{aligned} \mathrm{C}_{ijkl} =& B_1 A_{ijkl} + B_2(a_{ij}\delta_{kl}) + B_3(aik\delta_{jl} + ail\delta_{jk} + ajl\delta_{ik} + ajk\delta_{il}) + \\ & B_4(\delta_{ij}\delta_{kl} + B_5(\delta_{ik}\delta_{jl} + \delta_{il}\delta_{jk})). \end{aligned} \tag{B.1}$$

where the constants B_i are related to the components of the underlying unidirectional stiffness tensor, $\mathbf{C}_{\mathrm{D},ij}$ by the following expressions,

$$B_1 = \mathrm{C}_{\mathrm{D},11} + \mathrm{C}_{\mathrm{D},22} - 2\mathrm{C}_{\mathrm{D},12} - 4\mathrm{C}_{\mathrm{D},66} \tag{B.2a}$$

$$B_2 = \mathrm{C}_{\mathrm{D},12} + \mathrm{C}_{\mathrm{D},22} \tag{B.2b}$$

$$B_3 = \mathrm{C}_{\mathrm{D},66} + \frac{1}{2(\mathrm{C}_{\mathrm{D},23} - \mathrm{C}_{\mathrm{D},22})} \tag{B.2c}$$

$$B_4 = \mathrm{C}_{\mathrm{D},23} \tag{B.2d}$$

$$B_5 = \frac{1}{2(\mathrm{C}_{\mathrm{D},22} - \mathrm{C}_{\mathrm{D},23})} \tag{B.2e}$$

Appendix C

Process simulation of plates and fibre orientation mapping to the specimen mesh

Process simulations of the compression moulding of the HexMC and CF-SMC plates were performed. The software used is Moldex3D, which implements an improved Anisotropic Rotary Diffusion model (iARD) for the fibre orientation predictions [142]. Its parameters were calibrated to reproduce the average orientation tensor measured in the CF-SMC specimens, as explained in [66]. The calibrated parameters obtained in this way are presented in Table C.1. The same parameters are also used for the HexMC plate simulation. An planar random fibre orientation was set for the charges before the compression moulding process. Figure C.1 shows the results of both simulations, together with the location of the charges and the mapping locations of the specimens.

Table C.1: The calibrated parameters of the iARD model, used for the process simulation.

C_I	C_M	α
0.03	0.9	0.7

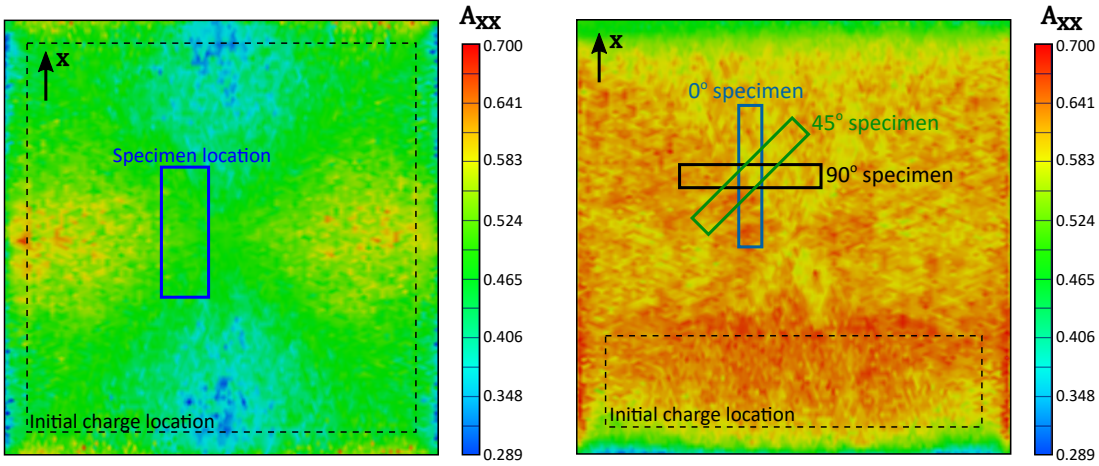

(a) Low-flow compression moulding simulation of the Hex MC material.

(b) High-flow compression moulding simulation of the CF-SMC material.

Figure C.1: Process simulation results.

Appendix D

Uncertainty of the definition of the notch failure region

The failure of a specimen in the FE framework is assumed to have failed at the notch if the location of the maximum value in the nonlocal F_{I} field occurs within a region close to the notch. The failure region defined in Figure 6.1b was defined based on the geometry of the notches; however, analysing the fracture of several notched specimens, as shown in figure D.1, one can see that the definition of the failure region is not necessarily bounded by the geometry of the notches due to the irregular crack path. In order to analyse the influence of the size of the failure region on the prediction evolution of the failure location for each notch type, an upper an lower bound was defined for the failure region (as shown in Figure D.1). The upper and lower bounds confine the crack paths of the specimens tested experimentally. Figure D.2 shows the influence of the size of the failure region on the prediction of the ratio of specimens that failure at the notch; it is shown that the numerical predictions do not change significantly when considering either the upper or lower bound for the failure region.

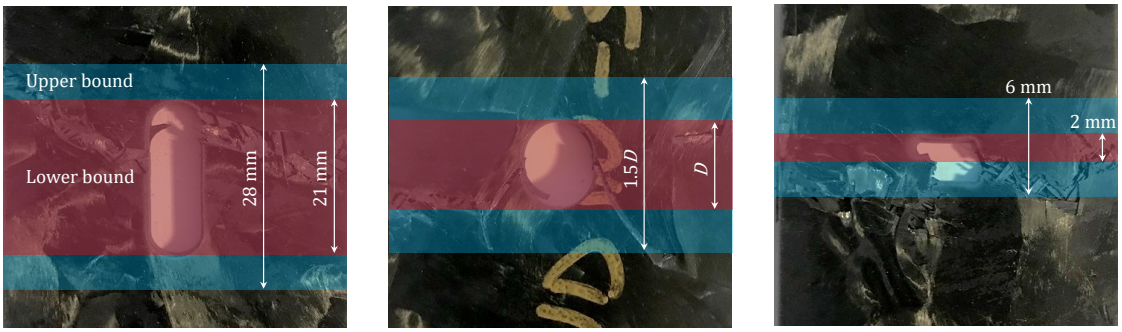

(a) Slotted notch. (b) Circular notch. (c) Sharp notch.

Figure D.1: Upper and lower bounds of the failure region for the different tested notched configurations.

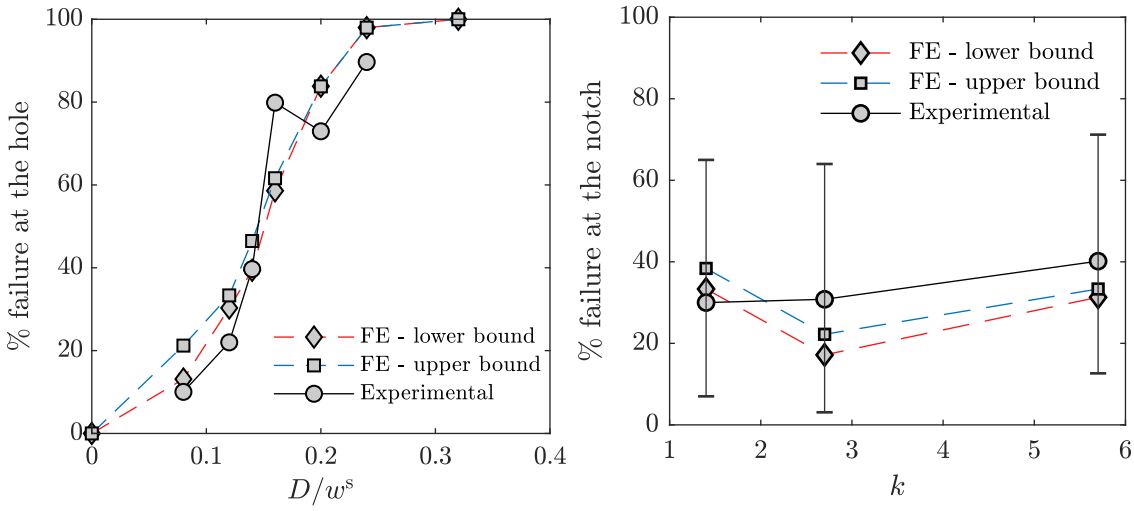

(a) Upper and lower bound for the predicted percentage of failures (with the nonlocal FE, $l_{\text{nl}} = 1.5\text{mm}$) that occurred at the hole, considering the upper and lower failure region bounds shown in Figure D.1b.

(b) Upper and lower bound for the predicted percentage of failures (with the adaptive nonlocal FE) that occurred at the notch, considering the upper and lower failure region bounds shown in Figure D.1.

Figure D.2: Influence of the size of the failure region in the numerical prediction of the ratio of notch failures for both the open hole and modified notch specimens.

Appendix E

Fatigue model appendices

E.1 Geometry of the cross-section of a fibre bundle

A level-$[i]$ sub-bundle with a fibre diameter ϕ^{f} and fibre volume fraction V^{f} has the following cross-sectional area (solely based on the fibres):

$$A^{[i]} = n^{[i]} \cdot A^{\mathrm{f}}, \qquad A^{\mathrm{f}} = \pi \frac{\left(\phi^{\mathrm{f}}\right)^2}{4}. \tag{A.1}$$

Considering a square fibre-packing and preferential interfacial failure (Figure E.1), the shear-lag perimeter $P^{[i]}$ of the sub-bundle is [114]:

$$\begin{aligned} &P^{[i]} = 3 \cdot P^{\mathrm{f}} + 4 \cdot \left[\left(\sqrt{n^{[i]} - 1} \right) \cdot t_{\mathrm{int}} + \left(\sqrt{n^{[i]} - 2} \right) \cdot \frac{P^{\mathrm{f}}}{2} \right], \quad \text{with} \\ &P^{\mathrm{f}} = \pi \cdot \phi^{\mathrm{f}} \quad \text{and} \quad t_{\mathrm{int}} = \left(\frac{\sqrt{\pi}}{2 \cdot \sqrt{V^{\mathrm{f}}}} - 1 \right) \cdot \phi^{\mathrm{f}}. \end{aligned} \tag{A.2}$$

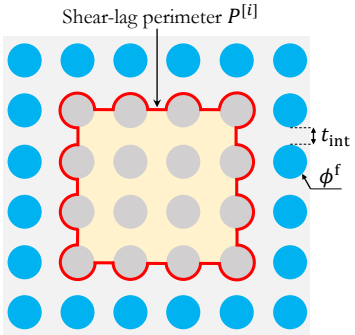

Figure E.1: Shear lag perimeter of a level-$[i]$ sub-bundle when considering a square fibre-packing and preferential interfacial failure [114].

E.2 Linear approximation to non-uniform stress fields near fibre/sub-bundle breaks

Figure E.2 shows the difference between (i) the analytical stress fields when a surviving fibre/sub-bundle undergoes non-uniform stress concentrations (Eq. 7.6c) and (ii) a linear approximation of those stress fields, which were assumed in the model (see Section 7.2.4.4). According to Eq. 7.6c, the actual (i.e. non-linear) stress fields in the surviving fibre/sub-bundle after the static loading cycle are

$$\sigma^{\mathcal{B}}(x) = \sigma^{\infty} + \frac{\tau_{\text{int}}}{\lambda^{[i]} T^{[i]}} \sin\left(\lambda^{[i]} \left[\frac{l_{\text{e}}^{[i]}}{2} - x\right]\right), \quad \text{for } |x| < l_{\text{e}}^{[i]}(\sigma^{\infty}, R^{\infty}, 0). \tag{B.3}$$

Following the WLT extended to non-uniform stresses [114], the survival probability of the fibre/sub-bundle under $\sigma^{\mathcal{B}}(x)$ ($S_{\text{K},0}(\sigma^{\infty})$) can be calculated from

$$\ln[S_{\text{K},0}^{[i]}(\sigma^{\infty})] = \frac{2}{l_{\text{e}}^{[i]}(\sigma^{\infty})} \int_{x=0}^{\frac{l_{\text{e}}^{[i]}}{2}} \ln[S_{\text{U},0}^{[i]}(\sigma^{\mathcal{B}})] \mathrm{d}x. \tag{B.4a}$$

Changing the integration variable to $\sigma^{\mathcal{B}}$,

$$x = \frac{1}{\lambda^{[i]}} \cdot \operatorname{asin}\left(\frac{\lambda^{[i]} \cdot T^{[i]}[\sigma^{\mathcal{B}} - \sigma^{\infty}]}{\tau_{\text{int}}}\right) \Rightarrow \mathrm{d}x = \frac{T^{[i]}}{\tau_{\text{int}} \sqrt{1 - \frac{[(\sigma^{\mathcal{B}} - \sigma^{\infty}) \cdot \lambda^{[i]} \cdot T^{[i]}]^2}{(\tau_{\text{int}})^2}}} \mathrm{d}\sigma^{\mathcal{B}}, \tag{B.4b}$$

thus

$$\ln[S_{\text{K,e}}^{[i]}(\sigma^{\infty})] = \frac{l_{\text{e}}^{[i]}}{l_0^{\text{f}}} \cdot \frac{T^{[i]}}{\tau_{\text{int}} \cdot \frac{l_{\text{e}}^{[i]}}{2}} \int_{\sigma^{\mathcal{B}}=\sigma^{\infty}}^{2\sigma^{\infty}} \frac{\ln[S_{\text{U},0}^{[i]}(\sigma^{\mathcal{B}})]}{\sqrt{1 - \left[\frac{(\sigma^{\mathcal{B}} - \sigma^{\infty}) \cdot \lambda^{[i]} \cdot T^{[i]}}{(\tau_{\text{int}})}\right]^2}} \mathrm{d}\sigma^{\mathcal{B}}. \tag{B.4c}$$

This expression can be used to evaluate $\ln[S_{\text{K,e}}^{[i]}(\sigma^{\infty})]$ numerically, considering the non-linear stress field $\sigma^{\mathcal{B}}(x)$ defined in Eq. 7.6c and B.3. This allows us to assess the accuracy of the linear approximation made in Eq. 7.20 to calculate $\ln[S_{\text{K,e}}^{[i]}(\sigma^{\infty})]$, with the results shown in Figure 7.8a.

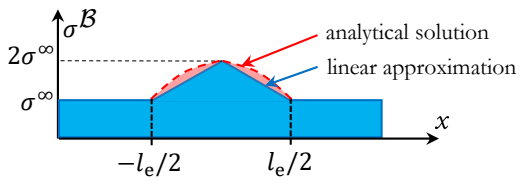

Figure E.2: Comparison between the linear approximation and the analytical solution of stress concentration stress fields in the surviving fibre/sub-bundle $\mathcal{B}$.